# Development and Use of Polarized Light Methods to Assess Structure and Composition of Biological Tissue

By

Michael F. G. Wood

A thesis submitted in conformity with the requirements for the degree of Doctor of Philosophy, Department of Medical Biophysics, University of Toronto

©Copyright by Michael F. G. Wood (2011)

# Abstract

Development and Use of Polarized Light Methods to Assess Structure and Composition of Biological Tissue

Michael F. G. Wood

Doctor of Philosophy

Department of Medical Biophysics
University of Toronto

2011

The use of polarized light for characterization of biological tissues has received increased attention in recent years due to the wealth of information available in the interactions of polarized light with tissue and the noninvasive nature of optical radiation. While the depolarizing effects of multiple scattering complicate the use of polarimetry in tissue, many biological constituents affect the polarization of light such as collagen, muscle fibers, and glucose. Thus, if the effects of scattering can be accounted for—or utilized in the analysis—polarized light can potentially be used as a probe of tissue status.

This thesis presents advancements in the techniques for the simulation of polarized light in tissue-simulating media, and explores two biomedical applications. Previous Monte Carlo models for simulation of polarized light propagation in tissue-simulating media do not include the effects of birefringence and optical activity, two polarizing effects of useful diagnostic potential. To overcome this limitation, our model was extended to include both these effects *simultaneously*, and then experimentally validated using a novel polarization phantom system. The use of polarized light for characterization of the myocardium, and specifically towards monitoring stem cell

regenerative treatments of myocardial infarction, was investigated experimentally as a novel application for polarimetry. The potential for this technique is based on the changes in myocardial structure that occur with infarction and subsequent regeneration, and the associated changes in tissue birefringence. The use of polarized light for noninvasive tissue analyte monitoring, particularly glucose, was also investigated based on the optical activity exhibited by many tissue analytes due to their chiral structure. In this study, a novel combined optical polarization and intensity approach was developed and tested on Monte Carlo simulated data. The studies presented in thesis introduce new methods for polarization simulation and analysis in biological tissue and demonstrate potential for polarimetry in monitoring myocardial regeneration and noninvasive measurements of tissue analytes.

*To Laura, my inspiration*

# Acknowledgements

Pursuing research as part of the Biophysics and Bioimaging group at the Ontario Cancer Institute and in the Department of Medical Biophysics has been an amazing experience. To work in such a multidisciplinary department has been an opportunity for which I am tremendously grateful.

My colleagues in our research group have provided so much assistance and support throughout my graduate studies and this work would not have been possible without them. Dr. Daniel Côté, Dr. Xinxin Guo, Dr. Nirmalya Ghosh, Dr. Robert Weersink, Dr. Brian Wilson, Dr. Eduardo Moriyama, Dr. Margarete Akens, Dr. Kai Zhang, Dr. Beau Standish, Luc Charron, Mathieu Roy, Shannon Dang, Nasit Vurgun, Dr. Anthony Kim, Dr. Adrian Mariampillai, and many other past and present members of our group, thank you all for your assistance and support.

To my supervisor, Dr. Alex Vitkin, thank you for taking me on as your student and guiding me through this long process. You have given me the perfect balance of support to pursue my own scientific interests and leadership when my ideas go awry. Thank you for countless meetings, editing of manuscripts, and being so readily available. Also, thank you to my committee members, Dr. Lothar Lilge and Dr. Don Plewes, your guidance throughout this process has been invaluable, and your time commitments are greatly appreciated.

Portions of this thesis were a collaborative effect with colleagues at the McEwen Centre for Regenerative Medicine, part of the Toronto General Research Institute. This

collaboration has been exciting and fruitful. Dr. Ren-Ke Li, Dr. Richard Wiesel, Dr. Jun Wu, and Shu-Hong Li, it has been a pleasure to work with you.

The financial support from the National Science and Engineering Research Council of Canada, the Canadian Foundation for Innovation, Ontario Centres of Excellence, and the Ontario Graduate Scholarship program is gratefully acknowledged.

Thank you to my family for your encouragement and assistance throughout my now long education, in particular my parents and my Great Aunt Ilse. Finally, thank you to my wife Laura and my new son Gabriel for your unconditional support and belief in me, you are my inspiration.

# Table of Contents

ABSTRACT ii

ACKNOWLEDGEMENTS v

TABLE OF CONTENTS vii

TABLE OF FIGURES ix

ABBREVIATIONS USED IN THESIS xi

FORMAT OF THESIS AND LIST OF RESULTING PUBLICATIONS xii

**1. INTRODUCTION 1**

**1.1 Overview of polarized light in biomedical optics 1**
1.1.1 Polarized light mathematics: Stokes-Mueller calculus 2
1.1.2 Polarized light effects in biological tissue 4
1.1.3 Biomedical applications 8

**1.2 Extending Monte Carlo model of polarized light propagation in tissue-like media 12**
1.2.1 Modeling polarized light propagation in tissue 13
1.2.2 Extending model to include optical activity and birefringence 16

**1.3 Polarimetric characterization of myocardial structure for monitoring regenerative treatments 18**
1.3.1 Myocardial infarction and regenerative (stem cell) treatments 19
1.3.2 Polarized light for myocardial structural characterization 23

**1.4 Non-invasive glucose monitoring with polarized light 26**
1.4.1 Diabetes mellitus and noninvasive glucose monitoring 26
1.4.2 Polarized light for glucose concentration determination 30

**2. EXTENSION OF POLARIZATION-SENSITIVE MONTE CARLO MODEL 33**

**3. CHARACTERIZATION OF MYOCARDIAL TISSUE STRUCTURE 48**

**3.1 Proof-of-Principle Feasibility Study 48**

**3.2 Point polarization measurements on myocardial tissues 52**

**3.3 Imaging polarization measurements on myocardial tissues 67**

**3.4 Influence of birefringence orientation and tissue fixation 84**
3.4.1 Orientation of birefringence 84
3.4.2 Tissue fixation 88

**3.5 Proof-of-Principle in vivo characterization of dermal tissue structure 93**

## 4. MODELING-BASED POLARIZED LIGHT TISSUE ANALYTE CONCENTRATION DETERMINATION 101

**4.1 Combined polarization and intensity approach 101**

**4.2 Separating chirality-induced and scattering-induced optical rotation 113**

## 5. SUMMARY, FUTURE WORK, AND CONCLUSIONS 115

**5.1 Extension of Monte Carlo model 115**
5.1.1 Summary 115
5.1.2 Future Work 116

**5.2 Characterization of myocardial tissue structure 118**
5.2.1 Summary 118
5.2.2 Future Work 119

**5.3 Tissue analyte concentration determination 127**
5.3.1 Summary 127
5.3.2 Future Work 129

**5.4 Conclusions and Accomplishments 130**

## APPENDIX A: EXAMPLE OF FORWARD AND REVERSE MUELLER MATRIX ANALYSIS 132

**A.1 Mueller matrix generation 132**
A.1.1 Scattering 133
A.1.2 Birefringence 134
A.1.3 Optical activity 134
A.1.4 Mueller matrix generation 135

**A.2 Mueller matrix decomposition 136**
A.2.1 Diattenuation 136
A.2.2 Depolarization 137
A.2.3 Linear retardance and optical rotation 138

**A.3 Summary 139**

**References 141**

# Table of Figures

**Fig. 1** Reference frame to express the polarization of a beam of light. The complex electric field $E$ is decomposed along two arbitrary orthogonal axes $\hat{e}_{\perp}$ and $\hat{e}_{\parallel}$ into directional field components $E_{\perp}$ and $E_{\parallel}$. …… 3

**Fig. 2** Illustration of angle $\phi$, made between the horizontal in the laboratory reference frame $\hat{e}_{\parallel}$ and the birefringent axis b (direction of varying refractive index). …… 7

**Fig. 3** Schematic representation of photon events modeled. The extension of the model for simultaneous modeling of birefringence and optical activity involved upgrades to the medium effects portion of the model, highlighted in red. ……... 15

**Fig. 4** Overview of myocardial infarction (heart attack) as a result of a coronary artery occlusion, in this case a blood clot lodging in a plaque. …… 20

**Fig. 5** Overview of remodeling as a result of myocardial infarction. The left ventricle after infarction in B shows scar formation, while C shows scar expansion, ventricular dilation, and myocardial wall thinning which occur as the infarct matures. …….. 20

**Fig. 6** Masson's trichrome histology of an axial section from an infracted rat heart four weeks post infarction. Muscle is stained red and collagen is stained blue. The infarction is evident by ventricular wall thinning and an increase in collagen content. ……... 22

**Fig. 7** Schematic of glucose regulator system. Diabetes disrupts either the production of, or the response to, insulin, resulting in the inability of cells to properly uptake glucose. Also shown is effect of glucagon, which works in opposition to insulin, in stimulating the break down of glycogen in the liver into glucose. …… 27

**Fig. 8** Retardance measurements on healthly, marginal, and infarcted regions of mouse myocardium sections. …… 51

**Fig. 9** Results of point measurements, error bars are the standard deviation. Results are for control (n = 4), stem cell treated (n = 3), and stem cell transfected with elastin treated (n = 4) myocardial samples. Asterisk denotes statistical significance ($p < 0.05$) with respect to the control. Note the additional increase in retardance (birefringence) with elastin transfection. ……. 80

**Fig. 10** Representative retardance image (a) for a stem cell transfected with elastin treated section with corresponding Masson's trichrome (b) stained histology image (collagen in blue, muscle in red). Retardance values are given in radians. …….. 81

**Fig. 11** Mean ± one standard deviation retardance pixel values from retardance images from health, marginal, and infracted regions. Results are for control (n = 4), stem cell treated (n = 3), and stem cell transfected with elastin treated (n = 4) animals, * denotes statistical significance ($p < 0.05$) with respect to the corresponding control. …… 82

**Fig. 12** Representative nonlinear microscopy image from infarcted regions of myocardial sample treat with stem cells transfected with elastin. The TPEF signal from cardiomyocytes is shown in red pseudo-color and the SHG from collagen is shown in green pseudo-color. …. 83

**Fig. 13** Monte Carlo simulation geometry. The medium was defined as an infinite slab in the x-y plane with optical properties mimicking the myocardium. The orientation of birefringence was varied from along the y-axis to the z-axis by angle $\varphi$. …….. 86

**Fig. 14** Monte Carlo simulated retardance values as a function of birefringence orientation $\varphi$ (0 deg, perpendicular to input beam, 90 deg, parallel to input beam). …… 87

**Fig. 15** Percent change (relative to fresh) of mean linear retardance and depolarization of porcine myocardium 1 day and 6 days post fixation. Error bars are the standard deviation.… 90

**Fig. 16** Percent change (relative to fresh) of mean linear retardance and depolarization of porcine liver 1 day and 6 days post fixation. Error bars are the standard deviation……. 92

**Fig. 17** Schematic of proposed dual PEM point measurement system: P, polarizers; $W_{p,}$ quarter waveplate; PEM, photoelastic modulators; and D, photodetector. The PEM modulator axes are oriented at 45 deg to each other. The system is shown in transmission mode; however, the detection optics could placed at any geometry. ……. 123

**Fig. 18** Schematic of proposed dual PEM imaging system: P, polarizers; $W_{p,}$ quarter waveplate; and PEM, photoelastic modulators. The PEMs modulator axes at the same orientation, however, have modulation frequencies differing by several to a few hundred Hz. The system is shown in transmission mode; however, the detection optics could placed at any geometry. …. 125

**Fig. 19** Schematic of proposed stroboscopic PEM imaging system: P, polarizers; $W_{p,}$ quarter waveplate; and PEM, photoelastic modulator. The PEM modulation signal is input to the pulse generator which turn drives a pulsed light source (e.g., diode laser). The system is shown in transmission mode; however, the detection optics could placed at any geometry. ….. 125

**Fig. 20** Schematic of possible catheterized polarimetry probe system. The input optics focus the light emitted from the fiber and control the polarization of the light incident on the tissue. The detection optics collect light emitted from the tissue and select for polarization detection states. …… 127

## Abbreviations Used in Thesis

3D – Three-Dimensional

APD – Avalanche Photodiode

CCD – Charge-Coupled Device

DNA – Deoxyribonucleic Acid

ECG – Electrocardiogram

HeNe – Helium-Neon

MB-PLS – Multiblock Partial Least Squares

MCML – Monte Carlo for Multi-Layered Media

MIR – Mid-Infrared

MRI – Magnetic Resonance Imaging

NIR – Near-Infrared

OCT – Optical Coherence Tomography

ORD – Optical Rotatory Dispersion

PEM – Photoelastic Modulator

PLS – Partial Least Squares

PS-OCT – Polarization-Sensitive Optical Coherence Tomography

RMSE – Root Mean Square Error

SHG – Second Harmonic Generation

SNR – Signal-to-Noise Ratio

TPEF – Two-Photon Excited Fluoresence

U-PLS – Unfold Partial Least Squares

## Format of Thesis and List of Resulting Publications

This thesis begins with an introductory chapter on polarized light and the use of polarized light in biomedical optics. The introductory chapter continues with an introduction to the three problems addressed in the following chapters, specifically: extending our Monte Carlo model to simulate the effects of birefringence and optical activity simultaneously in the presence of scattering, polarized light birefringence measurements for characterizing the myocardium, and the use of light polarization and intensity measurements for glucose monitoring. The format of each chapter in the body of the thesis includes: (1) a short introduction to the research study, (2) the corresponding peer-reviewed paper as it appears in its respective journal and (3) an addendum to the research study. The final thesis chapter provides summaries and conclusion and outlines future work.

**Publications appearing in this thesis:**

1. **M. F. G. Wood**, X. Guo, and I. A. Vitkin, "Polarized light propagation in multiply scattering media exhibiting both linear birefringence and optical activity: Monte Carlo model and experimental methodology," *J. Biomed. Optics* **12**, 014029 (2007). **(Chapter 2)**

2. N. Ghosh*, **M. F. G. Wood***, S. H. Li, R. D. Weisel, B. C. Wilson, R. K. Li, and I. A. Vitkin, "Mueller matrix decomposition for polarized light assessment of biological tissues," *Journal of Biophotonics* **2**, 145-156 (2009). **(Chapter 3.2)**
   * Authors contributed equally to this work and shared 1st authorship

3. **M. F. G. Wood,** N. Ghosh, M. Wallenburg, S. H. Li, R. D. Weisel, B. C. Wilson, R. K. Li, and I. A. Vitkin, "Polarization birefringence measurements for characterizing the myocardium, including healthy, infarcted, and stem cell regenerated tissues," *Journal of Biomedical Optics* **15**, 047009 (2010). **(Chapter 3.3.)**

4. **M. F. G. Wood**, N. Ghosh, E. H. Moriyama, B. C. Wilson, and I. A. Vitkin, "Proof-of-principle demonstration of a Mueller matrix decomposition method for

polarized light tissue characterization *in vivo*," *J. Biomed. Optics* **14**, 014029 (2009). **(Chapter 3.5)**

5. **M. F. G. Wood**, D. Côté, and I. A. Vitkin, "Concentration determination in simulated optically clear and turbid biological media," *J. Biomed. Optics* **13**, 044037 (2008). **(Chapter 4)**

**Conference proceedings:**

1. **M. F. G. Wood**, N. Ghosh, X. Guo, and I. A. Vitkin, "Phantoms for Polarized Light Exhibiting Controllable Scattering, Birefringence, and Optical Activity," *Proceedings of SPIE*, Photonics West, 6870-15 (2008).

2. **M. F. G. Wood,** N. Ghosh, S. H. Li, R. D. Weisel, B. C. Wilson, R. K. Li, and I. A. Vitkin, "Polarized light based birefringence measurements for monitoring myocardial regeneration," *Proceedings of SPIE*, 7179-7, Photonics West (2009).

**Additional publications arising from this thesis:**

1. X. Guo, **M. F. G. Wood**, and I. A. Vitkin, "Angularly-resolved linear Stokes polarimeter measurements of light scattered by turbid chiral media," *Journal of Biomedical Optics* **11**, 041105 (2006).

2. X. Guo, **M. F. G. Wood**, and I. A. Vitkin, "Monte Carlo study of pathlength distribution of polarized light in turbid chiral media," *Optics Express* **12**, 1348-1360 (2007).

3. X. Guo, **M. F. G. Wood**, and I. A. Vitkin, "Stokes Polarimetry in multiply scattering chiral media: effect of experimental geometry." *Applied Optics* **46**, 4491-4500 (2007).

4. X. Guo, **M. F. G. Wood,** and I. A. Vikin, "A Monte Carlo study of penetration depth and sampling volume of polarized light in turbid media," *Optics Communications* **281**, 380-386 (2008).

5. N. Ghosh, **M. F. G. Wood**, and I. A. Vitkin, "Simultaneous determination of linear retardance and optical rotation in birefringent, chiral, turbid media using Mueller matrix polarimetry: combined Monte Carlo and experimental methodolgy," *Journal of Biomedical Optics* **13**, 044036 (2008).

6. N. Ghosh, **M. F. G. Wood**, and I. A. Vitkin, "Polarimetry in turbid, birefringent, optically active media: a Monte Carlo study of Mueller matrix decomposition in the backscattering geometry," *Journal of Applied Physics* **105**, 102023 (2009).

7. B. Standish, K. Lee, J. Xiao, A. Mariampillai, N. Munce, **M. F. G. Wood**, B. C. Wilson, I. A. Vitkin, and V. Yang, "Interstitial Doppler optical coherence tomography as a local tumor necrosis predictor in photodynamic therapy of prostatic carcinoma: an *in vivo* study," *Cancer Research* **68**: 9987-9995 (2008).

8. X. Guo, M. F. G. **Wood**, N. Ghosh, and I. A. Vitkin, "Depolarization of light in turbid media: a scattering event resolved Monte Carlo study," *Applied Optics* **49**, 153-162 (2010).

9. N. Ghosh, **M. F. G. Wood**, I. A. Vitkin, "Influence of the order of the constituent basis matrices on the Mueller matrix decomposition-derived polarization parameters in complex turbid media such as biological tissues," *Optics Communications* **283**, 1200-1208 (2010).

10. M. A. Wallenburg, M. Pop, **M. F. G. Wood**, N. Ghosh, G. Wright, and I. A. Vitkin, "Comparison of optical polarimetry and diffusion tensor MR imaging for assessing myocardial anisotropy," *Journal of Innovative Optical Health Sciences* **3**, 109-121 (2010).

# 1. Introduction

This introductory chapter provides the background and motivation for this thesis. An overview of polarized light is first given along with a review of the current biomedical application of polarized light. This is followed by an introduction to each of the three thesis chapters: Monte Carlo model extension, characterization of myocardial tissue for monitoring regenerative treatments, and combined polarization and intensity based glucose monitoring.

## 1.1 Overview of polarized light in biomedical optics

Christiaan Huygens first put the concept of light polarization forward in 1690 to explain the effect of double refraction in calcite crystals, observed 21 years earlier by Rasmus Bartholinus.[1,2,3] While Huygen's theory was ultimately incomplete, it was the first to suggest the polarization of light. Sir Isaac Newton's treatise on optics[4] put forth the corpuscular or particle theory of light, and suggested that double refraction could be explained if particles of light were asymmetric. Later in 1808 Etienne-Louis Malus suggested that the light particles had poles, and thus referred this oriented light as polarized light.[5] In 1821 Augustin-Jean Fresnel demonstrated that the observed properties of light could only be explained if light was a transverse and thus polarized wave, rather than a particle or longitudinal wave as previously suggested.[6] A more complete understanding of light polarization was not reached until the theory of electromagnetism was developed by James Clerk Maxwell in 1873,[7] and confirmed with experiments by

Heinrich Hertz in 1888. Maxwell's electromagnetic theory was largely considered complete until the discovery of photons and wave-particle duality as part of quantum theory in the early twentieth century. While advent of quantum theory has not changed the representation and analysis of light polarization—these are still well described under electromagnetic theory—it does provide a more complete understanding of polarized light as individual photons now each have a polarization corresponding to their intrinsic spin.

Polarized light has been employed for many applications including elucidating the three dimensional characteristics of chemical bonds,[8] determining sugar concentrations in industrial processes,[9] quantifying protein structures in solutions,[10] and remote sensing in metrology and astronomy.[11,12] In addition to these and other applications, polarized light has also been employed for a number of biomedical applications.[13] In this section, a review of the applications of polarized light in biomedical optics is provided. We begin with the mathematical formalisms used to express the polarization of light.

### 1.1.1 Polarized light mathematics: Stokes-Mueller calculus

The polarization of a light beam and its interactions with the medium in which the beam propagates are most often expressed through either Jones[14] or Stokes-Mueller[15] calculus. However, for cases of multiple scattering media that randomize and thus depolarize light propagating through it, the later Stokes-Mueller formalism is preferable as it allows for the representation of depolarizing media and partially polarized light. This formalism—co-developed by George Gabriel Stokes in 1852 and Hans Mueller in 1943—represents the polarization of light as a four-element Stokes vector **S** of the form

$$\mathbf{S} = \begin{bmatrix} I \\ Q \\ U \\ V \end{bmatrix}. \tag{1}$$

The elements of this vector are defined with respect to a set of arbitrary orthonormal axes $\hat{\boldsymbol{e}}_{\perp}$ and $\hat{\boldsymbol{e}}_{\parallel}$ defining its reference frame as

$$I = E_{\parallel}E_{\parallel}^{*}+E_{\perp}E_{\perp}^{*}, \tag{2}$$

$$Q = E_{\parallel}E_{\parallel}^{*} - E_{\perp}E_{\perp}^{*}, \tag{3}$$

$$U = E_{\parallel}E_{\perp}^{*} + E_{\parallel}^{*}E_{\perp}, \tag{4}$$

and

$$V = i(E_{\parallel}E_{\perp}^{*} - E_{\parallel}^{*}E_{\perp}), \tag{5}$$

where $E_{\parallel}$ and $E_{\perp}$ are the complex electric fields of the net field $E$ along the respective axes in the photon's reference frame, with $i \equiv \sqrt{-1}$ and * indicates a complex conjugate. This is graphical represented below in Fig. 1.

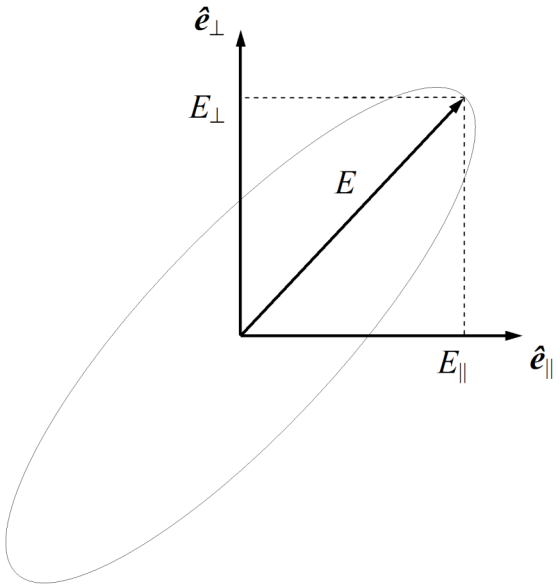



**Fig. 1** Reference frame to express the polarization of a beam of light. The complex electric field $E$ is decomposed along two arbitrary orthogonal axes $\hat{e}_{\perp}$ and $\hat{e}_{\parallel}$ into directional field components $E_{\perp}$ and $E_{\parallel}$.

When using the Stokes vector, $I$ represents the intensity of the light beam, $Q$ represents the linear polarization at 0° and 90°, $U$ represents the linear polarization at 45° and 135°, and $V$ represents the circular polarization.

To apply the polarizing effects of the medium through which the light is propagating, the Stokes vector is multiplied by a 4 × 4 Mueller matrix of the form

$$\mathbf{M} = \begin{bmatrix} m_{11} & m_{12} & m_{13} & m_{14} \\ m_{21} & m_{22} & m_{23} & m_{24} \\ m_{31} & m_{32} & m_{33} & m_{34} \\ m_{41} & m_{42} & m_{43} & m_{44} \end{bmatrix}. \quad (6)$$

Thus after propagating through a medium, the resulting Stokes vector of the output light $\mathbf{S}_o$, is given as the product of the input Stokes vector $\mathbf{S}_i$ and Mueller matrix $\mathbf{M}$ representing the medium, $\mathbf{S}_o = \mathbf{M}\mathbf{S}_i$. Measurements of both the Stokes vector and the Mueller matrix of a medium are possible using various experimental systems.

### 1.1.2 Polarized light effects in biological tissue

The effects of biological tissue on the polarization of light are due to variations in the speed at which light propagates through a medium, referred to the refractive index (expressed as the ratio of the speed of light in vacuum, $c \approx 3 \times 10^8$ m/s, over the speed in the medium). This change in the speed of light arises from the interactions of light with the molecules comprising the medium. As light propagates it excites electrons of the atoms that comprise the material. Assuming the atoms do not absorb this energy, the excited electrons re-emit light which then in turn excite electrons in another atoms. In between atoms the light propagates at $c$, however, the time required to excite the

electrons and re-emit the light slows the speed at which the light travels through the medium.

The primary and most significant effect of most tissues is depolarization due to multiple scattering. Biological tissue is heterogeneous, being comprised of numerous domains of differing refractive indices such as extracellular space, connective tissue, and cellular and sub-cellular components (cytoplasm, organelles, and the nucleus). In addition, many tissues have a layered structure and exhibit different refractive indices in each layer. These heterogeneities in refractive indices result in multiple scattering of light propagating through these tissue domains as a result of refraction. Multiple scattering events lead to randomization of the orientation of the polarization eventually leading to a bulk randomization of the polarization and overall depolarization of the light. The effect of the depolarization on the Stokes vector of the light can be expressed by a Mueller matrix $\mathbf{M}_{\mathrm{D}}$, where D denotes depolarization, of the form

$$\mathbf{M_D} = \begin{bmatrix} 1 & 0 & 0 & 0 \\ 0 & \beta_Q & 0 & 0 \\ 0 & 0 & \beta_U & 0 \\ 0 & 0 & 0 & \beta_V \end{bmatrix}, \tag{7}$$

where $\beta_Q$, $\beta_U$, and $\beta_V$ give the intensities (relative to the overall intensity $I$) of the Stokes vector elements Q, U, and V respectively, after propagating through the medium. The retained degrees of linear and circular polarization can be calculated from a Stokes vector as $\beta_L = (Q + U)^{1/2}/I$ and $\beta_C = V/I$ respectively, or using the elements of $\mathbf{M_D}$, as $\beta_L = (\beta_Q + \beta_U)^{1/2}$ and $\beta_C = \beta_V$. While the main implication of depolarization is a reduction in the overall polarization signal, it can be used as a metric of tissue structure and composition

as various tissues and tissue states will exhibit different scattering and thus depolarization properties.

In addition to spatially varying refractive indices, tissue also exhibits directionally varying refractive indices. The structural anisotropy exhibited by many tissues due to their fibrous (collagen, muscle, elastin, etc) structure results in different refractive indices along the length of the fibers versus perpendicular to the fibers. These directionally varying refractive indices are referred to as linear birefringence. Light polarized along either of these orthogonal directions propagates at different phase speeds leading to a phase shift between these polarization components termed retardance. The magnitude of the retardance $\delta$ (in radians) between the polarization states can be calculated as

$$\delta = \frac{2\pi\Delta n l}{\lambda}, \tag{8}$$

where $\Delta n$ is the difference between the refractive indices along the fibers versus perpendicular to it, $l$ is path-length of the light through the medium, and $\lambda$ is the wavelength of the light. The effect of birefringence can be applied to the Stokes vector of an input light beam by the Mueller matrix $\mathbf{M}_{\boldsymbol{\delta}}$, where $\delta$ denotes retardance, of the form

$$\mathbf{M}_{\delta} = \begin{bmatrix} 1 & 0 & 0 & 0 \\ 0 & \cos^2 2\phi + \cos\delta \sin^2 2\phi & (1-\cos\delta)\sin 2\phi \cos 2\phi & -\sin\delta \cos 2\phi \\ 0 & (1-\cos\delta)\sin 2\phi \cos 2\phi & \sin^2 2\phi + \cos\delta \cos^2 2\phi & \sin\delta \cos 2\phi \\ 0 & \sin\delta \sin 2\phi & -\sin\delta \cos 2\phi & \cos\delta \end{bmatrix}, \tag{9}$$

where $\phi$ is the angle between the horizontal in the laboratory frame and the direction in which the refractive index differs as illustrated in Fig 2. The effect of birefringence is highly dependant on the direction of the birefringent axis with respect to the polarization. A phase difference between orthogonal polarization components along the direction of

the differing refractive indices if both these components are non-zero (i.e., if light is fully polarized along only one differing refractive index direction then birefringence will have no effect).

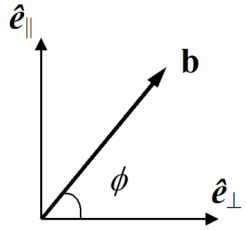



**Fig. 2** Illustration of angle $\phi$, made between the horizontal in the laboratory reference frame $\hat{e}_{\parallel}$ and the birefringent axis b (direction of varying refractive index).

Birefringence is a measure of tissue anisotropy or structural organization; as such tissues with a more fibrous structure will exhibit higher values of birefringence. This measure of the structure of the tissue can be indicative of the functional state or overall health of tissues that typically exhibit this property.

Tissue can also exhibit different refractive indices for circular polarization. Molecules present in tissue exhibiting a chiral or handed molecular configuration produce this effect termed optical activity. The handed asymmetry of these molecules results in different refractive indices for left and right circularly polarized light when dissolved in solution (as is the case in tissue where glucose is dissolved in blood, as well as extracellular and intracellular fluid). This effect is analogous to linear birefringence and accordingly optical activity is often termed circular birefringence. Linear polarized light can be expressed as equal components of right and left circular polarizations that when combined results in linear polarized light. If a linear polarized beam is considered to be formed of equal right and left circular polarizations a difference in refractive indices for

opposite circular polarizations results in a rotation of the plane of linear polarization. The rotation angle $\alpha$ is calculated as

$$\alpha = [\alpha]_{\lambda}^{T} lC, \tag{10}$$

where $[\alpha]_{\lambda}^{T}$ is the rotatory power of the specific molecule usually given in deg ml $g^{-1}$ $dm^{-1}$ (1 dm = 10 cm) and dependent on the wavelength $\lambda$ of the light and the temperature $T$, $l$ is the optical path-length through the media in dm, and $C$ is the of the molecule in g $ml^{-1}$. The effect of optical activity on the Stokes vector of input light is expressed as a rotation matrix $\mathbf{M}_{\alpha}$ of the form

$$\mathbf{M}_{\alpha} = \begin{bmatrix} 1 & 0 & 0 & 0 \\ 0 & \cos 2\alpha & \sin 2\alpha & 0 \\ 0 & -\sin 2\alpha & \cos 2\alpha & 0 \\ 0 & 0 & 0 & 1 \end{bmatrix}. \tag{11}$$

As the rotation produced by an optically active medium is proportional to the concentration of the optically active molecule, this optical activity induced rotation can be used to determine the concentration of the corresponding molecule.

### 1.1.3 Biomedical applications

The field of polarimetry is well established in optically clear media; however, applying these techniques to scattering and thus depolarizing media such as biological tissue complicates the measurement and analysis. As a result of the extensive depolarization of light in tissue, quantitative polarimetry is limited to either thin tissue for transmitted light or reflection measurements (light reflected/diffusely reflected from shallower depths will retain some polarization). Within these limitations, polarimetry has been employed for a

large number of applications. The polarization of light is effected by the scattering properties of tissue (such as scattering structure size and refractive index, as well as the overall scattering coefficient of the tissue); accordingly, polarized light can be used to probe these properties. The structural organization of many tissues, and resulting birefringence, affords polarized light the ability to quantify the structural organization of tissues. Lastly, polarized light can also be employed to measure the concentration of optically active molecules in tissue. In this section each of these applications is briefly reviewed and representative results are discussed. A significant amount of research has been conducted for the use of polarized light in biomedical optics; accordingly the references provided are by no means exhaustive.

While the depolarization caused by tissue is most often viewed as hindering the application of polarized light for biomedical applications, the first category of techniques in fact makes use of the depolarization of multiply scattered photons. If non-polarized photons are "gated out" then only those photons that have retained their polarization and thus have undergone fewer scattering events will be measured. As photons undergo scattering events, their polarization becomes randomized; accordingly photons that have undergone few or no scattering events will retain a polarization more similar to their initial polarization. This allows for polarization to be used as a method of gating light to discriminate between superficially scattered or ballistically transmitted light (preserving the initial polarization), and diffusely scattered or transmitted (depolarized) light. A number of researchers have employed this basic principle in biomedical optics. Schmitt *et al*.[16] used polarizing gating to discriminate short-path photons in scattering media. Demos and Alfano[17] employed polarization gating to measure the ballistic component of light

propagating through scattering samples. Jacques *et al.*[18,19] used polarized light gated imaging to study various skin pathologies including benign, pre-cancerous, and cancerous tissues. Polarized light was used to gate ballistically transmitted light in order to improve imaging resolution of objects embedded in highly scattering media by Gan and Gu.[20] Morgan and Stockford[21] employed polarization gating to reject surface reflections and image underlying superficial tissue, and Yong *et al.*[22] employed polarized light to measure the absorption of superficial tissues. The use of polarized light gating for depth selectivity was also investigated by Lie *et al.*[23] using a bioengineered tissue model.

Polarized light can also be used to probe the scattering properties of tissue, specifically the shape and refractive index of scattering structures as well as the overall scattering coefficient of the tissue. The resulting polarization of light after interacting with tissue will be effected by the properties of the individual scattering structures, as well as the overall distribution of scatterers. Of particular interest is single scattering, as this can be modeled with Mie scattering theory[24] and directly related to the properties of the scatterer. Backman *et al.*[25] and Gurjar *et al.*[26] employed spectroscopic polarization measurements of superficially scattered light to determine human epithelial properties, in particular to detect cellular morphology associated with pre-cancerous states. Similarly, Bartlett *et al.*[27] made use of polarized light spectroscopy to determine scattering particle size in mammalian cells and Mourant *et al.*[28] characterized mammalian cells using backscattered polarized light measurements. In addition, Jaillan and Saint-Jalmes[29] employed radially resolved polarization measurements to determine the scattering coefficient of scattering media.

The birefringence exhibited by structurally anisotropic tissues allows for polarized light to be used as a probe of their structural state. Many tissues exhibit structural birefringence including muscle, cartilage, and skin, generally due to their fibrous composition. Accordingly, birefringence measurements can be used to assess the health or functional state of these tissues, particularly with regards to their response to various pathologies and/or treatments. Sankaran *et al.*[30] investigated the propagation of different polarization states through tissue, including birefringent tissue, and the effect of these tissues of the degree of circular and linear polarization states. Wu and Walsh[31] performed polarization imaging on *ex vivo* rat tail tissue exhibiting birefringence. The birefringence of collagen in skin has been used to monitor low-intensity polarized laser treatment by da Silva *et al*.[32] and birefringence changes in the myocardium as a result of thermal injury have been investigated by Whittaker *et al*.[33] The use of polarization-sensitive optical coherence tomography (PS-OCT)[34] has been widely employed for birefringence measurements as it is provides depth resolution allowing for birefringence determination, rather than only retardance measurements, using the known depth and Eq. (8). PS-OCT has been investigated for imaging thermal damage in porcine tendon and skin by de Boer *et al.*[35] and in porcine myocardium by Schoenenberger *et al*.[36] for monitoring thermal therapies. Also, birefringence of the retinal nerve fiber has been measured *in vivo* via PS-OCT by Cense *et al*.[37] with application for early glaucoma detection.

Optically active (chiral) molecules results in a rotation of the plane of linear polarization as the light propagates through the medium that is proportional to the concentration of the molecules, as shown in Eq. (10). An optically active molecule

present in tissue that has received a great deal of attention is glucose. As the concentration of glucose can be determined via optical rotation measurements, the potential for a noninvasive method of measuring blood glucose concentrations for diabetic individuals has lead to research by a number of groups. However, these techniques are plagued by the depolarization caused by tissues and the presence of many other optically active tissue constituents—many of which are present at much greater concentrations than glucose. Coté *et al.*[38] and Bada *et al.*[39] have investigated the use of polarimetry measurements for glucose monitoring in the aqueous humor of the eye. The eye has advantages as a measurement site as it is the only optically transparent tissue sites, although debates exists as to how well the glucose levels in the aqueous humor correlation to blood glucose levels. Mehrübeoğlu *et al.*[40] investigated the use of diffuse reflectance polarization images for determining glucose concentrations in tissue-simulating phantoms. Manhas *et al.*[41] also investigated reflectance measurements for glucose concentration determination in tissue-simulating phantoms; they particularly focused on separating chirality-induced and scattering-induced rotations.

## 1.2 Extending Monte Carlo model of polarized light propagation in tissue-like media

This first chapter involved extension of our current Monte Carlo model for polarized light propagation in scattering media to overcome limitations of the model, specifically to extend the model to include both birefringence and optical activity simultaneously. As applications of polarized light involving both birefringence and optical activity were studied in the following thesis work, a model incorporating both these effects was

developed to assist in guiding these studies and analyzing results. Here, an overview of polarized light propagation in tissue modeling is provided, the limitations of the model are described, and our approaches for model extension and validation are introduced. The corresponding implementation, results, and discussion are presented in Chapter 2.

### 1.2.1 Modeling polarized light propagation in tissue

Forward modeling of polarized light propagation through turbid media such as biological tissue is tremendously useful, specifically for gaining insight into the physical process, to assist in the design and optimization of experimental studies, and in analyzing measured data. The best-suited method for polarimetric analysis is electromagnetic theory with Maxwell's equations; however, the use of these equations in scattering media is impractical due to the complexity of media.[42] In general, the use of Maxwell's equations is restricted to optical clear media with well-defined interfaces. Instead, light propagation through multiply scattering media is generally modeled through the radiative transport equation and its simplified variant, the diffusion equation.[43,44] However, these techniques are light-intensity techniques which typically neglect polarization. A more general and robust approach is the Monte Carlo method.

The Monte Carlo methods are a group of computation techniques, which rely on repeated random sampling to compute the results and are useful in applications where it is impossible or infeasible to furnish a solution with a deterministic (analytical) algorithm. Because Monte Carlo methods rely on repeated sampling of random numbers, they are ideally suited for computation on a computer. The concept was first employed by Ulam in 1946,[45] when he attempted to compute the chances of a particular solitaire game

being successful, and ended up simply laying out a number games and counting the number of successes. As part of simulations for the Manhattan project, Metropolis and Ulam[46] published the first description of the method, giving it the code name Monte Carlo. These methods are particularly useful for problems with a large number of degrees of freedom, such fluids and disordered materials, and have been widely employed in physical sciences, finance, business, telecommunications, and gaming industry, among others.

The first Monte Carlo model for light propagation in tissue was developed by Wilson and Adam in 1983.[47] Wang *et al.*[48] later developed what is now the most often employed Monte Carlo light-tissue model known as Monte Carlo for Multi-Layered Media (MCML). Both these models work by tracking individual photon packets as they propagate through the medium. However, these models were developed for intensity calculations only and as such neglects polarization. A number of more recent models have incorporated polarization by tracking the Stokes vector of the propagating photon packets[49,50,51,52,53,54,55] including a model developed in our group.[56,57] Currently, the Monte Carlo technique is considered the most general approach for simulation of polarized light propagation in multiply scattering media. However, as it is a stochastic technique, long computation times are generally required into order to achieve statistically meaningful results.

As the majority of polarization sensitive Monte Carlo models operate in a similar manner, a brief overview of the general method follows; more details on the specific implementations can be found in the previous references. It is generally assumed that each scattering event occurs independently and thus no optical coherence effects are

considered (even though some recent models do consider coherence[58]). The location, propagation direction, and polarization of each photon packet (here after simply, though not rigorously accurately, referred to as a photon) are initialized and modified as the packet propagates through the sample.

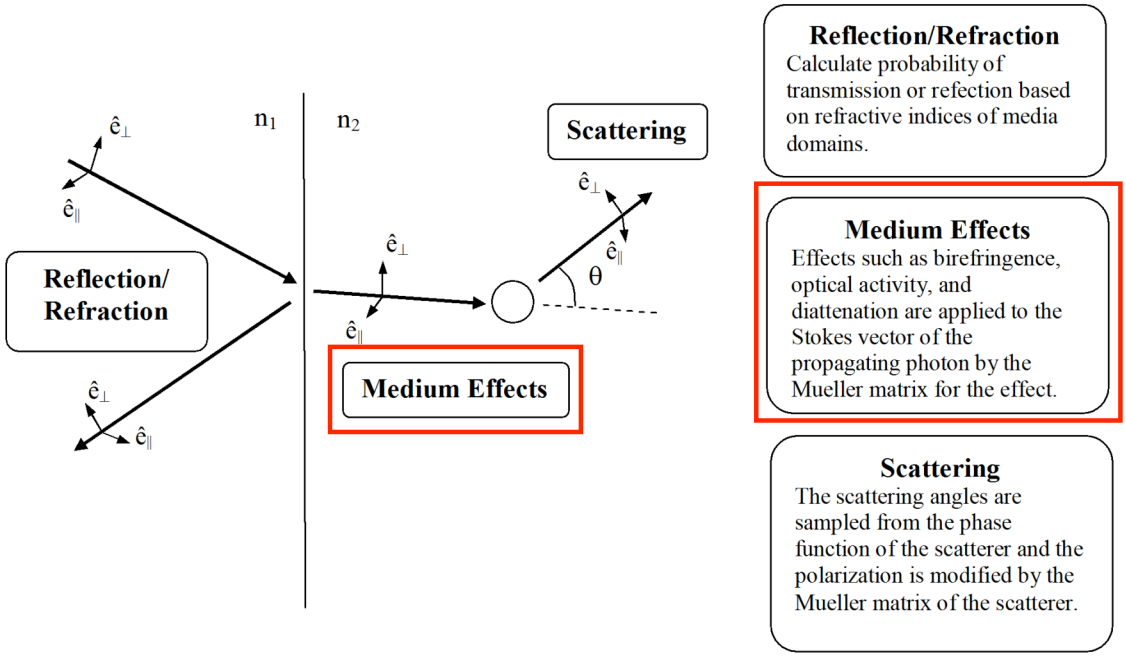



**Fig. 3** Schematic representation of photon events modeled. The extension of the model for simultaneous modeling of birefringence and optical activity involved upgrades to the medium effects portion of the model, highlighted in red.

An overview of the primary model components are shown in Fig 3. The polarization of the photon is represented as a Stokes vector expressed with respect to an arbitrary reference defined as a set of orthonormal axes ($e_\perp$ and $e_\parallel$) perpendicular to the direction of propagation. Polarization effects of the medium are applied to the Stokes vector of the photon via the corresponding Mueller matrix for the effect. The photons propagates a distance between scattering events randomly sampled from the probability distribution $\exp(-\mu_t d)$, where $\mu_t$ is the extinction coefficient of the medium (the sum of the

$\mu_a$ absorption and $\mu_s$ scattering coefficients), and $d$ is the distance between scattering events. Upon encountering a scattering event, a scattering plane and angle are sampled based on the polarization state of the photon and the Mueller matrix of the scatterer, and the propagation direction of the photon is modified accordingly. The polarization reference frame and polarization of the photon are modified by the change in propagation direction and Mueller matrix of the scatterer respectively. The Mueller matrix for the scattering event is calculated through Mie scattering theory for spherical particles[59] in most Monte Carlo models that incorporate polarization. While tissue is obviously not comprised of only spherical scattering particles, the angular scattering distribution of the spheres can be made similar to that for tissue. In models neglecting polarization, scattering angle distributions are most often modeled using the Henyey-Greenstein function.[60] When a photon encounters a domain interface (representing either tissue domains of differing optical properties or an external tissue boundary), the probability of either transmission or reflection is calculated using Fresnel coefficients. As no coherence properties are generally modeled, the final Stokes vectors can be calculated based on the sum of all photons detected at a spatial position (area or volume). In order to generate statistically acceptable final results, typically $10^7$-$10^9$ photons need to be tracked, depending on the required sensitivity and spatial resolution.

### 1.2.2 Extending model to include optical activity and birefringence

Previous Monte Carlo models adequately model the effects of multiple scattering on the polarization of propagating light; however, these models do not include all the polarization-influencing effects of tissue. In particular, birefringence due to anisotropic

tissue structures (e.g., collagen, elastin, and muscle fibers) and optical activity due to chiral molecules (e.g., proteins and glucose) have not *simultaneously* been included in any previous models. A number of models have included *either* effect,[61,62,63] but none have included both effects in the context of multiple scattering. This is due to the difficulty in modeling simultaneous polarization effects, particularly in the presence of multiple scattering. However, these effects must be incorporated into existing models in order to better simulate the propagation of polarized light in tissue, which often exhibits both these effects.

The difficulty in modeling these effects arises in applying these effects to the polarization of the propagating photons, particularly in combining the effects of birefringence and optical activity into a single Mueller matrix that can be applied to the Stokes vector of the photons. Sequential multiplication of the Mueller matrices ($\mathbf{M}_{\delta}\mathbf{M}_{\alpha}$ or $\mathbf{M}_{\alpha}\mathbf{M}_{\delta}$) is problematic as matrix multiplication is not commutative (i.e., $\mathbf{M}_{\delta}\mathbf{M}_{\alpha} \neq \mathbf{M}_{\alpha}\mathbf{M}_{\delta}$), and does not make physical sense as the effects occur simultaneously, not sequentially as matrix multiplication implies. Thus, the effects must be combined in a single matrix, and fortunately this can be accomplished via the Jones N-matrix formalism.[64] In this formalism the medium is represented by a series of infinitely thin optical elements making the ordering of these elements unimportant. If birefringence and optical activity are assumed to be independent of scattering events—a reasonable assumption given that these effects occur as the light propagates—then the Mueller matrix for the combined effect of birefringence and optical activity can be applied to the photons as they move between scattering events. The leads to the hypothesis of this thesis module that ***birefringence and optical activity could be modeled in multiply scattering media via***

***established Monte Carlo techniques, by incorporating the Jones N-matrix formalism to combine their effects and applying this combined effect between scattering events.***

The complete methodology and implementation along with studies completed to experimentally validate the extended model are given in the publication provided in Chapter 2. The experimental validation was a particularly important aspect of this study, as very few validation studies have been undertaken for polarization sensitive Monte Carlo models. In order to conduct these validation studies, a novel optical tissue phantom system was developed. The excellent agreement between simulated values and experimental measurements on the phantoms gives compelling evidence for the validity of the extended model.

## 1.3 Polarimetric characterization of myocardial structure for monitoring regenerative treatments

This second chapter investigated the use of polarization light birefringence measurements for myocardial structural characterization, particularly with application to monitoring regenerative treatments for myocardial infarction. This is the first of two applications studied in this thesis, the second being noninvasive glucose monitoring in chapter 4. Both of these studies made use of the extended Monte Carlo model from the previous chapter and in the case of myocardial characterization also involved significant experimental system development and analysis. An overview of myocardial infarction and stem cell regenerative treatments is provided here, along with background in optical methods for characterizing the myocardium including previous work involving polarized light. The corresponding experimental methodologies and studies are described in Chapter 3.

### 1.3.1 Myocardial infarction and regenerative (stem cell) treatments

Myocardial infarction (commonly referred to as a heart attack) is the leading cause of cardiovascular related death with an estimated 7.5 million worldwide each year—12% of all deaths.[65] Within Canada, acute myocardial infarction was responsible for over 17,000 deaths in 2005—7% of all deaths.[66] Myocardial infarction is caused by an occlusion (blockage) of a coronary artery, most often as the consequence of a rupture of an atherosclerotic plaque (lipids, white blood cells, and fibrous cap which have collected on the wall of an artery) as shown in Fig 4. A vessel that is narrowed by a plaque, but not yet blocked, results in coronary stenosis, a state that puts the individual at high risk for an infarction if the plaque should rupture or completely block the vessel. The ischemia as a result of an infarction, if left untreated, results in necrosis of the effected myocardial cells and after a period of time the formation of a collagenous scar. The infarction leads to structural remodeling of the myocardium, specifically expansion of the infarct, ventricular dilation, thinning of the ventricular wall, and scar formation as shown in Fig. 5. These remodeling processes result in disruption of normal cardiac function.

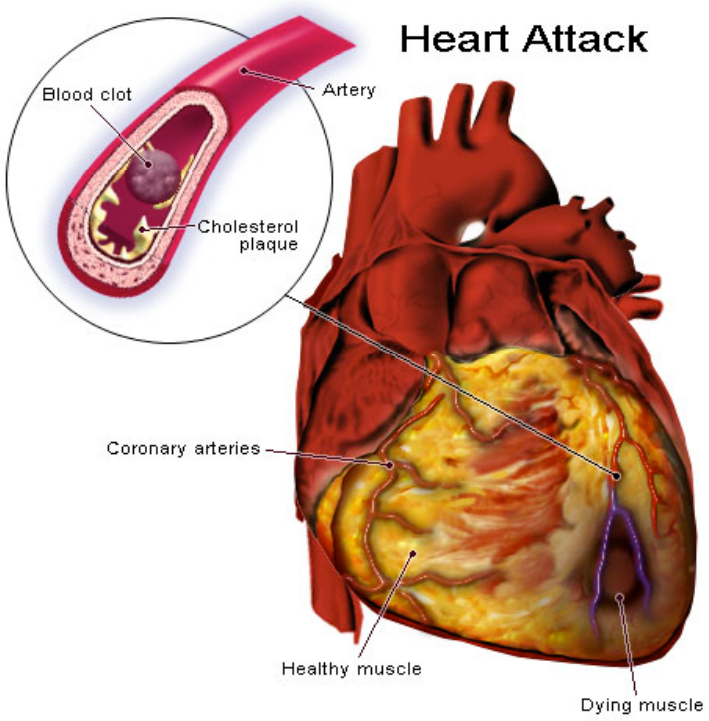



**Fig. 4** Overview of myocardial infarction (heart attack) as a result of a coronary artery occlusion, in this case a blood clot lodging in a plaque.[67]

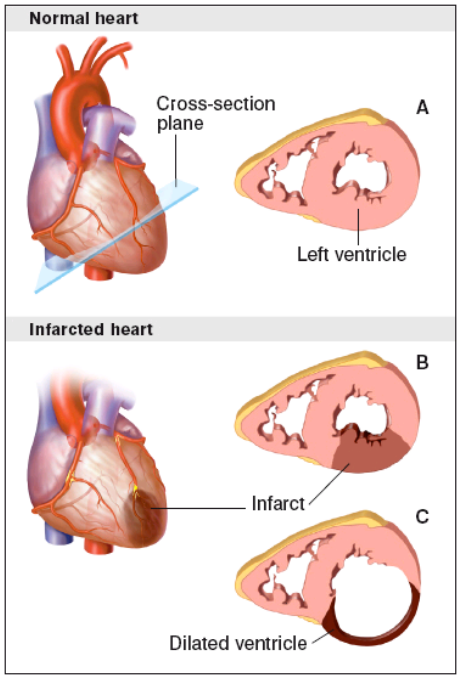



**Fig. 5** Overview of remodeling as a result of myocardial infarction. The left ventricle after infarction in B shows scar formation, while C shows scar expansion, ventricular dilation, and myocardial wall thinning which occur as the infarct matures.[68]

Due to the tremendous morbidity and mortality associated with myocardial infarction, a great deal of research and development has been undertaken towards developing effective interventions and treatments. The use of thrombolytic agents (clot busters) to breakdown the offending occlusion, and percutaneous coronary intervention (angioplasty) to widen the occlusion has led to significant improvement in outcomes. However, while these interventions can restore blood perfusion to deprived tissues, cardiomyoctyes (heart muscle fibers) do not regenerate, thus the damage suffered by myocardial infarction is essentially irreversible by normal physiological means. Because of this, further research is currently underway to promote regeneration of cardiac tissues, in particular the use of stem cell therapy.

The potential of stem cells to form any differentiated cell type in the body has led researchers to investigate their use for variety of degenerative diseases.[69,70] Stem cells as applied to myocardial regenerative therapy in particular has received a great deal of interest, as this therapy has been shown to improve cardiac function.[71,72] A variety of donor stem cell types have been proposed and investigated for use in myocardial regeneration including embryonic stem cells, skeletal myoblasts, mesechymal stem cells, bone marrow stem cells, and adult cardiac stem cells.[73] Debates continue—both a scientific and an ethical debate in the case of embryonic stem cells—as to the primary mechanisms for the improvement in cardiac function, particularly for non-embryonic stem cell types which have been shown to result in very limited re-growth of cardiomyocytes. In general, the improvement in function is attributed to the reduction of detrimental remodeling induced by stem cell therapy.[74]

The detrimental remodeling caused by myocardial infarction includes changes in the composition and structure of the tissue, particularly necrosis of cardiomyocytes and an increase in the collagen content (Type III) with scar formation.[75] Stem cell therapies have been shown to alter this remodeling; in particular, a decrease in collagen content and an increase in cardiac muscle have been measured in regenerating infracted myocardium.[76] In addition, the structural organization of the myocardium also changes significantly with infarction and regeneration. Healthy myocardium is primarily comprised of organized aligned arrays of cardiomyocytes, while the collagen in the scar tissue is largely disorganized. These content and structural changes are shown in a histological image in Fig. 6 for a rat heart following an induced infarction. While organization of the myocardium is difficult to visualize in the histology image, the content change from healthy myocardium comprised on primarily muscle, to the infarction comprised of scar collagen, is evident.

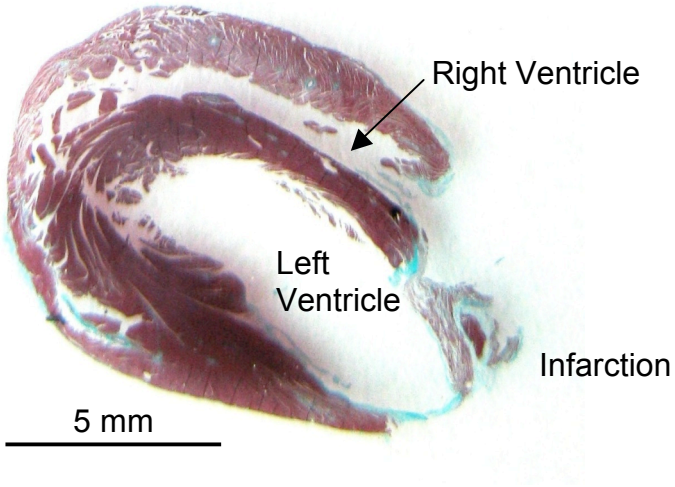



**Fig. 6** Masson's trichrome histology of an axial section from an infracted rat heart four weeks post infarction. Muscle is stained red and collagen is stained blue. The infarction is evident by ventricular wall thinning and an increase in collagen content.

### 1.3.2 Polarized light for myocardial structural characterization

As healthy myocardial tissue is highly anisotropic (structurally organized), it exhibits significant levels of linear birefringence. In contrast, infarcted scar tissue is primarily isotropic with randomly oriented collagen strands and thus will exhibit lower values of linear birefringence. Accordingly, measurements of birefringence may have utility in quantification of the structural changes that occur with infarction. In the context of stem cell regenerative treatments, the remodeling associated with infarction is reduced, and thus the reduction in birefringence that occurs with infarction should be accordingly lessened. Birefringence values may therefore be useful in monitoring these treatments and providing functional feedback regarding the treatments effectiveness.

The field of cardiac regeneration is currently in need of biomarkers regarding the status of treatments, particularly those with the potential to be employed *in vivo*. Through the use of fiber optics,[77] it is foreseeable that a polarization measurement probe could be directed into the chambers of the heart through catheter techniques currently employed in cardiac catheter labs. Thus, polarized light has potential to achieve the requirements of being sensitive to structural state of the myocardium—particularly with regards to tissue remodeling—and the potential to be employed *in vivo*. Accordingly, in this thesis module we hypothesized that ***birefringence measurements could be used to characterize the structural anisotropy of the myocardium and differentiate between healthy, infarcted, and regenerating tissue states, with potential for monitoring regenerative treatments.***

Polarized light has been previously employed in cardiological studies for structural assessment of *ex vivo* myocardium. Baba *et al.*[78] and Jouk *et al.*[79,80] assessed heart fiber (collagen and myocyte) orientation in myocardial sections using polarized

light microscopy. The later studies by Jouk *et al.* focused on determining the overall structure of the heart muscle by taking polarization microscopy images of axial sections throughout the heart. Whittaker *et al.*[81] used polarized light microscopy on silver-stained myocardial sections to assess the role of collagen in infarct expansion. PS-OCT has been used to image healthy and infracted *ex vivo* myocardium by Sun *et al*.[82] The use of picrosirius red staining for collagen along with polarization microscopy[83] has been widely used for quantifying collagen content and orientation in histological analysis of myocardial sections. Whittaker *et al.* used picrosirius red staining to examine the changes in collagen content and orientation in the myocardium after infarction[84,85] and after infarction and transplant of neonatal myocytes.[86] Tabel *et al*.[87] compared picrosirius red collagen content and organization with ultrasound signals to determine the influence of fiber morphology on echogenicity of myocardial scar tissue. Akhyari *et al*.[88] used picrosirius red staining to quantify extracellular matrix formation and organization to determine the effect of mechanical stretching on the formation of cardiac muscle grafts. Polarized light imaging of thin myocardial sections has also been used to distinguish between health and thermally damaged tissues by Thomsen et al.[89] However, no studies have investigated the potential for polarized light to characterize stem cell regenerating tissue; as well, no studies have focused on the use of polarized light in optically thick myocardium, rather focusing only on thin histological sections (less than 50 μm). Currently, polarized light is considered only a tool for microscopy, most often requiring the use of specific stains, rather than endogenous birefringence.

Non-polarization optical methods have been proposed and investigated for monitoring various aspects of stem cell cardiac therapy. These methods include

bioluminescence imaging for cell tracking,[90] near-infrared spectroscopy for monitoring perfusion,[91] and laminar optical tomography for monitoring electrophysiology,[92] among others.[93] However, currently no optical methods exist for assessing the structure of the myocardium and its response to infarction and stem cell therapy with the potential to be employed *in vivo*.

A variety of non-optical modalities have been proposed and developed for characterization of myocardial structure including ultrasound elastography,[94] electrical impedance mapping,[95] and diffusion tensor magnetic resonance imaging.[96] However, in the case of both ultrasound elastography and electrical impedance mapping neither provides information regarding the organization of the myocardium. While both these modalities do provide myocardial structural information, they do not measure organization of the myocardium, but rather the elastic and conductive properties respectively. Diffusion tensor magnetic resonance imaging (MRI), on the other hand, does provide metrics of fiber organization and orientation, although currently it suffers from long imaging times (in excess of 12 hours) and low spatial resolution (greater than 1 $mm^3$).

Polarized light is thus well poised for monitoring the structural state of myocardium. The studies conducted in this thesis module are discussed in detail in Chapter 3, along with several small investigations yet to be published. The work focused first on demonstrating a proof-of-principle for characterizing healthly, infarcted, and regenerating *ex vivo* sectioned myocardial tissue from mouse and rat infarction models. The ability to apply the polarimetry techniques *in vivo* was demonstrated using a mouse dorsal window chamber model. Finally, studies investigating the effects of formalin

fixation (required for tissue sectioning) and of the birefringence axis orientation were also conducted.

## 1.4 Non-invasive glucose monitoring with polarized light

This chapter investigated a combined optical polarization and intensity glucose monitoring methodology for determining blood glucose levels. The simulation studies conducted in this chapter made use of the extended model developed and tested in chapter 2. A review of diabetes and the need for noninvasive glucose monitoring is provided, along with an overview of the noninvasive techniques currently under development, in particular the optical methods. The corresponding research and results are described in Chapter 4.

### 1.4.1 Diabetes mellitus and noninvasive glucose monitoring

Diabetes mellitus is a chronic systemic disease, with no known cure, in which the body either fails to produce or fails to properly respond to the glucose regulatory hormone insulin. Recent estimations put the number of diabetics worldwide at 285 million and the number in Canada at over 3 million.[97] Approximately 5% of diabetics have what is referred to as type I insulin dependent diabetes, the remaining 95% have type II non-insulin dependent diabetes. Type I diabetes is characterized by the inability of the body to produce sufficient quantities of insulin, due to the body's own immune system turning against itself and destroying the insulin-producing β cells in the pancreas. The process by which this occurs is currently not well understood. In type II diabetes, the pancreas does

produces insulin, however, the cells in the body fail to respond correctly to the insulin and thus fail to properly uptake glucose, as shown in Fig. 7.

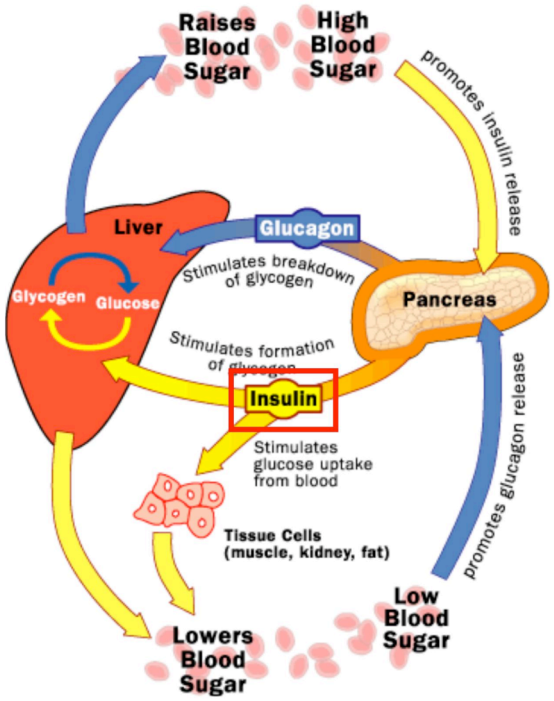



**Fig. 7** Schematic of glucose regulator system. Diabetes disrupts either the production of, or the response to, insulin, resulting in the inability of cells to properly uptake glucose. Also shown is effect of glucagon, which works in opposition to insulin, in stimulating the break down of glycogen in the liver into glucose.

Both type I and II diabetics suffer from the inability to properly regulate their blood glucose levels leading to periods when the blood glucose is either too high or to low (referred respectively as hyperglycemia and hypoglycemia). During the hypoglycemic periods, the body metabolizes fats and proteins for energy, as there is a lack of glucose in the blood. Hypoglycemia, if not treated, can lead to a number of complications ranging from weakness to coma and even death. Periods of hyperglycemia, on the other hand, lead to the majority of the chronic long-term complications including

kidney disease, blindness, nerve damage, heart disease, and gangrene all stemming from the damage produced by high levels of blood glucose on organs and tissues in the body.

The primary goal of diabetes therapy is to maintain normal blood glucose homeostasis through diet, medication, or insulin injections. Accordingly, frequent monitoring of blood glucose levels is of paramount importance in guiding these therapies. The most common current method of monitoring requires a small blood sample usually obtained through pricking a finger. This method is painful, messy, inconvenient, and carries a risk of infection. Because of this, compliance is low and many diabetics do not monitor their blood glucose levels as frequency as required to avoid the long-term complications of the disease (up to ten times a day for Type I diabetics). A noninvasive method for glucose monitoring would greatly aid in increasing the frequency of monitoring and lead to a decrease in complications associated with diabetes.

Because of the tremendous need for a less invasive method for blood glucose monitoring, there has been a significant amount of research conducted in a variety of fields into developing such a method.[98] Apart from diabetes there also exits a need for more frequent or continuous blood glucose monitoring for preterm infants and other at-risk infant groups including those suffering from fetal growth retardation, infants of diabetic mothers, as well as other more rare metabolic problems. The following section reviews the developing techniques for minimally-invasive and noninvasive *in vivo* glucose monitoring including electrochemical, and a number of optical techniques including infrared spectroscopy, photoacoustics, Raman spectroscopy, fluorescence, and polarimetry.

The electrochemical technique is based on the sensitive reaction between oxygen and glucose catalyzed by glucose oxidase and functions by measuring the generated peroxide or consumed oxygen. This technique was first developed in the 1960s[99] and has formed the basis for a number of developed sensors.[100,101] These sensors are stable, accurate, and sensitive *in vitro*; however, when placed *in vivo* intravascularly their performance reduces dramatically due to protein absorption followed by platelet activation and adhesion leading to either partial or complete failure of the system. More recently, work has shifted to measuring glucose in interstitial fluid rather than blood circumventing the issues encountered in whole blood.[102] However, problems still persist as a time lag exists between the glucose concentrations in blood and interstitial fluid; in addition, this is not a non-invasive method, as fluids must still be extracted.[103]

Of the optical techniques that have been proposed for glucose monitoring, infrared spectroscopy has received the majority of attention. This technique is based on the glucose-induced changes in tissue absorption and scattering. A large number of groups are currently working on a variety of methods to quantify these changes.[104,105,106,107,108,109] Spectroscopic measurements are generally made in either the near-infrared (NIR, 700 – 2000 nm) or in the mid-infrared (MIR, 2.5 – 50 μm), taking advantage of glucose specific absorption bands within these wavelengths ranges. While glucose specific features do exist in the spectra, the difficulty arises in distinguishing them from those caused by other tissue analytes as well as those due to tissue variations. Accordingly, a method of calibration is required in order to relate the changes in the measured signal to the levels of glucose. *In vivo* results have shown some promise and the outlook for these techniques is cautiously optimistic.

A number of other optical techniques are currently being investigated for noninvasive glucose monitoring. Photoacoustic techniques detect some manifestation of absorbed light though either thermal or thermo-mechanical effects.[110] Tissue is irradiated with a short laser pulse at a wavelength of one of the glucose absorption bands, leading to rapid heating of the tissue and a thermal wave emission that can be detected via the subsequent pressure wave with a piezoelectric transducer.[111] Raman spectroscopy of glucose has been investigated as a means of concentration determination in tissue, however, this technique has low sensitivity as the Raman signal is much weaker than either elastically scattered light or tissue fluorescence, making specialized equipment necessary.[112,113] A variety of fluorescence-based techniques has been proposed using the oxidation of glucose or affinity-binding methods with implantable sensors[114] or a contact lens.[115] Finally, as briefly mentioned, polarimetry has been proposed for noninvasive glucose monitoring.[116] Polarimetry has the advantage of being relatively specific to glucose due its unique optical activity spectrum. However, polarimetry suffers from depolarization produced by scattering and in the need to separate the glucose signal from that resulting from many other optically active molecules present in tissue with similar optical activity spectra.

### 1.4.2 Polarized light for glucose concentration determination

None of the previously discussed techniques have yet provided a noninvasive means of robustly measuring blood glucose concentrations *in vivo*. While many show promise, and some are nearing the required levels needed for clinical application (less than 15% error), none have been demonstrated to be a suitable replacement for traditional finger prick

methods. We propose that a dual modality optical approach may provide a more accurate means for optical non-invasive glucose sensing over other modalities currently being explored. Specifically, the combination of visible and NIR spectroscopy with spectral polarization information may provide the needed information to accurately and precisely measure blood glucose levels. In this thesis module we hypothesized that ***the combination of NIR spectroscopy and polarization spectroscopy will improve the ability to determine concentrations of optically active molecules such as glucose in scattering media over either modality alone***.

Previous work in our group has focused on exploring the use of polarized light for concentration determination of optically active molecules in scattering media.[117,118,119] From these studies it has been shown that it is possible to measure small optical rotations due to physiological levels of glucose (a 5 mM glucose produces 0.008 deg in rotation through an optical pathlength of 1 cm) in scattering phantoms. However, the confounding effects of scattering and other optically active tissue constituents present a formidable challenge for the application of polarized light-based approaches *in vivo*. Other groups have suggested using the aqueous humor of the eye as a possible measurement site in order to avoid the effects of scattering.[120] However, issues relating to the correlation of glucose concentrations in the aqueous humor, the presence of birefringence in cornea, and measurement convenience hinder this approach. Accordingly, the use of polarimeter as an adjuvant to other optical glucose sensing methods, such as NIR spectroscopy, may be a more practical alternative to a single modality tissue glucose sensor approach.

The theoretical modeling study conducted for this thesis module is summarized in its corresponding publication in Chapter 3. To test whether this combined optical

approach improves the ability to determine glucose concentrations, a blood plasma model was employed. This model contained glucose and plasma proteins and was used to generate polarization and intensity spectra for both clear and scattering media. In order to isolate the glucose specific signal from that due to other plasma constituents, multi-block chemometric techniques were used to combine and regress the spectra. A small additional study was also conducted to investigate whether chirality-induced optical rotation could be separated from scattering-induced rotation, as both are often exhibited by tissue. It is worth noting that such a multimodality approach is by no means limited to glucose concentration measurements, but could be applied to other constituents of interest in clear or scattering media.

# 2. Extension of polarization-sensitive Monte Carlo model

***Introduction***

Accurate modeling of polarized light propagation in biological tissue is tremendously useful in tissue polarimetry studies. The Monte Carlo method is currently the most practical approach for simulating polarized light propagation in multiply scattering media such as biological tissue. However, all previous implementations have not included all the polarizing effects of tissue, such linear birefringence and optical activity present *simultaneously* in a scattering environment, and have been limited in their selections of modeling geometry.

A polarization-sensitive Monte Carlo software module was initially developed by Dr. Daniel Côté,[56] a previous post doctoral fellow. This model is based on methods employed in previous polarization-sensitive studies.[54] A variety of scattering angle selection methods have been proposed and implemented, attempting to overcome the difficulties arising from the scattering phase function being dependent on both the properties of the scattering particle and the incident polarization. This dependence makes random sampling of the scattering phase function difficult, and in general necessitates use of the rejection method.[54] The phase function scattering angle selection methods employed in this model are based on those by Jailion and Saint-Jalmes[49] and Kaplan *et al*.[50] A distinguishing aspect of the model our group has developed is the flexible sample geometries that can be simulated. The surfaces of the samples are defined using either triangular or rectangular surface elements, allowing for the creation of a wide variety of

sample geometries (cube, layers, spheres, cylinders, etc). In addition, the use of these surface elements allows for generation of complex and arbitary user-defined geometries that can be tailored to complex sample shapes. This ability to handle unique sample geometries sets this model apart from others currently available.

This Monte Carlo software, as well as the majority of other implementations, simulated the interactions of polarized light with mono-disperse uniformly sized scattering particles. Using this approach, the optical properties (scattering, absorption, and scattering anisotropy) in a simulation can be matched to those in a tissue of interest. However, the scattering mechanisms in the model are different when compared to those in tissue. Tissue in general is not comprised of uniformly sized scattering particles, but rather a continuous variation in refractive indices. In spite of this difference, as the overall optical properties can be matched, these models do provide a valuable tool for simulation polarized light in scattering media such as tissue.

Previous models have also been lacking in their ability to simulate simultaneous polarization effects, due to the difficulty in forming the Mueller matrix for the combined effect in the presence of multiple scattering. However, the combined matrix can be calculated through the Jones N-matrix formalism,[64] and applied to the Stokes vector of the photon as it propagates between scattering events. The following publication describes the extension of our polarization-sensitive Monte Carlo model to include the effects of birefringence and optical activity simultaneously using the Jones N-matrix formalism. The specifics of the methods used to extend the formalism are described and experimental studies completed for validation are presented. As part of the validation experiments, a novel optical phantom system is also described.

At the time of writing, this extension to the model was proposed for the polarimetric glucose monitoring application presented in Chapter 4. However, while the extension was motivated for optical activity measurements in turbid media, it is widely applicable to all areas of tissue polarimetry. Accordingly, the extended model and the phantom system were also employed for the myocardial characterization application presented in the Chapter 3 to validate experimental analysis methods developed to quantify tissue retardance.

With regards to the author contributions to the publication, I researched the N-matrix and adapted the approach to multiply scattering media, coded the extension of the model, developed the phantoms system, conducted all simulations, and performed experimental measurements. Dr. Xinxin Guo, a previous postdoctoral fellow in our group, developed the polarimetry measurement system and provided guidance for the phantom measurements.

***Paper***

**M. F. G. Wood**, X. Guo, and I. A. Vitkin, "Polarized light propagation in multiply scattering media exhibiting both linear birefringence and optical activity: Monte Carlo model and experimental methodology," *J. Biomed. Optics* 12, 014029 (2007).

Journal of Biomedical Optics 12(1), 014029 (January/February 2007)

# Polarized light propagation in multiply scattering media exhibiting both linear birefringence and optical activity: Monte Carlo model and experimental methodology

**Michael F. G. Wood**
**Xinxin Guo**
Ontario Cancer Institute
Division of Biophysics and Bioimaging
University Health Network
and
University of Toronto
Department of Medical Biophysics
610 University Avenue
Toronto, Ontario M5G 2M9
Canada

**I. Alex Vitkin**
Ontario Cancer Institute
Division of Biophysics and Bioimaging
University Health Network
and
University of Toronto
Department of Medical Biophysics and Radiation Oncology
610 University Avenue
Toronto, Ontario M5G 2M9
Canada

**Abstract.** A Monte Carlo model for polarized light propagation in birefringent, optically active, multiply scattering media is developed in an effort to accurately represent the propagation of polarized light in biological tissue. The model employs the Jones *N*-matrix formalism to combine both linear birefringence and optical activity into a single effect that can be applied to photons as they propagate between scattering events. Polyacrylamide phantoms with strain-induced birefringence, sucrose-induced optical activity, and polystyrene microspheres as scattering particles are used for experimental validation. Measurements are made using a Stokes polarimeter that detects scattered light in different geometries, and compared to the results of Monte Carlo simulations run with similar parameters. The results show close agreement between the experimental measurements and Monte Carlo calculations for phantoms exhibiting turbidity and birefringence, as well as for phantoms exhibiting turbidity, birefringence, and optical activity. Other scattering-independent polarization properties can be incorporated into the developed Jones *N*-matrix formalism, enabling quantification of the polarization effects via an accurate polarization-sensitive Monte Carlo model. © *2007 Society of Photo-Optical Instrumentation Engineers.* [DOI: 10.1117/1.2434980]

Keywords: light polarization; Monte Carlo modeling; multiply scattering media; Stokes polarimeter; Jones *N*-matrix formalism.

Paper 06242R received Sep. 9, 2006; revised manuscript received Nov. 14, 2006; accepted for publication Nov. 14, 2006; published online Feb. 2, 2007.

## 1 Introduction

Recently, there has been increased interest in using polarized light for the assessment of biological tissues, due to the noninvasive nature of light-tissue interactions and the wealth of information potentially available. The field of traditional polarimetry is well established in clear media, but the multiple scattering and resulting light depolarization hinder the application of these techniques for the examination of turbid media such as biological tissue. However, many biological tissue constituents interact with polarized light, including collagen, muscle fibers, keratin, retina, and glucose.[1] Thus, if the depolarization effects of multiple scattering can be minimized or accounted for, polarized light can potentially serve as a sensitive probe of the state of tissue and its constituents.[2–6]

The use of polarized light for determining the concentrations of optically active molecules such as glucose is currently being explored.[7,8] A tremendous need exists for a noninvasive glucose monitor for diabetics to increase the frequency of monitoring and better guide treatments, thus preventing or delaying the long-term complications due to the disease. A variety of optical methods have been proposed for blood glucose monitoring including near-IR spectroscopy,[9] optical coherence tomography[10] (OCT), Raman spectroscopy,[11] photoacoustic techniques,[12] and fluorescence techniques.[13] While some of these techniques are approaching acceptable levels of accuracy *in vivo*, none have yet been approved for clinical use. Polarized light offers another potential method by exploiting changes in polarization caused by glucose, which result from its optical activity, and induced changes in the scattering properties due to the rise in refractive index with additional glucose.[14] Accordingly, we are investigating the potential to determine concentrations of optically active molecules such as glucose in scattering media in an effort to develop a suitable methodology to predict blood glucose levels *in vivo*.[8,14,15]

To aid in the investigation of polarized light propagation in turbid media such as biological tissue, accurate modeling is enormously useful for gaining physical insight, designing and optimizing experiments, and analyzing measured data. The use of electromagnetic theory with Maxwell's equations is the most rigorous and best-suited method for polarimetric analy-

Address all correspondence to Michael F. G. Wood, Ontario Cancer Institute, Division of Biophysics and Bioimaging, 610 University Avenue, Toronto, ON, Canada M5G 2M9; Tel: +1 416 946 4501 ext. 3280; Fax: +1 416 946 6529; E-mail: mwood@uhnres.utoronto.ca

1083-3668/2007/12(1)/014029/10/$25.00 © 2007 SPIE

sis; however, solving Maxwell's equations for polarized light propagation in turbid media is impractical.[16] Light propagation through scattering media can in principle be modeled through transport theory; however, transport theory and its simplified variant, the diffusion equation, are both intensity-based techniques, and hence typically neglect polarization.[17,18] A more general and robust approach is the Monte Carlo technique. The first Monte Carlo models were developed for intensity calculations only and neglected polarization, the most commonly used being that developed by Wang et al.[19] More recently, a number of implementations have incorporated polarization into their Monte Carlo models.[20–25] Currently, the Monte Carlo technique is the most general approach to simulate polarized light propagation in scattering media, although long computation times are often required to generate statistically meaningful results.

However, most current Monte Carlo models for polarized light propagation do not fully simulate all the polarization-influencing effects of tissue. To better model the propagation of polarized light in biological tissue, effects such as optical activity due to chiral molecules (e.g., glucose and proteins), and linear birefringence due to anisotropic tissue structures (e.g., collagen and muscle), must be incorporated into the model in the presence of scattering. This is particularly important for glucose polarimetry, as many biological tissues at accessible anatomical sites (skin, muscle) have anisotropic (birefringent) properties. A number of tissue Monte Carlo models have included either optical activity or birefringence alone.[26–28] However, none have included both these properties simultaneously in turbid media. This is primarily due to the difficulty in formulating the combined (simultaneous) effect for both these optical effects in the presence of scattering; however, as will be discussed, this task can be accomplished through the Jones $N$-matrix formalism. In this paper, we extend the Jones $N$-matrix formalism to model simultaneous birefringence and optical activity in the presence of depolarization phenomena. In addition, no Monte Carlo models that have incorporated birefringence have been experimentally validated due to the difficulty in creating phantoms with controllable birefringence. As we also discuss, this can be achieved through the use of strain-induced birefringence in hydrogel polymers.

The outline of this paper is as follows. First, optical activity and birefringence are reviewed and the Monte Carlo formalism for modeling the combined effect in turbid media is presented. As this work extends an existing clear media formalsim, we focus primarily on the additions to the formalism applicable to multiply scattering samples. Second, the experimental system and methods of analysis as well as the optical phantoms used in the validation experiments are described in detail. Third, the results of the validation experiments are presented and shown to correlate well with the extended polarization-sensitive Monte Carlo model predictions; in addition, the observed physical polarization phenomena are interpreted and discussed.

## 2 Basic Polarization-Sensitive Monte Carlo Formalism

This paper extends the Monte Carlo algorithm developed and validated by Côté and Vitkin.[29] Source code (ANSI C++) is available for free download from the Internet.[30] A brief summary of the formalism is given in the following; further details on the calculations and validation are available.[29,30]

It is assumed in this algorithm that scattering events occur independently and have no coherence effects. Medium domains through which the photons propagate are specified by a set of surface elements defined by two vectors and a normal vector pointing outward. The position, propagation direction, and polarization of each photon are initialized and modified as the photon propagates through the sample. The photon's polarization, with respect to a set of arbitrary orthonormal axes $\hat{\mathbf{e}}_{\perp}$ and $\hat{\mathbf{e}}_{\parallel}$ defining its reference frame, is represented as a four element Stokes vector[31] $\mathbf{S}$. The first element $I$ represents the intensity of the light beam, the second element $Q$ represents the linear polarization at 0 and 90 deg, the third element $U$ represents the linear polarization at 45 and 135 deg, and the fourth element $V$ represents the circular polarization. Polarization effects are applied to the Stokes vector using a $4\times4$ Mueller matrix[31] $\mathbf{M}$.

The photon propagates in the sample between scattering events a distance sampled from the probability distribution $\exp(-\mu_t d)$, where the extinction coefficient $\mu_t$ is the sum of the absorption $\mu_a$ and scattering $\mu_s$ coefficients, and $d$ is the distance traveled by the photon. On encountering a scattering event, a scattering plane and angle are statistically sampled based on the polarization state of the photon and the Mueller matrix of the scatterer. The photon's reference frame is first expressed in the scattering plane and then transformed through multiplication by a Mueller matrix calculated through Mie scattering theory.[32] On encountering a domain interface, the probability of either reflection or transmission is calculated. The Stokes vector and propagation direction of the photon are then modified according to either the reflection or transmission. If the photon is transmitted through the interface, the Stokes vector of the photon is recorded for that surface element. As no interference effects are considered, the final Stokes vector values are computed as the sum of all the appropriate photon subpopulations exiting the sample.

### 2.1 *Birefringence and Optical Activity Extension*

The Monte Carlo algorithm was extended to include the effects of optical activity and birefringence to better model biological tissue. An overview of these properties and the practical implications of modeling their effects are given in the following section.

Optical activity arises from either individual molecules exhibiting chirality (handedness) such as glucose in solution, or from a chiral structure of the material as in the case of quartz crystals. Optical activity results in a rotation of the plane of linearly polarized light. This rotation arises from the difference in the refractive indices for left and right circularly polarized light, due to either the molecular or structural asymmetry. When considering optical active molecules in solution the induced rotation through an angle $\alpha$ is given by

$$\alpha = [\alpha]_{\lambda}^{T} LC, \tag{1}$$

where $[\alpha]_{\lambda}^{T}$ is the rotatory power of the molecule usually given in deg ml g$^{-1}$ dm$^{-1}$ (1 dm=10 cm) and dependent on the temperature $T$ and wavelength $\lambda$ of the light, $L$ is the

photon path length through the medium, and $C$ is the concentration of the optically active molecules. Strictly speaking, Eq. (1) is valid only for clear media, as scattering results in an ambiguity in $L$; however, this ambiguity can be accounted for if Eq. (1) is applied to individual photons between scattering events, using the distance between scattering events $d$ in place of $L$. Typical rotations due to optical active molecules in tissue (proteins and other biological molecules) are of the order of fractions of a degree per centimeter. In our formalism, optical activity is specified as a rotation $\chi$ in degrees per centimeter where $\chi=[\alpha]_\lambda^T C$ and $\alpha=\chi d$. This rotation can then be applied to individual photons as they propagate between scattering events through multiplication of the Mueller matrix for a rotator.

Linear birefringence arises from a directional anisotropy in the refractive index of the medium through which the light is propagating. The axis along which the refractive index differs from that along other directions is referred to as the extraordinary axis. Axes perpendicular to the extraordinary axis along which the refractive index is uniform are referred as ordinary axes. The refractive indices along the extraordinary and ordinary axes are referred to as $n_e$ and $n_o$, respectively. This anisotropy in refractive indices $\Delta n=n_e-n_o$ leads to a difference in the phase speeds for light polarized parallel and perpendicular to the direction of the extraordinary axis and results in a retardation of parallel and perpendicular linear polarization components. In this formalism, we assume that the medium is uniaxial (the refractive index differs along only one axis) and that the direction of the axis and difference in refractive indices is constant throughout the sample. In addition, we assume that anisotropies in the refractive index of the medium have no effect on the phase function of the scattering events and no effect on reflections and transmissions from interfaces. Birefringence (and optical activity) is (are) assumed to only influence the polarization of photons as they move between scattering events. These assumptions are reasonable given the fact that typical birefringence values in biological tissue are small, typically $\Delta n<1\times10^{-2}$, and the resulting effects on the statistically sampled scattering phase function and Fresnel coefficient are small. Birefringence is specified in our current formulation by a vector defining the extraordinary axis $\mathbf{b}$, the extraordinary refractive index $n_e$, and the ordinary refractive index $n_o$.

As the photon propagates between scattering events, the difference in refractive indices seen by the photon depends on the propagation direction with respect to the extraordinary axis. The refractive index with the maximum difference from $n_o$ as seen by the photon referred to as $n(\theta)$, can be expressed as

$$n(\theta)=\frac{n_o n_e}{(n_e^2\cos^2\theta+n_o^2\sin^2\theta)^{1/2}}, \tag{2}$$

where $\theta$ is the angle between the photon's propagation direction $\hat{\boldsymbol{e}}_{\text{prop}}$ and the extraordinary axis[33] $\mathbf{b}$. The difference in refractive indices seen by the photon is then given by

$$\Delta n=n(\theta)-n_o. \tag{3}$$

This refractive index difference results in the retardation of orthogonal linear polarization states. As the photon moves, its polarization states along the ordinary and extraordinary axes undergo retardation $\delta$ given by

$$\delta=\Delta n\frac{2\pi d}{\lambda}, \tag{4}$$

where $d$ is the distance traveled by the photon between scattering events, and $\lambda$ is the wavelength of the light in vacuum. However, to apply the Mueller matrix for a retarder to the Stokes vector of the photon, the photon's reference frame must first be rotated so that $\hat{\mathbf{e}}_\parallel$ is parallel to the axis of maximal refractive index difference $\mathbf{b}'$. The axis $\mathbf{b}'$ is first found by rotating the extraordinary axis by an angle $90\ \text{deg}-\theta$ around a second axis defined by $\mathbf{b}\times\hat{\mathbf{e}}_{\text{prop}}$, as shown Fig. 1. The photon's reference frame is then rotated by an angle $\beta$ so that $\hat{\mathbf{e}}_\parallel$ is parallel to $\mathbf{b}'$. After this rotation of the reference frame, the Stokes vector of the photon is now expressed such that the calculated retardation from Eq. (4) can be applied to this Stokes vector through the multiplication of the Mueller matrix for a retarder.

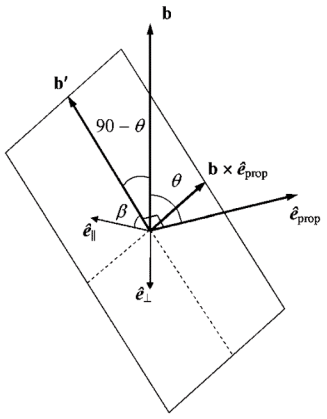



**Fig. 1** Schematic of manipulations required so that $\hat{\mathbf{e}}_\parallel$ in the photon's reference frame is parallel to the rotated extraordinary axis $\mathbf{b}'$. This is required so that the Mueller or Jones matrix for birefringence can be expressed only in terms of the retardation $\delta$ experienced by the photon; otherwise angular dependencies would also be present. The plane is defined by the photon's reference frame ($\hat{\mathbf{e}}_\perp$ and $\hat{\mathbf{e}}_\parallel$), $\theta$ is the angle between the photon's propagation direction $\hat{\mathbf{e}}_{\text{prop}}$ and the extraordinary axis $\mathbf{b}$, and $\beta$ is the angle between the direction of maximal refractive index difference $\mathbf{b}'$ and $\hat{\mathbf{e}}_\parallel$.

## 2.2 *N-Matrix Formalism*

The previously mentioned Mueller matrices correctly model the effects of optical activity and birefringence on the Stokes vector of the photons as they propagate between scattering events in the media. However, a problem arises in applying the combined effect when both are exhibited by the sample. Matrix multiplication of these Mueller matrices is not commutative, thus, different orders in which these effects are applied will have different effects on the polarization. Ordered multiplication of these matrices in fact does not make physical sense, as these effects are exhibited simultaneously and not one after the other as sequential multiplication implies. This necessitates the combination of the effects into a single

matrix describing them simultaneously. Conveniently, this can be accomplished through the Jones *N*-matrix formalism.

This method was first developed by Jones,[34] however, a more thorough derivation is provided in Kliger et al.[35] The full derivation[34,35] is not presented here, only a brief overview and the final results are given. Briefly, the issue of noncommutative matrices is overcome by representing the matrix of the sample as an exponential function of a sum of matrices, where each matrix in this sum corresponds to a single optical property. This overcomes the ordering issue as matrix addition is always commutative. However, this is valid only if the matrices are differential, representing the optical property over an infinitely small optical path length. These differential matrices are known as *N*-matrices and their "parent" nondifferential matrices are known as *M*-matrices. The differential *N*-matrices corresponding to each optical property exhibited by the sample are used to express the *M*-matrix for the combined effect. The formalism is expressed in terms of Jones matrices ($2\times2$) rather than the more commonly used Mueller matrices ($4\times4$) previously discussed. However, a Jones matrix can be converted to a Mueller matrix, provided there are no depolarization effects, as described in Schellman and Jensen.[36] This method is applicable to our formalism as depolarization is due to multiple scattering and no depolarization effects occur between scattering events. Once converted to a Mueller matrix, this matrix can be applied to the photons as they propagate between scattering events.

The *N*-matrix $\mathbf{N}$ expressing a single optical effect over an infinitely small path length is found from the corresponding *M*-matrix $\mathbf{M}$ (nondifferential) for a sample exhibiting only that effect and is defined by Jones as

$$\mathbf{N}=\left(\frac{d\mathbf{M}}{dz}\right)\mathbf{M}^{-1}, \tag{5}$$

where $z$ is the path length of the light through the sample. The elements of the *N*-matrix are defined as

$$\mathbf{N}=\begin{bmatrix} n_1 & n_4 \\ n_3 & n_2 \end{bmatrix}. \tag{6}$$

The *N*-matrix for optical activity as found from Eq. (5) and from the Jones matrix of a rotator is

$$\mathbf{N}_{\mathrm{OA}}(\chi)=\begin{bmatrix} 0 & \chi \\ -\chi & 0 \end{bmatrix}, \tag{7}$$

where $\chi=[\alpha]_\lambda^T C$ and is the rotation per unit distance (degrees per centimeter) as a result of the optically active molecules specified in the model. The *N*-matrix for linear birefringence as found from Eq. (5) and the Jones matrix of a retarder is

$$\mathbf{N}_{\mathrm{LB}}(g_0)=\begin{bmatrix} ig_0 & 0 \\ 0 & -ig_0 \end{bmatrix}, \tag{8}$$

where $g_0=\pi\Delta n/\lambda$ is the retardation per unit distance (in radians per centimeter). Because the photon's reference frame has been rotated so that $\hat{\mathbf{e}}_\perp$ is parallel to the extraordinary axis seen by the photon $\mathbf{b}'$, as discussed in the previous section, this *N*-matrix correctly represents the effect of birefringence as seen by the photon. The combined *N*-matrix is found by adding these matrices and dividing by two, giving the resulting *N*-matrix describing the two effects as

$$\mathbf{N}_{\mathrm{OA+LB}}=\frac{1}{2}\begin{bmatrix} ig_0 & \chi \\ -\chi & -ig_0 \end{bmatrix}. \tag{9}$$

Based on the final results of the derivation from Jones and Kliger et al.,[34,35] the elements of the *M*-matrix [defined similar to those of the *N*-matrix in Eq. (6)] for the combined effect are calculated from the corresponding *N*-matrix elements of $\mathbf{N}_{\mathrm{OA+LB}}$ ($n_1=ig_0$, $n_2=-ig_0$, $n_3=-\chi$, and $n_4=\chi$) as

$$m_1=\exp(T_N z)\left[(n_1-n_2)\frac{\sinh Q_N z}{2Q_N}+\cosh Q_N z\right], \tag{10}$$

$$m_2=\exp(T_N z)\left[-(n_1-n_2)\frac{\sinh Q_N z}{2Q_N}+\cosh Q_N z\right], \tag{11}$$

$$m_3=\exp(T_N z)\frac{n_3\sinh Q_N z}{Q_N}, \tag{12}$$

$$m_4=\exp(T_N z)\frac{n_4\sinh Q_N z}{Q_N}, \tag{13}$$

where $T_N$ and $Q_N$ are defined as

$$T_N=\frac{n_1+n_2}{2}, \tag{14}$$

$$Q_N=\left[\frac{(n_1-n_2)^2}{4}+n_3 n_4\right]^{1/2}. \tag{15}$$

The resulting *M*-matrix, now correctly combining the two effects, is then converted from a Jones to Mueller matrix and applied to the photon between scattering events. Note that the *N*-matrix formalism enables the combination of any number of polarizing effects, not just optical activity and linear birefringence, as has been done in this case. As such, the existing model can easily be modified to include any other combination of desired polarization effects; excluding depolarization phenomenon. The significance of this should not be understated as it enables the modeling of all polarization effects that may occur between scattering events.

## 3 Experimental Methods and Materials

As described, the Monte Carlo model was extended to include birefringence and optical activity. However, it is of paramount importance to ensure that the model correctly simulates what occurs physically through experimental validation. This is particularly challenging for polarization-sensitive Monte Carlo development research and, unfortunately, is sometimes neglected. The following section describes the experimental system and phantoms used for the validation experiments.

### 3.1 *Stokes Polarimeter*

To perform the validation experiments, polarimetric measurements were made using the experimental setup shown in Fig. 2, which has been slightly modified from that described in a

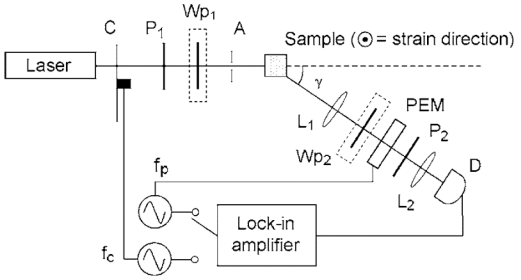



**Fig. 2** Schematic of Stokes polarimeter used for experimental measurements: *C*, mechanical chopper; $P_1$ and $P_2$, polarizers; $W_{p_1}$ and $W_{p_2}$, removable quarter-wave plates; *A*, aperture; $L_1$ and $L_2$, lenses; PEM, photoelastic modulator; *D*, photodetector; $f_c$ and $f_p$ modulation frequencies of mechanical chopper and PEM, respectively.

previous publication.[37] Unpolarized light at 632.8 nm from a HeNe laser (Research Electro-Optics, LHRR-120M) first passes through a mechanical chopper operating at a frequency $f_c$=500 Hz, then through a polarizer with its pass-axis at 0 deg (horizontal), and finally through a removable quarter-wave plate placed before the sample with its fast axis at 45 deg. The removable quarter-wave plate causes the light incident on the sample to be either circularly polarized when in place or linearly polarized when removed. The detection optics begin with another removable quarter wave plate at −45 deg, when in place allowing for the measurement of the Stokes parameters $Q$ and $U$ (linear polarization), and when removed allowing for the measurement of the Stokes parameter $V$ (circular polarization). Sample-scattered light then passes through a photoelastic modulator (PEM, Hinds Instruments IS-90 operating at $f_p$=50 kHz) with its fast axis at 0 deg, and its retardation modulated according to the sinusoidal function $\delta_{\mathrm{PEM}}(t)=\delta_o \sin \omega_p t$, where $\omega_p=2\pi f_p$, and $\delta_o$ is the user-specified amplitude of maximum retardation. The light finally passes through an analyzer orientated at 45 deg and the resulting modulated intensity of the light is measured by an avalanche photodiode (APD) detector (Hamamatsu, C5460). The detection arm of the setup is mounted on a rotatable platform to enable angularly ($\gamma$) resolved measurements of light scattered by the sample. A pair of lenses in the detection optics is used to give a detection area of 1 mm$^2$ (circular area) on the sample and an acceptance angle of 14 deg for light scattered by the sample. The detected signal is sent to a lock-in amplifier (Stanford Research Systems, SR830) with the reference input of the amplifier toggled between the signals from the chopper and PEM controllers. The Stokes parameters of the light scattered from the sample can be calculated from the first harmonic of the signal at the chopper frequency $V_{1f_c}$ and the first and second harmonics of the signal at the PEM frequencies $V_{1f_p}$ and $V_{2f_p}$, respectively. As is shown in a previous publication,[37] the Stokes parameters normalized by the intensity of the light ($q=Q/I$, $u=U/I$, and $v=V/I$) can be extracted as follows. With the detection quarter-wave plate ($W_{p_2}$) in place (linear detection), $q$ and $u$ are found from

$$q=\frac{V_{1f_p}}{\sqrt{2}J_1(\delta_o)V_{1f_c}}, \tag{16}$$

$$u=\frac{V_{2f_p}}{\sqrt{2}J_2(\delta_o)V_{1f_c}}, \tag{17}$$

where $J_1(\delta_o)$ and $J_2(\delta_o)$ are first- and second-order Bessel functions of the first kind evaluated at the amplitude of retardation $\delta_o$ of the PEM. With the detection quarter-wave plate ($W_{p_2}$) removed (circular detection), $v$ is found from

$$v=\frac{V_{1f_p}}{\sqrt{2}J_1(\delta_o)V_{1f_c}}. \tag{18}$$

Based on the calculated Stokes parameters the fraction of linear polarization $\beta_L$ and the fraction of circular polarization $\beta_C$ can be calculated as

$$\beta_L=(q^2+u^2)^{1/2}, \tag{19}$$

$$\beta_C=v. \tag{20}$$

### 3.2 *Polyacrylamide Phantoms*

To validate the developed Monte Carlo model, optical phantoms exhibiting controllable scattering, linear birefringence, and optical activity are required. The creation of phantoms with controllable scattering is easily accomplished through the addition of polystyrene mircospheres or Intralipid, and optical activity can be controlled through the addition of known amounts of chiral molecules such as glucose or sucrose. However, the problem of creating controllable birefringence is somewhat more difficult and has not been previously demonstrated for turbid tissue phantoms. For this study, strain-induced birefringence in a polymer hydrogel was used to create controllable linearly birefringent phantoms. Specifically, polyacrylamide was strained through extension to create birefringence along the direction of strain. This creation of birefringence through strain is also referred to as mechanical birefringence and is a result of the normally isotropic arrangement of the polymer molecules becoming anisotropic along the direction of the applied strain. In other words, the long polymer chains become aligned along the direction of strain and result in a higher refractive index along this direction. In the developed phantoms, scattering is produced through the addition of polystyrene microspheres, and optical activity in induced with the addition of sucrose.

The polyacrylamide phantoms were fabricated using a formulation adapted from Suroweic.[38] The polymerization of acrylamide was carried out using ammonium persulfate as the initiator, N,N′ methylenebisacylamide as a cross-linking agent, and tetramethylethylenediamine as the catalyst. The exothermic polymerization process was completed several minutes after the addition of the catalyst. The phantoms were polymerized in plastic molds with dimensions 1×1×4 cm, removed from the molds after 24 h and stored at 4°C until used. The density of polyacrylamide is $\rho_o$=1.01 g/cm$^3$ and the refractive index was measured through refractometry

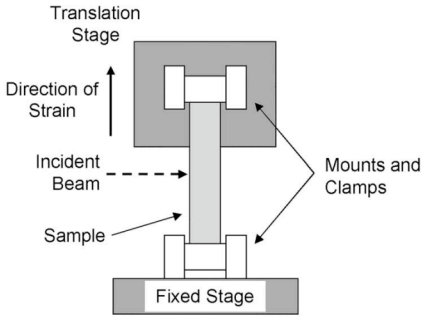



**Fig. 3** Diagram of mounting system used to strain phantoms to induce birefringence. The phantoms are strained vertically in the laboratory reference frame, producing an extraordinary axis along this direction.

(Abbe refractometer model 2WAJ) to be approximately 1.393 at 633 nm. Polystyrene microspheres (refractive index $n_s$ =1.59, density $\rho$=1.05 g/cm$^3$, radius $r$=0.7 $\mu$m) were added to the samples prior to polymerization as scattering particles. The scattering efficiency and anisotropy of these particles in polyacrylamide was calculated from Mie theory and found to be $Q_{\text{scat}}$=2.72 and $g$=0.95, respectively, at 632.8 nm. Based on the weight fraction $f_w$ of added microspheres, the scattering coefficient is calculated as

$$\mu_s = \frac{3Q_{\text{scat}} f_w \rho_o}{4r\rho}. \tag{21}$$

Two sets of phantoms were created with scattering coefficients of 30 and 60 cm$^{-1}$. A measured mass of sucrose was also added to some samples prior to polymerization to create phantoms with a known concentration of sucrose and, through Eq. (1), a known optical activity. Sucrose was used as an optically active molecule rather than glucose, because a reducing sugar such as glucose will interfere with the polymerization process. The addition of sucrose raises the refractive index of polyacrylamide by 0.026 per molar, requiring a recalculation of the scattering efficiency and scattering coefficients.[39] A third set of samples was created with 1 M of sucrose and, based on the recalculation of the scattering efficiency as $Q_{\text{scat}}$=2.22 and the anisotropy as $g$=0.96 at 632.8 nm, with a scattering coefficient of 60 cm$^{-1}$.

To apply controllable strain to produce linear birefringence, the phantoms were glued on both ends to plastic holders and clamped at one end to fixed mount and at the other to a linear translation stage (Fig. 3). The phantoms were stretched to induce birefringence along the direction of strain. To determine the magnitude of the induced birefringence with phantom extension, measurements were taken using the polarimeter with clear samples (no added microspheres or sucrose) strained vertically (90 deg to the lab bench) and input right circularly polarized light (input quarter-wave plate in place). Based on the measured Stokes parameters $u$ and $v$, the retardation was calculated as

$$\delta = \tan^{-1}\left(\frac{u}{v}\right), \tag{22}$$

or using Eqs. (17) and (18) as

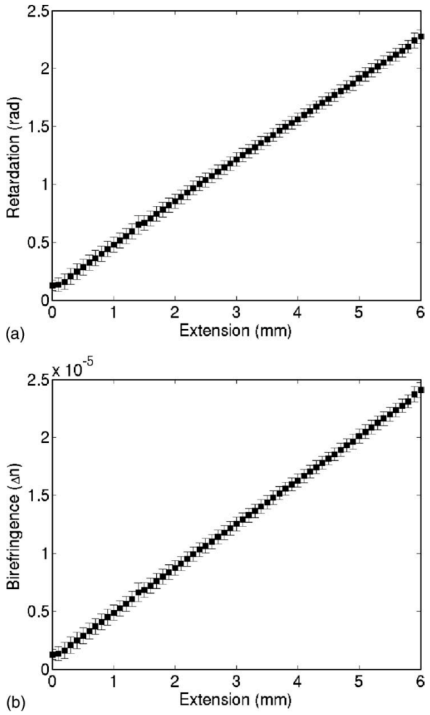



**Fig. 4** Measurements in the forward direction ($\gamma$=0 deg) through clear media of induced (a) retardation $\delta$ and (b) birefringence $\Delta n$ with phantom extension (strain). The birefringence values were corrected for lateral contraction due to extension so that they can be used in Monte Carlo simulations. The unstrained length of the samples is 4 cm.

$$\delta = \tan^{-1}\left[\frac{J_1(\delta_o)V_{2f_p}}{J_2(\delta_o)V_{1f_p}}\right]. \tag{23}$$

## 4 Results and Discussion

The induced retardation with extension (strain) is shown in Fig. 4(a) and can be seen to increase linearly. The small nonzero retardation at zero extension is due to small amounts of strain on the sample present when clamped to the mount and translation stage. From the measured retardation, one is able to calculate the difference in refractive indices from Eq. (3); however, the contraction (reduction in width) of the phantom due to the extension must be taken into account as this effectively reduces the path length through the sample. This contraction was estimated from the Poission ratio for polyacrylamide (the ratio of fractional change in width to fractional change in length[40]), which was estimated from unpublished reports and verified with measurements to be 0.33. Practically, this means that the sample width decreases from 1 cm (no strain) to 0.95 cm at maximum strain level (6 mm extension). This contraction was then taken into account when calculating the difference in refractive indices using Eq. (3). Figure 4(b) shows the difference in refractive indices corrected for contraction with extension of the polyacrylamide samples. The variability seen in the measurements is due to slight differ-

ences in mounting of the samples, slight differences between batches of samples, and small inhomogeneities in the birefringence of the samples. Overall, however, variability in batches is not significant and the samples appear homogeneous as measurements where made in varying vertical positions. In addition, the induced birefringence was examined spatially with crossed polarizers and was seen to be reasonably uniform. Based on these methods, we were able to produce phantoms with controllable scattering, birefringence, and optical activity and use the calculated physical parameters of these phantoms as input into the Monte Carlo model for validation.

The first set of Monte Carlo calculations and experiments involved validation of birefringence in the presence of scattering (no sucrose). The second set of calculations and experiments involved validation of both birefringence and optical activity (i.e., staining of samples and added sucrose) in the presence of scattering. In both cases, Monte Carlo simulations were run with input parameters matching those present physically in the fabricated phantoms, as calculated from the previously described methods. The photon collection geometry mimics that present experimentally with a detection area of 1 $mm^2$ (rectangular area now as opposed to the circular experimental area) and an acceptance angle of 20 deg (slightly larger than that employed experimentally).

Figures 5 and 6 show the experimentally measured and Monte Carlo calculated normalized Stokes parameters for two sets of samples with scattering coefficients of 30 and 60 $cm^{-1}$, respectively, as a function of strain-induced birefringence. Measurements and calculated values are shown for both the forward and lateral detection geometries ($\gamma$=0 deg and $\gamma$=90 deg in Fig. 2) with input right circularly polarized light (quarter-wave plate before the sample in place, as shown in Fig. 2). Input circularly polarized light is used as it eliminates the requirement for alignment of the sample's extraordinary axis with the input light's polarization to achieve the maximum effect from the birefringence. In both cases, the measurements and calculations were performed in the center of the sample faces. The samples were strained vertically (refer to Fig. 3), creating a vertical extraordinary axis as the induced retardation varied from $\delta$=0 to 1.4364 rad ($\Delta n$=0 to $1.628\times10^{-5}$). All Monte Carlo simulations were run with $10^8$ photons to achieve reasonably low statistical uncertainties in the calculated values. The experimental values plotted are the average from measurements on five samples. In isotropic turbid media (no birefringence) the effect of scattering on the polarization of the light in both the forward and lateral directions is a depolarization of the incident circularly polarized light. As one would expect, higher scattering coefficients result in greater depolarization. The effect of birefringence on the polarization becomes evident with increasing birefringence as a continuous change from the input right circularly polarized light to linear polarized light at 45 deg (Stokes parameter $U$). This is due to the retardation of orthogonal polarization states parallel and perpendicular to the extraordinary axis in the vertical direction. As this retardation increases with strain, the polarization begins to transfer from circular to linear polarization. The sample is in a sense acting as a turbid variable wave plate with its extraordinary axis in the vertical direction changing the polarization from circular to linear and depolarizing the light. The change from circular to linear polarization occurs more rapidly with increasing birefringence in the forward direction than in the lateral. This is likely a result of the longer optical path length of light that propagates directly through the sample, in comparison to that which is scattered and exits from the side of the samples. From Monte Carlo simulations, the average photon path length for light exiting in the lateral direction ($\gamma$=90 deg) was 1.042 and 1.362 cm for 30 and 60 $cm^{-1}$, respectively, versus 1.174 and 1.753 cm for 30 and 60 $cm^{-1}$, respectively, for light exiting the samples in the forward direction ($\gamma$=0 deg). The longer path length results in more retardation of the light, as seen in Eq. (4), and a larger change from circular to linear polarization. Close agreement can be seen between the Monte Carlo calculations and experimental results, indicating that the model correctly simulates the effect of linear birefringence in the presence of scattering. The calculated root mean square error (RMSE) between experimental and Monte Carlo calculations was 0.025 for 60 $cm^{-1}$ and 0.058 for 30 $cm^{-1}$. The slightly larger disagreement present between the calculations and measurements at 30 $cm^{-1}$ is likely caused by a greater variability in the magnitude of strain-induced birefringence between samples due to either variation in the mounting of the

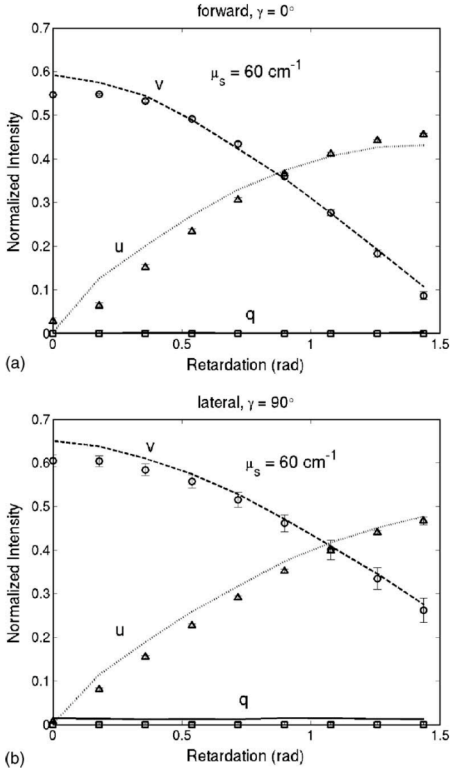



**Fig. 5** Experimental measurements (symbols) and Monte Carlo calculations (lines) of the normalized Stokes parameters $q$ (squares and solid line), $u$ (triangles and dotted line), and $v$ (circles and dashed line) in the (a) forward ($\gamma$=0 deg) and (b) lateral ($\gamma$=90 deg) detection geometries with input circularly polarized light and a scattering coefficient of 60 $cm^{-1}$. Birefringence is varied from $\delta$=0 to 1.4364 rad ($\Delta n$=0 to $1.628\times10^{-5}$). Experimental values are the means of measurements on five samples.

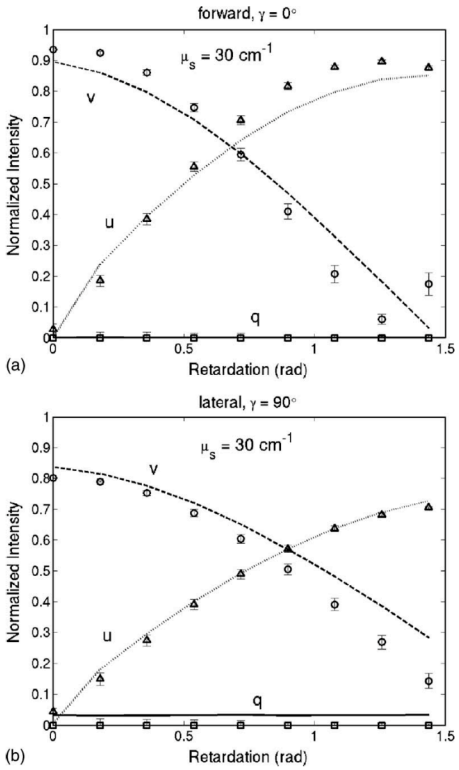



**Fig. 6** Experimental measurements (symbols) and Monte Carlo calculations (lines) of the normalized Stokes parameters $q$ (squares and solid line), $u$ (triangles and dotted line), and $v$ (circles and dashed line) in the (a) forward ($\gamma$=0 deg) and (b) lateral ($\gamma$=90 deg) detection geometries with input circularly polarized light and a scattering coefficient of 30 $cm^{-1}$. Birefringence is varied from $\delta$=0 to 1.4364 rad ($\Delta n$=0 to $1.628\times10^{-5}$). Experimental values are the means of measurements on five samples.

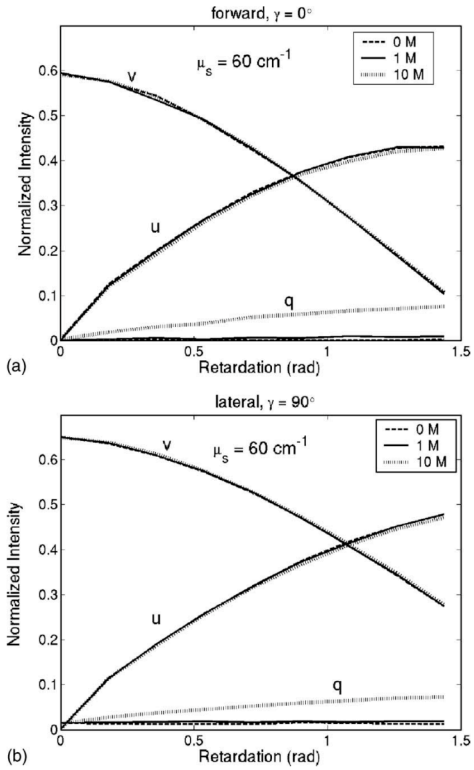



**Fig. 7** Monte Carlo calculations with optical activity $\chi$=0 deg $cm^{-1}$ (dashed lines), $\chi$=0.8194 deg $cm^{-1}$ (solid lines), and $\chi$ =8.194 deg $cm^{-1}$ (dotted lines) corresponding to 0, 1, and 10 M glucose concentrations, respectively. The normalized Stokes parameters are plotted in the (a) forward ($\gamma$=0 deg) and (b) lateral ($\gamma$=90 deg) detection geometries with input circularly polarized light and a fixed scattering coefficient of 60 $cm^{-1}$ for all glucose concentrations. Birefringence is varied from $\delta$=0 to 1.4364 rad ($\Delta n$=0 to $1.628\times10^{-5}$). Only a small chirality-induced change in $q$ is apparent.

samples or in the fabrication process. To our knowledge, this is the first experimental validation of a polarization-sensitive Monte Carlo model for turbid media incorporating birefringence.

Monte Carlo simulations and experimental measurements were then undertaken with turbid samples exhibiting both birefringence and optical activity. As previously mentioned, the magnitude of chirality-induced optical rotation in biological tissue is low, of the order of tens to hundreds of millidegrees per centimeter. This small effect is superimposed on the relatively large retardations (of the order of 180 deg/cm) caused by linear birefringence due to structural proteins and the large depolarization due to scattering. Accordingly, the effect of optical chirality/rotation on the polarization of light in biological tissue is significantly lower than that of scattering or birefringence. Figure 7 shows the normalized Stokes parameters from Monte Carlo simulations run with increasing magnitudes of optical activity. As before, the calculated values were in the forward and lateral geometries, the input light was circularly polarized, and the induced retardation was varied from $\delta$=0 to 1.4364 rad ($\Delta n$=0 to $1.628\times10^{-5}$). The magnitudes of optical activity were $\chi$=0 deg $cm^{-1}$, $\chi$=0.8194 deg $cm^{-1}$, and $\chi$=8.194 deg $cm^{-1}$ corresponding to 0, 1, and 10 M concentrations of glucose respectively (note that optical activity due to glucose was used in these calculations). The index-matching effect of chiral molecules has been ignored in these simulations to focus on the effects of birefringence and optical activity alone. Often changes in polarization are due to significant changes in the scattering properties.[14,37] As seen, the effect of optical activity is small and generally only evident at a 10 M glucose concentration, more that 1000 times greater than physiological levels. The difference caused by this large amount of added glucose (at least if the refractive index-matching effect is ignored), in fact, approaches the noise threshold for these calculations in the case of all Stokes parameters except $q$. The primary effect of optical activity is an increase in the normalized Stokes parameter $q$ with increasing birefringence. This increase results from the interplay of several mechanisms. Optical activity has no measurable effect on circularly polarized light, as rotating the plane of circularly polarized light introduces only a global phase shift, which is normally not detectable. Therefore, the effect of optical activity is evident only as the input

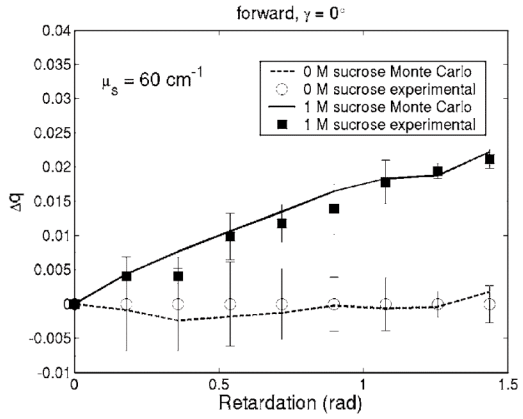



**Fig. 8** Experimental measurements and Monte Carlo calculations of the change in the normalized Stokes parameter $q$ with optical activity (solid lines and squares) and without optical activity (dotted lines and circles) in the forward ($\gamma$=0 deg) detection geometry with input circularly polarized light and a fixed scattering coefficient of 60 $cm^{-1}$. Birefringence is varied from $\delta$=0 to 1.4364 rad ($\Delta n$=0 to $1.628 \times 10^{-5}$) and the magnitude of optical activity is $\chi$=1.965 deg $cm^{-1}$, corresponding to a 1 M sucrose concentration.

light is retarded and transferred from the input circularly polarization to linearly polarization. As the light becomes linearly polarized at 45 deg (Stokes parameter $U$) due to the increasing birefringence, the plane of linear polarization is rotated due to the optical activity. This manifests as a small reduction in the normalized Stokes parameter $u$ and an increase in the normalized Stokes parameter $q$. The reduction in $u$ is small and difficult to see in the plots; however, the increase in $q$ due to rotation can be seen. This increase is not due to increasing rotation with increasing birefringence but is due to the increase in the fraction of linear polarization associated with the increasing birefringence. In other words, the total amount of linear polarization increases with increasing birefringence, and as a result so do the chirality-induced changes in both $q$ and $u$. We also see that $q$ increases more rapidly in the forward direction than in the lateral direction. As was described for birefringence, this may also be due to the larger path length traversed by light in the forward direction, producing a larger retardation and higher fraction of linear polarization. The longer path length also results in more optical rotation due to glucose chirality, thus also resulting in a larger value of $q$ in the forward direction.

To validate these Monte Carlo model predictions with both birefringence and optical activity, calculations and measurements were compared for samples with 1 M of sucrose ($\chi$ = 1.965 deg $cm^{-1}$), the retardation varied from $\delta$=0 to 1.4364 rad ($\Delta n$=0 to $1.628 \times 10^{-5}$), and a scattering coefficient of 60 $cm^{-1}$ (the refractive index-matching effect of sucrose was taken into account in calculation of the required weight fraction $f_w$ of microspheres). Results for input circularly polarized light and forward detection direction ($\gamma$ =0 deg) are shown in Fig. 8. In contrast to the previous calculations, the index-matching effect of sucrose was now taken into account. Figure 8 shows the change in the normalized Stokes parameter $q$ ($\Delta q$) with increasing birefringence both with and without added sucrose. The increase in $q$ from the induced optical rotation with increasing birefringence, as seen in the previous Monte Carlo simulations, is also evident. The calculated and measured values of $\Delta q$ with no added sucrose are also plotted to demonstrate the effect of optical activity. Close agreement is seen between the calculations and experimental measurements, thus indicating that the model correctly simulates the effects of birefringence, optical activity, and scattering on the polarization of light. To our knowledge this is the first polarization-sensitive model to incorporate all three effects and the first, albeit limited, validation of such a model.

This upgraded model will be used to investigate the potential for polarized-light-based detection of glucose in biological media. In the current validation study, incident circularly polarized light was used in all simulations and experiments, however, in future work incident linearly polarized light with varying orientations with respect to the direction of birefringence will be investigated. This will be done to test the ability to quantify optical activity in the presence of birefringence. Linearly rather than circularly polarized light may prove to be superior for measuring chirality-induced optical activity as the effects of optical activity are generally more pronounced. Current results with input circularly polarized light demonstrate that the effects of optical activity can be quantified (change in $q$), however, this was done with knowledge of the direction of birefringence and with uniform birefringence through the sample. Future work will investigate the ability to quantify the effects of optical activity in nonuniform birefringent media without prior knowledge of the direction of birefringence using both the Monte Carlo model and polyacrylamide phantoms. The spatial and angular dependence of polarization effects in turbid chiral media will also be examined in the presence of birefringence. Finally, this upgraded model will also be used to explore the use of spectroscopic polarimetry and chemometric analysis to extract the rotation only due to glucose from that of other chiral species present in tissue.

## 5 Conclusions

We demonstrate an experimentally validated Monte Carlo model for polarized light propagation in birefringent, optically active, turbid media. Birefringence and optical activity are two common phenomena in biological tissue; therefore the upgraded Monte Carlo model now more accurately simulates the interactions of polarized light in tissue. This is particularly important in the context of turbid polarimetry for glucose detection, as biological tissues are anisotropic, thus exhibiting linear birefringence. The problem of combining the effects of birefringence and optical activity in scattering media is resolved through use of the Jones $N$-matrix formalism, giving the Mueller matrix for the combined effect that can be applied to photons as they propagate between scattering events. This formalism also enables the incorporation of other scattering-independent optical polarization effects such as circular or linear dichroism. To validate this extended model, polarimetric measurements on light scattered by polyacrylamide phantoms with strain-induced birefringence and sucrose-induced optical activity were compared to Monte Carlo calculations with similar parameters. The results show close agreement between experimental measurements and Monte Carlo calculations, providing strong evidence for the validity of the

model. To our knowledge, this is the first polarization-sensitive Monte Carlo model to incorporate the effects of both birefringence and optical activity in scattering media, and the corresponding first validation studies.

## Acknowledgments

The authors would like to thank Dr. Daniel Côté for assistance with extending the polarization-senstive Monte Carlo code, and Mrs. Claire McCann for her assistance with the phantom fabrication. Financial support from the Natural Sciences and Engineering Research Council of Canada and the Ontario Graduate Scholarship Program is gratefully acknowledged.

## References

1. L. V. Wang, G. L Coté, and S. L. Jacques, "Special section guest editorial: tissue polarimetry," *J. Biomed. Opt.* **7**, 278 (2002).
2. J. F. de Boer and T. E. Milner, "Review of polarization sensitive optical coherence tomography and Stokes vector determination," *J. Biomed. Opt.* **7**, 359–371 (2002).
3. Y. L. Kim, Y. Liu, R. K. Wali, H. K. Roy, M. J. Goldberg, A. K. Kromin, K. Chen, and V. Backman, "Simultaneous measurement of angular and spectral properties of light scattering for characterization of tissue microarchitecture and its alteration in early precancer," *IEEE J. Sel. Top. Quantum Electron.* **9**, 243–256 (2003).
4. S. L. Jacques, J. C. Ramella-Roman, and K. Lee, "Imaging skin pathology with polarized light," *J. Biomed. Opt.* **7**, 329–340 (2002).
5. R. S. Gurjar, V. Backman, L. T. Perelman, I. Georgakoudi, K. Badizadegan, I. Itzkan, R. R. Dasari, and M. S. Feld, "Imaging human epithelial properties with polarized light scattering spectroscopy," *Nature Med.* **7**, 1245–1249 (2001).
6. S. G. Demos and R. R. Alfano, "Temporal gating in highly scattering media by the degree of optical polarization," *Opt. Lett.* **21**, 161–163 (1996).
7. J. S. Baba, B. D. Cameron, S. Theru, and G. L. Coté, "Effect of temperature, pH, and corneal birefringence on polarimeteric glucose monitoring in the eye," *J. Biomed. Opt.* **7**, 321–328 (2002).
8. D. Côté and I. A. Vitkin, "Balanced detection for low-noise precision polarimetric measurements of optically active, multiply scattering tissue phantoms," *J. Biomed. Opt.* **9**, 213–220 (2004).
9. K. Maruo, M. Tsurugi, J. Chin, T. Ota, H. Arimoto, Y. Yamada, M. Tamura, M. Ishii, and Y. Ozaki, "Noninvasive blood glucose assay using a newly developed near-infrared system," *IEEE J. Sel. Top. Quantum Electron.* **9**, 322–330 (2003).
10. K. V. Larin, M. Motamedi, M. S. Eledrisi, and R. O. Esenaliev, "Noninvasive blood glucose monitoring with optical coherence tomography," *Diabetes Care* **25**, 2263–2267 (2002).
11. A. M. K. Enejder, T. G. Scecina, J. Oh, M. Hunter, W. Shih, S. Sasic, G. L. Horowitz, and M. S. Feld, "Raman spectroscopy for noninvasive glucose measurements," *J. Biomed. Opt.* **10**, 031114 (2005).
12. "*The Glucon Solution: Clinical Trials*," available online at http://www.glucon.com (2006).
13. R. Badugu, J. R. Lakowicz, and C. D. Geddes, "Ophthalmic glucose monitoring using disposable contact lenses—a review," *J. Fluoresc.* **14**, 617–633 (2004).
14. K. C. Hadley and I. A. Vitkin, "Optical rotation and linear and circular depolarization rates in diffusively scattered light from chiral, racemic, and achiral turbid media," *J. Biomed. Opt.* **7**, 291–299 (2002).
15. I. A. Vitkin and E. Hoskinson, "Polarization studies in multiply scattering chiral media," *Opt. Eng.* **39**, 353–362 (2000).
16. A. J. Welch and M. J. C. van Gemert, *Optical-Thermal Response of Laser Irradiated Tissue*, Chap. 2, Plenum Press, New York (1995).
17. A. J. Welch, G. Yoon, and M. J. van Gemert, "Practical models for light distribution laser-irradiated tissue," *Lasers Surg. Med.* **6**, 488–493 (1987).
18. M. S. Patterson, B. C. Wilson, and D. R. Wyman, "The propagation of optical radiation in tissue I. Models of radiation transport and their application," *Lasers Med. Sci.* **6**, 155–166 (1990).
19. L. Wang, S. L. Jaques, and L. Zheng, "MCML—Monte Carlo modeling of light transport in multi-layered tissues," *Comput. Methods Programs Biomed.* **47**, 131–146 (1995).
20. F. Jaillon and H. Saint-Jalmes, "Description and time reduction of a Monte Carlo code to simulate propagation of polarized light through scattering media," *Appl. Opt.* **42**, 3290–3296 (2003).
21. B. Kaplan, G. Ledanois, and B. Drevillon, "Mueller matrix of dense polystyrene latex sphere suspensions: measurements and Monte Carlo simulations," *Appl. Opt.* **40**, 2769–2777 (2001).
22. M. Moscoso, J. B. Keller, and G. Papanicolaou, "Depolarization and blurring of optical images by biological tissues," *J. Opt. Soc. Am. A* **18**, 949–960 (2001).
23. J. R. Mourant, T. M. Johnson, and F. P. Freyer, "Characterization of mammalian cells and cell phantoms by polarized backscattering fiber-optic measurements," *Appl. Opt.* **40**, 5114–5123 (2001).
24. S. Bartel and A. H. Hielscher, "Monte Carlo simulations of the diffuse backscattering Mueller matrix for highly scattering media," *Appl. Opt.* **39**, 1580–1588 (2000).
25. L. V. Kuz'min, I. V. Meglinski, and D. Yu. Churmakov, "Coherent effects in multiple scattering of linearly polarized light," *Opt. Spectrosc.* **98**, 653–659 (2005).
26. W. Wang and L. V. Wang, "Propagation of polarized light in birefringent media: a Monte Carlo study," *J. Biomed. Opt.* **7**, 350–358 (2002).
27. S. V. Gangnus, S. J. Matcher, and I. V. Meglinski, "Monte Carlo modeling of polarized light propagation in biological tissue," *Proc. SPIE* **4619**, 281–288 (2002).
28. X. Wang, G. Yoa, and L. V. Wang, "Monte Carlo model and single scattering approximation of the propagation of polarized light in turbid media," *Appl. Opt.* **41**, 792–801 (2002).
29. D. Côté and I. A. Vitkin, "Robust concentration determination of optically active molecules in turbid media with validated three-dimensional polarization sensitive Monte Carlo calculations," *Opt. Express* **13**, 148–163 (2005).
30. D. Côté and I. A. Vitkin, "Pol-MC: a three dimensional polarization sensitive Monte Carlo implementation for light propagation in tissue," available online at http://www.novajo.ca/ont-canc-inst-biophotonics/.
31. C. F. Bohren and D. R. Huffman, *Absorption and Scattering of Light by Small Particles*, Chap. 2, Wiley, New York (1983).
32. H. C. van de Hulst, *Light Scattering by Small Particles*, Chap. 5, Dover, New York (1981).
33. B. E. A. Saleh and M. C. Teich, *Fundamentals of Photonics*, Chap. 6, Wiley-Interscience (1991).
34. R. Clark Jones, "New calculus for the treatment of optical systems. VII. Properties of the *N*-matrices," *J. Opt. Soc. Am.* **38**, 671–685 (1948).
35. D. S. Kliger, J. W. Lewis, and C. E. Randall, *Polarized Light in Optics and Spectroscopy*, Chap. 5, Academic Press–Harcourt Brace Jovanovich, New York (1990).
36. J. Schellman and H. P. Jenson, "Optical spectroscopy of oriented molecules," *Chem. Rev. (Washington, D.C.)* **87**, 1359–1399 (1987).
37. X. Guo, M. F. G. Wood, and I. A. Vitkin, "Angular resolved linear Stokes polarimeter measurements of light scattered by turbid chiral media," *J. Biomed. Opt.* **11**, 041105 (2006).
38. A. Suroweic, "PA Gel 915 MHz muscle-equivalent phantom material," *Int. J. Hyperthermia* **8**, 795–801 (1994).
39. J. Franklin and Z. Y. Wang, "Refractive index matching: a general method for enhancing the optical clarity of a hydrogel matrix," *Chem. Mater.* **14**, 4487–4489 (2002).
40. I. S. Sokolnikoff, *Mathematical Theory of Elasticity*, Krieger, Malabar (1983).

***Addendum***

After this manuscript was published, an error was discovered in range of retardance values listed for Figures 5 through 8. The retardance range of $\delta = 0$ to 1.4364 rad was incorrect and should be listed as $\delta = 0$ to 1.5633 rad. The values of birefringence $\Delta n$ used in the simulations are correct, thus the model generated data and the experimental data are correct. The error arose when converting from the birefringence values to retardance values via Eq. 8, as an incorrect pathlength was used. While this error is minor and does not impact the results or conclusions presented in the previous publication and chapter, it is noted here for completeness.

As was described in the previous section and publication, a hydrogel based phantom system was developed for the validation. As with the extended Monte Carlo model, this phantom system is the first to incorporate the effects of scattering, birefringence, and optical activity simultaneously. The phantom system is potentially useful for investigations requiring phantoms involving polarized light in biomedical optics as many tissues exhibit these three effects. Because of this novelty, the phantom work was also presented and published separately as a conference proceeding. As this system has already been described in the above publication, the description is not repeated here; however, the reader is referred to the conference proceeding for further information.

***Conference – Oral Presentation***

**M. F. G. Wood**, N. Ghosh, X. Guo, and I. A. Vitkin, "Phantoms for Polarized Light Exhibiting Controllable Scattering, Birefringence, and Optical Activity," *Proceedings of SPIE*, Photonics West, 6870-15 (2008).

The extended model and developed phantom system represent a more complete and accurate means of simulating the polarization properties of scattering media, both as a computer model and experimental phantom. The three most prominent polarization properties of tissue (scattering, birefringence, and optical activity) can be simultaneously controlled by both model and phantom, making this platform a flexible and accurate method for simulation and experimental polarization studies where known/controllable properties are required. However, the validity of the model and phantom to simulated biological tissue is somewhat questionable as the scattering mechanisms differ. The model and phantom are comprised of mono-disperse spherical particles, whereas the tissue scatterers are irregular in size, shape, and refractive index. That being said, the extended/developed model and phantom platform better model polarized light in tissue-like media than those previously employed.

# 3. Characterization of myocardial tissue structure

The current chapter describes the studies of polarized light-based characterization of the myocardium, in particular, towards potentially monitoring stem cell regenerative treatments of myocardial infarction. Studies conducted include: (1) a proof-of-principle study, (2) point and imaging measurements on regenerating myocardium, (3) investigations on the effect of birefringence orientation and tissue fixation, and (4) a demonstration of the polarization measurements *in vivo* with a window chamber model.

## 3.1 Proof-of-Principle Feasibility Study

Before embarking upon full-scale studies employing polarized light for myocardial characterization, particularly towards monitoring regenerative treatments, a pilot study was conducted to demonstrate the ability to characterize myocardial tissue. This study was conducted in collaboration with Dr. Ren-Ke Li and his regenerative medicine group at the Toronto General Research Institute. In this study, our ability to differentiate between healthy and infracted mouse myocardium was demonstrated. This animal study was conducted under institutional approval (University Health Network, Toronto, Ontario, Canada).

Myocardial infarctions were induced in two mice (n = 2) by permanent coronary artery ligation. The animals were sacrificed nine weeks post infarction to allow for the development of a mature infarct. The hearts were removed, fixed in 10% formalin solution and sectioned to 300 μm sagittally by vibratome (Leica). The fixation was

performed in order to both preserve the tissue and allow for sectioning. The sectioning was undertaken so that the thickness would be uniform between measurements, as the effect of birefringence (retardance) is dependent on the optical pathlength (see Eq. 8), a constant optical pathlength is required to compare measurements from different samples. Sectioning also reduces the depolarizing effects of scattering, allowing for a higher degree of retained polarization and thus more accurate measurements.

Measurements were performed on these samples using the system described in the previous chapter (see section 3.1 and Figure 2 starting on page 4 in the included publication) in the direct transmission geometry ($\gamma = 0^{o}$). The sections were mounted between a cover slip and glass slide to ensure a uniform thickness and slow tissue dehydration, and placed in the beam path. Light incident on the samples was right circularly polarized and the output normalized Stokes vector parameters of the light interacting with the samples were calculated (Eqs. 16 – 18 on page 5 in the publication from the previous chapter). The retardance of the interacting light was calculated based on the input light being circularly polarized using the measured normalized Stokes parameters as

$$\delta = \tan^{-1}\left(\frac{\sqrt{q^2 + u^2}}{v}\right). \tag{12}$$

This equation differs from that the method in the previous chapter (Eq. 22 on page 6 in the publication), as in those measurements the phantom birefringence was assumed to be only along the orientation of strain (vertically in the measurement plane). For these measurements an orientation of birefringence in the measurement plane could not be assumed, necessitating the use of Eq. 12. However, it should be noted that Eq. 12 does

not account for variations in the birefringence orientation not in the measurement plane; the effect of this angle variation on retardance measurements will be investigated in 3.4.1. Five measurements were performed in the infarcted, healthly, and marginal (transition region between infracted and healthly) regions of each heart.

The means of the five measurements in each region as well as the standard deviation are plotted in Fig. 8. A large decrease in retardance was measured from the healthy to marginal regions, with a further decrease in retardance from the marginal to the infarcted region. This decrease in retardance indicates a loss in tissue organization associated with infarction thought to be due to the necrois of cardiomyocytes and the formation of disorganized collagenous scar tissue. In the healthy state, the myocardium is comprised primarily of highly organized cardiac muscle fibers. This highly organized state produces high values of birefringence and thus high values of measured retardance. With infarction, the highly organized cardiac muscle fibers are replaced by disorganized scar tissue, resulting in much lower values of birefringence and accordingly much lower values of measured retardance.

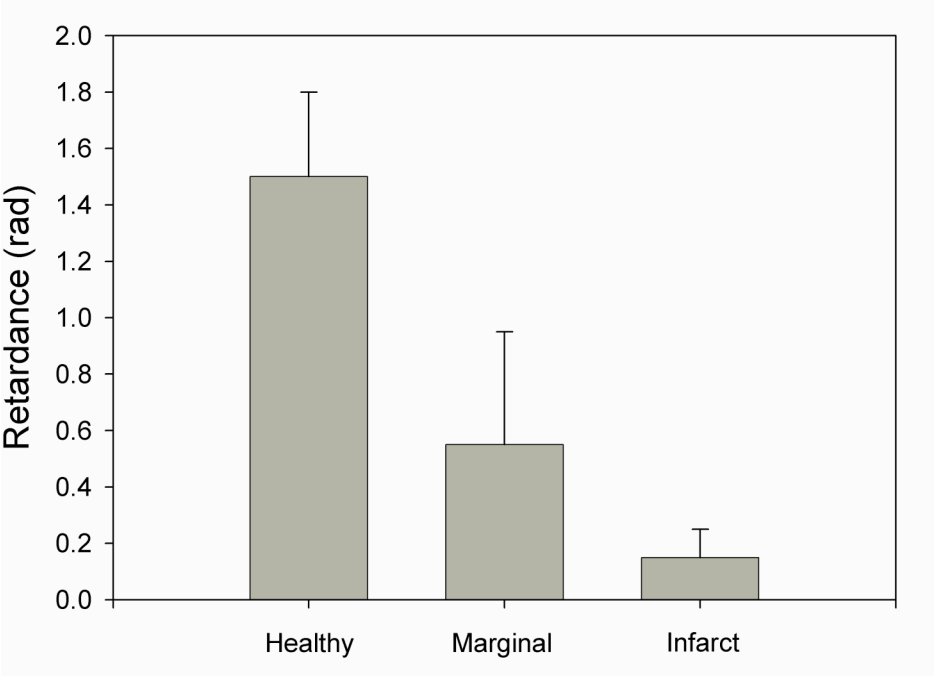



**Fig. 8** Retardance measurements on healthy, marginal, and infarcted regions of mouse 300 μm thick myocardium sections.

Based on these results, it is apparent that the healthy mouse myocardium exhibits significant birefringence. The structural changes in the myocardium associated with infarction produce a large decrease in birefringence that can be measured using polarized light as a reduction in retardance. Based on an optical pathlength of at least 300 μm (tissue thickness), and the measured retardance in the healthy, marginal, and infarcted region of approximately 1.4, 0.5, and 0.2 rad, respectively, the birefringence was calculated using Eq. 8 as at least $\Delta n = 4.7 \times 10^{-4}$, $1.7 \times 10^{-4}$, and $6.7 \times 10^{-5}$, respectively. The calculated healthy and infarcted birefringence values compare well with those from a previous study by Schoenenberger *et al.*[36] where birefringence of healthy and thermally damaged porcine myocardium was measured using PS-OCT as $6.6 \times 10^{-4}$ and $1.8 \times 10^{-4}$ respectively. These encouraging early results motivated further studies, particularly

towards characterizing myocardial structural changes associated with stem cell regenerative treatments.

## 3.2 Point polarization measurements on myocardial tissues

***Introduction***

Based on the positive results of the proof-of-principle study, further work was conducted for structural characterization of the myocardium. In this study, measurements were made on sectioned rat myocardium with induced infarcts where a group of animals had undergone stem cell regenerative treatment (with an untreated group as a control). The purpose of this study was to demonstrate the ability of polarimetry methods to characterize structural remodeling changes in the myocardium as a result of not only infarction, but regenerative treatment as well.

In addition to investigating the ability of polarimetry to characterize myocardial remodeling associated with stem cell regenerative treatments, this study also employed a more sophisticated method of analysis. In the previous section, the tissue-induced retardance was calculated based on the measured output Stokes vector of the light interacting with the sample via Eq. 12. While this is suitable as the effects of retardance on the polarization of the output light are dominant, it does neglect polarization changes that may be the result of scattering, optical activity, or diattenuation. As such, this method—while suitable for the previous proof-of-principle study—may well be prone to error. A more suitable method is to calculate the sample polarization transfer function in the form of a Mueller matrix and extract the values of retardance from this *complete* representation of the sample polarizing effects. The extraction of retardance and other

individual effects from the measured sample Mueller matrix is nontrivial. However, this can be accomplished by polar decomposition of the matrix.[121] Previous studies by our group have validated the used of the decomposition method for multiply scattering media such as tissue.[122] The validation was conducted using the Monte Carlo model and polarization phantom model developed in the previous chapter.

The methods involved in this study as well as results are presented in the following publication. This paper was broadly focused on the use of polarimetry for tissue characterization and includes sections not relevant to the application of polarized for myocardial characterization, in particular section 3.2, which focuses on the glucose concentration determination. This section will be discussed in detail in Chapter 3. I shared first authorship of this paper with Dr. Nirmalya Ghosh (a post doctoral fellow in our group); as we contributed equally in performing the experimental measurements and analysis as well as manuscript writing. The design and implementation of the animal model was overseen by Shu-Hong Li, a laboratory technician in Dr. Ren-Ke Li's group at the Toronto General Research Institute.

***Paper***

N. Ghosh*, **M. F. G. Wood***, S. H. Li, R. D. Weisel, B. C. Wilson, R. K. Li, and I. A. Vitkin, "Mueller matrix decomposition for polarized light assessment of biological tissues," *Journal of Biophotonics* **2**, 145-156 (2009).

* Authors contributed equally to this work and shared 1st authorship

***Conference – Poster Presentation***

**M. F. G. Wood**, X. Guo, D, Côté, I. A. and Vitkin, "Polarized light based measurements for myocardical characterization." *Proceedings of the Imaging Network of Ontario*

*(ImNO) 6th Annual Imaging Symposium*, March 28-29, 2007, University of Toronto, Toronto ON.

WILEY InterScience® DISCOVER SOMETHING GREAT

Early View publication on
www.interscience.wiley.com
(issue and page numbers not yet assigned;
citable using Digital Object Identifier – **DOI**)

J. Biophoton. 1–12 (2008) / **DOI** 10.1002/jbio.200810040

Journal of
BIOPHOTONICS

FULL ARTICLE

# Mueller matrix decomposition for polarized light assessment of biological tissues

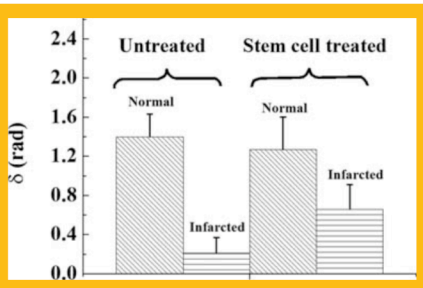
*Nirmalya Ghosh*[**,1] *Michael F. G. Wood*[**,1], *Shu-hong Li*[2], *Richard D. Weisel*[2], *Brian C. Wilson*[1], *Ren-Ke Li*[2], *and I. Alex Vitkin*[3,*]

[1] Ontario Cancer Institute, Division of Biophysics and Bioimaging, University Health Network, Toronto, Ontario, Canada; University of Toronto, Department of Medical Biophysics, Toronto, Ontario, Canada.
[2] Toronto General Research Institute, Division of Cardiovascular Surgery, Toronto, Ontario, Canada; Toronto General Hospital, Division of Cardiac Surgery, Toronto, Ontario, Canada; University of Toronto, Toronto, Ontario, Canada.
[3] Ontario Cancer Institute, Division of Biophysics and Bioimaging, University Health Network, Toronto, Ontario, Canada; University of Toronto, Department of Medical Biophysics and Radiation Oncology, Toronto, Ontario, Canada.

Received 8 July 2008, revised 15 August 2008, accepted 7 October 2008
Published online 24 October 2008

**Key words:** polarimetry, optical activity, birefringence, non-invasive tissue characterization, glucose, regenerative medicine

The Mueller matrix represents the transfer function of an optical system in its interactions with polarized light and its elements relate to specific biologically or clinically relevant properties. However, when many optical polarization effects occur simultaneously, the resulting matrix elements represent several "lumped" effects, thus hindering their unique interpretation. Currently, no methods exist to extract these individual properties in turbid media. Here, we present a novel application of a Mueller matrix decomposition methodology that achieves this objective. The methodology is validated theoretically via a novel polarized-light propagation model, and experimentally in tissue simulating phantoms. The potential of the approach is explored for two specific biomedical applications: monitoring of changes in myocardial tissues following regenerative stem cell therapy, through birefringence-induced retardation of the lights linear and circular polarizations, and non-invasive blood glucose measurements through chirality-induced rotation of the lights linear polarization. Results demonstrate potential for both applications.




Birefringence measurements in normal and infarcted regions of ex vivo untreated and stem cell treated rat myocardium. Note the higher birefringence values in the infarcted region with treatment

© 2008 by WILEY-VCH Verlag GmbH & Co. KGaA, Weinheim

## 1. Introduction

Polarimetry has played important roles in understanding the nature of electromagnetic waves [1], elucidating the three dimensional characteristics of chemical bonds [2], uncovering the asymmetric (chiral) nature of biological molecules [3], determining sugar concentrations in industrial processes [4], quantifying

* Corresponding author: e-mail: vitkin@uhnres.utoronto.ca
** Nirmalya Ghosh and Michael F. G. Wood contributed equally to this work.



© 2008 by WILEY-VCH Verlag GmbH & Co. KGaA, Weinheim

Journal of BIOPHOTONICS



protein properties in solutions [5], supplying a variety of nondestructive evaluation methods [6], developing advanced concepts such as polarization entropy [7], contributing to remote sensing in meteorology and astronomy [8, 9], differentiating between normal and pre-cancerous cells [10], as well as other biomedical applications [11, 12]. Traditional polarimetry is well suited for applications in optically clear media and for studies of surfaces; however, multiple scattering in optically thick turbid media such as most biological tissues causes extensive depolarization that confounds the established techniques. Further, even if some residual polarization signal can be measured [13], multiple scattering also alters the polarization state, for example by scattering-induced diattenuation [14] and by scattering-induced changes in the orientation of the linear polarization vector which appears as optical rotation [15]. Other simultaneously occurring polarization effects further confound quantitative polarimetry in complex materials; in tissues, these include linear birefringence due to anisotropic muscle fibers and structural proteins, and optical rotation due to optically active (chiral) molecules and structures. Thus, although a wealth of interesting tissue properties can potentially be probed with polarized light, accurate measurements and data analyses leading to unique interpretation of the polarization parameters are difficult. Hence, a method to account for the effects of multiple scattering, and to decouple the individual contributions of several effects occurring simultaneously is needed. Although recent work has shown promise for empirically extracting semi-quantitative information and relative changes from thick random media under controlled conditions [16–29], a more quantifiable and generally applicable technique is required. Here, we describe such a generalized method for polarimetry analysis in turbid media based on polar Mueller matrix decomposition. In addition, we present preliminary results for the use of this methodology for non-invasive tissue glucose measurements and monitoring regenerative treatments of myocardial infarction.

## 2. Methods and materials

### 2.1. Mueller algebra

The polarization of light is well described either via Jones or Mueller matrix algebra [30], although the latter is preferred when dealing with depolarizing interactions as engendered by multiply scattering media. Using the Mueller matrix approach, the intensity and polarization of a light beam are represented by a 4-element Stokes vector, **S**. The first element $I$ represents the intensity of the light beam, the second element $Q$ represents the linear polarization at 0° and 90°, the third element $U$ represents the linear polarization at 45° and 135°, and the fourth element $V$ represents the circular polarization. The effects of the medium under investigation are applied to this vector with a 4 × 4 Mueller matrix **M** via,

$$\mathbf{S_o} = \mathbf{M} \times \mathbf{S_i}\,, \tag{1}$$

$$\begin{bmatrix} I_o \\ Q_o \\ U_o \\ V_o \end{bmatrix} = \begin{bmatrix} m_{11} & m_{12} & m_{13} & m_{14} \\ m_{21} & m_{22} & m_{23} & m_{24} \\ m_{31} & m_{32} & m_{33} & m_{34} \\ m_{41} & m_{42} & m_{43} & m_{44} \end{bmatrix} \times \begin{bmatrix} I_i \\ Q_i \\ U_i \\ V_i \end{bmatrix} = \begin{bmatrix} m_{11}I_i + m_{12}Q_i + m_{13}U_i + m_{14}V_i \\ m_{21}I_i + m_{22}Q_i + m_{23}U_i + m_{24}V \\ m_{31}I_i + m_{32}Q_i + m_{33}U_i + m_{34}V \\ m_{41}I_i + m_{42}Q_i + m_{43}U_i + m_{44}V \end{bmatrix}, \tag{2}$$

where $\mathbf{S_o}$ and $\mathbf{S_i}$ are the output and input Stokes vectors, respectively, and $m_{ij}$ are the matrix elements. The functional forms of **M** for common interactions in clear materials are well known, so that a forward model to predict and analyze polarimetry measurements for transparent media can be readily developed. Turbidity poses significant challenges through the complications induced by multiple scattering. In addition, when several polarizations effects occur simultaneously: matrix multiplication is generally non-commutative ($\mathbf{M_A M_B} \neq \mathbf{M_B M_A}$) and, since no unique order can be assigned to simultaneous effects based on the underlying physics, the matrix-based description yields inconsistent results. An advanced approach, known as the N-matrix formalism, has been developed to tackle this non-commutative problem in clear media [31]. It makes use of differential matrices and replaces their product with a summation, which is then order-independent. We have recently extended and validated this approach in multiply scattering media, through a forward Monte Carlo-based model that can quantitatively describe the simultaneous effects of scattering, absorption, linear birefringence and optical activity [32]. This model is briefly reviewed below, as we draw upon it for validating the polar decomposition method described herein.

The outstanding challenge that we address here is the corresponding inverse problem. That is, given a particular Mueller matrix obtained from an unknown complex system, can it be analyzed to extract constituent polarization contributions? In tissue the most common polarimetry effects are depolarization, linear birefringence and optical activity [33]. These often occur simultaneously and each of these, if separately extracted from the "lumped" system Mueller matrix, holds promise as a useful biological metric. For example, chirality-induced optical rotation can be linked to the glucose concentration in the medium, and tissue structure anisotropy can be quantified by polarization birefringence measure-

© 2008 by WILEY-VCH Verlag GmbH & Co. KGaA, Weinheim 

ments. Here, we describe such a Mueller matrix decomposition method.

## 2.2. Inverse polar decomposition analysis

The Mueller matrix contains the combined effects of all polarizing properties of the sample. In order to isolate and quantify each effect separately, we decompose the measured matrix **M** into the product of three "basis" matrices [14, 34, 35],

$$\mathbf{M} = \mathbf{M_\Delta M_R M_D}\,, \tag{3}$$

where a depolarizing matrix $\mathbf{M_\Delta}$ accounts for the depolarizing effects of the medium, a retarder matrix $\mathbf{M_R}$ describes the effects of linear birefringence and optical activity, and a diattenuator matrix $\mathbf{M_D}$ includes the effects of linear and circular dichroism [34]. Using the known forms of these "basis" matrices, the measured **M** can be decomposed through a series of mathematical operations into the three "basis" matrices [34]. Once calculated, these constituent matrices are further analyzed to derive quantitative individual polarization medium properties (Figure 1). Lu and Chipman initially proposed this approach for optically clear media [34]. The validity of this approach in turbid media is demonstrated with both experimental and simulated data where the constituent properties are controlled and known *a priori*.

In biomedical polarimetry, three properties that are particularly important are depolarization, linear birefringence due to structural proteins (tissue anisotropy) and optical activity due to chiral molecules such as glucose. The depolarization is quantified through $\mathbf{M}_\Delta$ as the net depolarization coefficient, $\Delta$. The measurable effects of birefringence and optical activity (linear retardance $\delta$ and optical rotation $\psi$ respectively) are contained in $\mathbf{M_R}$. These three quantities are calculated from the elements of the $4 \times 4$ constituent matrices as [14, 34]

$$\Delta = 1 - \frac{|\mathrm{tr}\,(\mathbf{M_\Delta}) - 1|}{3}\,, \tag{4}$$

$$\delta = \cos^{-1}\left(\sqrt{(m_{\mathbf{R}22} + m_{\mathbf{R}33})^2 + (m_{\mathbf{R}32} - m_{\mathbf{R}23})^2} - 1\right), \tag{5}$$

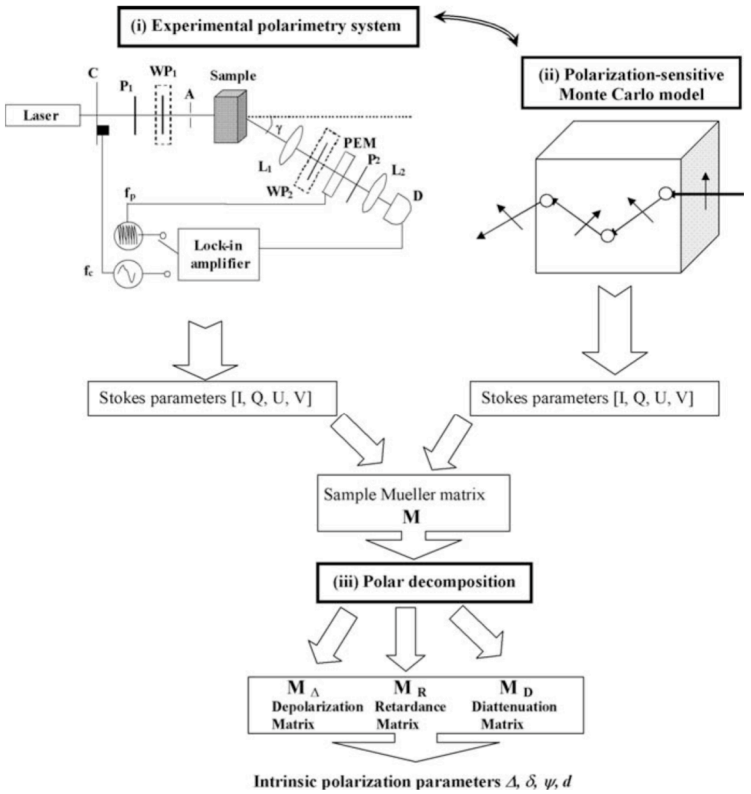



**Figure 1** Schematic of the turbid polarimetry platform: **(i)** experimental system based on polarization modulation and phase-sensitive synchronous detection, **(ii)** polarization-sensitive Monte Carlo simulations for forward modeling of simultaneous polarization effects in the presence of turbidity and **(iii)** the polar decomposition of the Mueller matrix to inverse calculate the constituent polarization contributions in complex turbid media. In the experimental system **(i):** C, mechanical chopper; $P_1$, $P_2$, polarizers; $WP_1$, $WP_2$, removable quarter wave plates; A, aperture; $L_1$, $L_2$ lenses; PEM, photoelastic modulator; D, photodetector; $f_c$, $f_p$ modulation frequencies of mechanical chopper and PEM, respectively. The detection optics can be rotated by an angle $\gamma$ around the sample.


© 2008 by WILEY-VCH Verlag GmbH & Co. KGaA, Weinheim

Journal of BIOPHOTONICS



and

$$\psi = \tan^{-1}\left(\frac{m_{\mathbf{R}32} - m_{\mathbf{R}23}}{m_{\mathbf{R}22} + m_{\mathbf{R}33}}\right), \quad (6)$$

where $m_{\mathbf{R}ij}$ are elements of the retardance matrix $\mathbf{M_R}$. In addition, the diattenuation $d$, which is due to differential attenuation (absorption and scattering) of orthogonal polarizations for both linear and circular polarization states, is determined as

$$d = \frac{1}{m_{\mathbf{D}11}}\sqrt{m_{\mathbf{D}12}^2 + m_{\mathbf{D}13}^2 + m_{\mathbf{D}14}^2}, \quad (7)$$

where $m_{\mathbf{D}ij}$ are elements of the diattenutation matrix $\mathbf{M_D}$.

Note that the matrix multiplication order in Eq. (1) appears ambiguous so that 6 different decompositions are possible. However, it has been shown that the matrix product in Eq. 1 or its reverse order ($\mathbf{M} = \mathbf{M_D}\,\mathbf{M_R}\,\mathbf{M}\Delta$) *always* leads to a physically realizable Mueller matrix [34]. Most importantly, the derived polarization parameters particularly useful in tissue characterization, $\Delta$, $\delta$, and $\psi$, are independent of the multiplication order of the basis matrices in Eq. (1) [34].

## 2.3. Polarimetry system

For experimental studies, we use a polarization modulation and phase-sensitive synchronous detection approach to measure the small polarization signals in a large depolarized background, as summarized in Figure 1. The details have been reported previously [15, 32]. Briefly, for this particular configuration, the polarization states are controlled using a polarizer and quarter wave-plate combination, enabling either linear or circular incidence. After interacting with the sample, the partially depolarized beam in a user-selected direction (angle $\gamma$) is modulated using a linearly-birefringent resonant photoelastic modulator (PEM). The light then passes through an analyzer, converting the polarization modulation to intensity modulation detectable by a photodetector. The resultant photocurrent is fed into a lock-in amplifier synchronous with the PEM modulation frequency for high signal to noise ratio (SNR) detection of the surviving polarization states. The Stokes vector of the output light is directly measured using the first and second harmonics of the lock-in detected signals [15, 32]. The complete Mueller matrix can be obtained by cycling the input polarization between four states (linear polarization at 0°, 45°, 90°, and right circular polarization), measuring the output Stokes vector for each respective input state, and performing simple algebraic manipulations [34]. Similar systems with electronically driven optical polarization modulators have demonstrated long-term instability caused by thermal effects [36, 37]. However, testing our system over extended periods of time (~hours) have shown that once warmed up (~10 min of operation), it is reasonably resistant to such instability.

For the experimental system, solid optical phantoms were developed using polyacrylamide as a base medium, with polystyrene microspheres to create turbidity, sucrose to induce optical activity, and mechanical stretching to cause linear birefringence allowing full experimental control of all constituent effects. The model allows for generation of Mueller matrices for media of any given properties.

## 2.4. Monte Carlo model

In addition to experimental polarimetry suitable for highly turbid media, we have also developed and validated a forward model for polarized light propagation in turbid media, using a Monte Carlo computational model [32, 38]. This statistical formalism, although less rigorous than the electromagnetic field modeling based on Maxwells equations, is well suited for describing light interactions with complex random media, and can be extended to include polarimetric descriptors [11, 39–41]. Our polarization-sensitive Monte Carlo model has been further extended to simulate simultaneous polarization effects in the presence of turbidity, employing the above-mentioned N-matrix formalism [31]. This is particularly important for simulation of biological tissue that often exhibits several polarization effects simultaneously. In the simulation, many photons ($10^7$–$10^9$) are tracked individually as they propagate and scatter through the media. Their fates are simulated using known single-interaction effects, applied in a statistical sense until they are absorbed or leave the media of interest. Repeating this process many times and keeping track of the resultant cumulative values generates quantities of interest such as Stokes vectors, Mueller matrices, pathlength distributions, and sampling volumes. The various polarizing effects of the medium are applied to the photons between scattering events. The Monte Carlo model has proven to be invaluable for data analysis, system validation, and guidance/design of experimental systems [42].

## 2.5. Myocardial samples

To investigate the use of this methodology for monitoring regenerative treatments of myocardial infarction, myocardial samples from a rat model of myocardial infarction and regeneration were used. All animal studies were carried out under institutional approval from the University Health Network, Toronto, Canada. The heart samples were obtained in an established

© 2008 by WILEY-VCH Verlag GmbH & Co. KGaA, Weinheim 

model in which myocardial infarction was induced in Lewis rats through coronary artery ligation. Mesenchymal stems cells transfected with human elastin gene were administered to the treatment group by intramyocardial injection at the site of infracted two weeks after the ligation procedure. Both the control ($n = 4$) and treatment ($n = 4$) groups were sacrificed after four weeks and the hearts were removed and fixed in 10% formalin. Finally, the fixed heart samples were sectioned into one mm thick axial slices and examined with the turbid polarimeter. It must be noted that although the tissue fixation process may alter the polarization properties of the tissue due to the cross-linking, it was required for tissue sectioning. The potential effects of the formalin fixation, and ways of eliminating it, are currently being investigated and will be reported in a forthcoming publication.

## 3. Results and discussion

### 3.1. Theoretical and experimental validation

This extended Mueller matrix decomposition methodology has seen only initial use in turbid media [14, 43], but has not been rigorously validated. Experimental validation was completed using the previously described polyacrylamide phantom system [32]. Table 1 shows the Mueller matrix measured in a turbid media and the corresponding decomposed $\mathbf{M}_\Delta$, $\mathbf{M}_\mathbf{R}$ and diattenuation $\mathbf{M}_\mathbf{D}$ matrices. This medium mimics the complexity of biological tissues, in that it exhibits linear birefringence (sample extension by 2 mm for strain applied along the vertical direction), chirality (concentration of 1 M of sucrose corresponding to magnitude of optical activity of $\chi = 1.96°$/cm), and turbidity (1.4 μm diameter polystyrene microspheres, resulting in a scattering coefficient of $\mu_s = 30\ \text{cm}^{-1}$ and anisotropy parameter $g = 0.95$ at $\lambda = 633$ nm). The measurement was performed in the forward direction ($\gamma = 0°$ in Figure 1) through a $1 \times 1 \times 4$ cm phantom. The complicated nature of the resultant Mueller matrix **M**, with essentially all 16 non-zero matrix elements being non-zero, highlights the challenge of extracting useful sample parameters from this complex intertwined information. In contrast, the three basis matrices derived from the decomposition procedure exhibit simpler structures with many zero off-diagonal elements, and are directly amenable to further analysis. Eqs. (2)–(5) were applied to the decomposed basis matrices to retrieve the individual polarization parameters ($\delta$, $\psi$, $\Delta$ and $d$). These are listed in Table 1, showing excellent agreement with the input values (within ±5% for all parameters).

**Table 1** *Top:* The experimentally recorded Mueller matrix and the decomposed matrices for a birefringent (extension = 2 mm), chiral (concentration of sucrose = 1 M, $\chi = 1.96°$/cm), turbid ($\mu_s = 30\ \text{cm}^{-1}$, g = 0.95) phantom. *Bottom:* The values for the polarization parameters extracted from the decomposed matrices via Eqs. (2)–(5) (2nd column). The input control values for linear retardance $\delta$ and optical rotation $\psi$ (3rd column) were obtained from measurement on a clear ($\mu_s = 0\ \text{cm}^{-1}$) phantom having the same extension (2 mm) and similar concentration of sucrose (1 M) as that of the turbid phantom, and corrected for the increased pathlength due to multiple scattering (determined from Monte Carlo modeling). The expected value for the depolarization coefficient Δ was determined from the Monte Carlo simulation of the experiment.

$$\mathbf{M} = \begin{pmatrix} 1.0000 & 0.0185 & 0.0029 & 0.0042 \\ 0.0172 & 0.7569 & -0.0405 & 0.0462 \\ 0.0034 & 0.0524 & 0.5450 & -0.5466 \\ 0.0024 & -0.0070 & 0.6244 & 0.5967 \end{pmatrix}$$

$$\mathbf{M}_\Delta = \begin{pmatrix} 1.0000 & 0 & 0 & 0 \\ 0.0031 & 0.7577 & 0 & 0 \\ 0.0031 & 0 & 0.7745 & 0 \\ -0.0017 & 0 & 0 & 0.8647 \end{pmatrix} \quad \mathbf{M}_\mathbf{R} = \begin{pmatrix} 1.0000 & 0 & 0 & 0 \\ 0 & 0.9972 & -0.0470 & 0.0578 \\ 0 & 0.0742 & 0.6964 & -0.7138 \\ 0 & -0.0067 & 0.7161 & 0.6980 \end{pmatrix} \quad \mathbf{M}_\mathbf{D} = \begin{pmatrix} 1.0000 & 0.0185 & 0.0029 & 0.0042 \\ 0.0185 & 1.0000 & 0.0000 & 0.0000 \\ 0.0029 & 0.0000 & 0.9998 & 0.0000 \\ 0.0042 & 0.0000 & 0.0000 & 0.9998 \end{pmatrix}$$

| Parameters | Input control values | Estimated values |
|---|---|---|
| Linear retardance ($\delta$) | 0.83 rad | 0.79 rad |
| Optical rotation ($\psi$) | 2.14° | 2.05° |
| Depolarization coefficient ($\Delta$) | 0.19 | 0.21 |
| Diattenuation ($d$) | 0 | 0.02 |



© 2008 by WILEY-VCH Verlag GmbH & Co. KGaA, Weinheim

Journal of BIOPHOTONICS



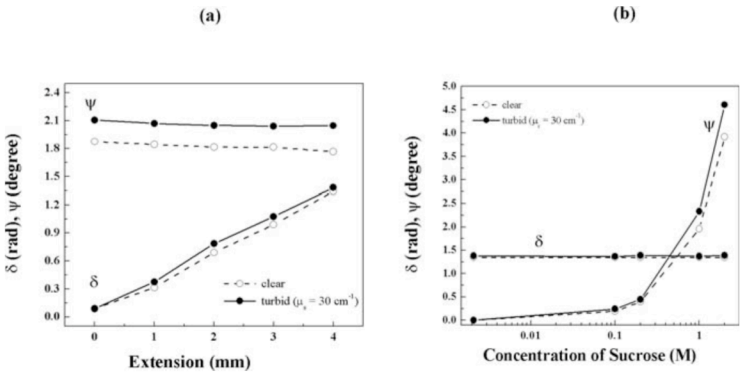



**Figure 2 (a)** Linear retardance, $\delta$, and optical rotation, $\psi$, estimated from the decomposition of experimentally recorded Mueller matrices from solid chiral phantoms ($\chi = 1.96°$/cm, corresponding to 1 M concentration of sucrose) with varying degrees of strain-induced birefringence (extension of 0–4 mm, $\delta = 0$–1.345). Results are shown for both clear ($\mu_s = 0$ cm$^{-1}$) and turbid ($\mu_s = 30$ cm$^{-1}$, g = 0.95) phantoms. The measurements were performed in the forward direction ($\gamma = 0°$) through a 1 × 1 × 4 cm phantom.
**(b)** $\delta$ and $\psi$ estimated from the decomposition of Monte Carlo-generated Mueller matrices from birefringent media (linear birefringence $\Delta n = 1.36 \times 10^{-5}$, corresponding to $\delta = 1.345$ rad [4 mm phantom extension] for a path length of 1 cm, $\Delta n$ is anisotropy in refractive indices, the difference in refractive index along the extraordinary axis and the ordinary axis) having varying levels of chirality ($\chi = 0$, 0.196, 0.392, 1.96 and 3.92°/cm, corresponding to concentration of sucrose of 0, 0.1, 0.2, 1 and 2 M, respectively). Results are shown for both clear ($\mu_s = 0$ cm$^{-1}$) and turbid ($\mu_s = 30$ cm$^{-1}$, g = 0.95) media.

The values for $\delta$ and $\psi$ determined from the decomposition of the measured Mueller matrices in both clear ($\mu_s$ = 0 cm$^{-1}$) and turbid ($\mu_s$ = 30 cm$^{-1}$, $g = 0.95$) optically active ($\chi = 1.96°$/cm) phantoms with increasing birefringence (sample extension of 0–4 mm, $\delta = 0$–1.345 rad), are shown in Figure 2A. This is an illustrative data set for forward-detection geometry only ($\gamma = 0°$ in Figure 1); investigations using other detection directions are in progress, since these may be more relevant in some specific biomedical applications. Again, the values from both clear and scattering samples are in close agreement with the controlled experimental inputs ($\psi \approx 1.96°$ and $\delta \approx 1.345$ rad at 4 mm of extension). Further, the similarity of the derived retardance and optical rotation in both clear and scattering media suggests that the depolarizing effects of multiple scattering have been properly isolated. The small increases in both linear retardance and optical rotation in the presence of turbidity are caused by the increase in optical pathlength due to multiple scattering, resulting in slight accumulations of $\delta$ and $\psi$ values (at least for this $\gamma = 0°$ detection geometry [34]). Figure 2B shows the derived linear retardance $\delta$ and optical rotation $\psi$ parameters, using Monte Carlo generated Mueller matrices, and with the chiral molecule concentration as an independent variable. Again, both the clear and turbid values compare well with the input parameter values ($\delta \approx 1.4$ rad and $\psi \approx 1.96°$ at 1 M sucrose), demonstrating the self-consistency of the decomposition analysis and successful decoupling of the effects. Note that none of these trends could be gleaned from the lumped Mueller matrix, where at best one would have to resort to semi-empirical comparison of changes in selected matrix elements, which contain contributions from several effects [15, 32]. Derivation and quantification of the absolute linear retardance $\delta$ and optical rotation $\psi$ values is enabled exclusively by the decomposition analysis. Based on these and other continuing studies [43], this approach seems to be valid for complex turbid media, and so may be applicable to studies of biological tissues, which is our primary goal.

### *3.2. Determining intrinsic optical activity: measurement of glucose in tissue*

An example of an important biomedical application is the quantification of the small optical rotations due to blood glucose in diabetic patients. Several different optical-based techniques have been investigated for this application, but none have provided a clinically useful solution to date [44]. The optical rotation due to glucose being a chiral molecule may, in principle, provide the sensitivity and specificity required. However, a major stumbling block is that the optical rotation due to chiral substances is swamped by the much larger changes in the orientation angle of the polarization vector due to scattering [15]. Hence, it is thus essential to isolate the optical rotation caused exclusively by glucose (or other chiral molecules of interest) from this background apparent rotation. The

© 2008 by WILEY-VCH Verlag GmbH & Co. KGaA, Weinheim 

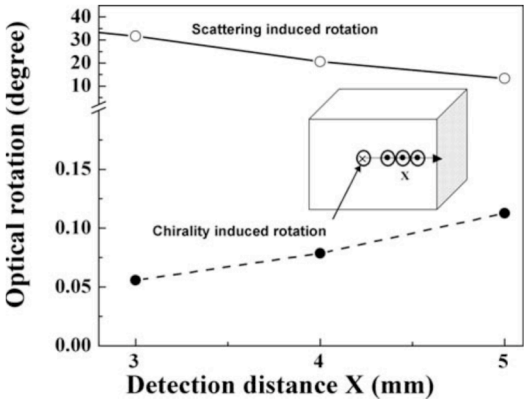



**Figure 3** Calculated optical rotation, $\psi$ (derived from the decomposition of Monte Carlo generated Mueller matrices: solid circles), of scattered light emerging in the backscattering direction as a function of distance from the center of the incident beam in a chiral ($\chi = 0.082°$/cm, corresponding to 100 mM concentration of glucose) isotropic turbid medium ($\mu_s = 30\ \text{cm}^{-1}$, $g = 0.95$, thickness $t = 1$ cm). The corresponding scattering-induced rotation of the polarization vector derived from the Stokes parameters of scattered light (for incident Stokes vector [1 0 1 0] $^T$) is shown by open circles. The inset shows the backwards detection geometry. The chirality-induced rotation approaches zero in the exact backscattering direction ($X = 0$, data not shown).

above matrix decomposition methodology can perform this task, as shown in Figure 3. This shows the variation in the derived optical rotation $\psi$ in the backward direction ($\gamma \sim 180°$, a geometry that is convenient for *in vivo* applications) as a function of the distance from the center of an incident beam in a chiral turbid medium ($\chi = 0.082°$/cm, corresponding to 100 mM concentration of glucose, $\mu_s = 30\ \text{cm}^{-1}$, $g = 0.95$, thickness = 1 cm). As can be seen, changes in the polarization caused by scattering are manifest as large apparent optical rotations [14, 15]. Decomposition analysis reveals that the effect is due to linear diattenuation (the difference in amplitude between the scattered light that is polarized parallel to and perpendicular to the scattering plane). This confounding effect is due mainly to the backscattered photons and gradually decreases as one goes away from the exact backscattering direction.

Decomposition of the Mueller matrix can thus decouple the irrelevant (chirality-unrelated) rotation from the much smaller $\psi$ rotation values caused by the circular birefringence of the medium. In combination with photon path-length distributions from Monte Carlo simulations [42], we are currently investigating methods for extracting the true chiral molecule concentrations from derived optical rotations. Spectroscopic-based polarimetry combined with chemometric regression analysis [45] is being investigated to isolate the rotation due to glucose from that caused by other chiral constituents [44].

### *3.3. Myocardial tissue monitoring for regenerative treatments*

The anisotropic organized nature of many tissues that stems from their fibrous structure leads to linear birefringence (or linear retardance), manifest as anisotropic refractive indices parallel and perpendicular to the fibers. Muscle fibers and extra-cellular matrix proteins (such as collagen and elastin) exhibit such linear birefringence [33]. Changes in this anisotropy resulting from disease progression or treatment response can alter the optical birefringence properties, making this parameter a potentially sensitive probe of tissue status. For example, upon suffering an infarction, a portion of the myocardium is deprived of oxygenated blood and subsequently cardiomyocytes die, being replaced by the fibrotic (scar) tissue [46]. Current methods to characterize the structure of the myocardium measure mechanical changes (e.g., elastography [47]) or electrical changes (e.g., impedance [48]). Recently, stem cell based regenerative treatments for myocardial infarction have been shown to reverse these trends by increasing the muscular and decreasing the scar tissue components [49–51]. These remodeling processes likely affect tissue structural anisotropy, and polarized light may offer a sensitive probe into the state of the myocardium after infarction and report on the success of regenerative treatments. This could be an invaluable quantitative and objective research tool in animal models and could be implemented via fiber-optic catheters in patients. As in other applications, these small birefringence alterations must be decoupled from the other confounding polarization effects that are present in the composite signals of the measured Mueller matrix elements.

Using the experimental turbid polarimetry set-up shown in Figure 1, we measured the Mueller matrices in transmission mode through 1-mm thick *ex vivo* myocardial samples from Lewis rats harvested after myocardial infarction, both with and without stem cell treatments. These were analyzed by the decomposition method to obtain $\delta$ values (Figure 4). A large decrease in linear retardance is seen in the infarcted region of the untreated myocardium (Figure 4a) due to the native, well-ordered anisotropic structure being replaced by disorganized isotropic scar tissue. An increase in $\delta$ towards the native (pre-infarct) in levels is seen in animals receiving stem cell therapy (Figure 4b) which leads to re-growth and re-organization of the damaged tissue, as indicated by the increased retardance levels. Shown in the bar graph of Figure 4c


© 2008 by WILEY-VCH Verlag GmbH & Co. KGaA, Weinheim

Journal of BIOPHOTONICS



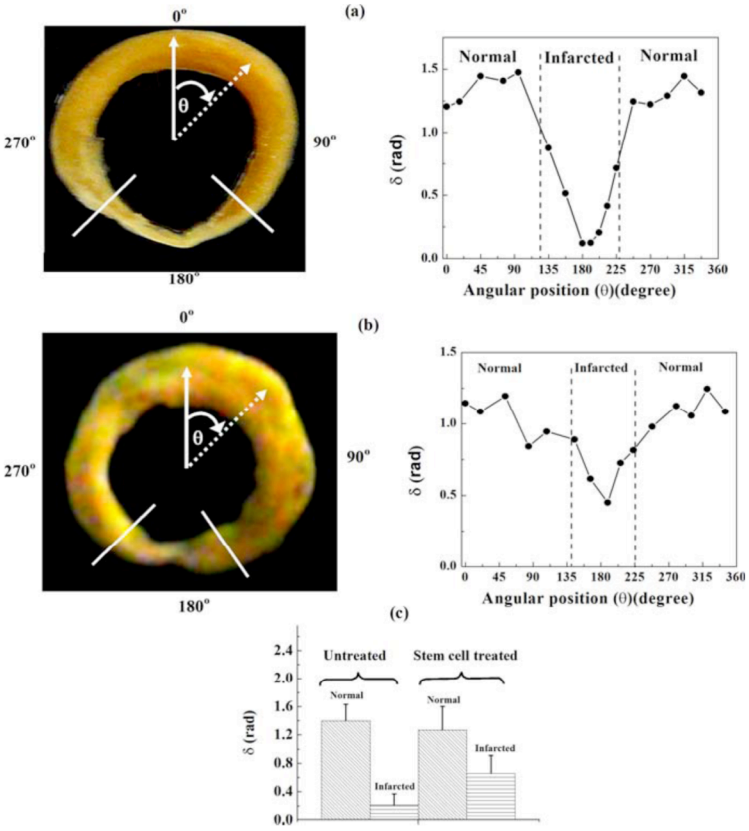



**Figure 4** (online colour at: www.biophotonics-journal.org) Linear retardance $\delta$ derived from transmission polarization measurements in 1-mm-thick sections from Lewis rat hearts following myocardial infarction. **(a)** untreated tissues, **(b)** tissues following stem-cell treatments. The marked sector around $\theta = 180°$ indicates the infracted region. Decreased birefringence levels in the infarcted region compared to normal regions are seen; this difference in reduced following stem-cell therapy as infracted region retardance values increase towards normal-tissue levels. The results from birefringence measurements from the controls and the stem-cell treated groups of infracted hearts are shown in histogram form in **(c)**. Error bars represent the standard deviation. Both untreated and stem-cell treated groups were comprised of 4 hearts and 5 measurements were preformed in each region (normal and infarcted).

are the mean linear retardance values from measurements of treated and untreated heart groups in the infarcted and normal regions. Statistically significant ($p = 0.03$) differences in derived retardance values exist between normal and infracted regions, and between infracted regions with and without stem-cell treatments. An increase in retardance in the infarcted regions of the treated hearts indicates reorganization and re-growth, as confirmed by a histologic examination. Of interest to note in these tissue measurements is that light absorption was present [52], as opposed to the phantom and Monte Carlo studies which had no absorption. While absorption does not affect the decomposition process, it does influence the polarization parameters. This is due to the reduction in the average optical pathlength through the medium (due the preferential absorption of longer path photons), resulting in different polarization values relative to a similar non-absorbing medium (specifically, lower values of optical rotation and retardance and higher surviving degree of polarization).

These intial *ex vivo* studies demonstrate the potential of polarimetric moitoring of myocardial tissues following stem cell therapy. Current work is directed towards developing an *in vivo* measurement system based on these principles using diffusely reflected light.

## 4. Conclusions

A Mueller matrix polar decomposition methodology has been validated and explored in chiral birefringent turbid media, including biological tissues. The individual polarization effects can be successfully decoupled and quantified, despite their simultaneous occurrence, even in the presence of the numerous complexities due to multiple scattering. This opens the door for a variety of powerful, noninvasive polarimetry-based techniques for biomedical applications, of which we have illustrated two important examples.

**Acknowledgements** This work was supported by the National Sciences and Engineering Research Council of Canada. We thank Dr. Daniel Côté for assistance with the Monte Carlo software and Dr. Xinxin Guo for assistance with the experimental system.

© 2008 by WILEY-VCH Verlag GmbH & Co. KGaA, Weinheim 



**Nirmalya Ghosh, PhD** is a physicist by training, with further specialization in biomedical optics, spectroscopy and biophotonics. He completed his M.S. in Physics from University of Kalyani, India and M. Tech. in Laser Technology from IIT Kanpur, India. He then joined Laser Biomedical Applications & Instrumentation Division (LBAID), Raja Ramanna Centre for Advanced Technology (RRCAT), Indore, Department of Atomic Energy (DAE), India as a scientist, where he started his research on biomedical applications of lasers. He completed his PhD in Physics from RRCAT, India and his thesis research was focused on understanding depolarization of light in a complex turbid medium like biological tissue and evaluating its use for biomedical imaging and diagnosis. At present he is conducting postdoctoral research in the field of biophotonics (with particular emphasis on tissue polarimetry) with Department of Medical Biophysics at the University of Toronto. He has published over twenty five papers in peer-reviewed journals, fifteen articles in edited volumes, and book chapters in the area of biomedical optics, spectroscopy and biophotonics.



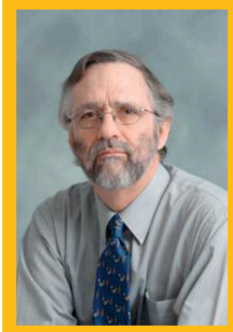
**Michael Wood** completed his undergraduate degree in Computer Engineering at the University of Western Ontario in 2004. Currently he is pursuing his PhD in Medical Biophysics at the University of Toronto where his work focuses on the use of polarized light for tissue characterization. He is the recipient of a postgraduate scholarship from the National Science and Engineering Research Council of Canada. He has 11 scientific publications and one book chapter.



**Shu-Hong Li** is a laboratory technician and manager in the Department of Cardiovascular research at the Toronto General Hospital. She received her masters in pharmaceutical sciences from the University of British Columbia in 2000. As part of Dr. Li's laboratory, her work is focused on finding optimal cell types for transplantation in the myocardium, and describing the optimal conditions under which the transplanted cells can achieve the most efficient repair.



**Richard Weisel, MD** is the Director of the Toronto General Research Institute. Improving quality of life for the cardiac patient has been a lifelong pursuit for Dr. Weisel. A graduate of Yale, Dr. Weisel received his training in Milwaukee and Boston, joining Toronto General Hospital in 1976. Since then, this preeminent clinician scientist has contributed to cardiology science through innovative research, international lectures, publications, and life-saving expertise as a cardiovascular surgeon. His major research interests lie in cell transplantation, myocardial protection and vascular biology. He has published over 300 publications in peer-reviewed journals and was a recipient of the Ontario Heart & Stroke Foundation's Career Investigator award for six consecutive years.



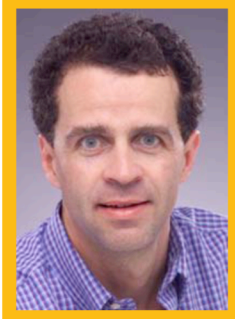
**Brian C. Wilson, PhD** was appointed Professor of Medical Biophysics and Head of the Division of Biophysics and Bioimaging at the Ontario Cancer Institute/Faculty of Medicine, University of Toronto in 1993. A graduate in particle physics from Glasgow University, he worked at the Institute of Cancer Research in London and then in Australia before moving to McMaster University in Canada in 1981, where he initiated a research program in translational and clinical biophotonics. He heads the biophotonics program of the Canadian Institute for Photonic Innovations, has held Visiting Professor positions at Harvard University and University of Sao Paulo, Brazil and is currently Professor-at-Large, University of Western Australia. He is co-founder of 2 start-up companies, with a 3rd on the way. He has published over 300 scientific papers and trained 50+ graduate students and fellows.



© 2008 by WILEY-VCH Verlag GmbH & Co. KGaA, Weinheim



**Ren-Ke Li, MD, PhD** is a Professor of Medicine in the Department of Surgery, Division of Cardiovascular Surgery and Department of Laboratory Medicine and Pathobiology at the University of Toronto and a Senior Scientist at the Toronto General Research Institute, University Health Network. He is the recipient of the Canada Research Chair in Cardiac Regeneration and a Career Investigator of the Heart and Stroke Foundation of Canada. Dr. Li has been on the forefront in the field of cell transplantation and tissue engineering. In 1996, he published the first demonstration that cells transplanted into myocardial scar tissue survived, differentiated into muscle tissue, and improved heart function. More recently, his group has defined optimal cell types for transplantation, and described the optimal conditions under which the transplanted cells can achieve the most efficient repair. Currently, they are attempting to determine the mechanisms by which transplanted cells exert their beneficial effects. Dr. Li has published 129 peer-reviewed papers.



**Alex Vitkin, PhD** is an engineering physicist/biomedical engineer specializing in medical physics and the application of lasers in medicine. He is currently a professor of medical biophysics and radiation oncology at the University of Toronto, a senior scientist in the division of biophysics and bioimaging at the Ontario Cancer Institute, and a clinical medical physicist at Princess Margaret Hospital (all in Toronto, Ontario, Canada). His research is in the field of biophotonics, with particular emphasis on Doppler optical coherence tomography, tissue polarimetry, and optical fiber sensors.
Dr. Vitkin has published over 90 scientific papers in peer-reviewed literature. He has served as the Guest Editor (Biophysics) for the Journal of Applied Physics, and is currently a topical editor of Optics Letters.

## References

[1] V. Ronchi, The Nature of Light (Harvard University Press, Cambridge, Massachusetts, 1970).
[2] J. Michl and E. W. Thulstrup, (Spectroscopy with Polarized Light (VCH, New York, 1986).
[3] R. A. Hegstrom and D. K. Kondepudi, The handedness of the universe, Scientific American January 108–115 (1990).
[4] C. A. Browne and F. W. Zerban, Physical and Chemical Methods of Sugar Analysis (Wily, New York, 1941).
[5] B. Jirgensons, Optical Rotatory Dispersion of Proteins and Other Macromolecules (Springer-Verlag, 1960).
[6] D. S. Kliger, J. W. Lewis, and C. E. Randall, Polarized Light in Optics and Spectroscopy (Academic Press–Harcourt Brace Jovanovich, New York, 1990).
[7] C. Brouseau, Fundamentals of Polarized Light a Statistical Approach (Wiley Interscience, 1998).
[8] M. Gadsden, P. Rothwell, and M. J. Taylor, Detection of circularly polarized-light from noctilucent clouds, Nature **278**, 628–629 (1979).
[9] A. Chrysostomou, P. W. Lucas, and J. H. Hough, Circular polarimetry reveals helical magnetic fields in the young stellar object HH 135–136, Nature **450**, 71–73 (2007).
[10] R. S. Gurjar, V. Backman, L. T. Perelman, I. Georgakoudi, K. Badizadegan, I. Itzkan, R. R. Dasari, and M. S. Feld, Imaging human epithelial properties with polarized light scattering spectroscopy, Nature Medicine **7**, 245–1249 (2001).
[11] V. V. Tuchin, L. Wang, and D. À. Zimnyakov, Optical Polarization in Biomedical Applications (Springer-Verlag, 2006).
[12] N. G. Khlebtsov, I. L. Maksimova, V. V. Tuchin, and L. Wang, Introduction to Light Scattering by Biological Objects, in: Handbook of Optical Biomedical Diagnostics, Vol. PM107, edited by V. V. Tuchin (SPIE Press, Bellingham, WA, 2002), chap. 1, pp. 31–167.
[13] M. Xu and R. R. Alfano, Random walk of polarized light in turbid media, Physical Review Letters **95**, 2139001 (2005).
[14] S. Manhas, M. K. Swami, P. Buddhiwant, N. Ghosh, P. K. Gupta, and K. Singh, Mueller matrix approach for determination of optical rotation in chiral turbid media in backscattering geometry, Optics Express **14**, 190–202 (2006).
[15] X. Guo, M. F. G. Wood, and I. A. Vitkin, Angular measurement of light scattered by turbid chiral media using linear Stokes polarimetry, Journal of Biomedical Optics **11**, 041105 (2006).
[16] K. Sokolov, R. Drezek, K. Gossage, and R. Richards-Kortum, Reflectance spectroscopy with polarized light: is it sensitive to cellular and nuclear morphology? Optics Express **5**, 302–317 (1999).
[17] S. L. Jacques, J. C. Ramella-Roman, and K. Lee, Imaging skin pathology with polarized light, Journal of Biomedical Optics **7**, 329–340 (2002).

© 2008 by WILEY-VCH Verlag GmbH & Co. KGaA, Weinheim

[18] V. Sankaran, J. T. Walsh, and D. J. Maitland, Comparative study of polarized light propagation in biologic tissues, Journal of Biomedical Optics **7**, 300–306 (2002).
[19] M. Bartlett, G. Huang, L. Larcom, and H. Jiang, Measurement of particle size distribution in mammalian cells in vitro by use of polarized light spectroscopy, Applied Optics **43**, 1296–1307 (2004).
[20] M. J. Rakovic, G. W. Kattawar, M. Mehruübeoglu, B. D. Cameron, L. V. Wang, S. Rastegar, and G. L. Coté, Light backscattering polarization patterns from turbid media: theory and experiment, Applied Optics **38**, 3399–3408 (1999).
[21] A. H. Hielscher, J. R. Mourant, and I. J. Bigio, Influence of particle size and concentration on the diffuse backscattering of polarized light from tissue phantoms and biological cell suspensions, Applied Optics **36**, 125–135 (1997).
[22] J. M. Schmitt, A. H. Gandjbakhche, and R. F. Bonner, Use of polarized light to discriminate short-path photons in a multiply scattering medium, Applied Optics **31**, 6535–6546 (1992).
[23] M. Dogariu and T. Asakura, Photon pathlength distribution from polarized backscattering in random media, Optical Engineering **35**, 2234–2239 (1996).
[24] W. S. Bickel, J. F. Davidson, D. R. Huffman, and R. Kilkson, Application of polarization effects in light scattering: a new biophysical tool, Proceedings of the National Academy of Sciences **73**, 486–490 (1976).
[25] I. A. Vitkin, R. D. Laszlo, and C. L. Whyman, Effects of molecular asymmetry of optically active molecules on the polarization properties of multiply scattered light, Optics Express **10**, 222–229 (2002).
[26] R. C. N. Studinski and I. A. Vitkin, Methodology for examining polarized light interactions with tissues and tissue-like media in the exact backscattering direction, Journal of Biomedical Optics **5**, 330–337 (2000).
[27] I. A. Vitkin, and E. Hoskinson, Polarization studies in multiply scattering media, Optical Engineering **39**, 353–362 (2000).
[28] D. Côté and I. A. Vitkin, Balanced detection for low-noise precision polarimetric measurements of optically active, multiply, scattering tissue phantoms, Journal of Biomedical Optics **9**, 213–220 (2004).
[29] K. C. Hadley and I. A. Vitkin, Optical rotation and linear and circular depolarization rates in diffusely scattered light from chiral, racemic, and achiral turbid media, Journal of Biomedical Optics **7**, 291–299 (2002).
[30] D. Goldstein, Polarized Light (Marcel Decker Inc., 2003).
[31] R. C. Jones, New calculus for the treatment of optical systems. VII. Properties of the N-matrices, Journal of the Optical Society of America **38**, 671–685 (1948).
[32] M. F. G. Wood, X. Guo, and I. A. Vitkin. Polarized light propagation in multiply scattering media exhibiting both linear birefringence and optical activity: Monte Carlo model and experimental methodology, Journal of Biomedical Optics **12**, 014029 (2007).
[33] L. V. Wang, G. L. Coté, and S. L. Jacques, Editors, Special Section on Tissue Polarimetry, Journal of Biomedical Optics **7**, 278–397 (2002).
[34] 34. S. Y. Lu and A. Chipman, Interpretation of Mueller matrices based on polar decomposition, Journal of the Optical Society of America A **13**, 1106–1113 (1996).
[35] J. Morio and F. Goudail, Influence of the order of diattenuator, retarder, and polarizer in polar decomposition of Mueller matrices, Optics Letters **29**, 2234–2236 (2004).
[36] R. G. Johnson, S. B. Singham, and G. C. Salzman, Polarized Light Scattering, Comments Mol. Cell. Biophys. **5**, 171–192 (1988).
[37] G. C. Salzmann, S. B. Singham, R. G. Johnson, and C. F. Bohren, Light Scattering and Cytometry, in: Flow Cytometry and Sorting, 2nd ed., edited by M. R. Melamed, T. Lindmo, and M. L. Mendelsohn (Wiley-Liss, New York, 1990), pp. 81–107.
[38] 38. D. Côté and I. A. Vitkin, Robust concentration determination of optically active molecules in turbid media with validated three-dimensional polarization sensitive Monte Carlo calculations, Optics Express **13**, 148–163 (2005).
[39] L. V. Kuzmin, I. V. Meglinski, and Churmakov, Coherent effects in multiple scattering of linearly polarized light, Optics and Spectroscopy **98**, 653–659 (2005).
[40] F. Jaillon and H. Saint-Jalmes, Description and time reduction of a Monte Carlo code to simulate propagation of polarized light through scattering media, Applied Optics **42**, 3290–3296 (2003).
[41] W. Wang and L. V. Wang, Propagation of polarized light in birefringent media: A Monte Carlo study, Journal of Biomedical Optics **7**, 350–358 (2002).
[42] X. Guo, M. F. G. Wood, and I. A. Vitkin, Monte Carlo study of path length distribution of polarized light in turbid media, Optics Express **15**, 1348–1360 (2007).
[43] N. Ghosh, M. F. G. Wood, and I. A. Vitkin, Simultaneous determination of linear retardance and optical rotation in birefringent, chiral, turbid medium using Mueller matrix polarimetry: combined Monte Carlo and experimental methodology, Journal of Biomedical Optics **13**, 044037 (2008).
[44] R. J. McNichols and G. L. Coté, Optical glucose monitoring in biological fluids: an overview, Journal of Biomedical Optics **13**, 044036 (2008).
[45] M. F. G. Wood, D. Côté, and I. A. Vitkin, Combined optical intensity and polarization methodology for analyte concentration determination in simulated optically clear and turbid biological media, Journal of Biomedical Optics, in press (2008).
[46] Y. Sun, J. Q. Zhang, J. Zhang, and S. Lamparter, Cardiac remodeling by fibrous tissue after infarction, Journal of Laboratory and Clinical Medicine **135**, 316–323 (2000).
[47] E. E. Konofaguo, J. Dhoogle, and J. Ophirm, Myocardial elastography – a feasibility study in vivo, Ultrasound in Medicine and Biology **28**, 475–482 (2002).
[48] M. A. Fallert, M. S. Mirotznik, S. W. Downing, E. B. Savage, K. R. Foster, M. E. Josephson, and D. K. Bogen, Myocardial electrical impedance mapping of is-


© 2008 by WILEY-VCH Verlag GmbH & Co. KGaA, Weinheim

Journal of BIOPHOTONICS



chemic sheep hearts and healing aneurysms, Circulation **87**, 199–207 (1993).

[49] D. Orlic, J. Kajstura, S. Chimenti, I. Jackoniuk, S. M. Anderson, B. Li, J. Pickel, K. MacKay, B. Nadal-Ginard, D. M. Bodine, A. Leri, and P. Anversa, Bone marrow cells regenerate infarcted myocardium, Nature **410**, 701–705 (2001).

[50] M. Jain, H. DerSimonian, D. A. Brenner, S. Ngoy, P. Teller, A. S. B. Edge, A. Zawadzka, K. Wetzel, D. B. Sawyer, W. S. Colucci, C. S. Apstein, and R. Liao, Cell therapy attenuates deleterious ventricular remodeling and improves cardiac performance after myocardial infarction, Circulation **103**, 1920–1927 (2001).

[51] X. Xu, Z. Xu, Y. Xu, and C. Cui, Selective down-regulation of extracellular matrix gene expression by bone marrow derived stem cell transplantation into infarcted myocardium, Circulation Journal **69**, 1275–1283 (2005).

[52] W. F. Cheong, S. A. Prahl, and A. J. Welch, A review of the optical properties of biological tissues, IEEE J. Quant. Electr. **26**, 2166–2185 (1990).

© 2008 by WILEY-VCH Verlag GmbH & Co. KGaA, Weinheim 

***Addendum***

In this study the first, to our knowledge, polarimetry measurements were conducted on infarcted *and* regenerating myocardial tissue. The partial rebound of retardance values after stem cell treatment indicates reorganization of the tissue and demonstrates potential for the technique to monitor regenerative treatments. The Mueller matrix decomposition employed for measurement analysis is a more robust method for retardance determination then the Stokes vector analysis conducted in the previous proof-of-principle study. The ability of the decomposition method to separately quantify all polarization parameters of tissue makes it versatile tool for tissue polarization analysis, as was demonstrated in the paper by the glucose monitoring application (which will be expanded upon in Chapter 4). While the point measurements made in this study can be used to provide somewhat localized retardance measurements, the measurements are the average of a relatively large volume when compared to the size of a rat heart. Full spatial mapping (i.e., imaging) would be advantages as this would allow for investigations of the birefringence variations throughout the myocardium. Additionally, the physiological changes leading to the changes in myocardial anisotropy require investigation, ideally in a non-destructive manner. Both these outstanding issues will be investigated in the next section.

## 3.3 Imaging polarization measurements on myocardial tissues

***Introduction***

The previous section presented results from point measurements on healthy, infracted, and regenerating regions of rat myocardial tissue. The spatial variations of birefringence in the myocardium between and within these regions are also of interest. The point

measurements represent a volume average made by the incident beam and the light collection optics (in the case of the previous study an approximately 1 $mm^3$ volume). Any birefringence spatial variations within this volume cannot be discriminated. In the previous study point measurements were preformed at varying positions around the wall of the myocardium and plotted as a function of angular positions (see Figure 4 on page 61), but these provide very low resolution (> 1 $mm^2$).

To overcome this limitation, a Mueller matrix *imaging* system was developed and used to image infracted and regenerating rat myocardial sections. Point measurements were also made in healthy, infracted, as well as marginal (region surrounding the infarct) and compared to the imaging results. As in the previous study, polar decomposition was used to extract the retardance induced by the samples. Nonlinear microscopy, specifically, two-photon excited fluorescence (TPEF) and second harmonic generation (SHG) were also preformed on the myocardial sections to gain physiological insight regarding the specifics of the structural changes in tissue, in particular changes in anisotropy. These nonlinear microscopy techniques allow for imaging of endogenous two-photon fluorescence from cardiac muscle and endogenous second harmonic generation from collagen. Finally, conventional histology was also performed (Mason's trichrome) and compared with polarimetry and multiphoton microscopy. The methods and results are presented in the following paper; preliminary results were also presented at a conference and in the corresponding proceeding.

I conducted all experimental measurements and analysis, with assistance from Dr. Nirmalya Ghosh. Marika Wallenburg, a Master's student in our laboratory, performed the nonlinear microscopy. Shu-Hong Li again conducted the design of the animal model.

***Paper***

**M. F. G. Wood,** N. Ghosh, M. Wallenburg, S. H. Li, R. D. Weisel, B. C. Wilson, R. K. Li, and I. A. Vitkin, "Polarization birefringence measurements for characterizing the myocardium, including healthy, infarcted, and stem cell regenerated tissues," *Journal of Biomedical Optics* **15**, 047009 (2010).

***Conference – Oral Presentation***

**M. F. G. Wood,** N. Ghosh, S. H. Li, R. D. Weisel, B. C. Wilson, R. K. Li, and I. A. Vitkin, "Polarized light based birefringence measurements for monitoring myocardial regeneration," *Proceedings of SPIE*, Photonics West 2009, 7179-7.

Journal of Biomedical Optics 15(4), 047009 (July/August 2010)

# Polarization birefringence measurements for characterizing the myocardium, including healthy, infarcted, and stem-cell-regenerated tissues

**Michael F. G. Wood**
Ontario Cancer Institute
Division of Biophysics and Bioimaging
University Health Network
and
University of Toronto
Department of Medical Biophysics
610 University Avenue
Toronto, Ontario M5G 2M9
Canada

**Nirmalya Ghosh**
IISER Kolkata, Mohanpur Campus
PO: BCKV Main Campus Oce
Mohanpur 741252, West Bengal
India

**Marika A. Wallenburg**
Ontario Cancer Institute
Division of Biophysics and Bioimaging
University Health Network
and
University of Toronto
Department of Medical Biophysics
610 University Avenue
Toronto, Ontario M5G 2M9
Canada

**Shu-Hong Li**
**Richard D. Weisel**
Toronto General Research Institute
Toronto General Hospital
Division of Cardiovascular Surgery
101 College Street
Toronto, Ontario M5G 1L7
Canada

**Brian C. Wilson**
Ontario Cancer Institute
Division of Biophysics and Bioimaging
University Health Network
and
University of Toronto
Department of Medical Biophysics
610 University Avenue
Toronto, Ontario M5G 2M9
Canada

**Ren-Ke Li**
Toronto General Research Institute
Toronto General Hospital
Division of Cardiovascular Surgery
101 College Street
Toronto, Ontario M5G 1L7
Canada

**I. Alex Vitkin**
Ontario Cancer Institute
Division of Biophysics and Bioimaging
University Health Network
and
University of Toronto
Department of Medical Biophysics
610 University Avenue
Toronto, Ontario M5G 2M9
Canada
and
University of Toronto
Department of Radiation Oncology
610 University Avenue
Toronto, Ontario M5G 2M9
Canada

Address all correspondence to: Michael F. G. Wood, Ontario Cancer Institute, Division of Biophysics and Bioimaging, 610 University Avenue, Toronto, ON, Canada M5G 2M9. Tel: 416 946 4501 ext. 3280; Fax: 416 946 6529; Email: mwood@uhnres.utoronto.ca

**Abstract.** Myocardial infarction leads to structural remodeling of the myocardium, in particular to the loss of cardiomyocytes due to necrosis and an increase in collagen with scar formation. Stem cell regenerative treatments have been shown to alter this remodeling process, resulting in improved cardiac function. As healthy myocardial tissue is highly fibrous and anisotropic, it exhibits optical linear birefringence due to the different refractive indices parallel and perpendicular to the fibers. Accordingly, changes in myocardial structure associated with infarction and treatment-induced remodeling will alter the anisotropy exhibited by the tissue. Polarization-based linear birefringence is measured on the myocardium of adult rat hearts after myocardial infarction and compared with hearts that had received mesenchymal stem cell treatment. Both point measurement and imaging data show a decrease in birefringence in the region of infarction, with a partial rebound back toward the healthy values following regenerative treatment with stem cells. These results demonstrate the ability of optical polarimetry to characterize the micro-organizational state of the myocardium via its measured anisotropy, and the potential of this approach for monitoring regenerative treatments of myocardial infarction. © *2010 Society of Photo-Optical Instrumentation Engineers.* [DOI: 10.1117/1.3469844]

Keywords: myocardial infarction; stem cells; regenerative medicine; extracellular matrix; polarimetry; birefringence; Mueller matrix; polar decomposition.

Paper 10004PR received Jan. 4, 2010; revised manuscript received May 27, 2010; accepted for publication Jun. 1, 2010; published online Aug. 2, 2010.

## 1 Introduction

Cardiovascular disease is the number one cause of death with an estimated 17.5 million deaths worldwide each year, accounting for some 30% of all deaths.[1] Myocardial infarction

1083-3668/2010/15(4)/047009/9/$25.00 © 2010 SPIE

(commonly referred to as heart attack) is the leading cause of cardiovascular disease-related death with an estimated 7.5 million deaths each year, accounting for some 12% of all deaths.[1] Most often a myocardial infarction is caused by an occlusion (blockage) of a coronary artery as a consequence of atherosclerotic plaque. The resulting ischemia causes necrosis of the affected myocardial cells and formation of fibrotic scar tissue. The infarction leads to remodeling of the myocardium, specifically expansion of the infarct, ventricular dilation, thinning of the ventricular wall, and scar formation, which in turn cause disruption of normal cardiac function.

The potential for stem cells to form any differentiated cell type in the body has led to investigation of use for a variety of degenerative diseases.[2,3] The use of stem cells for myocardial regenerative therapy in particular has been actively pursued, as it has been shown in some clinical trials to improve cardiac function.[4,5] A wide variety of donor stem cell types have been investigated for use in the myocardium, including skeletal myoblasts, mesenchymal stem cells, bone marrow stem cells, and adult cardiac stem cells.[6] While debate continues as to the primary mechanisms for the improvement in function, it is generally attributed to the reduction in deleterious remodeling.[7]

This remodeling involves changes in the myocardial content and structure, particularly necrosis of cardiomyocytes and an increase in collagen associated with scar formation.[8] As stem cell therapy alters this remodeling, a decrease in the collagen content and an increase in cardiac muscle has been measured in regenerating infarcted myocardium.[9] The structural organization of the myocardium also changes significantly with infarction and stem-cell-derived regeneration. Healthy heart tissue is comprised primarily of well-organized aligned arrays of cardiomyocytes, while the collagen in the infarcted scar tissue is largely disorganized. The anisotropic nature of fibrous tissues, such as healthy myocardium, results in a directionally varying optical refractive index (different refractive indices along the length of the fibers versus perpendicular to the fibers) referred to as linear birefringence. The infarcted scar tissue, on the other hand, is largely isotropic with its chaotic orientation of collagen stands, and accordingly should exhibit lower values of linear birefringence compared to healthy tissue. Polarimetry may thus be a useful approach to quantify these microstructural tissue anisotropies, and in particular to monitor changes in their values following regenerative (stem-cell-based) therapies, thus providing potential functional feedback on their effectiveness. We have recently reported polarimetric initial measurements on rat myocardial tissues with induced infarction and regenerative treatment.[10,11] Here, we expand on this initial study by performing polarization imaging in addition to point measurements; we also use nonlinear optical microscopy to provide additional insight into the causes of the observed polarization signals and the meaning of the observed trends.

Birefringence is a measure of structural anisotropy, and causes light polarized along the different refractive indices in the medium to propagate at different speeds, resulting in a change in relative phase, referred to as the retardance $\delta$. The retardance is related to the underlying birefringence by $\delta = 2\pi\Delta n d/\lambda$, where $\Delta n$ is the birefringence (difference in refractive indices), $\lambda$ is the wavelength of the light, and $d$ is the distance the light has propagated through the medium (optical path length). This change in phase leads to a net change in the overall polarization of the light, specifically a transfer between linear and circular polarization states, which can be measured as part of the overall polarization properties of the sample and used to calculate the retardance. To calculate the intrinsic birefringence of the sample, one must know the distance the light has propagated, a value often not known *a priori*, particularly in highly scattering media such as tissue; however, the retardance can be used as a measure of tissue anisotropy if the propagation distance is constant between measurements, as any difference in retardance will be due to birefringence only. Differences in optical properties of healthly versus infarcted myocardial can alter the optical path length; however, large magnitude changes in birefringence will still dominate the measured retardance.

Multiple elastic scattering of light in tissue rapidly depolarizes a polarized input beam. However, sufficient polarization is maintained in diffuse transmission through thin tissue layers (1 to 3 mm), or in diffuse reflection geometries from tissues of any thickness, to enable quantitative polarimetery.[10–13] We thus hypothesize that polarized light birefringence measurements can be used to characterize the structural anisotropy of heart tissue and differentiate between healthy, infarcted, and regenerating myocardium, with further potential for monitoring regenerative treatments. This study is part of our initial investigations[10,11] employing fixed and sectioned myocardial tissue, moving toward potentially applying this approach on bulk (unsectioned) samples, and ultimately *in vivo*. The ability to monitor the structural anisotropy of the myocardium would be useful through fiber optic devices in assessing longitudinally the structural remodeling that occurs with infarction and regenerative treatments, particularly with regards to a specific treatment's ability to alter these remodeling processes. Previous studies involving polarized light microscopy[14] and polarization-sensitive optical coherence tomography (PS-OCT)[15,16] have investigated the utility of polarized light to characterize the myocardium and its response to infarction. In these studies, a reduction of birefringence was measured in the infarction. The PS-OCT studies are of particular interest with regards to potential application *in vivo*, as they offer depth resolution (though limited to less than 2 mm in depth) and can be catheterized. However, no studies to date have used polarized light to characterize myocardial response to regenerative therapies.

A variety of optical methods are being proposed and investigated for monitoring various aspects of stem cell cardiac therapy.[17] These include bioluminescence imaging for cell tracking,[18] near-infrared spectroscopy for monitoring perfusion,[19] and laminar optical tomography for monitoring electrophysiology,[20] among others.[17] Currently, however, no optical method exists—apart from polarized-light-based techniques—for assessing the structure of myocardium, particularly with regards to the structural remodeling that occurs with infarction and regeneration, with the potential to be employed *in vivo* on bulk tissues. Other nonoptical modalities such as ultrasound elastography[21] and electrical impedance mapping[22] do provide information on the structural state of the myocardium. However, neither of these techniques provides information on the organizational structure of the tissue, but rather on the elastic and conductive properties, respectively. Diffusion tensor magnetic resonance imaging provides

information regarding fiber organization and orientation,[23] but currently is limited to *ex vivo* tissues and suffers from lower spatial resolution than optical methods. Thus, polarized-light-based birefringence measurements, if successful, may enable previously unavailable assessment of myocardial organization.

In this work, we expand on previous findings involving the use of polarization measurements in myocardial characterization;[10,11] in particular, we investigate polarization retardance imaging in addition to point measurements, and employ statistical significance testing. The outline of this work is as follows. An overview of the point measurement and imaging polarimetry systems used in this study is given, along with the polar decomposition methods for analyzing the measured polarimetry data. Nonlinear microscopy was used to complement the polarimetry results and to understand the causes of the measured birefringence signals, and is described next. Specifics of the animal model used for myocardial infarction and stem cell regeneration are reviewed. Finally, the birefringence point measurements and imaging results, and the nonlinear microcopy findings, are then presented, interpreted, and discussed. The work concludes with a summary of the findings and an outline of future research directions.

## 2 Methods and Materials

### 2.1 *Polarimetry Systems*

Point and imaging polarimetry systems were employed in this study. The former provides a high signal-to-noise ratio (SNR) polarimetric signal, while the imaging system, although having a lower SNR, allows spatial mapping of polarization values. Both systems measure the polarization of the light that has interacted with a sample, yielding results in the form of a Stokes vector, a description of the polarization state of the light. In addition, the polarization properties of the sample, described by its polarization transfer function in the form of a Mueller matrix, can also be measured by varying the input polarizations and measuring the respective outputs.[24] Specifically, a Stokes vector $\mathbf{S}=(IQUV)^T$ is a four-element vector describing the polarization of a beam of light. Its element $I$ represents the overall intensity of the beam, $Q$ gives the intensity of linear polarization along horizontal and vertical axes (with respect to an arbitrary reference frame), $U$ gives the intensity of linear polarization at $\pm 45$ deg, and $V$ gives the intensity of light that is circularly polarized. Analogously, a Mueller matrix $\mathbf{M}$ is a $4\times 4$ matrix describing the effects a particular optical element has on the polarization of the input light. The two descriptors are linked in the so-called Mueller calculus: given a beam with a Stokes vector $\mathbf{S}_i$ impinging on an optical element with a Mueller matrix $\mathbf{M}$, the light output from that element will have its polarization described by a Stokes vector as $\mathbf{S}_o=\mathbf{M}\mathbf{S}_i$.

A schematic of the point measurement system is shown in Fig. 1. The beam from a HeNe laser at 632.8 nm passes through a mechanical chopper operating at $f_c=300$ Hz for intensity modulation, then through a linear polarizer and quarter wave plate to control the polarization of the light incident on the sample by adjustment of their orientations. After interacting with the sample, light in the forward (20-deg solid angle) direction is collected with a lens and passes through a

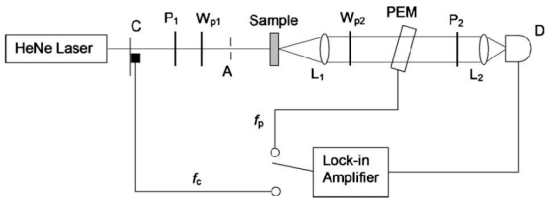



**Fig. 1** Schematic of point measurement polarimetry system. C, mechanical chopper; $P_1$, $P_2$, polarizers; $W_{p1}$, $W_{p2}$, quarter wave plates ($W_{p2}$ is removable); A, aperture; $L_1$, $L_2$, lenses; PEM, photoelastic modulator; D, avalanche photodiode; and $f_c$, $f_p$, modulation frequencies of mechanical chopper and PEM, respectively.

removable quarter waveplate oriented at −45 deg. The collected beam then passes through a photoelastic modulator (PEM, IS-90, Hinds Instruments, Hillsboro, Oregon), a linearly birefringent resonant device operating at $f_p=50$ kHz. The optical axis of the PEM is oriented at 0 deg and its magnitude of retardation is modulated according to the sinusoidal function $\delta_{\mathrm{PEM}}=\delta_o \sin \omega_p t$, where $\omega_p=2\pi f_p$, and $\delta_o$ is the user-specified amplitude of maximum retardation. When the removable quarter wave plate is in place, the Stokes vector parameters $Q$ and $U$ (linear polarization) are modulated; when removed, the Stokes vector parameter $V$ (circular polarization) is modulated. Finally, the beam passes through a linear analyzer oriented at +45 deg, converting the polarization-modulated light into intensity modulated light at 50 kHz (and its harmonic at 100 kHz), and is detected with an avalanche photodiode (APD C5460, Hamamatsu, Hamamatsu City, Japan). The resulting photocurrent is then sent to a lock-in amplifier for high SNR synchronous detection, with the reference signal toggled between 300 Hz, 50 kHz, and 100 kHz.

The specifics of the signal analysis can be found in previous publications.[25,26] Briefly, the normalized Stokes parameters ($q=Q/I$, $u=U/I$, and $v=V/I$) of the light that is collected from the sample are calculated from the synchronously detected lock-in amplifier signals at the first harmonic of the chopper frequency $V_{1fc}$ (300 Hz), and the first and second harmonics of the signal at the PEM frequency $V_{1fp}$ and $V_{2fp}$ (50 and 100 kHz, respectively). When the detection quarter wave plate is in place, the normalized Stokes parameters $q$ and $u$ are calculated from

$$q=\frac{V_{1fp}}{\sqrt{2}J_1(\delta_o)V_{1fc}}, \tag{1}$$

and

$$u=\frac{V_{2fp}}{\sqrt{2}J_2(\delta_o)V_{1fc}}, \tag{2}$$

where $J_1(\delta_o)$ and $J_2(\delta_o)$ are the first- and second-order Bessel functions evaluated at the user-selected PEM amplitude of maximum retardation. When the detection quarter wave plate is removed, the normalized Stokes parameter $v$ can then be calculated as

$$v=\frac{V_{1fp}}{\sqrt{2}J_1(\delta_o)V_{1fc}}. \tag{3}$$

By cycling through four different input polarization states, specifically linear polarizations at 0, 45, and 90 deg, and circularly polarized light (either right or left) denoted as $H$, $P$, $V$, and $R$, respectively, and measuring the corresponding output polarization states, the Mueller matrix of the sample can be calculated. Specifically, the measured outputs states for the four subscripted input states are combined to calculate the 16 elements of the sample Mueller matrix as

$$\mathbf{M}(i,j)=\begin{bmatrix} \frac{1}{2}(I_H+I_V) & \frac{1}{2}(I_H-I_V) & I_p-\mathbf{M}(1,1) & I_R-\mathbf{M}(1,1) \\ \frac{1}{2}(Q_H+Q_V) & \frac{1}{2}(Q_H-Q_V) & Q_p-\mathbf{M}(2,1) & Q_R-\mathbf{M}(2,1) \\ \frac{1}{2}(U_H+U_V) & \frac{1}{2}(U_H-U_V) & U_p-\mathbf{M}(3,1) & U_R-\mathbf{M}(3,1) \\ \frac{1}{2}(V_H+V_V) & \frac{1}{2}(V_H-V_V) & V_p-\mathbf{M}(4,1) & V_R-\mathbf{M}(4,1) \end{bmatrix}, \tag{4}$$

where the indices $i$ and $j$ denote the rows and columns, respectively. From this experimentally determined Mueller matrix, the sample polarizing properties, including birefringence, can be calculated, as shown in the later section on Mueller matrix decomposition.

A polarimetry imaging system was also developed for spatial mapping of polarization parameters, as shown in Fig. 2. The input beam from a diode laser at 635 nm (Thorlabs, Newton, New Jersey) first passes through a linear polarizer, removable quarter wave plate, and an aperture to control the beam polarization and width (approximately 1 cm diam) before being incident on the sample. A diode laser was employed rather than the HeNe used for point measurements, as additional power was required for a wide beam. After interacting with the sample, the light passes through a pair of lenses to collect and focus the beam, as well as a removable quarter wave plate and a linear analyzer to allow for intensity detection of the output linear polarizations by a charge-coupled camera (CCD) camera (CoolSNAP K4, Photometrics, Tucson, Arizona) with $2048\times2048$ pixels, $7.4\times7.4$-$\mu m^2$ pixel size, and field of view approximately $2\times2$ cm$^2$. The input beam was angled slightly off axis (7 deg) to avoid any directly transmitted light saturating the CCD. This imaging system does not employ synchronous lock-in detection, so the SNR of this system is reduced compared to the point measurements. Work is currently underway to incorporate synchronous measurements.

By using this imaging system, full Stokes parameters can be measured. By rotating the analyzing polarizer and inserting the quarter wave plate, the Stokes parameters $Q$ and $U$ can be measured from the detected intensities as,

$$Q=I_{0\ \mathrm{deg}}-I_{90\ \mathrm{deg}}, \tag{5}$$

$$U=I_{45\ \mathrm{deg}}-I_{135\ \mathrm{deg}}, \tag{6}$$

and

$$V=I_{QW180\ \mathrm{deg}}-I_{QW90\ \mathrm{deg}}, \tag{7}$$

where the subscripts indicate the orientation of the analyzer, and $QW$ in the subscript indicates that the detection quarter wave plate is in place. The measured Stokes parameters for each appropriate input state can then be used to construct the $4\times4$ Mueller matrix, although the necessary Mueller matrix elements to determine retardance can be obtained from the top left $3\times3$ matrix.[27]

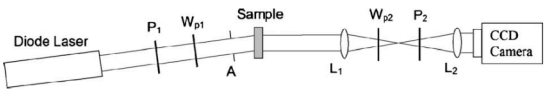



**Fig. 2** Schematic of imaging polarimetry system. $P_1$, $P_2$, polarizers; $W_{p1}$, $W_{p2}$, removable quarter waveplates; $A_1$, $A_2$, apertures; and $L_1$, $L_2$, lenses.

## 2.2 *Mueller Matrix Decomposition*

The Mueller matrix measured with either system describes the combined effects of all the polarizing properties of the sample. In the case of biological tissues, these effects are depolarization (due to scattering), optical activity, and birefringence. These effects occur simultaneously in tissue, making their unique quantification nontrivial, particularly as tissue is a turbid depolarizing medium. To quantify each of the effects separately (in this case, we are specifically interested in linear birefringence), it is possible to decompose the measured matrix $\mathbf{M}$ into the product of three basis constituent matrices,[28,29]

$$\mathbf{M}=\mathbf{M}_\Delta\mathbf{M}_\mathrm{R}\mathbf{M}_\mathrm{D}, \tag{8}$$

where the effects of depolarization are accounted for in the depolarizing matrix $\mathbf{M}_\Delta$, the effects of linear birefringence and optical activity (circular birefringence) are described by the retarder matrix $\mathbf{M}_\mathrm{R}$, and the effects of linear and circular dichrosim are described in the diattenuator matrix $\mathbf{M}_\mathrm{D}$. $\mathbf{M}$ can

be decomposed through a series of algebraic operations into these three basis matrices, using the method first described for clear media by Lu and Chipman.[28] We have adapted this approach for optically turbid media with simultaneously occurring polarization effects.[29] While the multiplication order in Eq. (7) appears ambiguous (matrices in general do not commute under multiplication, so that $\mathbf{AB} \neq \mathbf{BA}$), it has been shown that this product or its reverse order always leads to a physically realizable Mueller matrix.[28,30,31] The validity and accuracy of this approach in turbid media has been previously demonstrated with both simulated and experimental data.[26] In addition, the use of the top left $3 \times 3$ submatrix in the decomposition process for determining sample birefringence properties has also been previously demonstrated.[27]

The measurable effect of birefringence, linear retardance $\delta$, is contained in $\mathbf{M}_R$ and can be calculated from its elements as[28]

$$\delta = \cos^{-1}\{[(m_{R22} + m_{R33})^2 + (m_{R32} - m_{R23})^2]^{1/2} - 1\}, \quad (9)$$

where $m_{Rij}$ are the elements of $\mathbf{M}_R$. The decomposed values for linear retardance were recorded for the myocardial samples in this study for both point and imaging measurements. If the optical path length $d$ is known, the measured retardance can be used to calculate the sample birefringence, as is possible with PS-OCT measurements. However, in our case $d$ is not known due to scattering. Although we have used a polarization-sensitive Monte Carlo model to estimate the effective path lengths in various geometries and with different sample optical properties,[32,33] we chose here to report the retardance values in this study and did not attempt to deduce the underlying birefringence, as optical scattering and absorption properties of the myocardial tissue are not known. To compare retardance measurements, the propagation distance was held constant by performing measurements through samples sectioned to uniform thicknesses.

### 2.3 *Multiphoton Microscopy*

To determine the underlying microstructural, morphological, and compositional causes for the observed polarization signals, multiphoton microscopy was performed on the cardiac samples. Second harmonic generation (SHG) was used to image the extracellular collagen matrix, while two-photon excited fluorescence (TPEF) was used to image cardiomyocytes. This label-free microscopic and nondestructive approach yields inherently coregistered images of the collagen and the cardiomyocyte compartments, thus giving useful information on cardiac tissue microstructure and composition, including the infarction and regeneration processes.

Images were acquired with a confocal microscope (Zeiss, LSM 510 META NLO, Oberkochen, Germany) using a 20× 0.75-NA dry objective. The excitation wavelength was set to 840 nm using a tunable Ti:sapphire laser (Chameleon, Coherent Incorporated, Santa Clara, California). The SHG signal is emitted at half the excitation wavelength, 420 nm, while the TPEF signal is emitted at longer wavelengths above about 440 nm. Two wavelength filters were used to spectrally separate the signals: 398 to 430 nm for SHG, and 430 to 463 nm for TPEF. While fluorescence is also emitted at wavelengths greater than 463, this narrow wavelength range was chosen so that the TPEF signal would have approximately the same intensity as the SHG signal. Both SHG and TPEF signals were recorded in the back-scattered direction with a spectral detector. In all figures, the SHG signal is shown in green pseudocolor and the TPEF signal is shown in red pseudocolor. The imaging resolution was $0.45 \times 0.45$ $\mu$m per pixel with a field of view of 460 $\mu$m $\times$ 460 $\mu$m$^2$. The images were taken at a depth of approximately 50 $\mu$m from the surface of the sample, with the depth of focus being 1 $\mu$m.

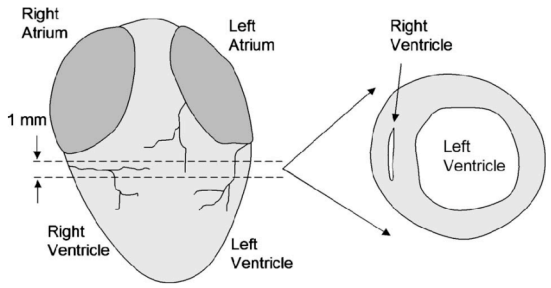



**Fig. 3** Schematic of rat heart showing location of axial section and schematic of a section.

### 2.4 *Myocardial Tissues*

To investigate the utility of birefringence measurements for monitoring regenerative treatments, samples from a rat model of myocardial infarction and regeneration were used. All animal studies were carried out under institutional approval (University Health Network, Toronto, Canada).

Myocardial infarctions were induced in adult Lewis rats by coronary artery ligation. One group of animals was used as a control ($n=4$), while mesenchymal stem cells were administered to a treatment group ($n=3$) by intramyocardial injection into the site of infarction, two weeks postligation. Both control and treatment groups were sacrificed four weeks postinfarction (2 weeks post-stem-cell injection for the treatment group), at which time the hearts were removed, fixed in 10% formalin, and sectioned by a vibratome to 1-mm-thick axial sections, as shown in Fig. 3. This sectioning was done to reduce the effects of excessive depolarization by multiple scattering in thick tissues. These 1-mm sections were also used for multiphoton microscopy. We chose transmission geometry for this initial study for ease of measurement and interpretation; polarization measurements in thick tissues (in reflection geometry) are being initiated. It should also be noted that the tissue fixation process may alter the birefringence properties of tissue through protein cross-linking, so that the absolute values derived in this study can have a systematic offset. However, this should not affect the observed relative changes in birefringence and trends therein. The effects of formalin fixation on tissue birefringence are currently being investigated. To perform the measurements, the sections were mounted on a glass microscope slide and placed horizontally in the beam path. To ensure that the tissues did not dry out, the measurements were performed quickly (less than 5 min). All measurements were performed at room temperature (25 °C). As the field of view for the multiphoton microscopy images is small relative to the size of the samples, whole slice histology was also conducted. One sample from each group

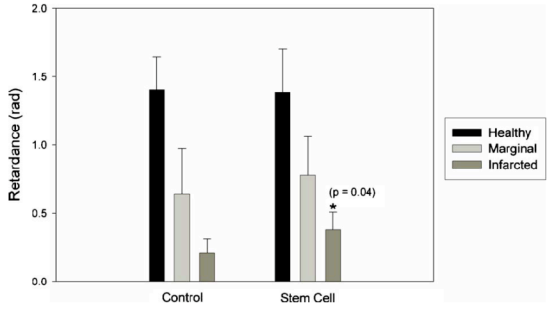



**Fig. 4** Results of point measurements; error bars are ± one standard deviation. Results are for control ($n=4$) and stem-cell-treated ($n=3$) animals. * denotes statistical significance ($p<0.05$) with respect to the corresponding control. Note the increase in retardance (birefringence) with stem cell treatment.

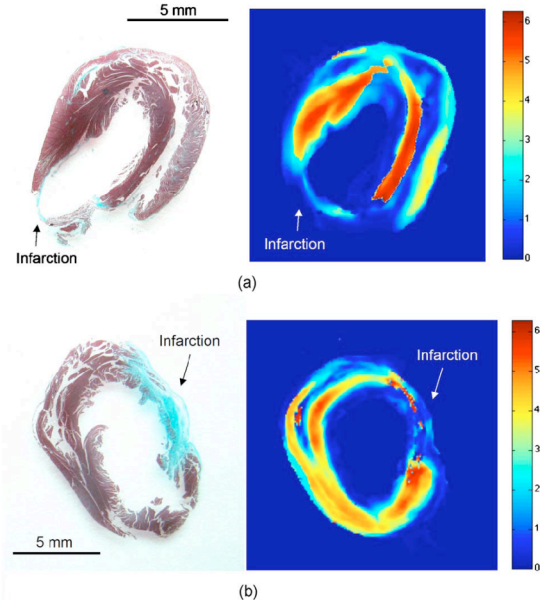



**Fig. 5** Representative retardance images for (a) control and (b) stem-cell-treated sections with corresponding Masson's trichrome stained histology images (collagen in blue, muscle in red). Retardance values are given in radians. (Color online only.)

was embedded in paraffin, stained with Masson's trichrome, and sectioned to 5 $\mu$m for histological examination. This enabled whole slice comparison between polarization and histology with regards to myocardial composition.

## 3 Results and Discussion

### 3.1 *Point Retardance Measurements*

Results from point retardance measurement on the control and treated tissues are shown in Fig. 4. For each sample, measurements were performed in the healthy (region distal to the induced infarct), marginal (region adjacent to the induced infarct), and infarcted scar region. Cardiology experts identified these regions based on ventricular wall thinning; the infarction can also be clearly identified by the histology images in Fig. 5 based on collagen content. In each of these regions, five measurements were made at different positions. The results are the mean of all measurements in that region for all samples within each group.

As expected, the myocardium exhibits significant birefringence, particularly in the healthy regions where retardance values of up to 1.4 radians were measured. If one assumes the light propagation distance to be at least the tissue thickness (1 mm), this corresponds to a birefringence value of $\Delta n \leqslant 1.4\times10^{-4}$, which is comparable to other organized tissues.[34] A large reduction in retardance was measured in the infarcted regions compared to the healthy tissue values, indicating a loss of tissue anisotropy and organization most likely due to the loss of cardiomyocyte fibers and their replacement with collagen-rich scar tissue. The normal myocardial tissue is comprised of highly organized cardiomyocytes surrounded with a fibrotic extracellular matrix, which results in a highly anisotropic structure; conversely, the infarction is primarily disorganized scar tissue comprised of randomly oriented, and thus optically isotropic, collagen fibers. The marginal regions represent a mixture of organized myocytes and disorganized collagen scar compartments, resulting in reduced retardance, although not as low as the scar tissue. These tentative interpretations are tested and confirmed by histology in Fig. 5 and the findings of nonlinear microscopy, as discussed in Sec. 3.3.

The tissue response to regenerative treatment is seen as a statistically significant rise ($p<0.05$, calculated using a two-tailed Student's t-test) in the measured retardance in the infarcted regions, as well as an apparent rise (although not statistically significant) in the marginal region. The addition of stem cells to the infarcted regions results in remodeling of the scar tissue, specifically a reduction in collagen and regrowth of myocytes leading to an improvement in cardiac function. This remodeling results in increased tissue anisoptropy and organization, manifesting as an increase in the retardance but without complete recovery to the normal tissue value. This is consistent with typical myocardial regenerative treatments, as full functional recovery is generally not achieved.[6] These results are consistent with our previous point measurements where a reduction in birefringence was measured with infarction, and an increase was also measured with regenerative treatment.[10]

### 3.2 *Retardance Imaging*

Point polarimetry measurements, sampling approximately 2- to 4-mm$^3$ volumes of tissues,[32,33] likely suffer from sampling bias in the heterogeneous, spatially varying tissues. To better understand how the birefringence values vary spatially in myocardial samples, 2-D retardance images were taken of all samples from the control ($n=4$) and treatment ($n=3$) groups. A retardance image from each group is shown in Fig. 5, together with Masson's trichrome stained histology from the respective sample for comparison. The retardance images show similar trends, as seen in the point measurement results, although some variation was seen as expected (difference in measurement geometry and spatial heterogeneity in tissue optical properties). The retardance is significantly reduced in the region of infarction and increases through the marginal region to higher levels in healthy tissues. In addition, the birefrin-

gence in the region of infarct increases with treatment. A reduction in ventricular thickness in the infarct and an increase in thickness with treatment are also visible. The histology images show the healthy myocardium to be nearly entirely composed of muscle (stained red) and little to no collagen (stained blue). This is in sharp contrast to the infarct, which is almost entirely comprised of scar collagen. Some muscle tissue can be seen in the infarct region of the treatment sample, likely as a result of stem-cell-induced regeneration. These imaging results are similar to our previous imaging study,[11] where a decrease in retardance with infarction and increase with treatment were also measured.

Considerable spatial variation is seen in the birefringence images; not only do the values change from infarct to normal, but also within each region as well. In general, higher values are measured in the middle of the myocardial wall, with lower values toward the edges. This is likely due to the change in orientation of the myocyte fibers through the wall, which undergo a 180-deg rotation from the outside of the ventricle to the inside[35]: on the inside and outside of the ventricle, the fibers are oriented perpendicular to our imaging plane, while in the center of the ventricular wall the fibers are parallel to the imaging plane. Hence, the retardance values are generally lower on the outside and inside walls, since the axis of birefringence (direction of the fibers) is along the direction of light propagation, and greater in the center where the axis of birefringence is perpendicular the direction of propagation. To investigate this further, we are currently examining the effects of birefringence axis orientation, and its spatial variation throughout the samples.

The spatial variations in the samples could be compounded by retardance phase wrap-around. Since retardance is a measure of the phase difference between two orthogonal polarizations states, once these states have gone out of phase by more than $\pi$ radians, the retardance will wrap-around and decrease. However, a wrap-around correction algorithm[36] was employed to detect and appropriately modify any retardance values that have undergone wrap-around. Details on the algorithm can be found in the reference. Additional intersample variations can arise from the uncertainty in the angle at which the samples were sectioned. As mentioned previously, higher retardance values are measured when the fibers are oriented parallel to the measurement plane than when the fibers are perpendicular.

Overall statistics from the images are shown in Fig. 6. Values are the mean and standard deviation of pixel retardance values from the entire healthy, marginal, and infarcted regions of all images for each group. The mean measured retardance values in the images are generally higher than the point measurements, most likely due to the difference in measurement geometry (input imaging beam is 7-deg off-axis) and the use of wrap-around correction. Reassuringly, the overall trend is similar to that of the point measurements. A statistically significant ($p<0.05$, calculated using a two-tailed Student's t-test) increase in the retardance was measured in the infarction relative to the control in stem-cell-treated samples, again indicating reorganization of the tissue through remodeling. The margin values remain fairly constant from group to group, while the retardance values in healthy regions increase from the control to the treated samples, although this increase was not found to be significant ($p>0.05$). The difference in retardance values between infarcted and healthy regions is somewhat lower than for the point measurements, likely due to the point measurements from the healthy regions being made in the center of the myocardial wall, where the retardance is the highest, while the image statistics are calculated from pixels averaged across the whole thickness of the myocardium. Also, differences in SNR can contribute to these discrepancies.

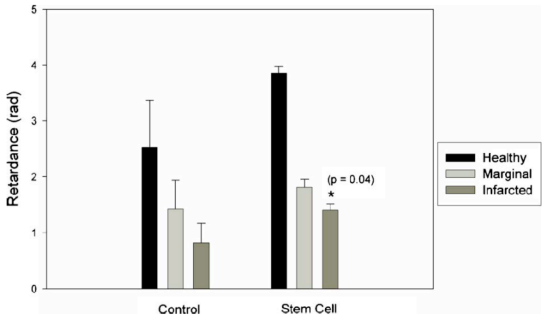



**Fig. 6** Mean ± one standard deviation retardance pixel values from retardance images from health, marginal, and infracted regions. Results are for control ($n=4$) and stem-cell-treated ($n=3$) animals. * denotes statistical significance ($p<0.05$) with respect to the corresponding control.

As considerable spatial variation is seen across the sections in the retardance images, the location of point measurement even within a specific region (i.e., healthy region, marginal zone, or infarcted tissue) can greatly influence the results. Thus, care must be taken when interpreting point measurements, as a single value may not be representative of the region. We are currently conducting further studies of the retardance variations, specifically by measuring the orientation of the birefringent axis and relating this to fiber orientations, as previously mentioned.

### 3.3 *Nonlinear Microscopy*

The underlying morphological, microstructural, and compositional changes responsible for the measured changes in birefringence were investigated using nonlinear microscopy, specifically SHG for collagen and TPEF for cardiomyocyte imaging.[20] Representative images from healthy and infarcted regions of a control sample are shown in Figs. 7(a) and 7(b), respectively, while a region of regenerating infarction is shown in Fig. 7(c).

The normal region of the control sample shows primarily highly organized cardiac muscle fibers and occasional collagen fibers, as expected, since collagen comprises less than 2% of healthy myocardial dry weight.[37] This correlates well with the histology shown in Fig. 5, where healthy myocardium contains little collagen. Thus, the healthy tissue can be considered to consist primarily of the cardiomyocytes, with interspersed small amounts of collagen, as seen in Fig. 5(a). This is in sharp contrast to the infarcted region where the opposite is true—the tissue is comprised primarily of scar collagen with decreasing amounts of surviving cardiomyocytes present. This again correlates well with histology shown in Fig. 5, where in contrast to the healthly myocardium, the infarction is nearly entirely composed of collagen. Regions in

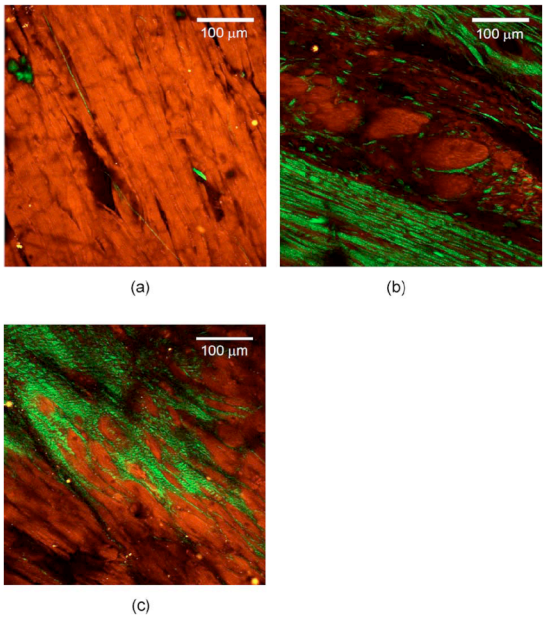



**Fig. 7** Representative nonlinear microscopy images from (a) healthy, (b) infracted, and (c) regenerating regions of myocardial samples. The TPEF signal from cardiomyocytes is shown in red pseudocolor, and the SHG from collagen is shown in green pseudocolor. (Color online only.)

the infarction image where no signals (neither SHG nor TPEF) were measured likely correspond to regions of myocyte necrosis. The cardiomyocyte compartment has been largely replaced by the collagen compartment due to myocyte death and the resulting collagen scar formation throughout the necrosed tissues. While the collagen fibers in the infarcted region do exhibit some local organization, the overall structure of the tissue is disorganized compared to the healthy tissue. The difference in measured retardance from these two regions is as expected due to the necrosis of the highly organized muscle fibers with high anisotropy, and the partial replacement of these fibers with scar collagen, which overall is relatively isotropic with accordingly low birefringence.

The regenerating infarcted tissue from the treatment sample shows collagenous scar tissue and reorganized collagen fibers, as well as muscle fibers that have likely regrown in the region. As the tissue is more organized than the scar tissue in the control infarction region, the higher retardance measured in these regions correspond to the reorganization of the tissue through remodeling (regrowth of myocytes and reduction in collagen), as reflected in the corresponding trend toward increasing anisotropy. Both cardiomyocyte and collagen compartments are present in the regenerating tissue; this is shown by the histology in Fig. 5 as well, where the regenerating scar tissue does contain some muscle. The cardiomyocyte compartment has infiltrated the scar collagen compartment due to the growth of the injected stem cells into cardiac muscle, and has possibly stimulated regrowth of cardiac muscle cells from the surrounding tissues. While the sampling volumes for the microscopy and polarimetry measurements are quite different, the fact that these morphological changes can be observed through polarimetry measurements demonstrates the potential of this technique to monitor regenerative treatments.

## 4 Conclusions and Future Work

We demonstrate the ability to characterize myocardial tissue using birefringence measurements, both in point sensing and large-area imaging modes. Specifically, changes in birefringence associated with structural remodeling due to myocardial infarction and regenerative treatments are successfully measured, showing potential for this technique to monitor these regenerative treatments. A decrease in birefringence is measured from healthy to infarcted myocardium; subsequently, an increase in birefringence ($p=0.04$) is measured in the infarctions that had undergone stem cell treatments. As the structural state and organization of the myocardium can be indicative of its functional state, the measurements of structural anisotropy via birefringence can be useful for monitoring of stem cell regenerative treatments. Conventional histology and label-free nonlinear microscopy are used to understand the underlying causes of the birefringence signals and aid in interpreting the signal trends. Work is currently underway in adapting these techniques to bulk tissues where transmission measurements are no longer feasible. This will require the use of diffuse reflectance polarization measurements and likely multiple spatially resolved measurements or polarimetry images to quantify tissue retardance. To aid these studies, work is underway in developing an imaging system with a SNR comparable to the point measurement system.

Additional work is also planned for monitoring the retardance in strained *ex vivo* myocardial tissue, simulating a contracting heart, as the birefringence will likely change under strain. This may provide additional structural and elastographic information concerning the myocardium, as different tissue states (i.e., healthy, marginal, infarcted, and regenerating) will respond differently to applied strain. Extending these techniques to *in vivo* measurements will involve a number of challenges, including cardiac motion, spatial localization, and delivery of the probe to the myocardial wall (most likely via a catheter). We are currently developing a rigid probe suitable for limited *in vivo* measurements (e.g., externalized heart), with further probe development currently in the planning stages. To our knowledge, this and our previous work[13] are the first studies of polarization birefringence measurements for differentiating healthy, infarcted, and regenerating myocardial tissue.

### *Acknowledgments*

Financial support from the Natural Sciences and Engineering Research Council of Canada, the Canadian Institutes of Health Sciences, the Canadian Foundation for Innovation, and the Ontario Graduate Scholarship Program is gratefully acknowledged.

### *References*

1. See http://www.who. int/cardiovascular_diseases/en/index.html.
2. K. R. Chien, "Regenerative medicine and human models of human disease," *Nature* **453**, 302–305 (2008).
3. T. Reya, S. J. Morrison, M. F. Clarke, and I. L. Weissman, "Stem cells, cancer, and cancer stem cells," *Nature* **414**, 105–111 (2001).

4. M. Jain, H. DerSimonian, D. A. Brenner, S. Ngoy, P. Teller, A. S. B. Edge, A. Zawadzka, K. Wetzel, D. B. Sawyer, W. S. Colucci, C. S. Apstein, and R. Liao, "Cell therapy attenuates deleterious ventricular remodeling and improves cardiac performance after myocardial infarction," *Circulation* **103**, 1920–1927 (2001).
5. D. Orlic, J. Kajstura, S. Chimenti, I. Jackoniuk, S. M. Anderson, B. Li, J. Pickel, K. MacKay, B. Nadal-Ginard, D. M. Bodine, A. Leri, and P. Anversa, "Bone marrow cells regenerate infarcted myocardium," *Nature* **410**, 701–705 (2001).
6. R. Passier, L. W. van Laake, and C. L. Mummery, "Stem-cell-based therapy and lessons from the heart," *Nature* **453**, 322–329 (2008).
7. N. Christoforou and J. D. Gearhart, "Stem cells and their potential in cell-based cardiac therapies," *Prog. Cardiovasc. Dis.* **49**, 396–413 (2007).
8. Y. Sun, J. Q. Zhang, J. Zhang, and S. Lamparter, "Cardiac remodeling by fibrous tissue after infarction," *J. Lab. Clin. Med.* **135**, 316–323 (2000).
9. X. Xu, Z. Xu, Y. Xu, and C. Cui, "Selective down-regulation of extracellular matrix gene expression by bone marrow derived stem cell transplantation into infarcted myocardium," *Circ. J.* **69**, 1275–1283 (2005).
10. N. Ghosh, M. F. G. Wood, S. Li, R. D. Weisel, B. C. Wilson, R. Li, and I. A. Vitkin, "Mueller matrix decomposition for polarized light assessment of biological tissues," *J. Biophoton.* **2**, 145–156 (2008).
11. M. F. G. Wood, N. Ghosh, S. Li, R. D. Weisel, B. C. Wilson, R. Li, and A. Vitkin, "Polarized light based birefringence measurements for monitoring myocardial regeneration," *Proc. SPIE* **7179**, 717908 (2009).
12. V. V. Tuchin, L. Wang, and D. À. Zimnyakov, *Optical Polarization in Biomedical Applications*, Springer-Verlag, Berlin (2006).
13. R. S. Gurjar, V. Backman, L. T. Perelman, I. Georgakoudi, K. Badizadegan, I. Itzkan, R. R. Dasari, and M. S. Feld, "Imaging human epithelial properties with polarized light scattering spectroscopy," *Nat. Med.* **7**, 1245–1249 (2001).
14. P. Whittaker, D. R. Boughner, and R. A. Kloner, "Analysis of healing after myocardial infarction using polarized light microscopy," *Am. J. Pathol.* **134**, 879–893 (1989).
15. M. J. Everett, K. Schoenenberger, B. W. Colston, and L. B. Da Silva, "Birefringence characterization of biological tissue by use of optical coherence tomography," *Opt. Lett.* **23**, 228–230 (1998).
16. C. Sun, Y. Wang, L. Lu, C. Lu, I. Hsu, M. Tsai, C. Yang, Y. Kiang, and C. Wu, "Myocardial tissue characterization based on a polarization-sensitive optical coherence tomography system with an ultrashort pulsed laser," *J. Biomed. Opt.* **11**, 054016 (2006).
17. B. C. Wilson, I. A. Vitkin, and D. L. Matthews, "The potential of biophotonic techniques in stem cell tracking and monitoring of tissue regeneration applied to cardiac stem cell therapy," *J. Biophoton.* **2**, 669–681 (2009).
18. N. Nyolczas, S. Charwat, A. Posa, R. Hemesberger, N. Pavo, H. Hemetsberger, I. J. Pavo, D. Glogar, G. Maurer, and M. Gyöngyösi, "Tracking the migration of cardially delivered therapeutic stem cells *in vivo*: state of the art," *Regen. Med.* **4**, 407–422 (2009).
19. S. P. Nighswander-Rempel, V. V. Kupriyanov, and R. A. Shaw, "Regional cardiac tissue oxygenation as a function of blood flow and $pO_2$: a near-infrared spectroscopic imaging study," *J. Biomed. Opt.* **11**, 054004 (2006).
20. E. M. C. Hillman, O. Bernus, E. Pease, M. B. Bouchard, and A. Pertsov, "Depth-resolved optical imaging of transmural electrical propagation in perfused heart," *Opt. Express* **15**, 17827–17841 (2007).
21. E. E. Konofaguo, J. D'hooge, and J. Ophir, "Myocardial elastography—a feasibility study *in vivo*," *Ultrasound Med. Biol.* **28**, 475–482 (2002).
22. M. A. Fallert, M. S. Mirotznik, S. W. Downing, E. B. Savage, K. R. Foster, M. E. Josephson, and D. K. Bogen, "Myocardial electrical impedance mapping of ischemic sheep hearts and healing aneurysms," *Circulation* **87**, 199–207 (1993).
23. E. X. Wu, Y. Wu, J. M. Nicholls, J. Wang, S. Liao, S. Zhu, C. Lau, and H. Tse, "MR diffusion tensor imaging study of postinfarct myocardium structural remodeling in a porcine model," *Magn. Reson. Med.* **58**, 687–695 (2007).
24. C. Brosseau, *Fundamentals of Polarized Light: A Statistical Optics Approach*, John Wiley and Sons, NewYork (1998).
25. X. Guo, M. F. G. Wood, and I. A. Vitkin, "Angularly resolved linear Stokes polarimeter measurements of light scattered by turbid chiral media," *J. Biomed. Opt.* **11**, 041105 (2006).
26. M. F. G. Wood, X. Guo, and I. A. Vitkin, "Polarized light propagation in multiply scattering media exhibiting both linear birefringence and optical activity: Monte Carlo model and experimental methodology," *J. Biomed. Opt.* **12**(1), 014029 (2007).
27. M. K. Swami, S. Manhas, P. Buddhiwant, N. Ghosh, A. Uppal, and P. K. Gupta, "Polar decomposition of $3\times3$ Mueller matrix: a tool for quantitative tissue polarimetry," *Opt. Express* **14**, 9324–9337 (2006).
28. S. Y. Lu and R. A. Chipman, "Interpretation of Mueller matrices based on polar decomposition," *J. Opt. Soc. Am. A* **13**, 1106–1113 (1996).
29. N. Ghosh, M. F. G. Wood, and I. A. Vitkin, "Mueller matrix decomposition for extraction of individual polarization parameters from complex turbid media exhibiting multiple scattering, optical activity, and linear birefringence," *J. Biomed. Opt.* **13**, 044036 (2008).
30. N. Ghosh, M. F. G. Wood, and I. A. Vitkin, "Polarimetry in turbid, birefringent, optically active media: a Monte Carlo study of Mueller matrix decomposition in the backscattering geometry," *J. Appl. Phys.* **105**, 102023 (2009).
31. N. Ghosh, M. F. G. Wood, and I. A. Vitkin, "Influcence of the order of the constituent basis matrices on the Mueller matrix decomposition-derived polarization parameters in complex turbid media such as biological tissue," *Opt. Commun.* **283**, 1200–1208 (2010).
32. X. Guo, M. F. G. Wood, and I. A. Vitkin, "Monte Carlo study of pathlength distribution of polarized light in turbid chrial media," *Opt. Express* **23**, 2348–1360 (2007).
33. X. Guo, M. F. G. Wood, and I. A. Vitkin, "A Monte Carlo study of penetration depth and sampling volume of polarized light in turbid media," *Opt. Commun.* **281**, 380–386 (2008).
34. X. Wang and L. V. Wang, "Propagation of polarized light in birefringent turbid media: A Monte Carlo study," *J. Biomed. Opt.* **7**, 350–358 (2002).
35. P. P. Sengupta, V. K. Krishnamoorthy, J. Korinek, J. Narula, M. A. Vannan, S. J. Lester, J. A. Tajik, J. B. Seward, B. K. Khandheria, and M. Belohlavek, "Left ventricular form and function revisited: applied translation science to cardiovascular ultrasound imaging," *J. Am. Soc. Echocardiogr* **20**, 539–551 (2007).
36. M. A. Wallenburg, M. F. G. Wood, N. Ghosh, M. Pop, G. Wright, and I. A. Vitkin, "Comparison of optical polarimetry and diffusion tensor MR imaging for assessing myocardial anisotropy," *J. Innov. Opt. Health Sci.* **3**, 109–121 (2010).
37. R. A. Kloner, M. C. Fishbein, C. M. Hare, and P. R. Maroko, "Early ischemic ultrastructural and histochemical alterations in the myocardium of rat following coronary artery occlusion," *Exp. Mol. Pathol.* **30**, 129–143 (1979).

***Addendum***

In addition to performing polarimetry measurements on the control and stem cell treated groups covered in the preceding publication, measurements were also conducted on a third group (n = 4) that had undergone treatment with mesenchymal stems cells transfected with the human elastin gene. The addition of elastin to the second group was hypothesized to increase elasticity in the regenerating tissue,[123] and accordingly enhance cardiac function, as decreased elasticity in infarcted myocardium is one of the causes of decreased functionality. This study was part of collaborative work investigating the use of transfected human elastin gene in cardiac stem cell therapy. While these measurements were completed at the same time as those previously presented, the results were not included in the manuscript because they are currently in preparation for separate publication.

The results of point measurements on healthy, marginal, and infarcted regions of rat myocardium for control (no treatment), stem cell treated, and treatment with stem cells transfected with elastin are shown below in Fig. 9. This figure is analogous to Fig. 4 from the publication, except measurements on stem cells transfected with elastin gene are now included for comparison. The measured retardance in the infarcted region of the hearts treated with stem cells transfected with elastin was significantly higher ($p < 0.05$, calculated using a two-tail students t-test) than control ($p = 0.01$) and significantly higher than the stem cell treated group ($p = 0.032$). This indicates an increased preservation and/or regeneration of myocardial structural organization associated with the expression of elastin in the infarction, suggesting treatment with these modified stem cells results in more beneficial remodeling of the myocardium. The expression of elastin in the infarct,

assuming the elastin fibers are arranged in an organized manner, will contribute to the overall birefringence and thus increase the measured retardance. It is interesting to note in Fig. 9 that the retardance values in the healthy region decrease slightly with treatment (although not statistically significantly). This may be due structural remodeling in the regions remote to the infarct, however, this has yet to be shown.

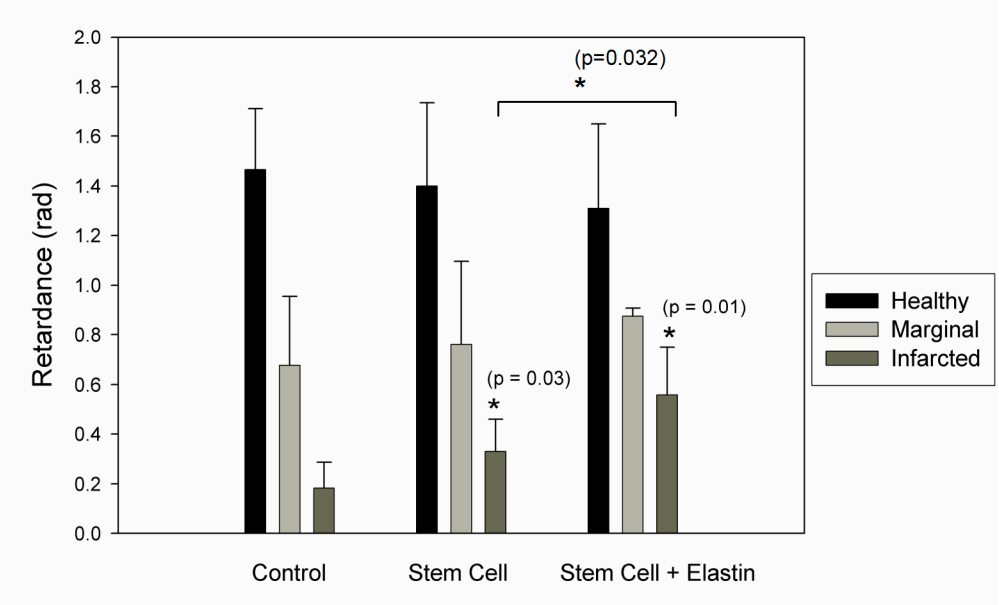



**Fig. 9** Results of point measurements, error bars are the standard deviation. Results are for control (n = 4), stem cell treated (n = 3), and stem cell transfected with elastin treated (n = 4) myocardial samples. Asterisk denotes statistical significance ($p < 0.05$) with respect to the control. Note the additional increase in retardance (birefringence) with elastin transfection.

Polarimetry imaging results on a sample from this additional group are shown in Fig. 10 along with corresponding histology (Masson's trichrome). The full image statistics for mean retardance values in healthy, margin, and infarcted regions from all groups are plotted in Fig. 11. A further increase in mean retardance was measured from stem cell treated group to the elastin-transfected group; however unlike the point measurements, due to a large variance in the retardance values for the elastin-transfected group, the increase failed statistical significance testing ($p > 0.05$) over both the control and stem

cell treated group. In spite of this, the rise may still be indicative of further remodeling and/or preservation of tissue organization and anisotropy due to the expression of elastin. Interesting to note in the histology image is the presence of significant collagen (blue) in the healthy regions of the myocardium. This is in contrast to the histology shown in the paper where very little collagen was present in the healthy regions. The reason for this additional collagen is unknown, but may be due to cardiac remodeling as result of the infarction and therapy.

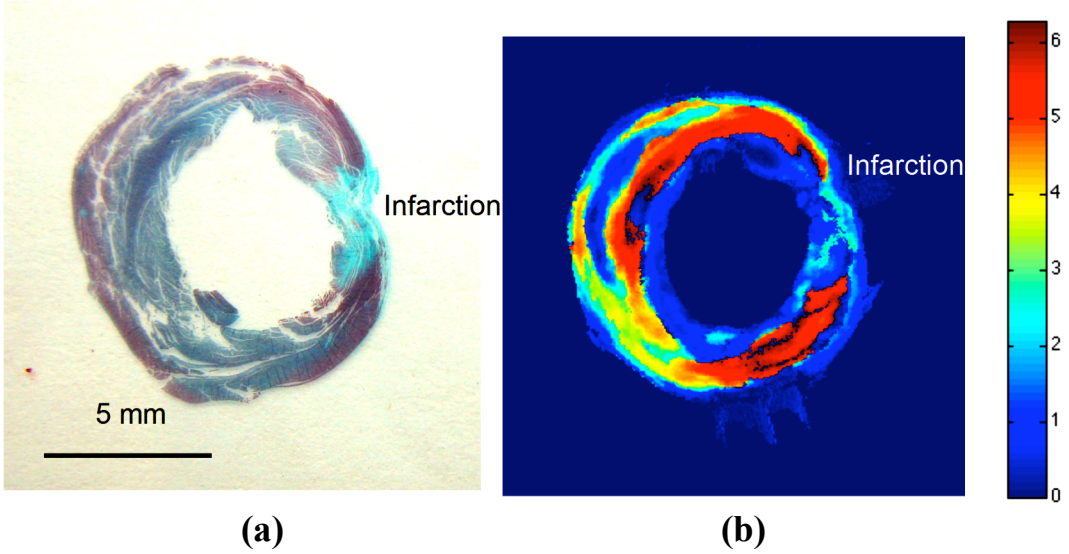



**Fig. 10** Representative retardance image (a) for a stem cell transfected with elastin treated section with corresponding Masson's trichrome (b) stained histology image (collagen in blue, muscle in red). Retardance values are given in radians.

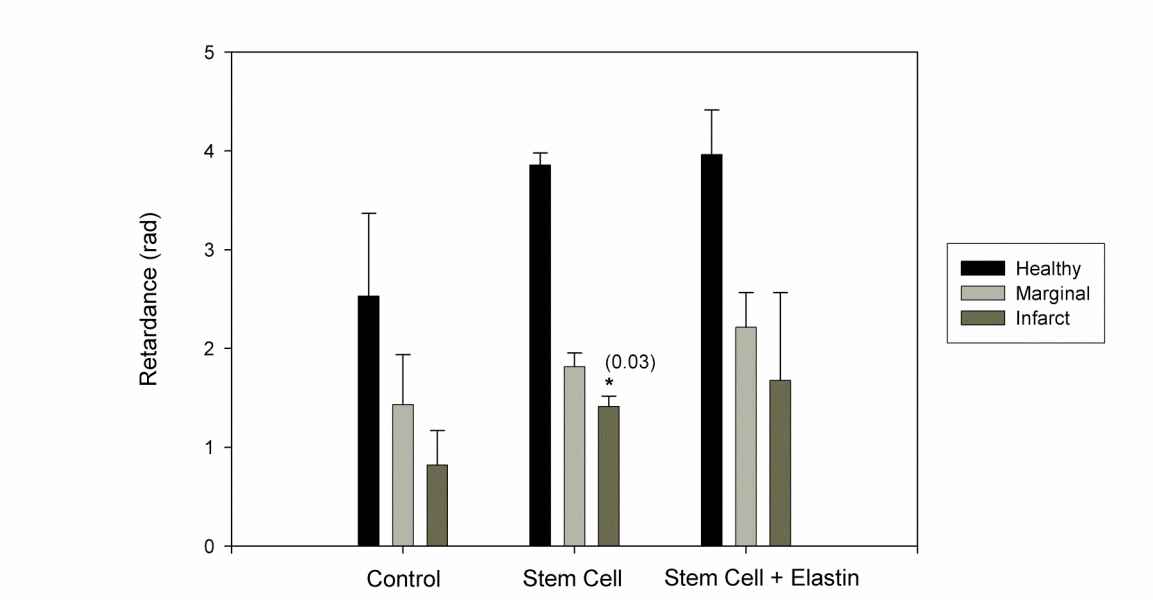



**Fig. 11** Mean ± one standard deviation retardance pixel values from retardance images from health, marginal, and infracted regions. Results are for control (n = 4), stem cell treated (n = 3), and stem cell transfected with elastin treated (n = 4) animals, * denotes statistical significance ($p < 0.05$) with respect to the corresponding control.

A representative SHG and TPEF microscopy image of the regenerating region of a heart section treated with stem cells transfected with elastin is shown below in Fig. 12 courtesy of Marika Wallenburg. When compared to the images in Fig. 7 (On page 76) from the publication in this section, the myocyte and collagen organization and content are similar to those in regenerating myocardium (c), indicating regeneration and reorganization due to treatment. It is difficult to determine if any additional regeneration was present as a result of elastin expression as the field of view for the microscopy images is small compared to the size of the regions of infarction. The hypothesis that the addition of elastin will result in additional regeneration due to increased elasticity is supported by the polarization measurements as a higher retardance is measured. However, as quantitative results from these mircroscopy images are difficult due to a small sampling area, these results do not provide enough information to support the

hypothesis. The similarity of this nonlinear microscopy image to that for other regenerating samples at least verifies that regeneration due to this stem cell treatment results in similar morphological changes, specifically, increase in myocyte content and reorganization/reduction of collagen.

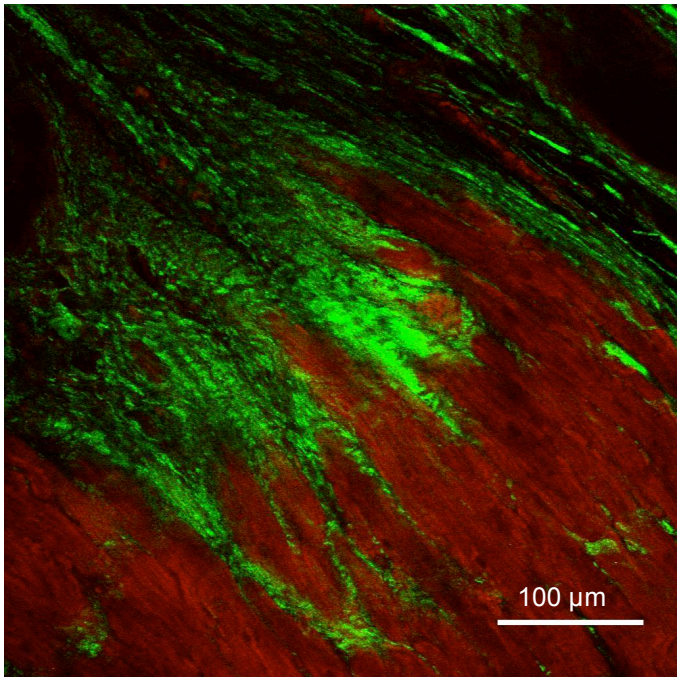



**Fig. 12** Representative nonlinear microscopy image from infarcted regions of myocardial sample treat with stem cells transfected with elastin. The TPEF signal from cardiomyocytes is shown in red pseudo-color and the SHG from collagen is shown in green pseudo-color.

In this study we demonstrated the potential for polarized light in monitoring regenerative treatments of myocardial infarction using both point and imaging systems. In addition, the underlying physiological changes leading to the loss of anisotropy with infarction and re-establishment/perseveration of anisotropy with stem cell treatment were investigated with nonlinear microscopy and conventional histology. While these positive results are motivating future work, several outstanding issues remain that require investigation. The first is the influence of the orientation of birefringence in scattering

media such as myocardium on the measurement of retardance, and the second is the effect of formalin fixation on tissue birefringence. Both these issues will be addressed in the following section. In addition, the measurement and analysis techniques have not been tested in a living system, thus their applicability in vivo is unkown. Accordingly, the final section of this chapter presents an in vivo demonstration of these techniques.

## 3.4 Influence of birefringence orientation and tissue fixation

### 3.4.1 Orientation of birefringence

The measured retardance is a function not only of the magnitude of birefringence, but also of the orientation the birefringent axis makes with respect to the direction of the light's propagation. The effect is concisely described by Eqs. 2 and 4 in the publication portion of Chapter 2, which gives the difference in the refractive index seen by the photon, $\Delta n$, where $\theta$ is the angle between the photon's propagation direction and the orientation of the extraordinary axis. These equations effectively describe that in a birefringent medium, as the angle between the propagation direction and extraordinary axis is reduced from 90 deg to 0 deg, the birefringence seen by the photon is reduced from $n_e - n_o$ to 0. This has impact on the measurement of retardance from myocardial samples as the orientation of muscle and collagen fibers varies spatially in the myocardium, as was described in the publication portion of section 3.3 (page 75). As such, the measured retardance is not always indicative of the magnitude of birefringence, as it is also influenced by the orientation of the extraordinary axis with respect to the light propagation direction. While this issue does not negate the previous results—it is unlikely

that infarction leads to uniform gross fiber reorientation—further research is required for the comprehensive interpretation of results.

To investigate the influence of birefringence orientation in scattering media, a Monte Carlo study—using the upgraded model—simulating the thin myocardial sections used in the previous studies was completed. The model geometry and parameters are summarized in Fig. 13. The sample was specified as an infinite slab 1 mm thick, with optical properties mimicking myocardial tissue[124] (scattering coefficient $\mu_s$ = 160 $cm^{-1}$, absorption coefficient $\mu_a$ = 0.5 $cm^{-1}$, and anisotropy g = 0.9) and birefringence $\Delta n = 1.4 \times 10^{-4}$ (the value estimated from our previous studies). The orientation of the extraordinary axis was varied from the y-axis (0 deg) to the z-axis (90 deg) by an angle $\varphi$ in 15 deg increments (results would be identical if the birefringence orientation was varied from the x-axis to the z-axis). The polarized beam (pencil beam, 632.8nm) was input along the z-axis, thus the orientation of birefringence was varied from being perpendicular to parallel to the direction of the input beam. Photons were collected in a rectangular area of 1 $mm^2$ in direct transmission with an acceptance angle of 20 deg to mimic previous experimental point measurements. Simulations were run with varying states of input polarization in order to construct the sample Mueller matrix (Eq. 4 from the publication portion of section 3.3, page 72), for light passing through the sample in the forward direction from the detection area within 20 deg acceptance angle. From this Mueller matrix the value of retardance was calculated via Mueller matrix decomposition (Eq. 9 from the publication portion of section 3.3, on page 73).

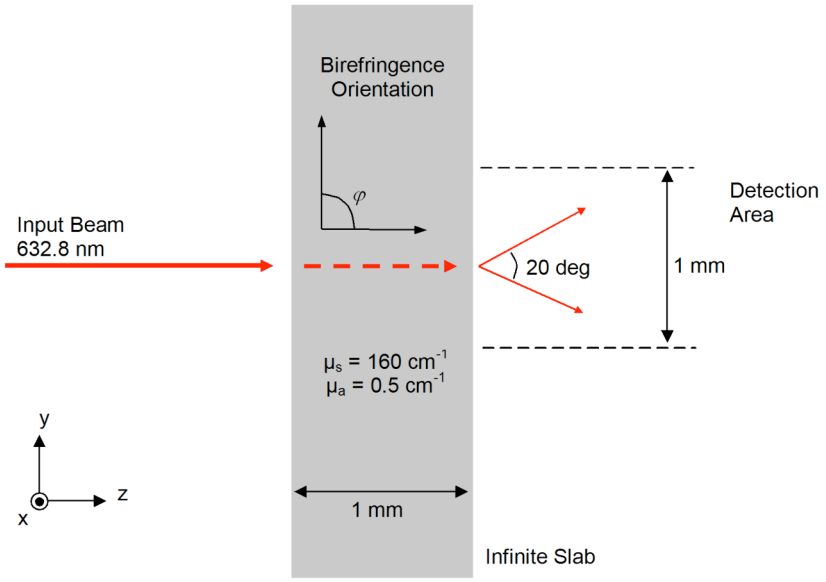



**Fig. 13** Monte Carlo simulation geometry. The medium was defined as an infinite slab in the x-y plane with optical properties mimicking the myocardium. The orientation of birefringence was varied from along the y-axis to the z-axis by angle $\varphi$.

The calculated retardance as a function of extraordinary axis angle $\varphi$ is plotted in Fig. 14 below. As expected, the induced retardance declines (from 1.39 to 2.2 × $10^{-5}$ rad) as the extraordinary axis is varied from being perpendicular to parallel with the input beam. This is due to the lower magnitude of birefringence seen by the majority of the photons as they propagate through the medium. For comparison, an identical simulation was also run with no birefringence ($\Delta n$ = 0) yielding a retardance of 1.57 × $10^{-5}$ rad (birefringence noise floor for these simulations), only slightly less than the value when $\varphi$ = 90 deg. This indicates that when the orientation of the fast axis in along the direction of input light propagation, even in scattering media, the effect of birefringence is nearly negligible in the forward direction.

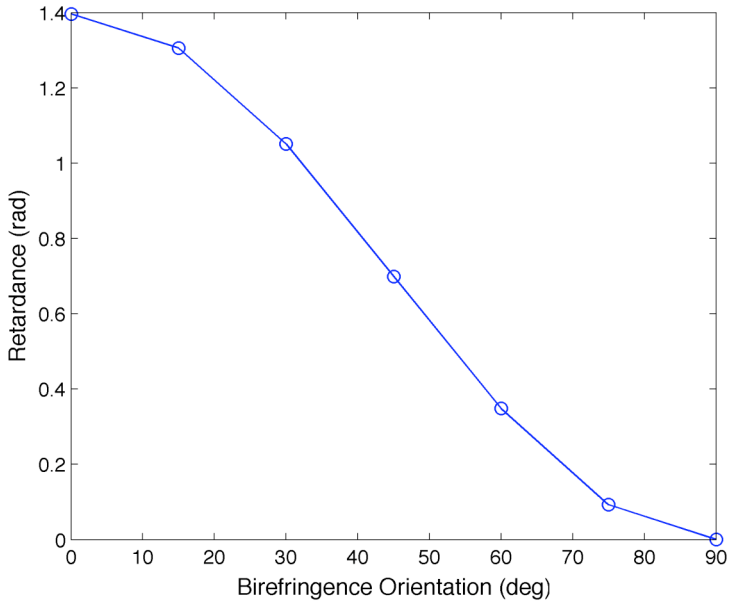



**Fig. 14** Monte Carlo simulated retardance values as a function of birefringence orientation $\varphi$ (0 deg, perpendicular to input beam, 90 deg, parallel to input beam).

Practically, for the interpretation of previous measurements on thin myocardial sections, this confirms our suspicion that low values of measured retardance do not necessarily indicate lower birefringence levels, and could instead simply reflect the orientation of the myocardial structure. This was seen in the previous section where lower values of retardance were measured near the inside and outside walls of myocardium where the myocyte fibers are suspected to be approaching perpendicularity with the input beam.[125] This variation of the retardance through the healthy myocardial wall is likely due to this variation in fiber orientation and presents a challenge to quantifying structural anisotropy based on retardance measurements, as spatial variations may be due to muscle or collagen fiber orientation, not intrinsic variations of birefringence. In spite of this, overall retardance values measured using either the point system or averaged from the retardance images are high when compared to infarcted regions. As well, the retardance

values measured in the infarcted regions do not exhibit this variation through the myocardial wall; in contrast, these values are uniformly low throughout the region. This gives an indication that the low retardance values measured in the infarct are not due to fibers being orientated parallel to the input beam, but rather due to the true intrinsic low tissue anisotropy. This is supported qualitatively by nonlinear microscopy where the structure of the infarcted tissue exhibits less anisotropy than healthy tissue.

To remove this dependence on birefringence orientation, a method to determine 3D orientation of the axis of birefringence was developed—based on aquiring two angularly resolved images—by Marika Wallenburg, a Masters student in our group.[126] In this technique two images are acquired by polarized light transmission through a sample, similar to the imaging approach in the publication portion of section 3.3 (page 72), with the sample rotated by an angle of ~12 deg between each image. For each image, the retardance and apparent direction of birefringence are calculated and, based on the change in sample orientation between the measurements; the intrinsic retardance and 3D orientation of the axis of birefringence are determined. While the applicability of this technique to bulk tissues—where transmission measurements are not possible—is questionable, the technique certainly has utility for *ex vivo* tranmission measurements.

### 3.4.2 Tissue fixation

In order to preserve the tissue used in the previous studies, all samples were fixed in 10% neutral buffered formalin solution. Fixation was additionally required for vibratome sectioning of tissues in order to ensure sufficient rigidity for cutting. However, the effect of fixation on the polarization properties of tissue is largely unknown. Formalin preserves

or fixes tissue by cross-linking amino groups in proteins with surrounding nitrogen atoms in protein or DNA; in addition, formalin is a disinfectant as it kills most bacteria and fungi. As this cross-linking alters the native structure of tissue, the birefringence—as well as other optical properties—may well be modified. Previous studies investigating the use of formalin fixed tissues for OCT studies have shown no change in effects for polarization-sensitive OCT[127] while others employing non-polarization OCT have measured an increase in scattering as well as tissue shrinkage.[128] As the effect of fixation on tissue birefringence is of particular interest, we performed a study to quantify any changes in optical polarization properties.

Fresh pig hearts, acquired from a local butcher, were used as myocardial samples for this study. The samples were immediately cut by hand into thin sections approximately 1 mm thick and 1 × 1 $cm^2$ in area. The thin sections were mounted between a glass side and cover slip, and imaged using the polarization imaging system presented in the publication portion of section 3.3 (page 72). Once imaged, the tissues were fixed in 10% neutral buffered formalin solution. The measurements were then repeated on each fixed tissue section, one day and six days post-fixation. The Mueller matrices were derived for each image pixel, and using polar decomposition the linear retardance and depolarization were calculated. These values were then averaged over the imaged region of tissue.

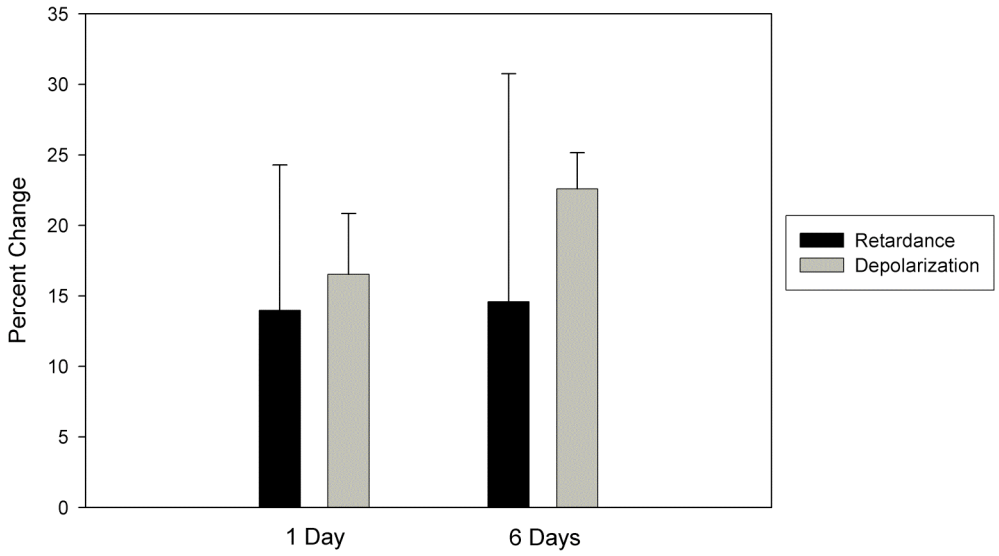



**Fig. 15** Percent change (relative to fresh) of mean linear retardance and depolarization of porcine myocardium 1 day and 6 days post fixation. Error bars are the standard deviation.

Results from measurements on porcine myocardium before and after fixation are shown in Fig. 15 as the percent change one day and six days post fixation. Percent change rather than actual change in retardance are displayed as the thickness of the hand cut tissue sections was variable between samples and making the measured retardance values difficult to compare, as the optical pathlength will vary between samples. Both the retardance and depolarization increase after fixation, by 14% and 17% change respectively, with the retardance remaining relatively constant from one day to six days post fixation, and the depolarization undergoing a further increase up to 23% change. In addition, a mass increase of 3% (most likely due to increased water retention as the tissue were stored in formalin solution) and a volume increase of 4% were also measured after fixation.

The increase in both retardance and depolarization after fixation can in part be accounted for by the increase in volume, resulting in a longer optical pathlength,

however, the volume increase is small (only 4%) compared to increases in measured retardance and depolarization. Assuming isotropic volume expansion, this corresponds to a thickness increase of only ~1.3%. Thus, the increases in retardance and depolarization must be due to underlying changes in the tissue structure.

Previous studies have measured an increase in tissue scattering as a result of fixation, due to the cross-linking of proteins creating a more highly scattering media.[127] We confirmed these optical property measurements on porcine myocardial using an double-integrating-sphere total reflection and transmission measurements and a Monte Carlo generated look-up table.[129] The scattering coefficient measurements showed an increase from 92 $cm^{-1}$ in fresh tissue to 132 $cm^{-1}$ with fixation at 635 nm (the absorption did not change with fixation). This accounts for the increase in depolarization, as increased scattering will lead to more randomization of incoming polarized light. In the case of retardance, the intrinsic birefringence may be increased as a result of protein cross-linking leading to a more anisotropic (more organized) arrangement of heart muscle fibers. This is partially supported by the fact that formalin fixation increases the strength and rigidly of tissue. Additionally, the increase in scattering due to fixation results in a longer optical pathlength, which in turn can result in increased retardance as the photons now travel a longer distance through the tissue (Eq. 8). At present, the cause for the increase in birefringence is unclear; it may be an intrinsic birefringence increase, the effect of additional scattering, or a combination of both. However, with regards to measurements on fixed versus fresh myocardium, we can conclude that the polarization properties are not radically altered by fixation. To our knowledge these are the first measurements investigating the effects of formalin on tissue polarization properties.

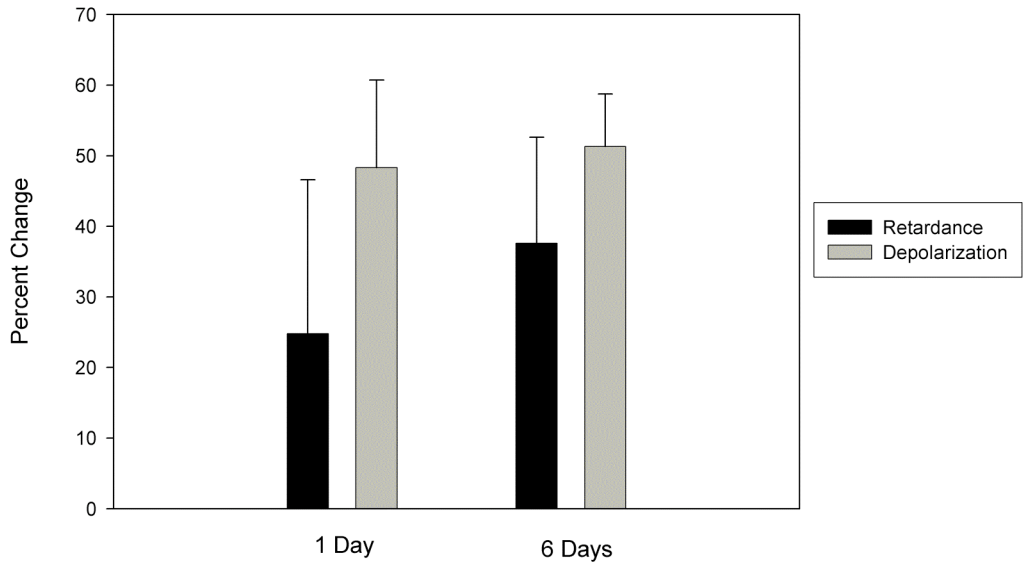



**Fig. 16** Percent change (relative to fresh) of mean linear retardance and depolarization of porcine liver 1 day and 6 days post fixation. Error bars are the standard deviation.

These measurements were repeated on porcine liver as a relatively low birefringent control following the same procedure as previous described. The percent change for birefringence and depolarization for one day and six days post fixation are shown above in Fig. 16. As was the case for the heart, an increase in both retardance and depolarization was measured after fixation, a percent change after one day and six days of 38% and 51% respectively. The increase in retardance for liver is interesting—while the retardance measured from the liver samples was low when compared to the myocardium (an average of 15 deg for liver compared to 200 deg for myocardium), a similar percent increase in retardance was still measured. As was previously discussed for the myocardium, this increase is likely due to the cross-linking of proteins producing a more organized and rigid tissue and/or the increase in tissue scattering as a result of fixation. A much larger increase in depolarization was measured after fixation for liver than for myocardium (23% for myocardium compared to 51% for liver); while this

increase is again likely due to the increase in scattering as a result of fixation, these results do suggest that the effects of formalin fixation maybe unique to the type of tissue.

The results of this study indicate that while the fixation process does alter the tissue birefringence and scattering, the increase, particularly for retardance in porcine myocardium is relatively small (~15% change after six days). With regards to our previous studies involving formalin fixed myocardium, this indicates that the retardance values measured are close to that of non-fixed tissue, and moreover, that the use of formalin likely does not impact the overall trends suggested by the results.

The work was carried out with Nasit Vurgun, a summer student in our laboratory, who conducted the experimental measurements, while I completed all other aspects of this study. This work is currently being prepared for publication as a technical note for Physics in Medicine and Biology.

## 3.5 Proof-of-Principle in vivo characterization of dermal tissue structure

***Introduction***

All tissue studies in the previous sections were conducted on *ex vivo* tissues. Thus, our polarization detection and analysis methodologies have not been tested for use in a living biological system. To correct this, a study was conducted to investigate, first, if our methods of polarimetry measurement and analysis could extract polarization parameters from living tissue, and second, if physiological changes in tissue structure could be measured in living tissue. This investigation was conducted as a proof-of-principle towards performing tissue structural characterization *in vivo*, in particular, for the

application of polarimetry in monitoring tissue regeneration, but with potential for other applications as well.

For this study a dorsal skinfold window chamber mouse model was employed,[130] as this model provides an easily accessible region of relatively optically thin (~500 μm) tissue, through which polarization transmission measurements can be performed. To induce a measurable physiological response, collagenase was injected into a region of the window chamber to denature dermal collagen and thus degrade the tissue extra-cellular matrix. This denaturation of collagen results in tissues structural changes similar to those that occur with myocardial infarction, specifically, a loss of tissue anisotropy. A region in the window chamber distal to the collagenase injection was left untreated as a control. Tissue birefringence and depolarization were measured using the point system before and after treatment with collagenase for both the treatment and control regions. Details on the methods and results are presented in the following publication.

I shared first authorship of this paper with Dr. Nirmalya Ghosh (a post doctoral fellow in our group). We contributed equally in performing the experimental measurements and analysis as well as in manuscript writing. Dr. Eduardo Moriyama implemented the window chamber animal model and assisted with the experimental measurements.

***Paper***

**M. F. G. Wood**, N. Ghosh, E. H. Moriyama, B. C. Wilson, and I. A. Vitkin, "Proof-of-principle demonstration of a Mueller matrix decomposition method for polarized light tissue characterization *in vivo*," *Journal of Biomedical Optics* **14**, 014029 (2009).

Journal of Biomedical Optics 14(1), 014029 (January/February 2009)

# Proof-of-principle demonstration of a Mueller matrix decomposition method for polarized light tissue characterization *in vivo*

**Michael F. G. Wood***
**Nirmalya Ghosh***
**Eduardo H. Moriyama**
**Brian C. Wilson**
Ontario Cancer Institute
Division of Biophysics and Bioimaging
University Health Network
610 University Avenue
Toronto, Ontario M5G 2M9 Canada
and
University of Toronto
Department of Medical Biophysics
610 University Avenue
Toronto, Ontario M5G 2M9 Canada

**I. Alex Vitkin**†
Ontario Cancer Institute
Division of Biophysics and Bioimaging
University Health Network
610 University Avenue
Toronto, Ontario M5G 2M9 Canada
and
University of Toronto
Department of Medical Biophysics and Radiation Oncology
610 University Avenue
Toronto, Ontario M5G 2M9 Canada

**Abstract.** We demonstrate the first *in vivo* use of a Mueller matrix decomposition method for polarization-based characterization of tissue. Collagenase is injected into a region of dermal tissue in a dorsal skin window chamber in a nude mouse to alter the structure of the extracellular matrix. Mueller matrices for polarized light transmitted through the window chamber in the collagenase-treated region, as well as a distal control region, are measured. From the measured matrices, the individual constituent polarization properties of the tissue are extracted through polar matrix decomposition. Large decreases in birefringence and depolarization are seen in the collagenase-treated region due to the destruction of collagen, showing the potential for this method to monitor the organization and structural anisotropy of tissue. This study represents the first *in vivo* demonstration of a Mueller matrix decomposition method for polarimetric tissue characterization.
© *2009 Society of Photo-Optical Instrumentation Engineers.* [DOI: 10.1117/1.3065545]

Keywords: polarized light; collagen; Mueller matrix; tissue characterization; extracellular matrix; window chamber model.

Paper 08287LR received Aug. 15, 2008; revised manuscript received Nov. 19, 2008; accepted for publication Nov. 19, 2008; published online Feb. 4, 2009.

## 1 Introduction

Many tissue constituents, including collagen, muscle fibers, keratin, and glucose, interact with polarized light.[1] Changes in tissue structure, in particular collagen content and organization, are associated with a number of pathologies.[2,3] The ability to extract individual polarization properties from tissues has a number of biomedical applications, including measurements of tissue organization and anisotropy via birefringence, and the changes in these following various treatments, as well as determining concentrations of optical active molecules such as glucose via optical rotation. However, light scattering in the visible-near-infrared wavelength range complicates the extraction of important polarization information in tissue, due to the resulting depolarization and alteration of the incident polarized light. In addition, as several polarizing effects in tissue occur simultaneously, they must be individually decoupled and recovered from the overall measured polarization signals.

To perform quantitative polarimetry in tissue, a method of extracting individual polarization effects in the presence of scattering must be employed. We have previously reported a sensitive polarimetry platform[4] that measures low polarization signals from scattering media, and employs a polar Mueller matrix decomposition method to decouple the combined effects[5] from the experimentally obtained Mueller matrices. Presently, to demonstrate this approach *in vivo*, we report on intravital measurements in a dorsal skin window chamber mouse model, using collagenase to induce changes in tissue structure and anisotropy (birefringence). The skin window chamber model is suitable for birefringence modulation via collagen alterations, as collagens are the main skin component, accounting for ~60% of the dry weight.[6]

## 2 Materials and Methods

The polarization of light is well described through either Jones or Mueller matrix algebra.[7] However, the latter allows for depolarization interactions and so is preferred for tissue polarimetry. In this approach, a four-element Stokes vector $\mathbf{S}$ describes the intensity and polarization of the light beam. The transfer function of the Stokes vector for the light propagation through a medium that alters the polarization state is represented as a $4\times4$ Mueller matrix $\mathbf{M}$. The interaction with any medium is described by $\mathbf{S_o}=\mathbf{MS_i}$, where $\mathbf{S_i}$ and $\mathbf{S_o}$ are the input and output Stokes vectors, respectively.

To measure the polarization effects in optically turbid samples, including tissues, we have developed a sensitive Stokes polarimeter system.[5] Briefly, this employs polarization

*These authors contributed equally to this work.
†Address all correspondence to: I. Alex Vitkin, Ontario Cancer Institute, Division of Biophysics and Bioimaging, 610 University Avenue, Toronto, ON, Canada M5G 2M9. Tel: +1 416 946 2990; E-mail: vitkin@uhnres.utoronto.ca

1083-3668/2009/14(1)/014029/5/$25.00 © 2009 SPIE

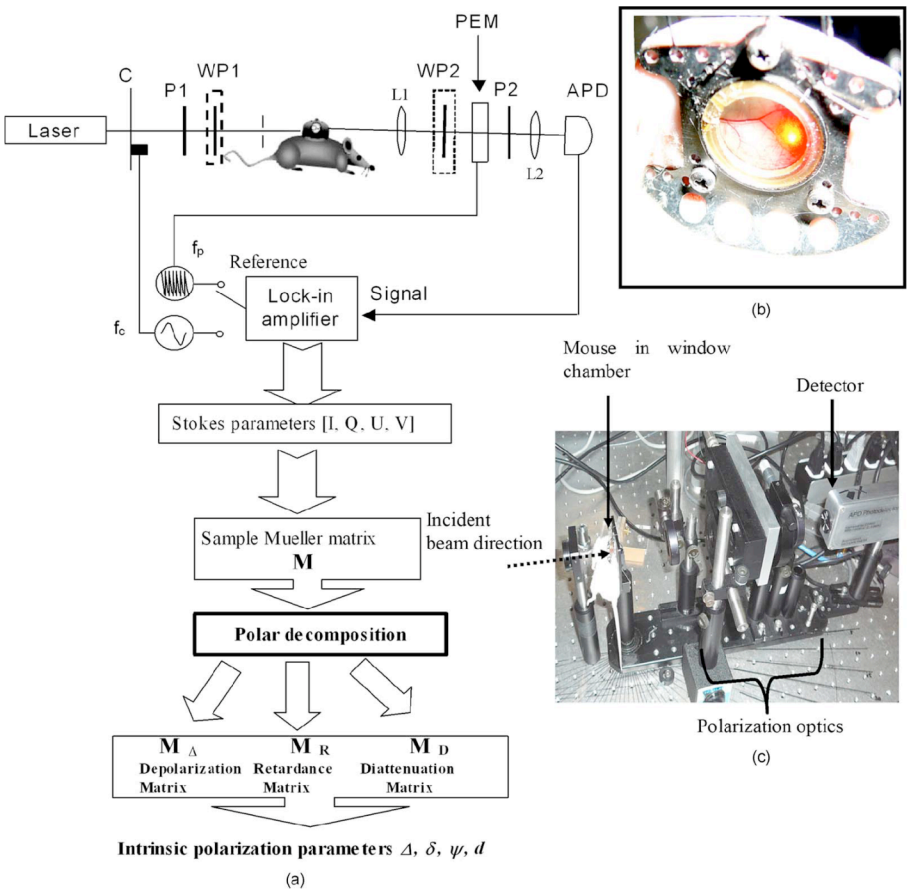



**Fig. 1** (a) Schematic of the measurements system and the polar decomposition method: C, mechanical chopper; P1 and P2, linear polarizers; WP1 and WP2, quarter waveplates; PEM, photoelastic modulator; L1 and L2, lenses; APD, avalanche photodiode; $f_c$ and $f_p$, modulation frequencies of mechanical chopper and PEM, respectively. (b) Photograph of the dorsal skin flap window chamber model in a mouse. Measurements were made in two regions (collagenase treated on the upper right, and control on the lower left) through the window chamber. In this photograph, the beam is incident in the treatment region showing the approximate region of measurement. Also note the increase in blood content in the treated region. (c) Photograph of the experimental system, showing the mouse with its implanted window chamber in the path of the interrogating beam.

modulation using a photoelastic modulator (IS-90, Hinds Instruments Hillsboro, Oregon) and synchronous lock-in detection (SR830, Stanford Research Systems, Sunnyvale, California), allowing sensitive low-noise measurements of the Stokes vector of the light interacting with a turbid sample. By cycling the polarization of the incident beam (HeNe laser, 15 mW, $\lambda = 632.8$ nm) using a linear polarizer and quarter-wave-plate combination, and measuring the output Stokes vectors, the Mueller matrix of the sample can be constructed.[5] A schematic of the experimental system is shown in Fig. 1.

However, in a complex medium such as biological tissues, several polarization-altering effects occur simultaneously, and the resultant measured Mueller matrix reflects these in a coupled complicated manner. Thus, a method to extract the individual effects is required to quantify contributions of individual polarization effects, such as birefringence, optical activity, and depolarization. To accomplish this, we have developed a polar decomposition method suitable for use in highly scattering samples,[5] where the measured matrix $\mathbf{M}$ is decomposed into "basis" matrices representing the individual effects. In this approach, a depolarization matrix $\mathbf{M}_\Delta$, a retardance matrix $\mathbf{M_R}$, and a diattenuation matrix $\mathbf{M_D}$ are employed, with $\mathbf{M}=\mathbf{M}_\Delta\mathbf{M_R}\mathbf{M_D}$.[8] From these decomposed matrices, useful polarization properties of interest can be decoupled and calculated. Specifically, the elements of $\mathbf{M}_\Delta$ can be used to calculate the net depolarization coefficient ($\Delta$), the elements of $\mathbf{M_R}$ can be used to calculate the linear retardance (birefringence $\delta$) and optical activity ($\psi$), and the elements of $\mathbf{M_D}$ can be used to calculate the diattenuation ($d$).[5,8] This decomposition process is summarized in Fig. 1.

We have previously validated this method theoretically with a polarization-sensitive Monte Carlo model and experimentally using tissue-simulating phantoms,[5] and performed measurements on *ex vivo* tissue samples.[9] To demonstrate its first use *in vivo*, we presently report measured changes in tissue structure using a dorsal skinfold window chamber mouse model.[10] In this model, the inner skin layer of an athy-

mic nude mouse (NCRNU-M, Taconic, Hudson, New York) was removed from a 10-mm-diam region on the dorsal surface and a titanium saddle was sutured in place to hold the skin flap vertically, as shown in Fig. 1. A protective glass coverslip ($145 \pm 15$ $\mu$m thick) was placed over the exposed tissue plane. Thus, a thin layer of tissue ($\sim 500$ $\mu$m) extends away from the animal, allowing for direct optical transmission measurements of polarized light through this layer, as shown in Fig. 1. This model enables accurate measurements in an *in vivo* setting, free of many of the challenges inherent in using fully 3-D tissue structures.

To induce changes in this skin preparation, 5 $\mu$l of collagenase (gelatinase) solution (Sigma-Aldrich, collagenase from *Clostridium histolyticum*) at a concentration of 1 mg ml$^{-1}$ was microinjected into one region of the tissue. Collagenase cleaves collagen fibers by breaking the peptide bonds connecting the monomer peptide units.[11] Since collagen fibers are one of the primary sources of tissue birefringence and scattering, their destruction should change the polarization of the light propagating through this treated tissue region. Measurements of **M** were performed both in the region of collagenase injection and a distant control region, as shown in Fig. 1. Measurements were made with a 1-mm-diam laser beam before collagenase treatment and for 5 h postinjection at 30-min intervals, with an additional measurement at 24 h. An ink circle with a diameter of approximately 2 mm was marked around the control and treated regions so that the measurements could be repeated and correlated with subsequent histology. The treatment and measurements were carried out under general anesthesia induced by intraperitoneal injection of ketamine/xylazene (80- and 5-mg Kg$^{-1}$, respectively). Before each measurement, the animal was reanesthetized. Values for birefringence, depolarization, optical activity, and diattenuation were extracted from the experimentally derived Mueller matrices at each time point, through the prior polar decomposition approach. On completion of the measurements (24-h postcollagenase injection), the animal was sacrificed and the control and treated tissues were removed, sectioned laterally, and stained with hematoxylin and eosin (HE) for histological examination.

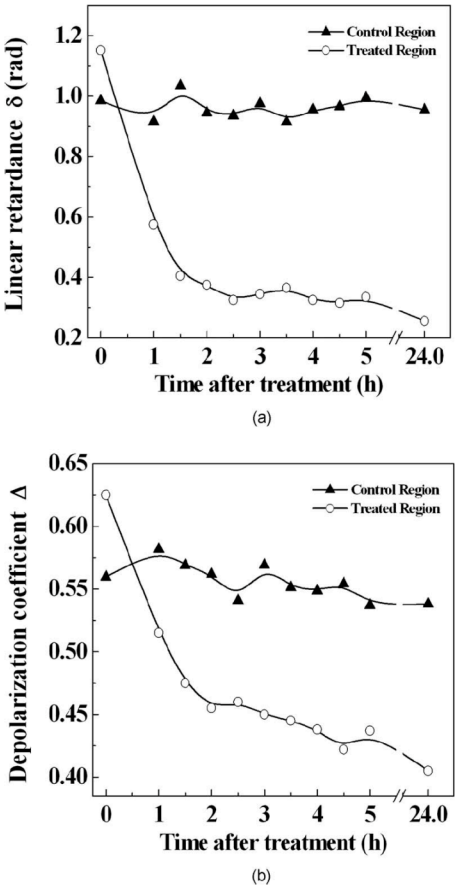



**Fig. 2** (a) Birefringence and (b) depolarization before and as a function of time after collagenase injection in the treated and control regions. Symbols are experimentally derived values.

## 3 Results and Discussion

The derived birefringence and net depolarization values in both collagenase-treated and control regions are shown in Fig. 2. Values for optical activity and diattenuation were also extracted; however, these did not change appreciably with treatment and so the data are not shown. Histology (HE stain) of treated and control regions are shown in Fig. 3. As expected, injection of collagenase induced structural changes in the skin, seen as a loss of collagen fibers and the presence of inflammation and vasodilatation, which resulted in a more irregular dermis structure compared to the control tissue (Fig. 3).

In Fig. 2(a), the calculated values of the birefringence $\delta$ in treated and control regions are plotted as a function of time following collagenase injection, the former showing a range from $\delta \approx 1.2$ rad to $\delta \approx 0.3$ rad, in contrast to the control region where the values remain essentially constant at $\delta \approx 1$ rad. (The small fluctuations in the control-tissue values give some indication of the reproducibility of the measurements over time.) The decrease in birefringence is likely due to denaturation of the collagen fibers, which reduces the structural anisotropy. This is confirmed by histology, where a reduction in collagen fibers is evident in the treatment region (Fig. 3).

Using the approximate light pathlength $l \approx 500$ $\mu$m (estimated here as the thickness of the tissue), the intrinsic birefringence $\Delta n$ (difference in directional refractive indices) can be estimated as $\Delta n = \delta\lambda / 2\pi l$, where $\lambda$ is the wavelength of the light (632.8 nm). Although the optical path length will be longer than the tissue thickness $l$ due to scattering,[12] the polarization preserving light, which we are measuring, will have a shorter path length than the overall path length. Using this relationship, the birefringence values in the treatment region prior to treatment and in the control region were calculated as $\Delta n \approx 2.4 \times 10^{-4}$ and $\Delta n \approx 2 \times 10^{-4}$, respectively. After treatment, the value decreased to $\Delta n \approx 0.6 \times 10^{-4}$. These birefringence levels compare reasonably well with those found in the literature for tissue birefringence; typical values are in the range of $1 \times 10^{-3}$.[13]

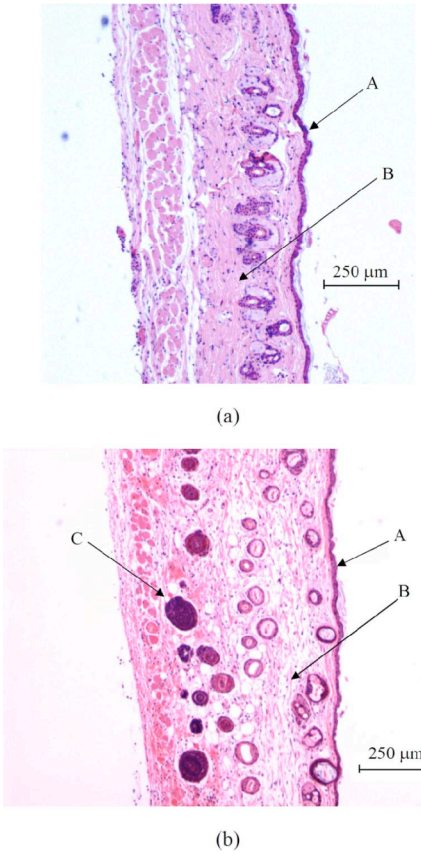



**Fig. 3** Histology (hematoxylin and eosin stain) for (a) control and (b) treated tissue sections, showing skin surface A and collagen fibers in the dermis B. In the collagenase-treated region in (b), reduction in dermal collagen fibers is evident, as is the presence of blood vessels with increased diameter C as a result of inflammatory response. The sectioning was done laterally through the skin flap. The external surface of the skin is on the right and the internal surface in contact with the glass coverslip is on the left.

A decrease in the net depolarization coefficient $\Delta$ after treatment, from ~0.63 to ~0.45, was measured in the treated region and is plotted together with the values in the control region in Fig. 2(b), the latter again being essentially constant. This reduction in depolarization is also due to the destruction of the collagen fibers, since these represent one of the primary scattering structures in tissue. As with changes in birefringence, this is also confirmed by histology: see Fig. 3(b).

Using these changes in the depolarizing properties of the tissue, we were able to approximate the scattering coefficient of the tissue using our polarization-sensitive Monte Carlo simulation platform.[12] Simulations were run with a 500-$\mu$m-thick slab geometry, where the absorption coefficient ($\mu_a$), scattering anisotropy ($g$), and birefringence were held constant at $\mu_a = 2.2\ \text{cm}^{-1}$, $g = 0.9$, and $\Delta n = 4 \times 10^{-4}$ for control/pretreatment, while $\Delta n$ was set to $1 \times 10^{-4}$ for post-treatment (optical properties estimated for skin). The scattering coefficient was varied from $\mu_s = 100$ to $250\ \text{cm}^{-1}$ in the simulations. Monte-Carlo-generated net depolarization values for those photons exiting the sample in the forward direction were calculated, from which the scattering coefficients corresponding to $\Delta = 0.63$ and $\Delta = 0.45$ were selected. Using this approach, $\mu_s$ was estimated as $182\ \text{cm}^{-1}$ for the pretreatment tissue and as $134\ \text{cm}^{-1}$ for the post-treatment tissue.

These results show the ability of the method to quantify changes in tissue structure using polarized light *in vivo*. The destruction of the collagen fibers in the extracellular matrix results in reduced tissue anisotropy and a reduction in scattering effects. These changes produce reduced tissue birefringence and depolarization, respectively, as measured via the experimental Mueller matrix, individually extracted through the polar decomposition method, and further quantified via polarization-sensitive Monte Carlo simulations. An important point to note is that, as seen in the upper-right photograph in Fig. 1, the treated region has markedly increased blood content compared to the control tissue, which would result in marked increase in the tissue absorption. Despite this, the Muller matrix decomposition technique is able to yield the underlying polarization parameters.

## 4 Conclusions

These results present the first *in vivo* demonstration of Mueller matrix decomposition-based polarimetric characterization of tissues. The interpretation of measured changes in values for birefringence and depolarization is consistent with histology results, and shows promise for the method's ability to accurately quantify biologically relevant tissue parameters such as scattering and birefringence. This initial proof-of-principle study is being followed up by more extensive investigations of the use of this method *in vivo*, both for noninvasive measurements of glucose and for monitoring the response of infarcted myocardial tissues to stem-cell therapies. These studies will investigate whether similar measurements can be made in reflection geometries on bulk tissues, considering the additional complicating factors present with such geometries (such as sampling volume calculations and the effect of additional tissue layers). Clearly, there are many other potential applications, both in tissue diagnostics and in treatment response monitoring.

### References

1. L. V. Wang, G. L. Coté, and S. L. Jacques, "Special section on tissue polarimetry," *J. Biomed. Opt.* **7**, 278 (2002).
2. J. A. Pearce and S. Thomsen, "Thermal damage process in myocardium," *IEEE Eng. Med. Biol. Mag.* **20**, 256–258 (1998).
3. K. Schoenenberger, B. W. Colston, Jr., D. J. Maitland, L. B. Da Silva, and M. J. Everett, "Mapping of birefringence and thermal damage in tissue by use of polarization-sensitive optical coherence tomography," *Appl. Opt.* **37**, 6026–6036 (1998).
4. X. Guo, M. F. G. Wood, and I. A. Vitkin, "Angular measurement of light scattered by turbid chiral media using linear Stokes polarimetry," *J. Biomed. Opt.* **11**, 041105 (2006).
5. N. Ghosh, M. F. G. Wood, and I. A. Vitkin, "Simultaneous determination of linear retardance and optical rotation in birefringent, chiral, turbid medium using Mueller matrix polarimetry: combined Monte Carlo and experimental methodology," *J. Biomed. Opt.* **13**, 044036 (2008).
6. C. R. Lovell, K. A. Smolenski, V. C. Duance, N. D. Light, S. Young, and M. Dyson, "Type I and III collagen content and fibre distribution in normal human skin during ageing," *Br. J. Dermatol.* **117**, 419–428 (1987).

7. D. Goldstein, *Polarized Light*, Marcel Dekker, Inc., New York (2003).
8. S. Y. Lu and A. Chipman, "Interpretation of Mueller matrices based on polar decomposition," *J. Opt. Soc. Am. A* **13**, 1106–1113 (1996).
9. N. Ghosh, M. F. G. Wood, S. H. Li, R. D. Weisel, B. C. Wilson, R. K. Li, and I. A. Vitkin, "Mueller matrix decomposition for polarized light assessment of complex media such as biological tissues," *J. Biophotonics* (in press).
10. M. Khurana, E. H. Moriyama, A. Mariampillai, and B. C. Wilson, "Intravital high-resolution optical imaging of individual vessel response to photodynamic treatment," *J. Biomed. Opt.* **13**(4), 040502 (2008).
11. J. L. Seltzer, A. Z. Eisen, E. A. Bauer, N. P. Morris, R. W. Glanville, and R. E. Burgeson, "Cleavage of type VII collagen by interstitial collagenase and type IV collagenase (gelatinase) derived from human skin," *J. Biol. Chem.* **264**, 3822–3826 (1989).
12. M. F. G. Wood, X. Guo, and I. A. Vitkin, "Polarized light propagation in multiply scattering media exhibiting both linear birefringence and optical activity: Monte Carlo model and experimental methodology," *J. Biomed. Opt.* **12**, 014029 (2007).
13. W. Wang and L. V. Wang, "Propagation of polarized light in birefringent media: A Monte Carlo study," *J. Biomed. Opt.* **7**, 350–358 (2002).

***Addendum***

In this study we demonstrated the use of our previously developed polarization measurement and analysis methods *in vivo*. A window chamber mouse model was employed, with collagenase injected into a region to induce a physiological change. The denaturation of collagen in the region of collagenase injection resulted in a large decrease in measured retardance as well as a decrease in depolarization. The ability of our methods to measure these changes demonstrates the potential to monitor physiological changes *in vivo*, and provide additional motivation for developing methods to assess myocardial structure *in vivo*.

# 4. Modeling-based polarized light tissue analyte concentration determination

The following chapter describes two studies conducted to investigate the feasibility of employing polarized light for tissue analyte concentration determination using optical activity. In the first study, a combined spectral polarization and intensity approach was developed and tested using simulated data. The second study, the ability to separate chirality and scattering induced optical rotation using Mueller matrix decomposition was determined, again using simulated data. This work was motivated by the need for noninvasive glucose concentration measurement; however, the techniques developed could be applied for measurements of other optically active analytes.

## 4.1 Combined polarization and intensity approach

***Introduction***

NIR spectroscopy is currently one of the most promising optical approaches for noninvasive glucose monitoring. However, as with other techniques it suffers in a lack of specificity (many other tissue constituents also absorb NIR light) and sensitivity (the amount of absorption due to glucose is relatively small as its concentration is low compared to other tissue analytes). Thus, improvements in the technique or novel approaches are needed in order to reach the required accuracy for clinical use. We have hypothesized that combining NIR spectroscopy with polarization spectroscopy may improve the ability to determine glucose concentrations, as they provide complementary information—a measure of two different properties of the glucose molecule. To

investigate the potential of such a combined approach, a simulation study was conducted using the extended Monte Carlo model and employing multi-block chemometric techniques.

A blood plasma model consisting of glucose and plasma proteins in water at physiological concentrations was simulated for testing of the combined method. Intensity and polarization spectra were generated from this model for both clear and scattering media. As both the absorption and polarization signals are due not only to glucose, but also to tissue constituents (in this case, proteins and water), a method to extract the glucose specific signal was required. In this case, where both optically activity and NIR absorption are both exploited, the simulated data must also be combined in a meaningful way to improve the predictive ability. To do this, multi-block chemometric techniques were used to, first, to combine the simulated intensity and polarization spectra, and second, to build a regression model to predict the glucose concentration. Details and results of this study are provided in the following publication.

With regards to the publication contributions, I designed and conducted all simulations and data analysis in the study and wrote the manuscript. Dr. Daniel Côté assisted with Monte Carlo software.

***Paper***

**M. F. G. Wood**, D. Côté, and I. A. Vitkin, "Concentration determination in simulated optically clear and turbid biological media," *Journal of Biomedical Optics* **13**, 044037 (2008).

Journal of Biomedical Optics 13(4), 044037 (July/August 2008)

# Combined optical intensity and polarization methodology for analyte concentration determination in simulated optically clear and turbid biological media

**Michael F. G. Wood**
Ontario Cancer Institute
Division of Biophysics and Bioimaging
University Health Network
and
University of Toronto
Department of Medical Biophysics
610 University Avenue
Toronto, Ontario, Canada M5G 2M9

**Daniel Côté**
Université Laval
Departement de Physique
Centre de Recherche Université Laval Robert Giffard
2601 Ch. de la Canardiere, F-6500
Québec, Quebec, Canada, G1J 2G3

**I. Alex Vitkin**
Ontario Cancer Institute
Division of Biophysics and Bioimaging
University Health Network
and
University of Toronto
Departments of Medical Biophysics and Radiation Oncology
610 University Avenue
Toronto, Ontario, Canada M5G 2M9

**Abstract.** The use of a combined spectral intensity and polarization signals optically scattered by tissue to determine analyte concentration in optically clear and turbid biological media was explored in a simulation study. Blood plasma was chosen as the biological model and glucose as the analyte of interest. The absorption spectrum and optical rotatory dispersion were modeled using experimental data and the Drude's equation, respectively, between 500 and 2000 nm. A polarization-sensitive Monte Carlo light-propagation model was used to simulate scattering media. Unfold partial least squares and multiblock partial least squares were used as regression methods to combine the spectral intensity and polarization signals, and to predict glucose concentrations in both clear and scattering models. The results show that the combined approaches produce better predictive results in both clear and scattering media than conventional partial least squares analysis, which uses intensity or polarization spectra independently. This improvement was somewhat diminished with the addition of scattering to the model, since the polarization signals were reduced due to multiple scattering. These findings demonstrate promise for the combined approach in clear or moderately scattering biological media; however, the method's applicability to highly scattering tissues is yet to be determined. The methodology also requires experimental validation. © *2008 Society of Photo-Optical Instrumentation Engineers.* [DOI: 10.1117/1.2968198]

Keywords: polarized light; optical activity; optical absorption; blood plasma; Monte Carlo simulations; partial least squares regression; multiblock chemometrics; noninvasive glucose monitoring.

Paper 07422R received Oct. 11, 2007; revised manuscript received Mar. 18, 2008; accepted for publication Mar. 31, 2008; published online Aug. 11, 2008.

## 1 Introduction

Diabetes mellitus is a chronic systemic disease with no known cure in which the body either fails to produce, or fails to properly respond to, the glucose regulator hormone insulin. Estimates put the number of diabetics in North America at 15 million and the number worldwide at over 100 million, with these numbers expected to rise dramatically over the next 30 years.[1] The primary goal of diabetes therapy is to maintain normal blood glucose homeostasis through diet, exercise, medication, or insulin injections. Accordingly, frequent monitoring of blood glucose levels is of paramount importance in guiding these therapies. Conventional "finger-prick" methods have low compliance due to their invasive nature, and as a result, many diabetics do not monitor their blood glucose levels as frequently as needed to obtain the medical care that could avoid long-term complications of the disease. A noninvasive method for glucose monitoring would greatly aid in increasing the frequency of monitoring and lead to a decrease in the complications associated with diabetes.

Due to this tremendous need for a less invasive method of blood glucose monitoring, a significant amount of research in a variety of fields has focused on developing such a method. Apart from diabetes, there is also a need for more frequent or continuous monitoring of preterm infants and other at-risk infants as well as people with rare metabolic disorders.[2] Among the many approaches being investigated, research is underway to develop optical methods for noninvasive monitoring, including infrared spectroscopy,[3,4] optical coherence tomography (OCT)[5], photoacoustic techniques,[6,7] Raman spectroscopy,[8] fluorescence techniques,[9] and polarimetry.[10–12] While some of these techniques are approaching acceptable levels of accuracy *in vivo*, none have been approved for clinical use; therefore, improvements in these modalities, combin-

Address all correspondence to: Michael F. G. Wood, Ontario Cancer Institute, Division of Biophysics and Bioimaging, 610 University Avenue, Toronto, ON, Canada M5G 2M9; Tel:+1 416 946 4501; Fax:+1 416 946 6529; E-mail: mwood@uhnres.utoronto.ca.

1083-3668/2008/13(4)/044037/9/$25.00 © 2008 SPIE

ing these modalities, or other modalities are needed.

Nearly all of the techniques in development measure a signal due not only to glucose but also to many other biological constituents. As a result, the techniques suffer in their specificity to glucose. In addition, the techniques lack sensitivity because the signal due to glucose is generally much smaller than that due to other constituents. In this work, we propose a combined modality optical approach to determine glucose concentration in biological media. Specifically, combining near-infrared (NIR) spectroscopy signals, arguably the most promising optical method, with spectral polarization information lends itself well to a hybrid approach, because simultaneous measurements can be made with a single polarization-sensitive optical system.[13] This combination exploits three optical effects of glucose: its NIR absorption spectrum, its optical rotatory dispersion (ORD, also known as optical activity), and its refractive index matching effect.[14] For the simulation study described in this paper, only the first two effects were explored, NIR absorption and ORD, since these are specific to glucose. The refractive index matching effect is the change in the refractive index of the media with changes in constituent concentrations and is not specific to a single analyte.[14] However, this effect may add further sensitivity and will be investigated in future work. Although glucose was used as the constituent of interest for this study, the technique is applicable for other absorbing and optically active constituents and may well have application to other biological and nonbiological systems [e.g., detection of optically active drugs, remote sensing of planetary (chiral) atmospheres].

To test the combination of NIR and ORD spectroscopy for concentration determination, a model of blood plasma containing glucose and plasma proteins was used to generate intensity and polarization spectra in both clear and scattering media. As with nearly all of the developing optical techniques, this requires extraction of the signal specific to glucose from a signal also influenced by many confounding factors (plasma proteins and water in this case). The field of chemometrics[15] provides a number of well-developed techniques for analyzing measurements of complex chemical systems to yield constituent concentrations or other properties of interest. Most of these techniques regress one block of data, such as a set of NIR absorption spectra, to a single sample property of the sample, such as glucose concentrations, to build a predictive model. In our case, we wish to regress two blocks of data (NIR intensity and ORD polarization spectra) to improve the predictive abilities of the model. This requires the use of multiblock chemometrics to combine two or more of the data sets into a single predictive model.

The outline of this paper is as follows. First, the blood plasma model used in this study to generate the intensity and polarization signals as a function of wavelength is described. Both a clear and a scattering model were employed in this study to investigate our approach under these two conditions of increasing biological relevance. Second, the chemometric techniques used for concentration predictions are briefly reviewed, and the procedure for building and testing the predictive regression model is described. Third, the results of the predictions are presented for both the clear and scattering model, and the findings and their implications are discussed.

**Table 1** Mean and standard deviation of blood plasma component concentrations (g/100 ml). The standard deviation of fibrinogen was estimated based on standard deviations of albumin and globulin.

| Analyte | Mean | Standard Deviation |
|---|---|---|
| Albumin | 4.2 | 0.54 |
| Globulin | 2.8 | 0.47 |
| Fibrinogen | 0.3 | 0.045 |
| Glucose | 0.18 | 0.113 |

## 2 Blood Plasma Model

To investigate the abilities of a combined intensity and polarization method to predict analyte concentrations, a simulated blood plasma model was employed as a biological model. The model was implemented using MATLAB 7 (The MathWorks, Inc). Blood plasma is the liquid components of blood with the blood cells removed, the primary constituents being the proteins albumin, globulins, and fibrinogen as well as glucose. Other constituents of blood plasma such as cholesterol and urea were omitted in this model, because they exist in lower levels.[16] As noted above, due to the considerable interest in noninvasive glucose monitoring, glucose was chosen as the analyte of interest for this study. The mean and standard deviation of the concentrations of plasma components, in units of g/100 ml, from a group containing both healthy and diabetic individuals are shown in Table 1.[16] Concentrations of the plasma components were randomly generated in this model using these means and standard deviations and assuming a normal distribution. The wavelength range of 500 to 2000 nm was chosen for this study because it is the most frequently employed spectral window, due to relatively low hemoglobin absorption, and includes the effects of both absorption and optical activity. The following sections describe the methods used to create the clear and scattering blood plasma models.

### 2.1 *Absorption and Optical Rotatory Dispersion*

The effects of absorption due to water, plasma proteins, and glucose in the visible and NIR were modeled using experimental data from a number of reports.[17–20] Since data for individual plasma protein absorption dispersion could not be found, the representative plasma total protein (albumin, globulin, and fibrinogen) absorption was used. Figure 1 shows the absorption coefficients $\mu_a(\lambda)$ per concentration of analyte ($cm^{-1}\,g^{-1}$ dl), given as a function of wavelength for water, total protein, and glucose. To calculate the absorption due to water, the mass displacement caused by the addition of the proteins and glucose was calculated and subtracted from the mass of the initial water. This corrected mass of water was then used to calculate the absorption due to water using the data in Fig. 1. The absorption due to the total protein and glucose was calculated simply by using the mass of each constituent and the appropriate data from Fig. 1. The total absorption coefficient was then calculated as the sum of the absorption coefficients due to each component.

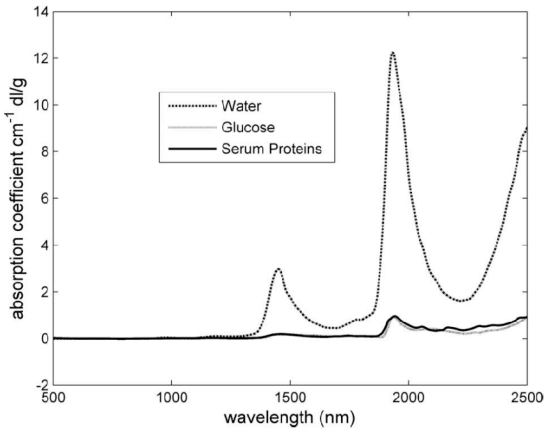



**Fig. 1** Absorption spectra of blood plasma proteins and glucose in the visible and NIR.

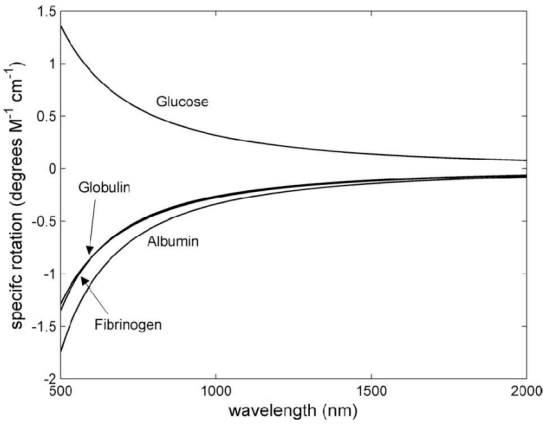



**Fig. 2** Optical rotatory dispersion of blood plasma proteins and glucose as given by Drude's equation in the visible and NIR.

The effects of optical activity due to proteins and glucose in the visible and NIR were modeled using Drude's equation,

$$[\alpha]_\lambda = \frac{A}{\lambda^2 - \lambda_c^2}, \tag{1}$$

where $[\alpha]_\lambda$ is the specific rotation of the molecule in units of rotation per concentration and pathlength (deg ml g$^{-1}$ dm$^{-1}$) at the wavelength $\lambda$, $A$ is a constant specific to the molecule, and $\lambda_c$ is the center wavelength.[21] The parameters of Drude's equation for the plasma proteins[21] and glucose[22] are given in Table 2 and plotted in Fig. 2. The resulting rotation in degrees is calculated as

$$\alpha(\lambda) = \frac{[\alpha]_\lambda C l}{100}, \tag{2}$$

where $C$ is the concentration of the molecule in g/100 ml, and $l$ is the optical pathlength in dm (dm=0.1 m). The total rotation due to all components in plasma was calculated as the sum of the rotations due to each component.

Given the concentrations of the plasma components, the absorption and optical rotation signals as a function of wavelength, $\mu_a(\lambda)$ and $\alpha(\lambda)$, can be calculated using the data in Fig. 1 and Eq. (2), respectively. The full polarization state of the light before and after passing through the plasma sample can be described with a four-element Stokes vector $\mathbf{S}$.[23] The first element $I$ represents the intensity of the light beam, the second element $Q$ represents the linear polarization at 0 and 90 deg, the third element $U$ represents the linear polarization at 45 and 135 deg, and the fourth element $V$ represents the circular polarization. Polarization effects are applied to the Stokes vector using a 4×4 Mueller matrix $\mathbf{M}$. Given the input state of polarization $\mathbf{S}_\mathrm{i}$, the output state $\mathbf{S}_\mathrm{o}$ after passing through the clear sample is calculated as

$$\mathbf{S}_\mathrm{o} = \mathbf{M}_\mathrm{a}\mathbf{M}_\mathrm{r}\mathbf{S}_\mathrm{i}, \tag{3}$$

$$\begin{bmatrix} I_o(\lambda) \\ Q_o(\lambda) \\ U_o(\lambda) \\ V_o(\lambda) \end{bmatrix} = \begin{bmatrix} e^{-\mu_a(\lambda)l} & 0 & 0 & 0 \\ 0 & e^{-\mu_a(\lambda)l} & 0 & 0 \\ 0 & 0 & e^{-\mu_a(\lambda)l} & 0 \\ 0 & 0 & 0 & e^{-\mu_a(\lambda)l} \end{bmatrix} \times \begin{bmatrix} 1 & 0 & 0 & 0 \\ 0 & \cos(2\alpha(\lambda)) & \sin(2\alpha(\lambda)) & 0 \\ 0 & -\sin(2\alpha(\lambda)) & \cos(2\alpha(\lambda)) & 0 \\ 0 & 0 & 0 & 1 \end{bmatrix} \times \begin{bmatrix} I_i(\lambda) \\ Q_i(\lambda) \\ U_i(\lambda) \\ V_i(\lambda) \end{bmatrix}, \tag{4}$$

where the first matrix $\mathbf{M}_\mathrm{a}$ applies the effect of absorption by reducing the intensity of the beam, and the second matrix $\mathbf{M}_\mathrm{r}$ applies the effect of optical activity by rotating the plane of linear polarization of the input beam. The order of these matrix multiplications is not important, since $\mathbf{M}_\mathrm{a}$ is symmetrical about its diagonal. Equation (4) is valid only for optically clear media; the presence of multiple scattering necessitates the use of scattering models such as the Monte Carlo method described below.

Six wavelength-dependent signals were available to build the regression model (refer to Sec. 3) and predict the glucose concentrations in clear (nonscattering) media [$\mu_a(\lambda)$ and $\alpha(\lambda)$

**Table 2** Parameters of Drude's equation for plasma proteins and glucose.

| Analyte | $A$ | $\lambda_c$ |
|---|---|---|
| Albumin | $-1.75\times10^7$ | 264 |
| Globulin | $-1.48\times10^7$ | 211 |
| Fibrinogen | $-1.37\times10^7$ | 260 |
| Glucose | $1.72\times10^7$ | 150 |

calculated based on the constituent concentrations, and the Stokes parameters $I_o(\lambda)$, $Q_o(\lambda)$, $U_o(\lambda)$, and $V_o(\lambda)$ calculated using Eq. (4) based on the input polarization]. In an experimental situation, the measurements of the Stokes parameters would be made and $\mu_a(\lambda)$ and $\alpha(\lambda)$ would be calculated based on measured Stokes parameters. Using the described methods to calculate absorption and optical activity, intensity and polarization spectra were generated from 500 to 2000 nm in 2-nm intervals with physiological levels of the plasma constituents, and with the optical pathlength through the plasma being 1 cm. The light incident on the sample was set to be linearly polarized horizontally ($\mathbf{S}_i=[1\ 1\ 0\ 0]^T$). To assess the predictive abilities of the models in an experimental situation, simulated Gaussian noise was added to each signal with an increasing standard deviation. This added uncertainty simulated both source and measurement noise.

### 2.2 *Scattering Monte Carlo Model*

To investigate the ability to predict analyte concentrations using the combined method in scattering biological media such as tissue, a Monte Carlo model for polarized light propagation in multiply scattering media was used. This validated model,[24,25] available for download,[26] records individual photon packet polarizations in the form of Stokes vectors and includes the effects of multiple scattering, absorption, optical activity, and linear birefringence. The model tracks a large number of photons as they propagate and multiply scatter through the sample, then sums the photons to calculate their macroscopic properties of interest.

To reduce the computational time needed to generate data, simulations were run to create a lookup-table with absorption and optical activity as the independent parameters. This lookup table approach is similar to that taken in other Monte Carlo studies.[27] The computational time required was reduced in two ways: first, the number of simulations needed was reduced because data for each full spectrum were not required, since each spectrum could be generated from the lookup table; second, fewer photons were needed in each simulation because the lookup table could be smoothed to reduce the noise due to the statistical nature of the model. To create the lookup table, the values of absorption and optical activity were varied in the full range of blood plasma physiological levels as found from the compiled data. The changes in refractive index and the resulting effects on scattering due to the variations in plasma components were ignored in this study to reduce the parameter space of the lookup table, and thus to reduce the number of simulations required. This approximation is a reasonable first step; in fact, its inclusion, while complicating the analysis, may actually improve the ability to predict analyte concentrations due to an increased sensitivity to concentration changes in both light intensity and polarization.[13] In addition, refractive index dispersion in all materials was ignored to reduce the required simulations. Finally, the linear birefringence was set to zero since this effect was ignored in the current study.

Simulations were run with the absorption coefficient varied between 0 and 30 $cm^{-1}$ in 2-$cm^{-1}$ increments, and with the optical activity varied between 0 and 0.009 rad $cm^{-1}$ (0 and 0.5157 deg $cm^{-1}$) in 0.001 rad $cm^{-1}$ (0.05730 deg $cm^{-1}$) increments, to create a $10\times16$ lookup table. All simulations were run with $3\times10^8$ photons. The sample was a $1\times1\times1$ $cm^3$ cube with a scattering coefficient of 60 $cm^{-1}$, which is somewhat lower than that of tissues; this coefficient was selected for this feasibility investigation to reduce the simulation times by reducing the number of photons required so each photon would retain a higher degree of polarization. The scattering particles in the medium were simulated to represent spherical polystyrene microspheres with a diameter of 1.4 $\mu$m. The refractive indices of the scattering particles and the surrounding media were 1.59 and 1.33, respectively (corresponding to polystyrene and water), giving an anisotropy $g=0.93$ for the microspheres at 633 nm. The photons exiting the sample were binned in 1 $mm^2$ detection areas with an acceptance angle of 20 deg to approximate a typical experimental measurement. The forward direction (direct transmission) was chosen as the geometry of interest to compare the results with those from the clear plasma model. As in the clear media case, the light incident on the sample was set to be horizontally linearly polarized ($\mathbf{S}_i=[1\ 1\ 0\ 0]^T$). Spectra were then generated with the lookup table to create wavelength-dependent Stokes parameters [$I_o(\lambda)$, $Q_o(\lambda)$, $U_o(\lambda)$, and $V_o(\lambda)$] between 500 and 2000 nm in 2-nm intervals using the appropriate values for optical activity and absorption at each wavelength. The orientation of polarization $\gamma(\lambda)$ as a function of wavelength was found from the output Stokes parameters as

$$\gamma(\lambda)=\frac{1}{2}\tan^{-1}\left[\frac{U_o(\lambda)}{Q_o(\lambda)}\right]. \tag{5}$$

The orientation of polarization was directly proportional to the optical rotation $\alpha(\lambda)$ because it changed with the rotation, and could be used in place of $\alpha(\lambda)$ in the regression calculations. Five spectroscopic signals [$I_o(\lambda)$, $Q_o(\lambda)$, $U_o(\lambda)$, $V_o(\lambda)$, and $\gamma(\lambda)$] were available to build the regression model and predict the glucose concentrations from the scattering model. In addition to the noise due to multiple scattering—and similar to the clear model—simulated Gaussian noise was added to each Stokes parameter with an increasing standard deviation to asses the predictive abilities of the methodology when experimental noise (i.e., source output fluctuations and measurement uncertainties) was present.

## 3 Chemometric Methods

Two chemometric algorithms, unfold partial least squares (U-PLS),[28] and multiblock partial least squares (MB-PLS).[29] were used to combine the intensity [$I(\lambda)$ and $\mu_a(\lambda)$] and polarization [$Q(\lambda)$, $U(\lambda)$, $V(\lambda)$, and $\gamma(\lambda)$] data in a model to predict the glucose concentration. These two methods were chosen because they employ the widely used conventional partial least squares (PLS) regression algorithm currently used in most glucose monitoring techniques. The Multiblock Toolbox for MATLAB was used to implement the algorithms.[30] This section will briefly review these two algorithms; further details are available in the cited references.

Both algorithms are based on the widely used PLS regression method. In PLS, a regression relationship is found between a descriptor block or matrix of data (in our case, a set of intensity or polarization spectra) and a response block or matrix (in our case, a set of corresponding glucose concentra-

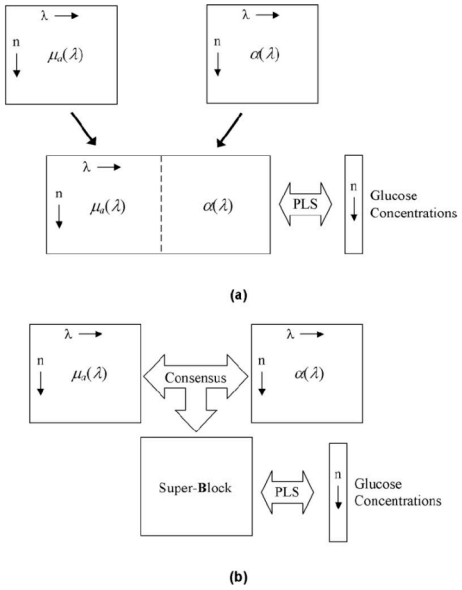



**Fig. 3** Schematic summarizing how (a) U-PLS, and (b) MB-PLS combine and regress the generated intensity and polarization data.

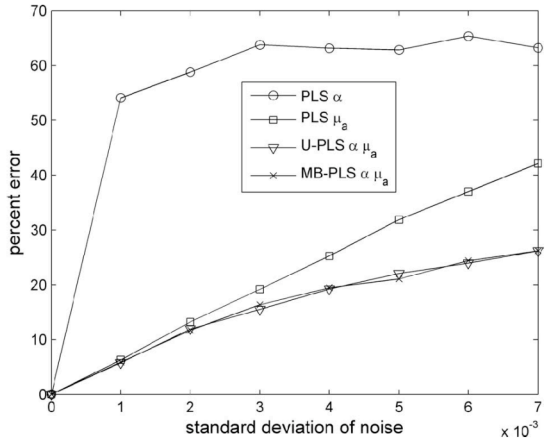



**Fig. 4** Percent error as a function of simulated noise for $\mu_a(\lambda)$ and $\alpha(\lambda)$ in clear media regressed individually and in combination using PLS, U-PLS, and MB-PLS. Points are prediction results and lines are a guide for the eye.

tions). This is achieved by decomposing both the descriptor and response blocks into so-called latent variables that describe the maximum variance in the data. The regression is calculated based on how the variances in each block explain each other—in other words, finding the covariance between the blocks. In situations where there is more than one descriptor block, as is the case with the intensity and polarization measurements, a method of combining the information in both descriptor blocks must be used to predict the response block.

The most rudimentary approach for combining and regressing the data is U-PLS. In this method, each descriptor block is placed in a single combined block, as shown in Fig. 3, and normal PLS regression is performed on this combined descriptor block. In other words, as the name suggests, U-PLS "unfolds" the multiblock data into a single block. The inclusion of more information in the combined descriptor block can improve the predictive ability of the model. A more sophisticated method of combining and regressing the data is MB-PLS. In this method, the blocks are kept separate; however, the blocks are used to create a single super descriptor block that is then regressed to the response block using PLS. The creation of this super block involves finding the common information contained in each of the descriptor blocks, referred to as the "consensus" in the literature. In other words, the variations in the signals that are common in both descriptor blocks are identified as the consensus between the two blocks. Since each block contains measurements done on the same samples, looking at the common information contained in each block can provide better predictive ability for analytes that affect both measurement techniques (as in the plasma model). For example, glucose (as well as plasma proteins) influences both the intensity and polarization signals, causing a common variation in both signals that should be identified in the calculation of the consensus.

Once the regression techniques have been chosen, two steps are required to develop a chemometric model: calibration and testing. In calibration, often referred to as training, a set of data (both descriptor and response blocks) is used to create the PLS model. In our case, a set of intensity and polarization spectra (descriptor blocks) and glucose concentrations corresponding to each spectra (response blocks) were used to calculate the regression parameters using either U-PLS or MB-PLS. Once the model is built in the calibration step, it must be tested with new data to ensure the validity of the model and to assess its predictive ability. In our test, a new set of intensity and polarization spectra, along with corresponding glucose concentrations, was generated for the purpose of testing both regression techniques. The size of both the calibration and testing data sets was 400 spectra with corresponding glucose concentrations. The predictive ability of the methods was determined by calculating the root mean square error of prediction (percent error) using the testing data set, with increasing noise added to both the training and testing spectra. The percent error was then used to calculate the error as a percentage of the mean glucose concentration. Results from conventional PLS regression on intensity and polarization spectra separately were also calculated to quantify the improvement in the combined methodology.

## 4 Results and Discussion

### 4.1 *Clear Media*

The percent error values for the clear plasma model are shown in Figs. 4–6. They demonstrate the improved predictive abilities of the combined intensity and polarization approach. The descriptor block contained 400 spectra between 500 and 2000 nm in 2-nm intervals, with each spectrum having a corresponding glucose concentration in the response block. For reference, a typical human blood glucose level is 0.18 g/100 ml (from Table 1); to be within the generally ac-

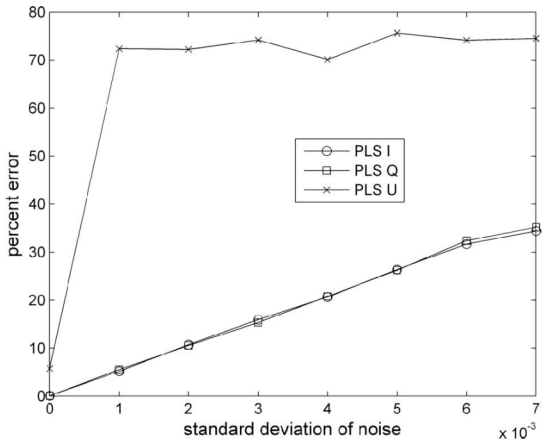



**Fig. 5** Percent error as a function of simulated noise for $I(\lambda)$, $Q(\lambda)$, and $U(\lambda)$ in clear media regressed individually using PLS. Points are prediction results and lines are a guide for the eye.

ceptable level of error for glucose monitoring of 15%[31] (some other reports indicate 20%[32]), the predictive error should be less than 0.027 g/100 ml. Figure 4 plots the results from regressing $\alpha(\lambda)$ and $\mu_a(\lambda)$ individually, with increasing noise added to the signals using conventional PLS, and the combined regression results using U-PLS and MB-PLS. In this case, the standard deviation of the added noise was specified as a percentage of the mean value of each intensity and polarization signal. This was done to corrupt the signals at approximately the same rate, because the signals differed considerably in magnitude. Figure 4 shows that regressing the absorption spectra $\mu_a(\lambda)$ produced much better predictive results (i.e., less corrupted by noise) than regressing the optical activity spectra $\alpha(\lambda)$. This is due to the similarity in the ORD of the plasma components, as shown in Fig. 1, making them difficult for the PLS regression to separate. However, when

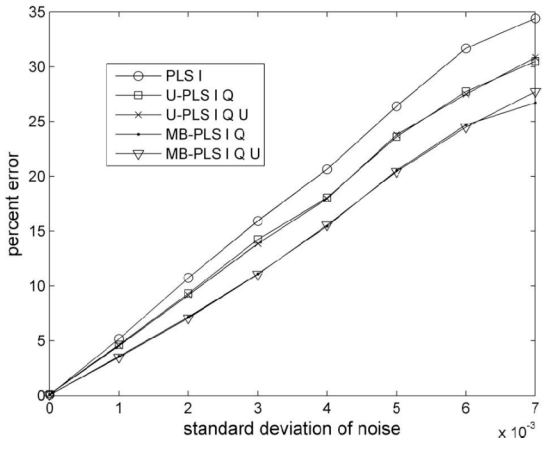



**Fig. 6** Percent error as a function of simulated noise for $I(\lambda)$, $Q(\lambda)$, and $U(\lambda)$ in clear media combined and regressed using PLS, U-PLS, and MB-PLS. Points are prediction results and lines are a guide for the eye.

the absorption and optical activity spectra were regressed with the combined methods (either with U-PLS or MB-PLS), there was considerable improvement over regressing the absorption spectra (or ORD) alone. Both combined methods produced an approximately 25% reduction in percent error with the maximum added noise over $\mu_a(\lambda)$ alone. As hypothesized, the combination of the information in both these spectra decreased the predictive error. Given the poor results of the optical activity spectra regression, the large improvement when it was combined with the absorption spectra was somewhat surprising. Evidently, enough information was contained in the optical activity spectra to complement the absorption spectra and improve the combined regression results.

To test the regression methods on more experimentally realistic signals (i.e., on results from a typical polarimeter[13]), the Stokes vectors of the output light from the clear plasma model were calculated using Eq. (4) with input horizontally and linearly polarized light ($\mathbf{S}_i=[1\ 1\ 0\ 0]^T$). The results from regressing the Stokes parameters individually [including the intensity $I(\lambda)$] using conventional PLS with increasing noise added to each parameter are shown in Fig. 5. Stokes parameter $V(\lambda)$ (circular polarization) was omitted because it contained no information in the present model. Predictions with the parameter $U(\lambda)$ produced poor results because the input light was horizontally polarized, yielding small values of $U(\lambda)$ that were rapidly corrupted by the added noise. A small change due to the rotation of the polarization from optical activity was present; however, this small change was quickly swamped by the added noise. Predictions using either $I(\lambda)$ or $Q(\lambda)$ parameters produced similar and far superior results. The predictive errors using $I(\lambda)$ and $Q(\lambda)$ were very similar since they contained nearly identical information due to the fully horizontal polarization of the input light $[I_i(\lambda)=Q_i(\lambda)]$. Stokes parameter $Q(\lambda)$ was attenuated by the absorption and slightly reduced while the optical activity while the polarization vector was rotated. In this case, even though $Q(\lambda)$ was affected by both absorption and optical activity, there was no improvement gained over $I(\lambda)$, which contained only absorption information. This suggests that even though $Q(\lambda)$ was affected by both absorption and optical activity, it was difficult for PLS to decouple the effects.

The results from combined regression methods for the Stokes parameters are shown in Fig. 6, along with the result for the regression of $I(\lambda)$ alone (from Fig. 5) for comparison. Both U-PLS and MB-PLS produced lower predictive errors than regressing $I(\lambda)$ alone. In both cases, combining either $I(\lambda)$ and $Q(\lambda)$ or $I(\lambda)$, $Q(\lambda)$, and $U(\lambda)$ resulted in similar predictive errors, yielding little additional information in the $U(\lambda)$ signal as discussed above. However, MB-PLS produced significantly lower predictive errors than U-PLS. The reductions in percent error for U-PLS and MB-PLS were approximately 8% and 15%, respectively, at the maximum noise level. These results differed from the results of predicting using $\alpha(\lambda)$ and $\mu_a(\lambda)$, where U-PLS and MB-PLS prediction accuracy were nearly the same. Evidently, the creation of the consensus super-block in MB-PLS by combining the common information in each descriptor block leads to better predictive power in the case of the Stokes parameters. This is likely due to the mix of absorption and optical activity information contained in Stokes parameters $Q(\lambda)$ and $U(\lambda)$ as opposed to the

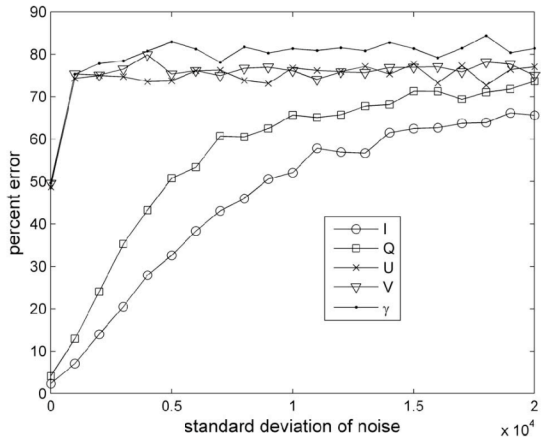



**Fig. 7** Percent error as a function of simulated noise for $I(\lambda)$, $Q(\lambda)$, $U(\lambda)$, $V(\lambda)$, and $\gamma(\lambda)$ in scattering media regressed individually using PLS. Points are prediction results and lines are a guide for the eye.

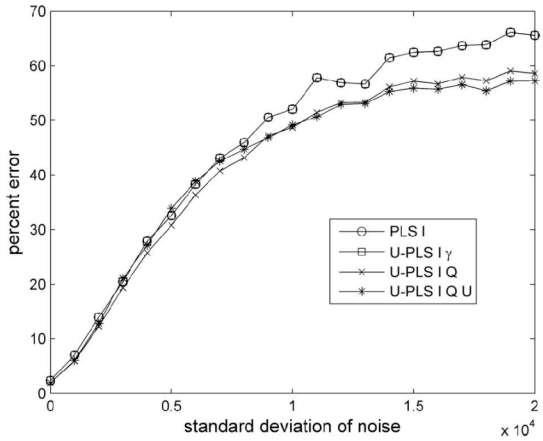



**Fig. 8** Percent error as a function of simulated noise for $I(\lambda)$, $Q(\lambda)$, $U(\lambda)$, and $\gamma(\lambda)$ in scattering media combined and regressed using PLS and U-PLS. Points are prediction results and lines are a guide for the eye. Note that the points overlap for $I(\lambda)$ regressed using PLS and $I(\lambda)$ and $\gamma(\lambda)$ combined and regressed using U-PLS.

pure optical activity and absorption channels $\alpha(\lambda)$ and $\mu_a(\lambda)$. This mixing may make it difficult for the regression methods to decouple the effects when building the predictive models. These results suggest that regressing absorption combined with optical rotation, rather than the measured Stokes parameters, provides better predictive abilities [an improvement of approximately 25% for combined $\alpha(\lambda)$ and $\mu_a(\lambda)$ versus an improvement of approximately 15% for the combined Stokes parameters]. However, when optical rotation is calculated based on measured Stokes parameters, the magnitude of noise will increase as the parameters are divided in Eq. (5). Therefore, as shown later, the potential improvement is diminished. To summarize, it is apparent from these results that combining the information contained in the intensity and polarization spectra improves the predictive abilities for glucose in simulated clear media.

### 4.2 *Scattering Media*

The results of predictive calculations using the data generated by the Monte Carlo model for scattering media are shown in Figs. 7–9. Similar to the clear media, the descriptor block contained 400 spectra between 500 and 2000 nm in 2-nm intervals with each spectrum having a corresponding glucose concentration in the response block. As also was the case for the clear media, a reduction in predictive error was achieved by combining the intensity and polarization signals. Figure 7 plots the percent error for the Stokes parameters $I(\lambda)$, $Q(\lambda)$, $U(\lambda)$, and $V(\lambda)$, plus the orientation of the polarization $\gamma(\lambda)$ calculated using Eq. (5), with each regressed individually. In contrast to Fig. 5, the results for the parameter $V(\lambda)$ are now shown, since scattering produced some transfer of linear-to-circular polarization [giving a nonzero value of $V(\lambda)$] and therefore some information is now contained in $V(\lambda)$. As expected, when using single information channels, regression using $I(\lambda)$ produced the lowest predictive error. The other Stokes parameters and $\gamma(\lambda)$ suffered (to various extents) in predictive ability as a result of the depolarizing effects of multiple scattering. This depolarizing reduced the values of the Stokes parameters, leading to large corruption, relative to $I(\lambda)$, by the added simulated noise. The fraction of retained polarization for the incident fully linear (horizontally) polarized light was approximately 50% after propagating through the media. As a result, the values of the Stokes parameters $Q(\lambda)$, $U(\lambda)$, and $V(\lambda)$ were significantly reduced. Because the incident light was horizontally polarized, $Q(\lambda)$ yielded much lower predictive errors than either $U(\lambda)$, $V(\lambda)$, or $\gamma(\lambda)$, although the percent error was still higher than that for $I(\lambda)$ due to depolarization.

The predictive errors for the combined regression methods are shown in Figs. 8 and 9, along with the results for the regression of $I(\lambda)$ alone for comparison (from Fig. 6). In addition to the combinations of the Stokes vectors, the orienta-

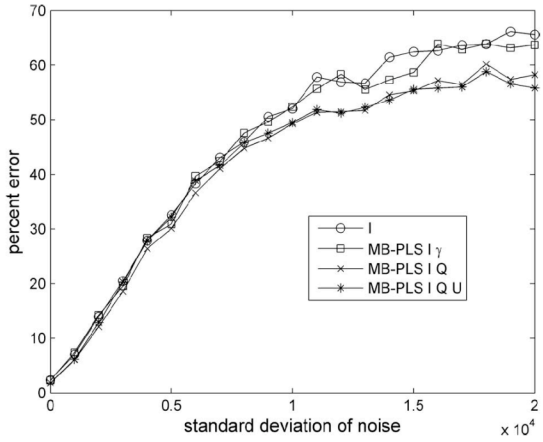



**Fig. 9** Percent error as a function of simulated noise for $I(\lambda)$, $Q(\lambda)$, $U(\lambda)$, and $\gamma(\lambda)$ in scattering media combined and regressed using PLS and MB-PLS. Points are prediction results and lines are a guide for the eye.

tion of the polarization vector $\gamma(\lambda)$ as calculated by Eq. (5) was also combined and regressed with $I(\lambda)$ using U-PLS and MB-PLS. All the combined methods with Stokes parameters improved the predictive power; however, the improvement was more modest than that for clear media calculations. In addition, little difference was observed between the percent errors for U-PLS and MB-PLS, as was seen for the clear media, with the overall reduction in error being approximately 8% for all combined Stokes parameter prediction methods. Also, the combination of $I(\lambda)$ and $\gamma(\lambda)$ through U-PLS or MB-PLS produced little or no improvement. In fact, the predictions when using U-PLS shown in Fig. 8 overlapped with predictions when using $I(\lambda)$ alone. This is likely due to an increase in noise when calculating $\gamma(\lambda)$ through Eq. (5), which led to a decrease in predictive power [i.e., the effective error on $\gamma(\lambda)$ was approximately two times that for the other parameters]. As previously discussed, the lower improvements are due to the depolarizing effects of multiple scattering and the subsequent reduction in the Stokes parameters $Q(\lambda)$, $U(\lambda)$, and $V(\lambda)$. However, even with the lower improvement for the combined approaches in scattering media, the results still demonstrate the potential for the method. A significant improvement in prediction is still achieved with the combination of intensity and polarization information from multiply scattering media. Future work will further investigate the influence of scattering in an effort to determine at what level of scattering an improvement is still realized. Since this rather large reduction in improvement has already been observed from clear media to a scattering coefficient of 60 $cm^{-1}$, it would seem unlikely that predictions with more realistic tissue-scattering values ($\sim$100 $cm^{-1}$) would exhibit significant improvement. However, this is yet to be determined, and smoothing or other preprocessing steps could be used to reduce the signal noise. The present results demonstrate the potential for the methodology in clear or moderately scattering biological fluids such as blood plasma, or extra-cellular fluid and tissues such as the aqueous humor of the eye.

Four additional areas have been identified for further investigation and will be explored in future work. First, the effects of refractive index matching due to variations in constituents[13] will be added to the model to investigate how these effects influence the predictive abilities of the regression techniques. The changes in the refractive index and resulting changes in the scattering properties of the media will influence both the intensity and polarization of the light propagating through the media and may add some additional sensitivity to the constituent concentration changes. It is possible that this may improve the predictive power of this methodology. Second, the influence of other common biological optical effects such as linear birefringence[25] on the abilities of the regression methods will also be investigated. Linear birefringence has the effect of transferring the polarization state from linear to circular or vice versa, and will interfere with the effects of optical activity. The extent to which this influences the abilities of the methodology will be investigated by employing a method of polar Mueller matrix decomposition to decouple the two effects.[33,34] This will be done in both clear and scattering media with increasing scattering coefficients. Third, the effect of detection geometry and wavelength range will also be investigated to determine the optimal experimental parameters for the measurement of intensity and polarization signals.[11,13] This will involve both simulations and experimental work. Fourth, experimental testing must be completed to validate the combining methodology, because the current results are for simulated measurements only. This will involve the design, construction, and testing of a combined spectral intensity and polarimetry system suitable for experimental measurements.

## 5 Conclusions

We have simulated and analyzed a combined intensity and polarization method for analyte concentration determination in clear and scattering biological-like media with glucose as the analyte of interest. The determination of glucose concentrations in biological media is a crucially important unsolved problem in clinical medicine, because a tremendous need exists for a noninvasive method that diabetics can use to monitor their blood glucose levels. The methodology was tested using a simulated blood plasma model for both clear and scattering media. The spectral intensity and polarization data generated through this model were used to build and test predictive chemometric models that combined the two data sets. The results showed that the combination of these two modalities improved the predictive ability over the use of intensity or polarization data alone, for both simulated clear and scattering media, thus demonstrating potential for the methodology. This improvement is reduced in scattering media due to light depolorization. Thus, the applicability of these methods may be limited in higher scattering media; however, further study is required to investigate this. In addition, the effects of refractive index matching, tissue birefringence, detection geometry, and wavelength range, which have not been included in the current model, require further study. The development of a suitable combined intensity and polarization system and experimental testing of the methodology is also required for validation. The applicability of this methodology is not limited to glucose sensing, because other analytes of interest could be targeted. The methodology is also not limited to biological media, since nonbiological applications for concentration determination of absorbing optically active molecules exist—for example, in remote sensing scenarios. To our knowledge, this is the first demonstration of a combined spectral intensity and polarization methodology for analyte concentration determination.

### *Acknowledgments*

The authors would like to thank Dr. Robert Weersink for assistance with the chemometric software and Drs. Xinxin Guo and Nirmalya Ghosh (all from the Ontario Cancer Institute) for assistance with the preparation of this manuscript. Financial support from the Natural Sciences and Engineering Research Council of Canada and the Ontario Graduate Scholarship Program is gratefully acknowledged.

### *References*

1. J. A. Tamada, M. Lesho, and M. J. Tierney, "Keeping watch on glucose: new monitors help fight the long-term complications of diabetes," *IEEE Spectrum* **39**, 52–57 (2002).
2. Y. Wickramasinghe, Y. Yang, and S. A. Spencer, "Current problems and potential techniques in *in vivo* glucose monitoring," *J. Fluoresc.* **14**, 513–520 (2004).

3. K. Maruo, M. Tsurugi, J. Chin, T. Ota, H. Arimoto, Y. Yamada, M. Tamura, M. Ishii, and Y. Ozaki, "Noninvasive blood glucose assay using a newly developed near-infrared system," *IEEE J. Sel. Top. Quantum Electron.* **9**, 322–330 (2003).
4. W. Schrader, P. Meuer, J. Popp, W. Kiefer, J. Menzeback, and B. Schrader, "Noninvasive glucose determination in the human eye," *J. Mol. Struct.* **735–736**, 299–306 (2005).
5. K. V. Larin, M. Motamedi, M. S. Eledrisi, and R. O. Esenaliev, "Noninvasive blood glucose monitoring with optical coherence tomography," *Diabetes Care* **25**, 2263–2267 (2002).
6. H. Mackenzie, H. S. Ashton, S. Spiers, Y. Shen, S. S. Freeborn, J. Hannigan, J. Lindberg, and P. Rae, "Advances in photoacoustic noninvasive glucose testing," *Clin. Chem.* **45**, 1587–1595 (1999).
7. Glucon, "The Glucon Solution: Clinical Trials," http://www.glucon.com (2006).
8. A. M. K. Enejder, T. G. Scecina, J. Oh, M. Hunter, W. Shih, S. Sasic, G. L. Horowitz, and M. S. Feld, "Raman spectroscopy for noninvasive glucose measurements," *J. Biomed. Opt.* **10**, 031114 (2005).
9. R. Badugu, J. R. Lakowicz, and C. D. Geddes, "Ophthalmic glucose monitoring using disposable contact lenses—a review," *J. Fluoresc.* **14**, 617–633 (2004).
10. D. Côté and I. A. Vitkin, "Balanced detection for low noise precision polarimetric measurements of optically active, multiply scattering tissue phantoms," *J. Biomed. Opt.* **9**, 213–220 (2004).
11. X. Guo, M. F. G. Wood, and I. A. Vitkin, "Monte Carlo study of pathlength distribution of polarized light in turbid media," *Opt. Express* **15**, 1348–1360 (2007).
12. Q. Wan, G. L. Coté, and J. B. Dixon, "Dual-wavelength polarimetry for monitoring glucose in the presence of varing birefringence," *J. Biomed. Opt.* **10**, 024029 (2005).
13. X. Guo, M. F. G. Wood, and I. A. Vitkin, "Angular resolved linear Stokes polarimeter measurements of light scattered by turbid chiral media," *J. Biomed. Opt.* **11**, 041105 (2006).
14. K. C. Hadley and I. A. Vitkin, "Optical rotation and linear and circular depolarization rates in diffusely scattered light from chiral, racemic, and achiral turbid media," *J. Biomed. Opt.* **7**, 291–299 (2002).
15. M. Otto, *Chemometrics: Statistics and Computer Application in Analytical Chemistry*, 2nd Ed., Wiley, New York (2007).
16. K. H. Hazen, M. A. Arnold, and G. W. Small, "Measurement of glucose and other analytes in undiluted human serum with near-infrared transmission spectroscopy," *Anal. Chim. Acta* **371**, 255–267 (1998).
17. K. Murayama, K. Yamada, R. Tsenkova, Y. Wang, and Y. Ozaki, "Near-infrared spectra serum albumin and γ-globulin and determination of their concentrations in phosphate buffer solution by partial least squares regression," *Vib. Spectrosc.* **18**, 33–40 (1998).
18. G. Yoon, A. K. Amerov, K. J. Jeon, and Y. Kim, "Determination of glucose concentration in a scattering medium on selected wavelengths by use of an overtone absorption band," *Appl. Opt.* **41**(7), 1469–1475 (2002).
19. S. Kasemsumran, Y. Du, K. Murayama, M. Huehne, and Y. Ozaki, "Simultaneous determination of human serum albumin, γ-globulin, and glucose in a phosphate buffer solution by near-infrared spectroscopy with moving window partial least-squares regression," *Analyst (Cambridge, U.K.)* **128**, 1471–1477 (2003).
20. Y. Kim and G. Yoon, "Prediction of glucose in whole blood near-infrared spectroscopy: influence of wavelength region, preprocessing, and hemoglobin concentration," *J. Biomed. Opt.* **11**(4), 041128 (2006).
21. B. Jirgensons, *Optical Rotatory Dispersion of Proteins and Other Macromolecules*, Springer-Verlag, New York (1969).
22. R. J. McNichols and G. L. Coté, "Optical glucose monitoring in biological fluids: an overview," *J. Biomed. Opt.* **5**(1), 5–16 (2000).
23. C. F. Bohren and D. R. Huffman, "Electromagnetic theory," Chapter 2 in *Absorption and Scattering of Light by Small Particles*, Wiley, New York (1983).
24. D. Côté and I. A. Vitkin, "Robust concentration determination of optically active molecules in turbid media with validated three-dimensional polarization sensitive Monte Carlo calculations," *Opt. Express* **13**, 148–163 (2005).
25. M. F. G. Wood, X. Guo, and I. A. Vitkin, "Polarized light propagation in multiply scattering media exhibiting both linear birefringence and optical activity: Monte Carlo model and experimental methodology," *J. Biomed. Opt.* **12**(1), 014029 (2007).
26. D. Côté and I. A. Vitkin, "Pol-MC: a three dimensional polarization sensitive Monte Carlo implementation for light propagation in tissue," http://www.novajo.ca/ont-canc-inst-biophotonics/ (2005).
27. M. Tarumi, M. Shimada, T. Murakami, M. Tamura, M. Shimada, H. Arimoto, and Y. Tamada, "Simulation study of in vitro glucose measurements by NIR spectroscopy and a method of error reduction," *Phys. Med. Biol.* **48**, 2373–2390 (2003).
28. S. Wold, P. Geladi, K. Esbensen, and J. Öhman, "Multi-way principal components and PLS analysis," *J. Chemom.* **1**(1), 41–56 (1987).
29. L. E. Wangen and B. R. Kawalski, "A multiblock partial least squares algorithm for investigating complex chemical systems," *J. Chemom.* **3**, 3–20 (1988).
30. F. van den Berg, "Multi-block toolbox for Matlab," http://www.models.kvl.dk/source/MBToolbox/, accessed Feb. 2007.
31. American Diabetes Association, "Consensus statement on self-monitoring of blood glucose," *Diabetes Care* **10**, 95–99 (1987).
32. J. J. Mahoney and J. M. Ellison, "Assessing glucose monitor performance—a standardized approach," *Diabetes Tech. Therapeut.* **9**, 545–552 (2007).
33. S. Yau Lu and R. A. Chipman, "Interpretation of Mueller matrices based on polar decomposition," *J. Opt. Soc. Am. A* **13**, 1106–1113 (1996).
34. S. Manhas, M. K. Swami, P. Buddhiwant, N. Ghosh, P. K. Gupta, and K. Singh, "Mueller matrix approach for determination of optical rotation in chiral turbid media in backscattering geometry," *Opt. Express* **14**, 190–202 (2006).

***Addendum***

This study demonstrates a combined optical approach for concentration determination of optically active and absorbing analytes. This combined approach was tested in simulated blood serum media and found to improve predictive abilities over either modality alone for both clear and scattering media, providing a 25% and 8% reduction in percent error respectively. These results show promise for the approach, in particular for glucose monitoring in biological fluids and potentially in tissue, as well as for other applications requiring analyte concentration measurements, such as quality control and remote sensing. The application of this technique to scattering media—such as biological tissue—is complicated by the resulting depolarization and additional noise, as was shown in the study. Scattering also modifies the polarization state; in certain geometries this can lead to a scattering-induced apparent rotation that is often much greater then the chirality-induced rotation.[131] Separating this scattering-induced rotation from the chirality-induced rotation is investigated in the following section. While the effects of scattering reduce the predictive abilities of the methodology, an improvement over each single modality was shown in this study for simulated scattering media (scattering coefficient of 60 $cm^{-1}$). However, this improvement was significantly reduced when compared to that in clear media. Whether or not an improvement is still gained in higher scattering media such as tissues (scattering coefficient generally > 100 $cm^{-1}$), is yet to be shown and should be investigated in future studies.

## 4.2 Separating chirality-induced and scattering-induced optical rotation

A serious hurdle for the use of optical activity for determining chiral tissue analyte concentrations (e.g., glucose) in scattering media is the fact that the small rotation due to glucose is often swamped by the much larger apparent rotation induced by scattering. This issue is particularly important in the backscattering geometry—a potentially clinically important arrangment—where the scattering induced rotations can be large. These large rotations caused by scattering are not due to rotation of the light as it propagates through the media, but are due to preferential scattering of orthogonal linear polarizations at different scattering angles. As the intensity of these linear polarizations are unequally scattered, the overall polarization undergoes diattenuation that, without further analysis, appears as a rotation of the polarization. Thus, in the Mueller matrix representing the media they should be represented as diattenution rather than true optical rotation as produced by a chiral molecule, and the ability to differentiate between these two sources of rotation should be possible through Mueller matrix decomposition. This ability was successfully demonstrated in the publication in Chapter 3 (section 2). This manuscript is not duplicated here, instead the reader is referred the previous section.

***Paper***

N. Ghosh*, **M. F. G. Wood***, S. H. Li, R. D. Weisel, B. C. Wilson, R. K. Li, and I. A. Vitkin, "Mueller matrix decomposition for polarized light assessment of biological tissues," *Journal of Biophotonics* **2**, 145-156 (2009).

* Authors contributed equally to this work and shared 1st authorship

In section 3.2 we established the ability of polar decomposition to separate scattering-induced and chirality-induced optical rotation. This was demonstrated in backscattered Monte Carlo simulated media exhibiting both scattering and optical activity. Prior to decomposition, the overall simulated rotation was in excess of 20 deg (5 mm from incident beam as shown in Fig. 3 on page 60), most of this due to scattering. After decomposition, the chirality-induced rotation was calculated to be approximately 0.1 deg (5 mm from the incident beam), corresponding well with the simulated value of optical activity (0.082 deg/cm) for this detection geometry where the average optical pathlength was 1.2 mm (as calculated from the Monte Carlo model). The fact these effects can be separated through Mueller matrix decomposition is tremendously useful for chirality-based tissue analyte measurements. As the presented results are from a simulation study, further experimental investigations are required. In addition, these results are from a relatively low scattering media (scattering coefficient of 30 $cm^{-1}$) when compared to tissue, thus further investigations is also required in more highly scattering media.

# 5. Summary, future work, and conclusions

In this final chapter the results of the three thesis themes are summarized and avenues of future research are identified and discussed. In conclusion, overall achievements from this body of work are also presented.

## 5.1 Extension of Monte Carlo model

### 5.1.1 Summary

The Monte Carlo model developed in our group for simulation of polarized light was extended to include the effects of optical activity and linear birefringence *simultaneously* in multiply scattering media. Optical activity in tissue is induced by chiral constituents including proteins and glucose, while birefringence is a result of anisotropic tissue structures such as extracellular matrix proteins (i.e., collagen and elastin) and muscle fibers, among others. Both these effects can be indicative of tissue status and thus potentially could be employed to measure/monitor valuable tissue metrics such as tissue glucose levels and myocardial health, as was in fact explored in this thesis. The primary challenge in modeling the two effects was determining the Mueller matrix for the combination of the effects; as described, this was calculated through the Jones *N*-matrix formalism. This combined matrix could then be applied between scattering events as the photons propagate through the medium. The use of the *N*-matrix formalism also allows for other polarization effects to be modeled such as diattenutation and circular dichroism.

In order to experimentally validate the extended model, a phantom system was developed that could also simultaneously exhibit scattering, optical activity, and birefringence. This was accomplished using polystyrene microspheres as scattering

structures, sucrose for optical activity, and strain-induced birefringence from polyacrylamide gel. Monte Carlo generated data was compared to experimental results where the phantom properties matched those in the simulations. Close agreement between the simulations and experimental measurements was shown, strongly supporting the validity of the extended model. This extended and validated model is, to our knowledge, the first polarization-sensitive Monte Carlo model with the ability to incorporate all polarizing effects. In addition, the phantom system developed is novel, as no previous systems have incorporated scattering, birefringence, and optical activity simultaneously.

### 5.1.2 Future Work

While this model better simulates the interactions of polarized light with tissue, significant differences still exist, particularly with regards to the scattering mechanisms used in the model compared to that in tissue. This and other polarization-sensitive Monte Carlo models generally approximate the scattering of tissue with uniform diameter spherical particles. The use of spherical particles is advantages, particularly for polarization models, as the full scattering phase function can be calculated via Mie theory and the scattering properties can be "tuned" by changing the diameter and refractive index of the particles. However, the situation in tissue is vastly different. Instead of uniformly shaped scatterers, the structures in tissue (cells, organelles, nuclei, etc) vary in shape and size. In addition, the refractive indices of these structures also vary considerably. Thus, the validity of using uniformly sized spherical scatterers to approximate the polarization scattering properties of tissue is questionable.

As part of future work we propose to test the validity of employing uniform spherical scatterers to simulate tissue scattering in both Monte Carlo models and tissue phantoms. This will be accomplished by comparing polarization measurements on tissues with those on phantoms and Monte Carlo generated data with matching optical properties. How well the tissue measurements correlate with phantom and Monte Carlo results will give an indication of the validity of this modeling approach.

Improvements to the scattering calculations used in the model to better simulate the scattering mechanisms of tissue are also possible. Work by Schmitt,[132] has demonstrated that a distribution of scatterer sizes better models the scattering present in tissue. This concept has been employed in previous models by allowing for a number of scatterer sizes in a single simulation, rather then only one size as is currently done.[48] The selection of the particle size for a particular scattering event would be based on the specified particle size distribution, which can be chosen to best model the tissue. This upgrade is attractive due to the ease of incorporation in the current model. All that is required is the calculation of a number of scattering phase functions (rather than one) before the start of photon tracking based on the specified scatterer size distribution. These calculated phase functions would be used to create a look-up table from which the appropriate phase function for a scatterer size could be selected based on the size distribution of the scatterers. In addition, the development of a relatively simple scatterer size selection algorithm using the desired particle size distribution would be required. While significant differences would still exist between biological tissue and this model, it may provide a more accurate means for polarized light simulation in tissue.

## 5.2 Characterization of myocardial tissue structure

### 5.2.1 Summary

The work completed in chapter two demonstrated the ability to characterize myocardial tissue structure, with application towards monitoring regenerative treatments of myocardial infarctions. A small proof-of-principle pilot study first established that polarized light birefringence measurements could differentiate between healthy and infarcted *ex vivo* sectioned mouse myocardium. Further studies with infarcted and regenerating rat *ex vivo* sectioned rat myocardium demonstrated the ability to differentiate between infarcted and regenerating myocardium. The ability to differentiate between these tissue states was based on changes in tissue anisotropy associated with structural remodeling in the myocardium, due to infarction and regeneration. Healthy myocardium is highly organized and thus anisotropic, however, after remodeling due to infarction the affected myocardium becomes significantly less organized due to scar formation. Stem cell regenerative treatments reduce the remodeling associated with infarction and accordingly lead to greater anisotropy (preservation) after infarction. These changes in anisotropy manifest as changes in tissue birefringence that can be measured using polarized light. Polarization measurements in these studies were conducted using both point and imaging systems that measured the Mueller matrix (polarization transfer function) of the sample. This matrix was then decomposed into constituent matrices by polar decomposition from which the polarization properties such as birefringence could be calculated. These studies, to our knowledge, are the first to demonstrate the ability to differentiate between infarcted and regenerating myocardial tissue using polarized light

and to propose the use of such a method for monitoring regenerative treatments of myocardial infarction.

The orientation of the birefringence with respect to the propagation direction of the photons in scattering media was investigated and found to have a significant influence on the detected retardance. The issue of formalin fixation was also studied with regards to its effect of fixation on tissue birefringence and depolarization. Fixation was found to increase both effects; however, the increase for birefringence was relatively small (~15%). Finally, a demonstration study for *in vivo* measurements was conducted on mouse window chamber model to demonstrate our ability to perform polarization measurements and analysis in a living organism. To our knowledge this was the first demonstration of Mueller matrix measurements coupled with polar decomposition performed *in vivo*.

### 5.2.2 Future Work

While the completed studies demonstrate the potential for the application of polarized light for monitoring regenerative treatments of myocardial infarction, significant work is needed before the approach could employed *in vivo*. Specific challenges include: performing measurements in backscatter geometry, correction for cardiac motion, and development of a probe capable of being catheterized. It must be demonstrated that the relatively small changes in tissue birefringence associated with regeneration can be measured in the presence of the complicating factors present for *in vivo* measurements. It should be noted, however, that even if the technique were to prove unfeasible for *in vivo*

monitoring, utility still exists in the evaluation of *ex vivo* tissues as part of regenerative studies.

All measurements to date have been performed in transmission, a geometry that for myocardial tissue requires sectioning, and is thus clearly not clinically relevant. As such, a method for retardance quantification in the backscattering geometry must be developed. This geometry presents a challenge, as the optical pathlength of detected light will now be much more dependent on the tissue optical properties, rather than was the case with transmitted light where one can assume the pathlength is at least the tissue thickness or somewhat greater. Additionally, backscatter detection will be biased to shorter pathlength photons, as those that propagate further into the tissue will tend to be absorbed, potentially making the measured retardance signal significantly smaller than for transmission measurements. In spite of these challenges, if the pathlength between measurements can be kept constant or the change in pathlength accounted for, the tissue birefringence can be quantified.

The development of a backscatter birefringence detection methodology will begin with a simulation study using the extended Monte Carlo model. Simulations with varying optical properties (scattering and absorption) as well as varying birefringence magnitude, in the range of those present in myocardial tissues, will be conducted. The spatial distribution of backscattered retardance and optical pathlength will be recorded (i.e., retardance image). These results will be examined to determine the effect of optical property variations on photon pathlength, and the effect of birefringence variations on detected retardance. The goal of these studies is to assess if sufficient consistency in photon pathlength and detected retardance is present with these variations. If spatial

detection points where both the pathlength and retardance remain relatively constant, these points could conceivably be used for backscattering birefringence measurement. Once developed, the methodology could be further tested on controllable birefringent phantoms such as the polyarcylamide phantoms developed and employed in Chapter 2.

Another complicating factor that will be present for *in vivo* measurements is cardiac movement, specifically tissue expansion/contraction associated with a beating heart. During the cardiac cycle the myocardium contracts to pump blood through both the pulmonary and systemic circulation systems. This presents a challenge for polarimetry measurements as the myocardium both moves and changes shape during this process. To account for this, a method a gating based on the cardiac cycle could be employed. In such a method, repeated measurements would be made at the same point in the cardiac cycle to ensure myocardium was in the same position and in similar state of deformation. This could be accomplished by either gating based on a recorded electrocardiogram (ECG), either in real time or retrospectively—if measurements are acquired with sufficient speed.

However, the tissue deformation associated with myocardial contraction and expansion may provide additional polarization information. As the tissue contracts and expands its structure changes, and in particular the anisotropy and thus birefringence of the tissue likely also change. These time-dependent changes in tissue mechanical properties, and possibly tissue birefringence, may well have differing magnitudes depending on the state of the tissue (i.e., healthy, infarcted, regenerating). For instance, myocardial infarction leads to increased stiffness and the inability to expand and contract, thus decreasing myocardial function. This is in contrast to healthy myocardium, which is more elastic. Preliminary testing using confined compression stress relaxation testing

suggests that infarcted myocardium is indeed considerably stiffer than healthy myocardium. These preliminary measurements were conducted by Dr. Cari Whyne, at the Orthopedic Biomechanical Laboratory at Sunnybrook Research Institute, Toronto, Canada. Accordingly, potential exists for polarization in characterizing the mechanical state of the myocardium, and possibly for an elastrographic polarimetry approach where time-resolved measurements are made throughout the cardiac cycle. This will be investigated in future studies, first to determine if retardance measurements can be related to myocardial mechanical metrics, and second to determine if myocardial expansion and contraction produces varying retardance and if this can be related to the health of the myocardium. This will be examined using *ex vivo* myocardium by mechanically stretching the tissue to induce strain.

Associated with development of a backscattering birefringence detection methodology and potential gated/elastographic measurements, is the upgrading of both point and imaging systems. Upgrades are necessary as backscattered detection will require additional accuracy and sensitively not currently possessed by our systems, and gated/elastrographic measurements will require faster measurement and imaging times. Our current systems also involve rotating polarizers and inserting/removing polarization optics between the measurements of each Stokes parameters, significantly slowing the measurement process. Thus upgrades to the systems to remove the necessity of moving parts are advantages. In addition, the upgraded systems will allow for measurements at multiple wavelengths, which will enable us to experimentally explore spectroscopic applications, such as optical activity concentration measurements of glucose discussed in chapter 4.

For the point measurement, our current system will be upgraded to a dual photoelastic modulator (PEM) system[133] will be constructed as shown in Fig 17. In this system two PEMs operating at different frequencies are mounted such that their modulator axes are at 45 deg with respect to each other. The resulting intensity-modulated photodetected signal can be lock-in amplified at the first and second harmonics of both PEM reference frequencies to provide the necessary signals to calculate all four Stokes parameters (I, Q, U, and V) simultaneously. This system has the advantage over our current setup as no moving parts are required and the Stokes parameters can be determined at a fast acquisition rate (greater then 100 samples per second). Such systems have been previously been employed to measure polarization signals less than $10^{-6}$ of the total light intensity,[134] and thus are highly accurate.

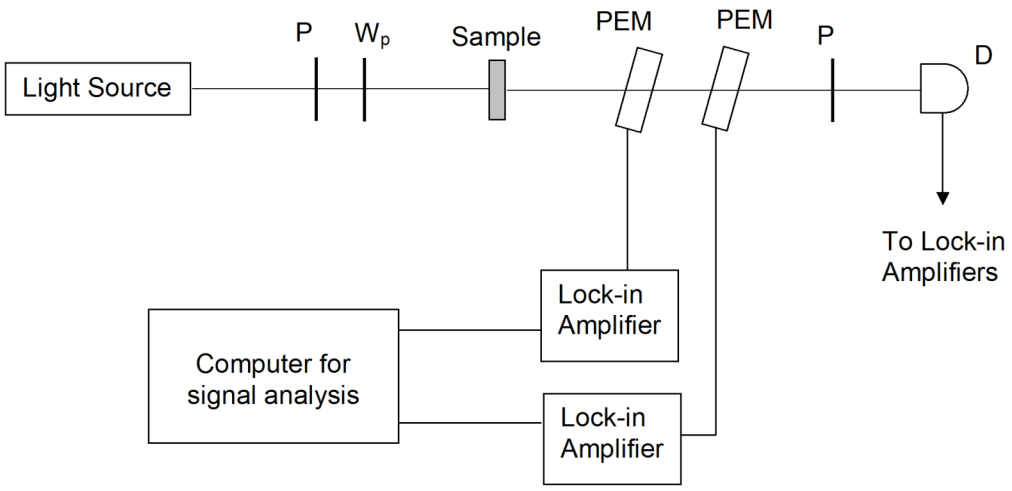



**Fig. 17** Schematic of proposed dual PEM point measurement system: P, polarizers; $W_p$, quarter waveplate; PEM, photoelastic modulators; and D, photodetector. The PEM modulator axes are oriented at 45 deg to each other. The system is shown in transmission mode; however, the detection optics could placed at any geometry.

The present imaging system will also be upgraded such that a modulated polarization signal is produced, allowing for higher SNR detection, also with no or few

moving parts (rotation and/or removal of polarizers or waveplates). An approach similar to that employed by Diner *et al*.,[135] where two PEMs with slightly different operating frequencies (differing by several to a few hundred Hz) create a relatively slow polarization modulated beat signal compared to the PEM operating frequencies (on the order of Hz compared to kHz). This slow beat signal modulates the polarization at a rate lower than the frame acquisition rate for many available CCD cameras, allowing for time-resolved detection of the polarization-modulated signal and increasing the SNR of the detected polarization. The proposed setup schematic is shown in Fig. 18. Other possible imaging schemes include a PEM-based stroboscopic illumination approach similar to Han and Chao,[136,137] where the light source is strobed at an integer multiple of the PEM frequency (i.e., harmonics of the PEM frequency). In this approach light from the sample is detected at only specific time points in the PEM modulation cycle. This allows for imaging of the polarizations emitted from the sample at specific PEM retardances, and thus selecting for different output polarizations. The setup schematic for this approach is shown in Fig. 19. Both schemes are currently under consideration for the upgraded imaging system.

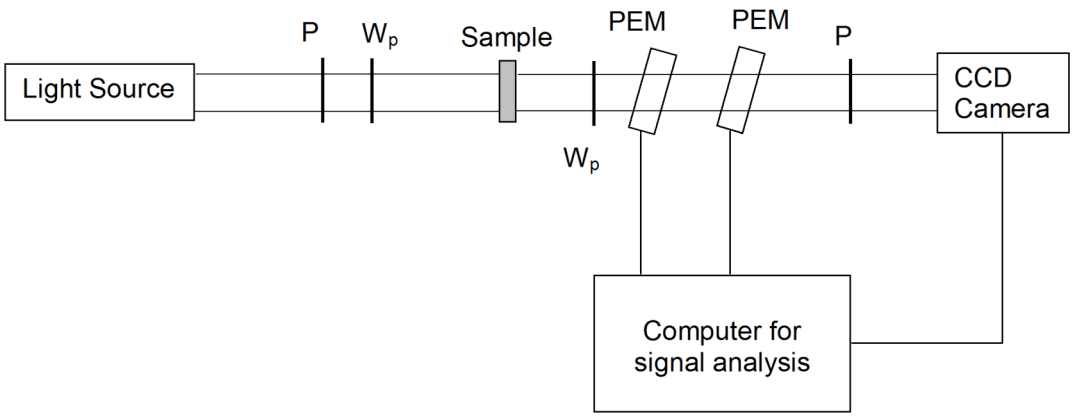



**Fig. 18** Schematic of proposed dual PEM imaging system: P, polarizers; $W_p$, quarter waveplate; and PEM, photoelastic modulators. The PEMs modulator axes at the same orientation, however, have modulation frequencies differing by several to a few hundred Hz. The system is shown in transmission mode; however, the detection optics could placed at any geometry.

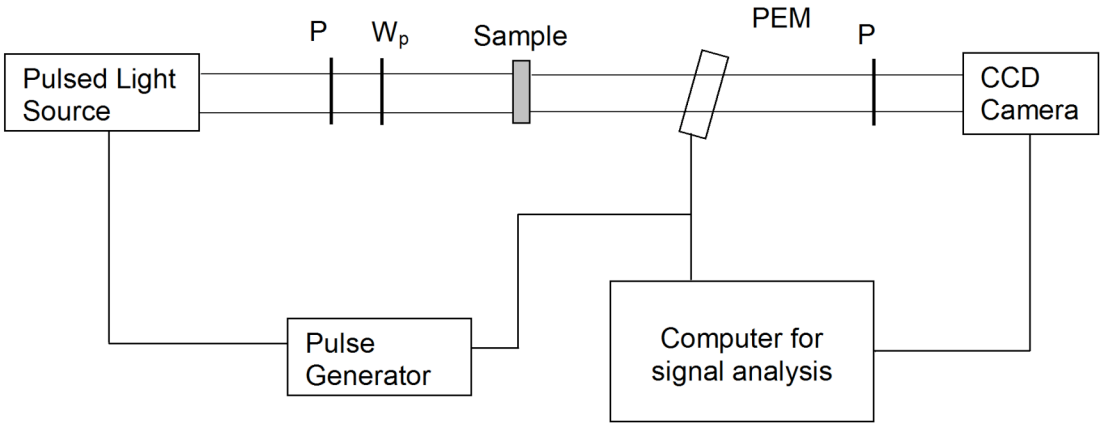



**Fig. 19** Schematic of proposed stroboscopic PEM imaging system: P, polarizers; $W_p$, quarter waveplate; and PEM, photoelastic modulator. The PEM modulation signal is input to the pulse generator which turn drives a pulsed light source (e.g., diode laser). The system is shown in transmission mode; however, the detection optics could placed at any geometry.

All measurements performed in these studies were conducted on sectioned *ex vivo* myocardium. As the motivation for this work is monitoring stem cell treatments, a method of performing these measurements *in vivo* is obviously required. To perform

these measurements *in vivo*, the least invasive and most logical approach would be via an intra-ventricular catheterization approach, similar to that performed as part of cardiac electrophysiology studies in catheterization labs. In these procedures, a catheterized electrode probe is inserted into either an artery or vein (most often the femoral artery) and navigated through the vessel into the chambers of heart under fluoroscopic image guidance. Once in the heart, localized electrical measurements are performed to assess the myocardial conduction properties. It is conceivable that a similar approach could be taken where localized polarimetry measurement could be performed instead of or along with electrical measurements, where light delivery and detection are achieved through fiber optics. However, many technical challenges must first be overcome.

The primary challenge in conducting these fiber-based measurements is the polarization-modifying effects of fiber optics. A single mode fiber optic will theoretically preserve the polarization of an input beam; however, stress-induced birefringence in the core of a fiber leads to significant modification of the polarization state. It is possible that the polarizing effects of the fiber could be accounted for if the stresses on the fiber remain constant between measurements; however, this is difficult to achieve, as any change in the fiber shape will change the applied stress. Even if the stress remains constant, preliminary experiments conduct by our group suggest that removing the effects of the fiber are difficult due to measurement variations. A more achievable approach may be to place the polarization optics at the distal end of the probe, so that the fiber simply acts as a light delivery conduit, rather than to deliver the polarization of the light as well. This is schematically shown in Fig. 20. The disadvantage of this approach is that all polarization optics (i.e., polarizers, waveplates, PEM, etc) would have to be sufficiently

miniaturized to enable mounting on the distal end of the probe and made compatible with an *in vivo* probe. Miniaturized polarizers and waveplates currently exist for telecommunication applications, however, the miniaturization PEMs and any mechanical rotation devises would require significant engineering. While challenging, if further studies indicate sufficient motivation for performing these measurements *in vivo*, this may be the most realizable approach.

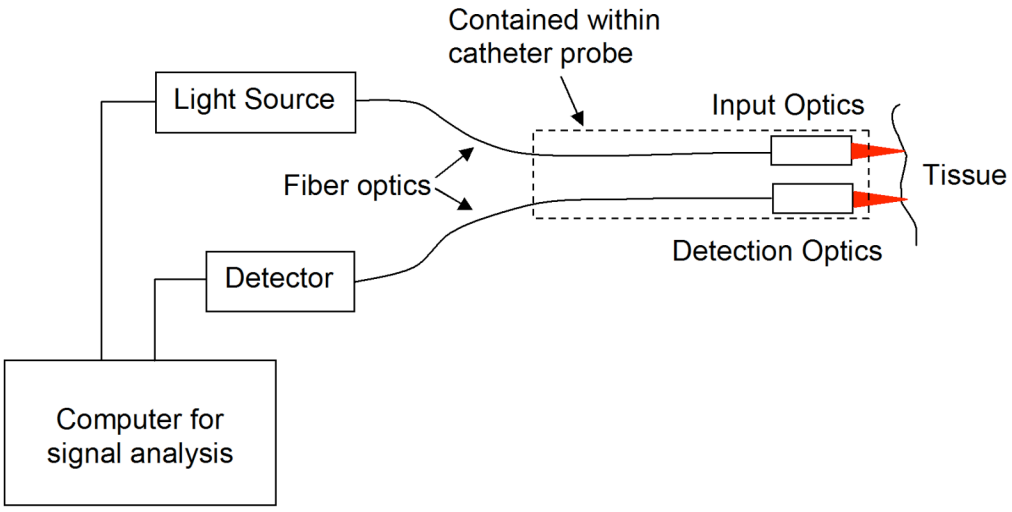



**Fig. 20** Schematic of possible catheterized polarimetry probe system. The input optics focus the light emitted from the fiber and control the polarization of the light incident on the tissue. The detection optics collect light emitted from the tissue and select for polarization detection states.

## 5.3 Tissue analyte concentration determination

### 5.3.1 Summary

In the final research chapter of this thesis, two simulation studies were conduct towards polarized-light-based concentration determination of optically active molecules, particularly towards noninvasive glucose monitoring. These simulation studies were

conducted to determine the potential for this application in a controlled environment. While the focus of these studies was for glucose concentration measurements, the approach could also be employed for other optically active analytes.

The first simulation study investigated the potential for a dual modality optical glucose sensing approach, specifically the combination of spectral polarization and NIR absorption signals. Simulated polarimetry and NIR absorption spectra from a blood serum model were combined and regressed using multi-block chemometric techniques to extract common information from the two spectra. The combined approach was found to improve the predictive abilities for glucose concentration measurements over either modality alone, for both optically clear and scattering media. However, the improvement was significantly diminished with the addition of scattering, due to depolarization of the polarization spectra and increased noise in the absorption spectra. The level of scattering tested in this initial study was lower than that generally present in tissue ($\mu_s$ = 60 $cm^{-1}$ in this study, compared to values generally greater than $\mu_s$ = 100 $cm^{-1}$ in tissue), suggesting that this approach may be limited to clear or low scattering biological media. This study was, to our knowledge, the first to investigate a dual optical modality glucose sensing approach.

The second smaller simulation study investigated the ability of Mueller matrix decomposition to separate chirality-induced optical rotation from scattering-induced optical rotation. Both optically active molecules and tissue scattering produce what is measured as optical rotation, particularly in the backscattering detection geometries. However, different mechanisms are responsible for this rotation. In the context of potentially employing polarized light for glucose measurements, it is important to

separate these effects, as we are primarily interested in only the chirality-induced rotation. In this study, the ability of polar Mueller matrix decomposition to separate these effects (as they are expressed by different Mueller matrices) was tested on Monte Carlo simulated data in the backscattering direction. The results of the decomposition show that it is indeed possible to separate these effects and has motivated further work.

### 5.3.2 Future Work

As discussed, the dual modality glucose sensing study was conducted on relatively low scattering media. As a result, an additional study to determine the upper limits of media scattering at which an improvement is still gained should be conducted. These additional studies should simulate media with a scattering coefficient in the range of that found in tissue ($\mu_s$ = 100 to 200 $cm^{-1}$). The results of this study will determine what degree of polarization is required for the combined modality to still impart an improvement over absorption data alone. This degree of required polarization could then be used to guide what tissue sites could potentially be employed for future studies.

As both studies completed in this chapter were based on simulated data, both require experimental validation. The upgrades to the point polarimetry system discussed in the previous section will enable much more accurate measurements, thus enabling for detection of much lower levels of optically active molecules than currently possible with our system. An important upgrade also required is the ability to perform spectroscopic polarimetry measurements. This is particularly important for the dual modality glucose sensing, which requires spectroscopic data. To accomplish this, either multiple sources at different wavelengths or a broadband source with a monochromator will be required. All

components in these systems, except the PEMs, operate over a reasonably wide wavelength range (either visible or visible to NIR). While the PEMs operate from 200 to 2000 nm, the user-selected magnitude of retardance must be selected for a specific wavelength, as the PEM strain (voltage) required to induce this retardance will be different for each wavelength. As such, spectroscopic measurements will have to be conducted a single wavelength at a time, in a wavelength-scanning manner. To experimentally validate the dual modality method, controlled phantoms will also be required. These can be aqueous-based phantoms with either polystyrene microspheres or intralipid used as scattering particles, bovine serum as optically active proteins, and glucose. Using such a phantom system along with a spectral polarimetry system, the dual modality approach could be experimentally tested.

## 5.4 Conclusions and Accomplishments

The field of tissue polarimetry is an emerging area of biophotonics that has received increased attention in recent years. While potential applications have been demonstrated, challenges remain experimentally for measurement techniques and signal analysis. In addition, simulation techniques for polarized light in tissue are in need of advancements to more accurately represent tissue. These shortcomings in the field, as well as novel applications of polarized light in biomedical optics, were investigated in this thesis.

The extended Monte Carlo model, tissue phantom system, and dual modality glucose sensing are novel polarimetry techniques and provide additional useful tools for our research group as well as others in the field. As well, the application of birefringence

measurements for monitoring stem cell therapies of myocardial infarction is a novel application for which we have demonstrated potential and are pursing further studies.

# Appendix A: Example of forward and reverse Mueller matrix analysis

In this supplement, an example of forward and reverse Mueller matrix modeling is given to illustrate the methods employed in this thesis. The generation of a Mueller matrix (forward modeling) can be accomplished through either the upgraded Monte Carlo modeling or experimental measurements on the developed polyacryamide phantoms. In this example, we use an experimentally measured matrix from a phantom with known properties. Given a Mueller matrix, the polarization effects contained within this matrix can then be extracted using polar decomposition (reverse modeling). It is demonstrated that by decomposing the measured Mueller matrix, we can extract the input polarization values used to generate the original matrix. This generated matrix is the same as given in Chapter 3 on page 59 that was used as part of validation studies for Mueller matrix decomposition. However, in this example additional details are provided regarding both the measurement/generation of the matrix as well as the polar decomposition process.

## A.1 Mueller matrix generation

Generation of a Mueller matrix with user-defined polarization parameters can be accomplished through either Monte Carlo with our upgraded model, or through measurements on the developed polyacryamide phantoms with known polarization properties. In both cases, the scattering, birefringence, and optical activity of the sample, and thus the polarization parameters forming the Mueller matrix, are known inputs. Both the model and the experimental phantom represent powerful Mueller matrix generating

tools to controllably model the effects of polarized light in tissue-like media. The Monte Carlo model employs the Jones N-matrix formalism to combine the effects of birefringence and optical activity, in the presence of scattering, as discussed on pages 37-38. In this example, we generate a Mueller matrix through fabrication and experimental measurements on a polyarylamide phantom. However, in the following sections we describe the general approach for both the model and experimental phantom. The phantom for this study was a polyacrylamide $1 \times 1 \times 4$ cm$^3$ cuboid, fabricated following the methods on page 39 and 40.

### A.1.1 Scattering

In both model and phantoms experiments, scattering is dealt with through the inclusion mono-dispersed spherical micro-particles. For the phantoms, this is generally accomplished through the use of polystyrene microspheres (refractive index $n$ = 1.59, density $\rho$ = 1.05 g/cm, and diameters ranging from 0.1 to 10 μm). In the Monte Carlo model, both the size of the spheres and their refractive index are specified as inputs, which are then used to calculate the scattering cross section, phase function, single scattering Mueller matrix, and scattering anisotropy. The overall scattering coefficient of the medium is controlled by the volume fraction of spheres present (number of spheres per unit volume). In the model, the scattering coefficient is specified, while in the phantom the appropriate weight fraction of spheres needed to create the desired volume fraction, and thus scattering coefficient, is calculated through Equation (21) on page 40. In this example, a phantom was fabricated with polystyrene microspheres (diameter = 1.4

μm, scattering efficiency = 2.22, single scattering anisotropy $g$ = 0.95 calculated from Mie theory) with a scattering coefficient of $\mu_s = 30\ cm^{-1}$.

### A.1.2 Birefringence

Birefringence in the Monte Carlo model is specified both in terms of its direction (by a three element directional vector) and by the magnitude of the extraordinary refractive index, making the model highly flexible in terms of values of birefringence that can be simulated. This is in contrast to the phantoms where birefringence is induced by strain (extension), and is thus more limited in terms of the magnitudes and orientation of birefringence that can be generated. In Figure 4 on page 40, the induced birefringence and retardance (related by Equation (8) on page 6) as a function of phantom extension are plotted. These calibration plots can are used to experimentally induce a desired birefringence (retardance) in a phantom by extending the sample by a set distance. It should be noted that these calibrations are valid only for polyacrylamide as fabricated following the directions in the paper. In this example, the sample was extended by 2 mm to induce a retardance of 0.83 rad (effect of birefringence for light propagating ballistically through the phantom, with the slight phantom width reduction corrected for).

### A.1.3 Optical activity

Similar to birefringence, optical activity is specified in the model as a rotation in radians per cm, again making the model tremendously flexible in regards to the values of optical activity that can be simulated. In contrast, the phantom is more limited as physical

quantities of optically active molecules must be added, thus limiting the values of the resultant optical activity. In the presented example, sucrose is added as an optically active molecule with a rather high concentration of 1 M, giving a magnitude of optical activity of 1.96 deg/cm. Sucrose was used instead of glucose, as it does not interfere with the polymerization of polyacrylamide.

### A.1.4 Mueller matrix generation

Given either a specified Monte Carlo model (or fabricated phantom), simulations (or measurements) with varying input polarization states can be conducted to generate the sample Mueller matrix, following Equation (4) on page 72. In this example, the necessary measurements were conducted using the experimental system, described on page 38, to construct the Mueller matrix, yielding:

$$\mathbf{M} = \begin{bmatrix} 1 & 0.0185 & 0.0029 & 0.0042 \\ 0.0172 & 0.7569 & -0.0405 & 0.0462 \\ 0.0034 & 0.0524 & 0.545 & -0.5466 \\ 0.0024 & -0.007 & 0.6244 & 0.5967 \end{bmatrix}.$$

The complexity of this measured Matrix is evident as all 16 elements are non-zero, demonstrating the difficulties in extracting quantitative polarimetric information. This experimentally measured Mueller matrix will now be decomposed (reverse analysis) to extract the individual polarization parameters.

## A.2 Mueller matrix decomposition

A given Mueller matrix can be expressed as the product of three sub-matrices, $\mathbf{M} = \mathbf{M_\Delta M_R M_D}$, where these sub-matrices represent the effects of depolarization, linear and circular retardance, and diattenuation (different absorptions for either linear or circular polarization states) respectively. Other orderings of these matrices are possible,[122] however, this particular order has been shown to always lead to physically realizable matrices in the decomposition process. From these decomposed "basis" sub-matrices, the individual effects of diattenuation, depolarization, retardance, and optical activity can be extracted. The following section presents the decomposition and extraction of the individual polarization parameters from the experimentally measured Mueller matrix.

### A.2.1 Diattenuation

The first step in polar decomposition is the calculation of the diattenuation matrix $\mathbf{M_D}$ from the overall matrix $\mathbf{M}$. This is accomplished through equations 2 – 4 in Manhas *et al*.[41] In this example, the diattenation matrix was calculated as:

$$\mathbf{M_D} = \begin{bmatrix} 1 & 0.0185 & 0.0029 & 0.0042 \\ 0.0185 & 1 & 0 & 0 \\ 0.0029 & 0 & 0.9998 & 0 \\ 0.0042 & 0 & 0 & 0.9998 \end{bmatrix}.$$

Note the perfect symmetry in the off-diagonal elements, and that the diagonal elements are all equal to or approximately 1. These characteristics are consistent with a matrix representing diattenuation. From this calculated diattenation matrix, the sample diattenuation $d$ can be calculated from the following equation,

$$d = \frac{1}{\mathbf{M}_D(1,1)}\sqrt{\mathbf{M}_D(1,2)^2 + \mathbf{M}_D(1,3)^2 + \mathbf{M}_D(1,4)^2}\,. \qquad \text{(A.1)}$$

From this equation, the diattenation is now calculated as 0.02, which is reasonable as no linear or circular diattenation was included in the model. It should be noted that the normalizing term in Equation (A.1) is generally not required as the initial Mueller matrices are generally normalized by element **M**(1,1) as part of the measurement process.

### A.2.2 Depolarization

As the matrix representing diattenuation was calculated in the previous section and is now no longer needed, this matrix $\mathbf{M_D}$ can removed from the overall matrix **M** by inverse multiplying,

$$\mathbf{M}' = \mathbf{M}\mathbf{M_D}^{-1} = \mathbf{M_\Delta}\mathbf{M_R}, \qquad \text{(A.2)}$$

leaving only the product of the depolarization $\mathbf{M_\Delta}$ and retardance $\mathbf{M_R}$ matrices, now defined as **M**′. Employing equations 6 - 8 in Manhas *et al*.[41] the depolarization matrix $\mathbf{M_\Delta}$ is calculated from **M**′, and in this example resulting in:

$$\mathbf{M_D} = \begin{bmatrix} 1 & 0 & 0 & 0 \\ 0.0031 & 0.7577 & 0 & 0 \\ 0.0031 & 0 & 0.7745 & 0 \\ -0.0017 & 0 & 0 & 0.8647 \end{bmatrix}.$$

Note that all non-diagonal elements in this matrix are approximately zero, consistent with a depolarizing matrix. The sample net depolarization **Δ** can now be calculated,

$$\Delta = 1 - \frac{\left|\mathrm{tr}(\mathbf{M}_\Delta) - 1\right|}{3}. \qquad \text{(A.3)}$$

The net depolarization from the Mueller matrix measured in this example is $\Delta = 0.21$, meaning that of when input fully polarized light is incident on the phantom, the output beam will have its polarization reduced by 21% (degree of polarization of light now 79%). This value is reasonable given the concentration of microspheres added to the phantom, and has also been verified by Monte Carlo simulations with matching optical properties where the depolarization was calculated as 0.19.

### A.2.3 Linear retardance and optical rotation

Similar to the previous section, the matrix for sample depolarization can now be removed from the $\mathbf{M}'$ by inverse multiplication,

$$\mathbf{M_R} = \mathbf{M_\Delta}^{-1}\mathbf{M}', \tag{A.4}$$

now leaving only the Mueller matrix representing the effects of linear birefringence (retardance) and optical activity (optical rotation), referred to as the retarder matrix $\mathbf{M_R}$. In this example, the retarder matrix was calculated as:

$$\mathbf{M_R} = \begin{bmatrix} 1 & 0 & 0 & 0 \\ 0 & 0.9972 & -0.047 & 0.0578 \\ 0 & 0.0742 & 0.6964 & -0.7138 \\ 0 & -0.0067 & 0.7161 & 0.6980 \end{bmatrix}.$$

The non-zero matrix elements in the bottom right 3 × 3 sub-matrix are consistent with a retarder matrix expressing both linear birefringence and optical rotation. From this final decomposed matrix, both the retardance $\delta$ and optical rotation $\psi$ can be calculated using the following equations,

$$\delta = \cos^{-1}\left(\sqrt{\left(\mathbf{M_R}(2,2)+\mathbf{M_R}(3,3)\right)^2+\left(\mathbf{M_R}(3,2)+\mathbf{M_R}(2,3)\right)^2}-1\right), \tag{A.5}$$

and $$\psi = \tan^{-1}\left(\frac{\mathbf{M_R}(3,2) - \mathbf{M_R}(2,3)}{\mathbf{M_R}(2,2) + \mathbf{M_R}(3,3)}\right). \quad \text{(A.6)}$$

This yields $\delta$ = 0.79 rad and $\psi$ = 2.05 deg, respectively. These calculated values correspond well with the input values of 0.83 rad and 1.84 deg (thickness slightly less than 1 cm due to width contraction) for retardance and optical activity, respectively. While scattering can induce changes in retardance and optical rotation due to polarization randomization and increased photon pathlength, in this case as scattering was relatively low ($\mu_s$ = 30 cm$^{-1}$) and forward peaked ($g$ = 0.95), thus the effects were small. The slightly higher optical rotation may be due to increased optical pathlength as a result of scattering, and the lower measured retardance may be a result of polarization randomization. The deviations between decomposed (calculated) values and experimental results my also be due to small measurement errors.

## A.3 Summary

This example demonstrates the generation of a sample Mueller matrix through either Monte Carlo modeling or experimental measurements on controllable phantoms, and the decomposition of the generated matrix into the sub-matrices to describe and extract the individual polarization interactions. From these decomposed matrices, the medium effects (specifically diattenuation, depolarization, retardance, and optical rotation) can be calculated. In this worked out example, it was shown that the effects calculated from the decomposition of the measured matrix closely match those specified as experimental input values. The results are summarized in Table A.1 below. The close agreement

between and extracted values demonstrates the validity of our forward (Monte Carlo and experimental phantoms) and reverse (Mueller matrix decomposition) approaches.

| **Parameter** | **Input experimental values (forward analysis)** | **Decomposed values (reverse analysis)** |
|---|---|---|
| Diattenuation | 0 | 0.02 |
| Depolarization | 0.19 | 0.21 |
| Retardance | 0.83 rad | 0.79 rad |
| Optical Rotation | 1.84 deg | 2.05 deg |

**Table A.1** Input experimental phantom parameters compared with those calculated from decomposing the measured Mueller matrix.

## *References*


1. D. S. Kliger, J. W. Lewis, and C. E. Randall, *Polarized Light in Optics and Spectroscopy*, Academic Press, San Diego (1990).

2. E. Bartholinus, "Eperimenta crystalli Islandici disdiaclastici quibus mire et insolita refractio delegitur," *Hafniae*, (1670).

3. C. Huyghens, *Traité de al Lumierè*, Van der Aa, Leiden, (1690).

4. I. Newton, *Opticks*, Royal Society, London, (1704).

5. E. Malus, "Su rune proprété de la lumière réfléchie," *Mem. Soc. Arcueil* **1**, (1808).

6. A. J. Fresnel, *Oeuvres Complètes*, L'Imprimeria Impériale, Paris, (1866).

7. J. C. Maxwell, "A dynamic theory of the electromagnetic field," *Proc. Roy. Soc.* **13**, (1864).

8. J. Michl and E. W. Thulstrup, *Spectroscopy with Polarized Light*, VCH, New York (1986).

9. C. A. Browne and F. W. Zerban, *Physical and Chemical Methods of Sugar Analysis*, Wily, New York (1941).

10. B. Jirgensons, *Optical Rotatory Dispersion of Proteins and Other Macromolecules*, Springer-Verlag (1960).

11. M. Gadsden, P. Rothwell, and M. J. Taylor, "Detection of circularly polarized-light from noctilucent clouds," *Nature* **278**, 628-629 (1979).

12. A. Chrysostomou, P. W. Lucas, and J. H. Hough, "Circular polarimetry reveals helical magnetic fields in the young stellar object HH 135-136," *Nature* **450**, 71-73 (2007).

13. V. V. Tuchin, L. Wang, and D. À. Zimnyakov, *Optical Polarization in Biomedical Applications*, Springer-Verlag, (2006).

14. R. C. Jones, "New calculus for the treatment of optical systems," *J. Opt. Soc. Am.* **32**, 488-493 (1941).

15. E. Hecht, *Optics*, 4nd Ed, Addison-Wesley, San Francisco (2002).

16. J. M. Schmitt, A. H. Gandjbakhche, and R. F. Bonner, "Use of polarized light to discriminate short-path photons in a multiply scattering media," *Applied Optics* **31**, 6535-6546 (1992).

17. S. G. Demos and R. R. Alfano, "Temporal gating in highly scattering media by the degree of optical polarization," *Optics Letter* **21**, 161-163 (1996).

18. S. L. Jacques, J. C. Ramella-Roman, and K. Lee, "Imaging skin pathology with polarized light," *J. Biomedical Optics* **7**, 329-340 (2002).

19. S. L. Jacques, R. Samatham, S. Isenhath, and K. Lee, "Polarized light camera to guide surgical excision of skin cancers," *Proc. of SPIE* **6842**, 68420I (2008).

20. M. Gan and M. Gu, "Image reconstruction through turbid media under a transmission-mode microscope," *J. Biomedical Optics* **7**, 372-377 (2002).

21. S. P. Morgan and I. M. Stockford, "Surface-reflection elimination in polarization imaging of superficial tissues," *Optics Letters* **28**, 114-116 (2003).

22. K. Y. Yong, S. P. Morgan, I. M. Stockford, and M. C. Pitter, "Characterization of layered scattering media using polarized light measurements and neural networks," *J. Biomedical Optics* **8**, 504-511 (2003).

23. Y. Liu, Y. L. Kim, and V. Backman, "Development of a bioengineered tissue model and its application in the investigation of the depth selectivity of polarization gating," *Applied Optics* **44**, 2288-2299 (2005).

24. H. van de Hulst, *Light Scattering by Small Particles*, Dover, New York, 1957.

25. V. Backman, R. Gurjar, K. Badizadegan, I. Itzkan, R. R. Dasari, L. T. Perelman, and M. S. Feld, "Polarized light scattering spectroscopy for quantitative measurement of epithelial cellular structures in situ," *IEEE J. Selected Topics in Quantum Electronics* **5**, 1019-1027 (1999).

26. R. S. Gurjar, V. Backman, L. T. Perelman, I. Georgakoudi, K. Badizadegan, I. Itzkan, R. R. Dasari, and M. S. Feld, "Imaging human epithelial properties with polarized light scattering spectroscopy," *Nat. Med.* **7**, 1245-1249 (2001).

27. M. Bartlett, G. Huang, L. Larcom, and H. Jiang, "Measurement of particle size distribution in mammalian cells *in vitro* by use of polarized light spectroscopy," *Appl. Opt.* **43**, 1296-1307 (2004).

28. J. R. Mourant, T. M. Johnson, and F. P. Freyer, "Characterizing mammalian cells and cell phantoms by polarized backscattering fiber-optic measurements," *Appl Opt.* **40**, 5114-5123 (2001).

29. F. Jaillon and H. Saint-Jalmes, "Scattering coefficient determination in turbid media with backscattred polarized light," *J. Biomedical Optics* **10**, 034016 (2005).

30. V. Sankaran, J. T. Walsh, and D. J. Maitland, "Comparative study of polarized light propagation in biologic tissues," *J. Biomedical Optics* **7**, 300-306 (2002).

31. P. J. Wu and J. T. Walsh, "Stokes polarimetry imaging of rat tail tissue in a turbid medium: degree of linear polarization image maps using incident linearly polarized light," *J. Biomedical Optics* **11**, 014031 (2006).

32. D. F. T da Silva, B. C. Vidal, D. M. Zezell, T. M. T. Zorn, S. C. Núñez, and M. S. Ribeiro, "Collagen birefringence in skin repair in response to red polarized-laser therapy," *J. Biomedical Optics* **11**, 024002 (2006).

33. P. Whittaker, S. Zheng, M. J. Patterson, R. A. Kloner, K. E. Daly, and R. A. Hartman, "Histologic signatures of thermal injury: applications in t ransmyocardial laser revascularization and radiofrequency ablation," *Lasers in Surgery and Medicine* **27**, 305-318 (2000).

34. J. F. de Boer and T. E. Milner, "Review of polarization sensitive optical coherence tomography and Stokes vector determination," *J. Biodmed. Opt.* **7**, 359-371 (2002).

35. J. F. de Boer, S. M. Srinivas, A. Malekafzali, Z. Chen, and J. S. Nelson, "Imaging thermally damaged tissue by polarization sensitive optical coherence tomography," *Optics Express* **3**, 212-218 (1998).

36. K. Schoenenberger, B. W. Colston, D. J. Maitland, L. B. Da Silva, and M. J. Everett, "Mapping of birefringence and thermal damage in tissue by use of polarization-sensitive optical coherence tomography," *Applied Optics* **37**, 6026-6036 (1998).

37. B. Cense, T. C. Chen, B. H. Park, M. C. Pierce, and J. F. de Boer, "*In vivo* birefringence and thickness measurements of the human retinal nerve fiber layer using polarization-sensitive optical coherence tomography," *J. Biomedical Optics* **9**, 121-125 (2004).

38. G. L. Coté, M. D. Fox, and R. B. Northrop, "Noninvasive optical polarimetric glucose sensing using a true phase measurement techniques," *IEEE Transactions on Biomedical Engineering* **39**, 752-756 (1992).

39. J. S. Baba, B. D. Cameron, S. Theru, and G. L. Coté, "Effect of temperature, pH, and corneal birefringence on polarimetric glucose monitoring in the eye," *J. Biomedical Optics* **7**, 321-328 (2002).

40. M. Mehrübeoğlu, N. Kehtarnavaz, S. Rastegar, and L. V. Wang, "Effect of molecular concentrations in tissue-simulating phantoms on images obtained using diffuse reflectance polarimetry," *Optics Express* **3**, 286-297 (1998).

41. S. Manhas, M. K. Swami, P. Buddhiwant, N. Ghosh, P. K. Gupta, and K. Singh, "Mueller matrix approach for determination of optical rotation in chiral turbid media in backscattering geometry," *Optics Express* **14**, 190-202 (2006).

42. A. J. Welch and M. J. C. van Gemert, *Optical-Thermal Response of Laser Irradiated Tissue*, Chapter 2, Plenum Press, New York (1995).

43. A. J. Welch, G. Yoon, and M. J. Gemert, "Practical models for light distribution in laser-irradiated tissue," *Lasers in Surgery and Medicine* **6**, 488-493 (1987).

44. M. S. Patterson, B. C. Wilson, and D. R. Wyman, "The propagation of optical radiation in tissue I. Models of radiation transport and their application," *Lasers Medical Science* **6**, 155-166 (1990).

45. R. Eckhard, "Stan Ulam, John Von Neuman and the Monte Carlo method," *Los Alamos Science* **15**, 131-136 (1987).

46. N. Meterpolis and S. Ulam, "The Monte Carlo method," *Journal of the American Statistical Association* **24**, 101-121 (1949).

47. B. C. Wilson and G. Adam, "A Monte Carlo model for the absorption and flux distributions of light in tissue," *Medical Physics* **10**, 824-830 (1983).

48. L. Wang, S. L. Jacques, and L. Zheng, "MCML – Monte Carlo modeling of light transport in multi-layered tissues," *Computer Methods Programs Biomed.* **47**, 131-146 (1995).

49. F. Jaillon and H. Saint-Jalmes, "Description and time reduction of a Monte Carlo code to simulate propagation of polarized light through scattering media," *Applied Optics* **42**, 3290-3296 (2003).

50. B. Kaplan, G. Ledanois, and B. Drevillon, "Mueller matrix of dense polystyrene latex sphere suspensions: measurements and Monte Carlo simulations," *Applied Optics* **40**, 2769-2777 (2001).

51. M. Moscoso, J. B. Keller, and G. Papanicolaou, "Depolarization and blurring of optical images by biological tissues," *J. Optical Society of America A* **18**, 946-960 (2001).

52. S. Bartel and A. H. Hielscher, "Monte Carlo simulations of the diffuse backscattering Mueller matrix for highly scattering media," *Applied Optics* **39**, 1580-1588 (2000).

53. L. V. Kuz'min, I. V. Meglinski, and D. Y. Churmakov, "Coherent effects in multiple scattering of linearly polarized light," *Optics and Spectroscopy* **98**, 653-659 (2005).

54. J. C. Ramella-Roman, S. A. Prahl, and S. L. Jacques, "Three Monte Carlo programs of polarized light transport into scattering media: part I," *Optics Express* **13**, 4420-4438 (2005).

55. J. C. Ramella-Roman, S. A. Prahl, and S. L. Jacques, "Three Monte Carol programs of polarized light transport into scattering media: part II," *Optics Express* **13**, 10392-10405 (2005).

56. D. Côté and I. A. Vitkin, "Robust concentration determination of optically active molecules in turbid media with validated three-dimensional polarization sensitive Monte Carlo calculations," *Optics Express* **13**, 148-163 (2005).

57. D. Côté and I. A. Vitkin, "Pol-MC: a three-dimensional polarization-sensitive Monte Carlo implementation for light propagation in tissue," Available at: http://www.novajo.ca/ont-canc-inst-biophotonics/.

58. S. A. Prahl, D. D. Duncan, D. G. Fischer, "Monte Carlo propagation of spatial coherence," *Proceedings of SPIE* **7187**, 71870G-1 (2009).

59. C. F. Bohren and D. R. Huffman, *Absorption and Scattering of Light by Small Particles*, Chapter 4, Wiley-Interscience (1983).

60. L. Henyey and J. Greenstein, "Diffuse radiation in the galaxy," *Astrophysics Journal* **93**, 70-83 (1941).

61. W. Wang and L. V. Wang, "Propagation of polarized light in birefringent media: a Monte Carlo study," *J. Biomedical Optics* **7**, 350-358 (2002).

62. S. V. Gangnus, S. J. Matcher, and I. V. Meglinski, "Monte Carlo modeling of polarized light propagation in biological tissue," *Proceedings of SPIE* **4619**. 281-288 (2002).

63. X. Wang, G. Yoa, and L. V. Wang, "Monte Carlo model and single scattering approximation of the propagation of polarized light in turbid media," *Applied Optics* **41**, 792-801 (2002).

64. R. C. Jones, "New calculus for the treatment of optical systems. VII. Properties of the *N*-matrix," *J. Optical Society of America* **38**, 671-685 (1948).

65. World Health Organization, http://www.who.int/cardiovascular_diseases/en/index.html, accessed December 2009.

66. Statistics Canada, "Deaths by selected grouped causes, sex, and geography — Canada," www.statscan.gc.ca, accessed December 2009.

67. MedicineNet.com, "Heart attack (mycardial infarction)," http://www.medicinenet.com/heart_attack/article.htm, accessed May 2010.

68. C. A. Goldthwaite, "Mending a broken heart: stem cells and cardiac repair," http://stemcells.nih.gov/info/2006report/2006Chapter6.htm, National Institutes of Health, accessed Sept 2010.

69. K. R. Chien, "Regenerative medicine and human models of human disease," *Nature* **453**, 302-305 (2008).

70. T. Reya, S. J. Morrison, M. F. Clarke, and I. L. Weissman, "Stem cells, cancer, and cancer stem cells," *Nature* **414**, 105-111 (2001).

71. M. Jain, H. DerSimonian, D. A. Brenner, S. Ngoy, P. Teller, A. S. B. Edge, A. Zawadzka, K. Wetzel, D. B. Sawyer, W. S. Colucci, C. S. Apstein, and R. Liao, "Cell therapy attenuates deleterious ventricular remodeling and improves cardiac performance after myocardial infarction," *Circulation* **103**, 1920-1927 (2001).

72. D. Orlic, J. Kajstura, S. Chimenti, I, Jackoniuk, S. M. Anderson, B. Li, J. Pickel, K. MacKay, B. Nadal-Ginard, D. M. Bodine, A. Leri, and P. Anversa, "Bone marrow cells regenerate infarcted myocardium," *Nature* **410**, 701-705 (2001).

73. R. Passier, L. W. van Laake, and C. L. Mummery, "Stem-cell-based therapy and lessons from the heart," *Nature* **453**, 322-329 (2008).

74. N. Christoforou and J. D. Gearhart, "Stem cells and their potential in cell-based cardiac therapies," *Progress in Cardiovascular Diseases* **49**, 396-413 (2008).

75. Y. Sun, J. Q. Zhang, J. Zhang, and S. Lamparter, "Cardiac remodeling by fibrous tissue after infarction," *J. Lab. Clin. Med.* **135**, 316-323 (2000).

76. X. Xu, Z. Xu, Y. Xu, and C. Cui, "Selective down-regulation of extracellular matrix gene expression by bone marrow derived stem cell transplantation into infarcted myocardium," *Circ. J.* **69**, 1275-1283 (2005).

77. M. G. Shim, B. C. Wilson, E. Marple, and M. Wach, "Study of fiber-optic probes for in vivo medical Raman spectroscopy," Applied Spectroscopy 52, 619-627 (1999).

78. J. S. Baba, J. C. Criscione, K. K. Hudson, and G. L. Coté, "Application of Polarization microscopy for the non-stained determination of myo-lamina morphology in the Rat," *Proc SPIE* **5325**, 111-114 (2004).

79. P. Jouk, Y. Usson, G. Michalowicz, and F. Parazza, "Mapping of the orientation of myocardial cells by means of polarized light and confocal scanning laser microscopy," *Microscopy Research and Technique* **30**, 480-490 (1995).

80. P. Jouk, A. Mourd, V. Milisic, G. Michalowicz, A. Raoult, D. Caillerie, and Y. Usson, "Analysis of the fiber architecture of the heart by quantitative polarized light microscopy. Accuracy, limitations and contribution to the study of the fiber architecture of the ventricles during fetal and neonatal life," *European Journal of Cardio-thoracic Surgery* **31**, 915-921 (2007).

81. P. Whittaker, D. R. Boughner, and R. A. Kloner, "Role of collagen in acute myocardial infarct expansion," *Circulation* **84**, 2123-2134 (1991).

82. C. Sun, Y. Wang, L. Lu, C. Lu, I. Hsu, M. Tsai, C. Yang, Y. Kiang, and C. Wu, "Myocardial tissue characterization based on a polarization-sensitive optical coherence tomography system with an ultrashort pulsed laser," *J. Biomedical Optics* **11**, 054016 (2006).

83. L. C. U. Junqueira, G. Bignolas, and R. R. Brentani, "Picrosirius staining plus polarization microscopy, a specific method for collagen detection in tissue sections," *Histochemical Journal* **11**, 447-455 (1979).

84. P. Whittaker, D. R. Boughner, and R. A. Kloner, "Analysis of healing after myocardial infarction using polarized light microscopy," *American Journal of Pathology* **134**, 879-893 (1989).

85. P. Whittaker, R. A. Kloner, D. R. Boughner, and J. G. Pickering, "Quantitative assessment of myocardial collagen with picrosirius red staining and circularly polarized light," *Basic Research in Cardiology* **89**, 397-410 (1994).

86. P. Whittaker, J. Müller-Ehmsen, J. S. Dow, L. H. Kedes, and R. A. Kloner, "Development of abnormal tissue architecture in transplanted neonatal rat myocytes," *Annals of Thoracic Surgery* **75**, 1450-1456 (2003).

87. G. M. Tabel, P. Whittaker, K. Vlachanossios, M. Sonawala, and P. A. Chandraratna, "Collagen fiber morphology determines echogenicity of

myocardial scar: implications for image interpretation," *Echocardiography* **23**, 103-107 (2006).

88. P. Aknyari, P. Fedak, R. D. Weisel, T. J. Lee, S. Verma, D. A. G. Mickle, and R. Li, "Mechanical stretch regimen enhances the formation of bioengineered autologous cardiac muscle grafts," *Circulation* **106**, I 138-142(2002).

89. S. Thomsen, J. A. Pearce, and W. Cheong, "Changes in birefringence as markers of thermal damage in tissues," *IEEE Transactions on Biomedical Engineering* **36**, 1174-1179 (1989).

90. N. Nyolczas, S. Charwat, A. Posa, R. Hemesberger, N. Pavo, H. Hemetsberger, I. J. Pavo, D. Glogar, G. Maurer, and M. Gyöngyösi, "Tracking the migration of cardially delivered therapeutic stem cells *in vivo*: state of the art," *Regenerative Medicine* **4**, 407-422 (2009).

91. S. P. Nighswander-Rempel, V. V. Kupriyanov, and R. A. Shaw, "Regional cardiac tissue oxygenation as a function of blood flow and $pO_2$: a near-infrared spectroscopic imaging study," *J. Biomed. Optics* **11**, 0540004 (2006).

92. E. M. C. Hillman, O. Bernus, E. Pease, M. B. Bouchard, and A. Pertsov, "Depth-resolved optical imaging of transmural electrical propagation in perfused heart," *Optics Express* **15**, 17827-17841 (2007).

93. B. C. Wilson, I. A. Vitkin, and D. L. Matthews, "The potential of biophotonic techniques in stem cell tracking and monitoring of tissue regeneration applied to cardiac stem cell therapy," *J. Biophotonics* **2**, 669-681 (2009).

94. Konofaguo, E. E., D'hoogle, J. and Ophirm, J., "Myocardial elastography – a feasibility study *in vivo*," *Ultrasound in Medicine and Biology* **28**, 475-482 (2002).

95. Fallert, M. A., Mirotznik, M. S., Downing, S. W., Savage, E. B., Foster, K. R., Josephson, M. E. and Bogen, D. K., "Myocardial electrical impedance mapping of ischemic sheep hearts and healing aneurysms," *Circulation* **87**, 199-207 (1993).

96. E. X. Wu, Y. Wu, J. M. Nicholls, J. Wang, S. Liao, S. Zhu, C. Lau, and H. Tse, "MR diffusion tensor imaging study of post infarct myocardium structural remodeling in a procine model," *Magnetic Resonance in Medicine* **58**, 687-695 (2007).

97. Canadian Diabetes Association, http://www.diabetes.ca/about-diabetes/what/prevalence/, accessed January 2010.

98. J. A. Tamada, M. Lescho, and M. J. Tierney, "Keeping watch on glucose: new monitors help fight the long-term complications of diabetes," *IEEE Spectrum* **Sept**., 2-7, (2003).

99. L. C. Clark and C. Lyons, "Electrode systems for continuous monitoring in cardiovascular systems," *Ann. N. Y. Acad. Sci.* **102**, 29-45 (1960).

100. D. S. Bindra, Y. Zhang, G. S. D. Wilson, R. Sternberg, D. R. Thevenot, D. Moatti, and G. Reach, "Design and in vitro studies of a needle-type glucose sensor for subcutaneous monitoring," *Anal. Chem.* **63**(17), 1692-1696 (1991).

101. Q. Yang, P. Atanasov, and E. Wilkins, "A needle-type sensor for monitoring glucose in whole blood," *Biomed. Intrum. Technol.* **31**(1), 54-62 (1997).

102. A. Maran, C. Crepaldi, A. Tiengo, et al. "Continuous subcutaneous glucose monitoring in diabetic patients: A multicenter analysis," *Diabetes Care* **25**, 347-352 (2002).

103. J. Pickup, "Sensitive glucose sensing in diabetics," *Lancet* **355**, 426-427 (2000).

104. M. A. Arnold, J. J. Burmeister, and G. W. Small, "Phantom glucose calibration models from simulated noninvasive human near-infrared spectra," *Anal. Chem.* **70**, 1773-1281 (1998).

105. M. Tarumi, M. Shimada, T, Murakami, M. Tamura, M. Shimada, H. Arimoto, and Y. Tamada, "Simulation study of in vitro glucose measurements by NIR spectroscopy and a method of error reduction," *Phys. Med. Biol.* **48**, 2373-2390 (2003).

106. K. V. Larin, M. Motamdie, M. S. Eledrisi, and R. O. Esenaliev, "Noninvase blood glucose monitoring with optical coherence tomography," *Diabetes Care* **25**, 2263-2267 (2002).

107. W. Schrader, P. Meuer, J. Popp, W. Kiefer, J. Menzebach, and B. Schrader, "Non-invasive glucose determination in the human eye," *J. Molecular. Struct.* **735-736**, 299-306 (2005).

108. J. W. Buchert, "Thermal emission spectroscopy as a tool for non-invasive blood glucose measurements," *Proc. SPIE* **5566**, 100-110 (2004).

109. J. T. Olesberg, L. Liu, V. V. Zee, and M. A. Arnold, "In vivo near-infrared spectroscopy of rat skin tissue with varying blood glucose levels," *Proc. SPIE* **5325**, 11-20 (2004).

110. A. Rosencwaig, *Photoacoustics and Photoacoustic Spectroscopy*, R. E. Kliger

Publishing, 1977.

111. H. MacKenzie, H. S. Ashton, S. Spiers, Y. Shen, S. S. Freeborn, J. Hannigan, J. Lindberg, and P. Rae, "Advances in photoacoustic noninvasive glucose testing," *Clinc. Chem.* **45**, 1587-1595 (1999).

112. A. J. Berger, I. Itzkan, and M. S. Feld, "Feasibility of measuring blood glucose concentration by near-infrared Raman spectroscopy," *Spetrochimica Acta Part A* **53**, 287-292 (1997).

113. A. M. K. Enejder, T. G. Scecina, J. Oh, M. Hunter, W. Shih, S. Sasic, G. L. Horowitz, and M. S. Feld, "Raman spectroscopy for noninvasive glucose measurements," *J. Biomed. Opt.* **10**, 031114 (2005).

114. Y. Wickramasinghe, Y. Yang, and S. A. Spencer, "Current problems and potenial techniques in in vivo glucose monitoring," *J. Fluorescence* **14**, 513-520 (2004).

115. R. Badugu, J. R. Lakowicz, and C. D. Geddes, "Ophthalmic glucose monitoring using disposable contact lenses-a review," J. Fluorescence **14**, 617-633 (2004).

116. R. J. McNichols and G. L. Coté, "Optical glucose sensing in biological fluids: an overview," *J. Biomed. Opt.* **5**, 5-16 (2000).

117. K. C. Hadley and I. A. Vitkin, "Optical rotation and linear and circular depolarization rates in diffusely scattered light from chiral, racemic, and achiral turbid media," *J. Biomed. Opt.* **7**, 291-299 (2002).

118. D. Côté and I. A. Vitkin, "Balanced detection for low noise precision polarimetric measurements of optically active, multiply scattering tissue phantoms," *J. Biomed. Opt.* **9**, 213-220 (2004).

119. X. Guo, M. F. G. Wood, and I. A. Vitkin, "Angular resolved linear Stokes polarimeter measurements of light scattered by turbid chiral media," *J. Biomed. Opt.* **11**, 041105 (2006).

120. Q. Wan, G. L. Coté, and J. B. Dixon, "Dual-wavelength polarimetry for montiroing glucose in the presence of varying birefringence," *J. Biomed. Opt.* **10,** 024029 (2005).

121. S. Y. Lu and A. Chipman, "Interpretation of Mueller matrices based on polar decomposition," *J. Optical Society of America A* **13**, 1106-1113 (1996).

122. N. Ghosh, M. F. G. Wood, and I. A. Vitkin, "Simultaneous determination of linear retardance and optical rotation in birefringent, chiral, turbid medium using

Mueller matrix polarimetry: combined Monte Carlo and experimental methodology," *J. Biomed. Opt.* **13**, 044937 (2008).

123. T. Mizuno, T. M. Yau, R. D. Weisel, C. G. Kiani, and R. K. Li, "Elastin stabilizes an infarct and preserves ventricular function," *Circulation* **112**, I81-I88 (2005).

124. W. F. Cheong, S. A. Prahl, and A. J. Welch, "A review of the optical properties of biological tissues," *IEEE J. Quant. Elec*. **26**, 2166-2185 (1990).

125. P. P. Sengupta, V. K. Krishnamoorthy, J. Korinek, J. Narula, M. A. Vannan, S. J. Lester, J. A. Tajik, J. B. Seward, B. K. Khandheria, M. Belohlavek, "Left ventricular form and function revisited: applied translation science to cardiovascular ultrasound imaging," *J. Am. Soc. Echocardiogr.* 20, 539-551 (2007).

126. M. A. Wallenburg, M. F. G. Wood, N. Ghosh, M. Pop, G. Wright, I. A. Vitkin, "Comparison of optical polarimetry and diffusion tensor MR imaging for assessing myocardial anisotropy," *Journal of Innovative Optical Health Sciences*, in press, JIOHS-D-10-00002R1 (2010).

127. S. D. Giattina, B. K. Courtney, P. R. Herz, M. Harman, S. Shortkroff, D. L. Stamper, B. Liu, J. G. Fujimoto, and M. E. Brezinski, "Assessment of coronary plaque collagen with polarization sensitive optical coherence tomography," *International Journal of Cardiology* **107**, 400-409 (2006).

128. P. H. Hsiung, P. R. Nambiar, and J. G. Fujimoto, "Effect of tissue preservation on imaging using ultrahigh resolution optical coherence tomography," *J. Biomed. Optics* **10**, 064033 (2005).

129. J. W. Pickering, S. A. Prahl, N. van Wieringen, G. F. Beek, H. J. C. M. Sterenborg, and M J. C. van Gemert, "Double-integrating-sphere system for measuring the optical properties of tissue," *App. Opt.* **32**, 399-410 (1993).

130. M. Khurana, E. H. Moriyama, and B. C. Wilson, "Intravital high-resolution optical imaging of individual vessel response to photodynamic treatment," *J. Biomed. Opt.* **13**, 040502 (2008).

131. X. Guo, M. F. G. Wood, and I. A. Vitkin, "Stokes polarimetry in multiply scattering chiral media: effect of experimental geometry," *Applied Optics* **46**, 4491-4500 (2007).

132. J. M. Schmitt and G. Kumar, "Optical scattering properties of soft tissue: a discrete particle model," *Applied Optics* **37**, 2700-2797 (1998).

133. T. C. Oakberg, *Application Note – Stokes Polarimeter*, Hinds Intruments Inc, (1991), http://www.hindsinstruments.com/wp-content/uploads/StokesPolarimetry.pdf, accessed Oct 2010.

134. J. C. Kemp, G. D. Henson, C. T. Steiner, E. R. Powell, "The optical polarization of the Sun measured at a sensitivity of parts per million," *Nature* **326**, 270-273 (1987).

135. D. J. Diner, A. Davis, B. Hancock, G. Gutt, R. A. Chipman, and B. Cairns, "Dual-photoelastic-modulator-based polarimetric imaging concept for aerosol remote sensing," *Applied Optics* **46**, 8428-8445(2007).

136. C. Y. Han and Y. F. Chao, "Photoelastic modulated imaging ellipsometry by stroboscopic illumination technique," *Review of Scientific Instruments* **77**, 023107 (2006).

137. H. M. Tsai and Y. F. Chao, "Optimization of a four-temporal phase lock for photoelastic-modulated polarimetry," *Optics Letters* **34**, 2279-2281 (2009).